

Department of Applied Geology

**U-Th-Pb Systematics of Opaline Silica: Implications for the Dating of Surface
Processes**

Suzanne L Simons

**This thesis is presented for the Degree of
Doctor of Philosophy
of
Curtin University**

November 2015

DECLARATION

To the best of my knowledge and belief this thesis contains no material previously published by any other person except where due acknowledgment has been made.

This thesis contains no material which has been accepted for the award of any other degree or diploma in any university.

A handwritten signature in blue ink, appearing to read "S. A. J."

2 · 11 · 15

ACKNOWLEDGEMENTS

I would like to express my sincere appreciation to my supervisor Dr. Alexander Nemchin for his time and long standing guidance and encouragement despite numerous setback and time lapses. Without his assistance and faith in the value of this topic, this research would not have been possible.

I would like to thank the Cooperative Research Centre for Landscape Environments and Mineral Exploration for funding this research and to Curtin University for access to SHRIMP.

Several people contributed valuable and rare samples for this study - Dr. Alex Bevan, Terry Moxon, Gabor Papp and Dr. Leonid Neymark - I am very grateful. I would like to thank the staff of the School of Applied Geology, Curtin University of Technology for their support and access to samples, equipment and last minute help.

Lastly I would like to thank all my family and friends to constantly said to me “you should just finish it”. You all helped in one way or another.

ABSTRACT

U–Pb and U-series analyses of U-rich, relative to both Th and Pb, opal samples using sensitive high-resolution ion microprobe (SHRIMP) demonstrates the ability of this technique for dating opals with ages ranging from several tens of thousands of years to millions of years and from a variety of deposition environments. This experimental study increases the understanding of opal as a geochronometer and explores the stability of U-Th-Pb systematics in opaline silica.

Opal often shows microlayering reflecting the time sequence of silica deposition during slow growth. The major advantages of the technique, compared to the conventional thermal ionisation mass spectrometry (TIMS), are the high spatial resolution ($\sim 20\text{ }\mu\text{m}$ spot size), which minimizes analysing multiple layers with different ages, and the ability to analyse *insitu* all of the isotopes required to determine both U–Pb and U-series ages combined with a relatively short analysis time. Limitations of the technique include concentrations of U in opal less than $\sim 20\text{ ppm}$ which results in insufficient secondary ion beam intensities and the drift of U–Pb ratios in all analyses with time which were only weakly correlated with changes in other ratios. This drift is difficult to correct for and remains the main factor limiting the precision and accuracy of the U–Pb SHRIMP opal ages. Assumption of similar behaviour of the standard and unknown opals under similar analytical conditions allowed successful determination of ages with precisions of $\sim 10\%$. The $^{230}\text{Th}/\text{U}$ dating technique is used for samples younger than ~ 300 to $\sim 350\text{ ka}$ and occasionally for samples as old as $\sim 500\text{ ka}$, if the analytical errors are sufficiently small. $^{206}\text{Pb}-^{238}\text{U}$ and $^{207}\text{Pb}-^{235}\text{U}$ systems can be used to date opals of any age but are limited by the proportion of initial (non-radiogenic) Pb in the sample. SHRIMP-based U-series and U–Pb ages are consistent with TIMS dating results of the same materials and known geological timeframes.

SHRIMP $^{238}\text{U}-^{234}\text{U}-^{230}\text{Th}-^{206}\text{Pb}-^{235}\text{U}-^{207}\text{Pb}$ analysis of high U, low Th opal from $\sim 270\text{ m}$ below land surface in the unsaturated zone at Yucca Mountain, Nevada, resulted in ages varying from $11.8\pm 3.4\text{ Ma}$ near the base of the sample, close to the

contact with the host rock to as young as 48 ± 7 kyr for the outermost hemisphere consistent with the deposition sequence from the base to the top of the coating. SHRIMP discordance patterns are characterised by $T(^{238}\text{U}-^{234}\text{U}-^{206}\text{Pb})=T(^{238}\text{U}-^{230}\text{Th}-^{206}\text{Pb})>T(^{238}\text{U}-^{234}\text{U}-^{230}\text{Th})$ and $T(^{238}\text{U}-^{234}\text{U}-^{206}\text{Pb})=T(^{238}\text{U}-^{230}\text{Th}-^{206}\text{Pb})>T(^{235}\text{U}-^{207}\text{Pb})$ for young opal and $T(^{238}\text{U}-^{206}\text{Pb}) > T(^{235}\text{U}-^{207}\text{Pb})$ for older opal with both discordance patterns indicating an initial excess of ^{234}U . $T(^{238}\text{U}-^{234}\text{U}-^{206}\text{Pb})$ are older than both $T(^{238}\text{U}-^{234}\text{U}-^{230}\text{Th})$ and $T(^{235}\text{U}-^{207}\text{Pb})$ supporting initial presence of ^{222}Rn . The presence of excess ^{222}Rn increases the $^{206}\text{Pb}-^{238}\text{U}$ age by less than 100 kyr and in most cases by less than 20 kyr. Calculated growth rates range between 0.63 ± 0.45 to 1.08 ± 0.41 mm/Ma suggesting a slow and uniform deposition rate despite significant climate variations over the past 10 Ma.

Narrow opaline silica veins in groundwater calcretes from Yalgoo, Western Australia are one of the latest silicification events in the Yilgarn Craton. ^{230}Th -based ages vary systematically from ~ 150 kyr in the centre of the vein to ~ 40 kyr near the contact. Calculations investigating detrital ^{230}Th suggest that it is negligible. Precipitation of opal in water unsaturated conditions was continuous but variable and a growth rate of 10-100 $\mu\text{m}/\text{kyr}$ was calculated. Vein growth required simultaneous dissolution of calcrete and precipitation of opaline silica in a sub-vertical orientation. Oscillation of precipitation rates are evident with maxima at 45, 70, 90, 115-120 and 130-140 kyr suggesting opal deposition rates increased under the cooler climate conditions when compared to the Pleistocene paleoclimate.

Limestone hosted agate from South Dakota, USA was analysed using SHRIMP despite uranium concentration <50 ppm. No age data has previously been available for agates from this area and calculated U-Pb ages range from 35.4 ± 1.5 Ma to 638 ± 22 Ma. Low fractions of common Pb estimated from both ^{204}Pb and ^{208}Pb counts suggest that the correction for initial Pb is relatively insignificant. The spread in ages indicates the presence of two or more generation of opal and in some samples can be correlated with the variation in U concentration and suggests that the U-Pb system of agate sample did not remain closed. The spread in ages for all samples can be explained by either; a continuous deposition event, a series of individual deposition events or evidence of reworking due to silica remobilisation which effectively resets the U-Pb system. Comparison of the ages with the geological

timeframe of the host rock concludes that deposition was not penecontemporaneous with the formation of the host rock.

CONTENTS

1	Introduction	1
1.1	Purpose, scope and aims.....	1
2	U-Th-Pb Isotope Systematics and Geochemistry	3
2.1	Nuclides and radioactivity.....	3
2.2	Law of radioactive decay	4
2.3	Decay series, equilibrium and disequilibrium	5
2.3.1	Radioactive decay series.....	5
2.3.2	Secular equilibrium and disequilibrium	10
2.4	Geochemistry of uranium, thorium and lead	14
2.4.1	Accessibility and mobilisation	14
2.4.1.1	U, Th and Pb-bearing minerals	14
2.4.1.2	Weathering and release of U, Th and Pb	16
2.4.2	Transportation of nuclides	21
2.4.3	Other nuclides	24
2.5	Opal Mineralogy and environments of formation	26
2.5.1	Mineralogy	26
2.5.2	Environment of opal formation	29
2.5.2.1	Hydrothermal systems	31
2.5.2.2	Groundwater	32
2.5.3	Biogenic opal	32
2.5.4	Previous work	33
3	Analytical Techniques	36
3.1	Introduction	36
3.2	Sample collection and selection	36
3.3	SHRIMP	37
3.3.1	Advantages	37
3.3.2	Disadvantages	38
3.3.3	Simultaneous U-Pb and U-series analysis	38
3.4	^{238}U - ^{234}U - ^{230}Th - ^{206}Pb - ^{235}U - ^{207}Pb system applied to the opal chronology	39
3.5	Samples	41
3.5.1	Opal standard M21277	41

3.5.2 Opals from Guanajuato, Mexico and Hosszú Hill, Hungary	41
3.6 Analytical procedure – TIMS	43
3.6.1 Details of the analytical procedure – TIMS	43
3.7 Results –TIMS	44
3.7.1 Opal standard M21277	44
3.7.2 Opals from Guanajuato, Mexico	44
3.8 Analytical procedure – SHRIMP	44
3.8.1 General approach	44
3.8.2 Details of the analytical procedure – SHRIMP	47
3.8.3 Behaviour of secondary beam and calculation of isotope ratios	49
3.9 Data reduction	51
3.10 Results – SHRIMP	53
3.10.1 Data for opal standard M21277- establishing optimal analytical conditions	53
3.10.2 Th/U and Pb/U ratios	57
3.10.3 Opal from Guanajuato, Mexico	63
3.10.4 Opal from Hosszú Hill, Hungary	64
3.11 Summary and conclusions	70
4 Opal from Yucca Mountain, Nevada, USA	72
4.1 Introduction	72
4.2 Geological and hydrological units	73
4.3 Structural geology	76
4.4 Origin of opaline silica – two models	77
4.4.1 Evidence for meteoric model	78
4.4.2 Infiltrating waters	78
4.5 Previously determined ages and rates	84
4.6 Opaline silica depositional models	86
4.7 Results	88
4.7.1 HD2059	88
4.7.2 HD2019a	102
4.7.3 HD2074	104
4.8 Discussion	113
4.8.1 Summary of SHRIMP opal chronology	113
4.8.2 Observed age discordance	114

4.8.3 Deposition rates	116
4.9 Conclusions	117
5 Opal From River Valley Calcretes in the Yilgarn Craton, Western Australia	120
5.1 Introduction	120
5.2 Location and geological setting of samples	120
5.2.1 Precambrian geology	121
5.2.2 Permian and Cainozoic rocks	123
5.2.3 Timing of regolith development	124
5.2.4 Opaline silica veins in calcrete deposits in the Yilgarn Craton	126
5.3 Yalgoola Well, Western Australia	129
5.4 Nangcarrong Spring, Western Australia	130
5.5 SHRIMP analytical protocol and initial data reduction	132
5.6 Results	134
5.6.1 Yalgoola Well.....	136
5.6.2 Nangcarrong Spring.....	142
5.7 Discussion	142
5.7.1 Opaline silica vein orientation and formation	143
5.7.2 Interpolation of data for individual profiles	144
5.7.3 Continuous or episodic growth rates?	146
5.7.4 Opal deposition rates compared to Yucca Mountain	150
5.7.5 Opal deposition and global climate	150
6 Agate From South Dakota, USA	153
6.1 Introduction	153
6.2 Geology of South Dakota – Black Hills area	154
6.3 Agate composition and structure	155
6.4 Different types of agates – volcanic-hosted vs. sedimentary-hosted	157
6.4.1 Volcanic-hosted agate	157
6.4.2 Sedimentary-hosted agate	159
6.5 Dating results for South Dakota agate	160
6.5.1 SG7	161
6.5.2 Badlands	170
6.5.3 Prairie	172
6.6 Discussion	175

7 Conclusions	178
7.1 Advantages and disadvantages of the technique	178
7.2 U-series and U-Pb ages	179
7.3 Rates of deposition	180
7.4 Opal from various environments	180
References	181

LIST OF FIGURES

Figure 2.1 The basic structure of an atom, showing the electrons as solid red dots and the nucleus (protons and neutrons) as blue dots.	3
Figure 2.2 ^{232}Th decay series	7
Figure 2.3 ^{238}U decay series	8
Figure 2.4 ^{235}U decay series	9
Figure 2.5 Geochemical mobility and range of radionuclides. Range is depicted as the product of both half-life and solubility of each nuclide. Nuclides represented by circles are products of alpha decay and are susceptible to mobilisation by alpha recoil (from Osmond and Cowart, 1992)	17
Figure 2.6 Models of recoil causing $^{238}\text{U}/^{234}\text{U}$ disequilibrium. A) The recoiling nucleus finds itself in an unusual lattice site where it acquires an unusual charge state. B) The recoiling nucleus is stopped in the intergranular material. C) The nucleus recoils into an adjacent grain from which it escapes by diffusion along the damage track. D) The same as for C except that the damage is removed chemically by intergranular liquid (from Fleischer and Rabbe, 1978)	19
Figure 2.7 Conditions for diffusional Pb loss in metamict zircon. Curves represent time-temperature conditions under which a zircon of 100 μm radius will lose the indicated fraction of Pb. Also plotted is a curve which indicates the time-temperature conditions under zircon with 100 ppm uranium will become metamict. Times in excess of a billion years are necessary in order for the zircon to accumulate sufficient radiation damage to become metamict. Significant Pb loss will be likely only in the region below this curve (from Cherniak and Watson, 2000).	21
Figure 2.8 The range of predominance of dissolved thorium species in pure water. The distribution of thorium-hydroxy complexes vs pH at 25°C with $\Sigma\text{Th} = 0.01 \text{ ppb}$ in pure water (from Langmuir and Herman 1980).....	23
Figure 2.9 Crystal structure of cristobalite (from Heaney, 1994).....	26
Figure 2.10 Crystal structure of tridymite (from Heaney, 1994)	27
Figure 2.11 X-ray diffraction scans of opal-A, opal-CT and opal-C with quartz (Q) impurities present within opal-A (from Elzea and Rice, 1996)	28
Figure 3.1 (A) Photograph of the Mexican opal and host rock from Guanajuato, Mexico. (B) Photograph of the same opal and host rock under UV light showing the green fluorescence of the opal reflecting the uranium concentration.	42
Figure 3.2 (A) Photograph of the Hungarian opal sample from Hosszú Hill, Hungary showing the homogenous and transparent nature of the opal. (B) Photograph of the same opal under UV light showing the green fluorescence of the opal.....	42
Figure 3.3 Within-run variations of ^{238}U and ^{206}Pb counts (black dots – first run of a spot; open circles – second run). All plots show non-linear behaviour prohibiting line	

fitting, which is commonly used for initial SHRIMP data reduction. Uncertainties are shown as 2σ error bars in this and all other figures	50
Figure 3.4 Within-run behaviour of $^{206}\text{Pb}/^{238}\text{U}$ (black dots – first run of a spot; open circles – second run). During the second analysis of the same spot, the $^{206}\text{Pb}/^{238}\text{U}$ continues to decrease despite the refocusing of the secondary beam	55
Figure 3.5 A) Log-log plot showing session-by-session variations of $^{230}\text{Th}^{16}\text{O}/^{238}\text{U}^{16}\text{O}$ vs. $^{238}\text{U}/^{238}\text{U}^{16}\text{O}$ observed during analyses of opal standard M21277. B) Weighted average of all $^{230}\text{Th}/^{238}\text{U}$ obtained for the standard during this study.....	58
Figure 3.6 Non-radiogenic Pb corrected $^{206}\text{Pb}^*/^{238}\text{U}$ obtained during multiple runs of opal standard M21277. Both ^{204}Pb and ^{208}Pb corrections give very similar results. Larger deviation of points from the reference line for the O_2^- primary beam is a consequence of lower counting rate. The absolute value of ratios obtained with the O_2^- as a primary beam is much closer to the true value (shown as dashed lines) when compared to the ratios determined with O^- primary beam	62
Figure 3.7 $^{206}\text{Pb}^*/^{238}\text{U}$ vs. $^{238}\text{U}/^{238}\text{U}^{16}\text{O}$ log-log plot for the single SHRIMP session where each spot was analysed twice. The data show two components present in the drift of the Pb/U. The first component is correlated with the change in $^{238}\text{U}/^{238}\text{U}^{16}\text{O}$ during the run and can be corrected by the linear extrapolation of the data to the Y-axis. The second component apparently does not correlate with the $^{238}\text{U}/^{238}\text{U}^{16}\text{O}$ and causes systematically lower Pb/U for all second analyses of all spots. (Best fits are shown as dotted lines; First and second analyses of the same spot are connected with the tie lines).....	62
Figure 3.8 An $\ln(^{206}\text{Pb}^*/^{238}\text{U})$ vs. $\ln(^{238}\text{U}/^{238}\text{U}^{16}\text{O})$ plot showing the variation of Pb-U ratios obtained during all five scan runs of opal standard M21277. Squares and circles represent analyses with O_2^- and O^- primary beam, respectively (filled circles are analyses with ^{235}U and $^{238}\text{U}^{16}\text{O}$ – based run table). The Y-axis values for this plot are calculated from the measured $^{206}\text{Pb}/^{238}\text{U}$ ratios applying the ^{208}Pb non-radiogenic Pb correction and taking natural logarithms, whereas the X-axis values are obtained by taking the natural logarithms of measured $^{238}\text{U}/^{238}\text{U}^{16}\text{O}$ ratios	63
Figure 3.9 U-Pb SHRIMP (open ellipses) and TIMS (filled ellipses) data for the opal sample from Guanajuato, Mexico. The non-radiogenic Pb corrected Pb-U ratios, obtained with SHRIMP, have been normalised using sample M21277 as a standard.	66
Figure 3.10 U-Pb SHRIMP data for the opal sample from Hosszú Hill, Hungary (run with ^{238}U and $^{238}\text{U}^{16}\text{O}$ masses analysed is represented by the dark grey ellipses; run with ^{235}U and $^{235}\text{U}^{16}\text{O}$ masses analysed is shown as the light grey ellipses). The non-radiogenic Pb corrected Pb-U ratios have been normalised using sample M21277 as a standard	67
Figure 4.1 Geology of the Yucca Mountain area and location of the Exploratory Studies Facility tunnel (from Neymark and Amelin, 2008).. ..	73
Figure 4.2 Principal stratigraphic units at Yucca Mountain (from Stuckless and Dudley, 2002 with ages from Sawyer <i>et al.</i> , 1994)	75

Figure 4.3 Generalised east-west section through Yucca Mountain showing hydrological units (after Zhang <i>et al.</i> , 2006)	76
Figure 4.4 Showing the approximate location of the water table, unsaturated zone (UZ), saturated zone and the repository (from Wilson <i>et al.</i> , 2003).....	76
Figure 4.5 Schematic drawing of vapour phase parting and lithophysal cavity showing the high porosity, vapour-phase-altered selvage, and possible fracture flow paths intersecting both the parting, up dip from the cavity and the cavity. Flow paths are shown as arrows. Secondary calcite and silica are on the floor of the cavity, with a basal zone of enhanced porosity that may reflect the later dissolution (from Whelan <i>et al.</i> , 2002)	81
Figure 4.6a Typical mineral sequence coatings on a lithophysal cavity floor (from Whelan <i>et al.</i> , 1998).....	81
Figure 4.6b Typical mineral sequence coatings on a steeply dipping fracture surface (from Whelan <i>et al.</i> , 1998).....	82
Figure 4.7 A combination of white and short-wave ultraviolet light showing thin blades of calcite (grey) with clear bulbous cluster of opal (green) on top of angular sceptre head calcite overgrowths at the tips of calcite blades (from Paces <i>et al.</i> , 2001)	83
Figure 4.8 Conceptual models of episodic/instantaneous and continuous mineral deposition (from Paces <i>et al.</i> , 2001)	87
Figure 4.9. U-Pb and U-series ages of opal sample HD2059 from Yucca Mountain (Nevada, USA); (A) diagram showing areas within a slice of the sample analysed using ID-TIMS (modified from Neymark <i>et al.</i> , 2002); (B) UV-light image of different slice of the same sample analysed with SHRIMP with the ages of investigated opal parts (dark blue is non-luminescent calcite and green is opal); (C) distance vs. age plot for the outermost part of the opal sample (analysed spots are shown as red dots on the insert; area of the insert is shown as red square in B)	89
Figure 4.10. ^{206}Pb vs ^{238}U and ^{207}Pb vs ^{235}U plots for sample HD2059. Data are not corrected for the common Pb. Intercepts with the Y-axis determine initial Pb composition	90
Figure 4.11. Central part of the coating showing the location of the three veinlets and analyses in each of the veinlets. Yellow spots are from day 1 and red spots are from day 2.....	99
Figure 4.12 The $^{206}\text{Pb}/^{238}\text{U}$ vs. $^{207}\text{Pb}/^{235}\text{U}$ concordia plot of the central veins. Red ellipses denote veinlet 1; blue ellipses denote veinlet 2; green ellipses denote veinlet 3	100
Figure 4.13 The $^{206}\text{Pb}/^{238}\text{U}$ vs. $^{207}\text{Pb}/^{235}\text{U}$ concordia plot of the central veins corrected for the initial $^{234}\text{U}/^{238}\text{U}$ activity ratio as estimated by Paces <i>et al.</i> , (2004a). Red ellipses denote veinlet 1; blue ellipses denote veinlet 2; green ellipses denote veinlet 3	101

Figure 4.14. SHRIMP data for sample HD2019a; also showing a close-up of analysed areas	103
Figure 4.15 Polished cross section of an opal hemisphere from sample HD2074, showing thin, concentric layering. SHRIMP results are shown as a distance vs. age plot	106
Figure 4.16 SHRIMP analyses within the samples HD2074 and HD2059 for the areas, where ^{234}U is not equilibrated with ^{238}U . Circles correspond to the outermost analyses of hemisphere (sample HD2074, ^{238}U - ^{234}U - ^{230}Th age is plotted against the ^{238}U - ^{234}U - ^{206}Pb age); squares are the inner parts of the same hemisphere (^{235}U - ^{207}Pb age is plotted against the ^{238}U - ^{234}U - ^{206}Pb age); triangles are the outer opal coating of sample HD2059 (^{235}U - ^{207}Pb age is plotted against the ^{238}U - ^{234}U - ^{206}Pb age)	114
Figure 5.1 Tectonic division of the Yilgarn Craton, showing subdivision into terranes and showing the location of Yalgoo (modified from Cassidy <i>et al.</i> , 2006).....	121
Figure 5.2 Drainage map of southern Western Australia showing the location of the Meckering and Menzies lines (after Butt <i>et al.</i> , 1977) and the location of Yalgoola Well, Nangcarrong Spring and the Greenough River.....	128
Figure 5.3 The location of Yalgoola Well, Nangcarrong Spring and the town of Yalgoo. Pink colour represent the granites of the Murchison Domain and green is the greenstones of the Murchison Domain (modified from Watkins and Hickman, 1990).	129
Figure 5.4 Images showing the slab and mount under plain light (A) and under UV light (B). White squares show part of the slab that was used for SHRIMP analyses	130
Figure 5.5 Images showing the slab and mount under plain light (A) and under UV light (B). White squares show part of the slab that was used for SHRIMP analyses. Opal is the white mineral that fluoresces bright green under UV light	131
Figure 5.6 $^{230}\text{Th}/^{238}\text{U}$ and $^{234}\text{U}/^{238}\text{U}$ activity ratios measured in the standard opal M-21277 during three runs of Yalgoola Well sample	133
Figure 5.7 $^{230}\text{Th}/^{238}\text{U}$ and $^{234}\text{U}/^{238}\text{U}$ activity ratios measured in the standard opal M-21277 during two runs of Nangcarrong Spring sample	134
Figure 5.8 $^{207}\text{Pb}/^{206}\text{Pb}$ vs. $^{204}\text{Pb}/^{206}\text{Pb}$ plot of the first run for opal samples from Yalgoola Well, Western Australia. The red dot is modern Stacey-Kramers Pb Composition.	135
Figure 5.9 Results of U-series analyses of opal samples from Yalgoola Well (Yalgoo) and Nangcarrong Spring. A) analysed areas shown under the UV light (indicative of increase U concentration in the opal samples) with the location of analytical spots shown as circles of different colour. B) Th-ages along the individual profiles in the samples (error bars are 2σ). C) age distribution histograms for two analysed samples with average ages calculated for the identified maximums	137

Figure 5.10 Variation of opal growth rate in time determined from individual profiles for Yalgoola Well and Nangcarrong Spring samples.....	145
Figure 5.11 Constraining growth curves for the analytical profiles; top diagram shows an idealised sketch of a profile across the opal sample with the SHRIMP spots where lengths bound by boundaries half way between the spots are assumed to have an age similar to a SHRIMP spot between these boundaries; bottom diagram illustrates transformation of these length and age information to construct an average cumulative growth curve (shown in blue).....	146
Figure 5.12 Cumulative precipitation curves that describe silica precipitation with time for the three profiles from the Yalgoola Well (left) and Nangcarrong Spring (right), respectively	148
Figure 5.13 Average growth rate variation in time for Yalgoola Well (red) and Nangcarrong Spring (blue) samples	149
Figure 5.14 Correlation between the recorded opal growth rate and the global climate variation. A) opal growth rate variations; B) Southern Hemisphere summer (December-February) insolation pattern (Berger and Loutre, 1991); C) Temperature variation during the last 160 kyr, recorded by the Vostok ice core (from Jouzel <i>et al.</i> , 1987)	149
Figure 6.1 Location of the Black Hills, South Dakota, USA with the geology (from Martin <i>et al.</i> , 2004) with inset showing location of South Dakota (in red) within the USA	153
Figure 6.2 A) SG7 in plain light and B) under UV light	161
Figure 6.3 $^{207}\text{Pb}/^{235}\text{U}$ vs. $^{206}\text{Pb}/^{238}\text{U}$ concordia corrected for ^{208}Pb	162
Figure 6.4 $^{206}\text{Pb}/^{238}\text{U}$ weighted average age corrected for ^{208}Pb	163
Figure 6.5 $^{207}\text{Pb}/^{235}\text{U}$ weighted average age corrected for ^{208}Pb	163
Figure 6.6 A) Badlands in plain light and B) under UV light	170
Figure 6.7 $^{207}\text{Pb}/^{235}\text{U}$ vs. $^{206}\text{Pb}/^{238}\text{U}$ concordia diagram corrected for ^{208}Pb	171
Figure 6.8 Prairie sample under plain and UV light, highlighting the difference between the opal and host rock. Square shows area selected for SHRIMP analyses	172
Figure 6.9 Location of SHRIMP spots on Prairie sample (spots Pr6-3 and Pr6-27 are excluded from the dataset)	173
Figure 6.10 $^{207}\text{Pb}/^{235}\text{U}$ vs. $^{206}\text{Pb}/^{238}\text{U}$ concordia corrected for ^{208}Pb	174

LIST OF TABLES

Table 3.1 U-Pb and U- series TIMS data for opal sample M21277 used as a SHRIMP standard* and Mexican opal (all errors are 2σ)	46
Table 3.2 Run tables used for SHRIMP opal analysis	48
Table 3.3 The within session and external reproducibility of $^{234}\text{U}/^{238}\text{U}$, $^{230}\text{Th}/^{238}\text{U}$ and $^{206}\text{Pb}/^{238}\text{U}$ ratios in standard opal M21277; all data represent weighted averages of standard analyses collected for the individual sessions, their 95% confidence limits and MSWDs, calculated by ISOPLOT (Ludwig, 1999)	59
Table 3.4 SHRIMP data for two hyalite samples (errors are 2σ)	68
Table 4.1 SHRIMP results for opal samples from Yucca Mountain, USA (errors are 1σ) ..	91
Table 4.2 SHRIMP results for opal samples from Yucca Mountain (ages in kyr and initial $^{234}\text{U}/^{238}\text{U}$, errors are 2σ)	107
Table 5.1 U/PbSHRIMP data from the first run for opal samples from Yalgoola Well, Western Australia (errors are 1σ)	135
Table 5.2 SHRIMP results for opal samples from Yalgoola Well and Nangcarrong Spring, Western Australia (errors are 1σ)	138
Table 6.1 SHRIMP results for agate samples, South Dakota, USA (errors are 1σ).....	164
Table 6.2 SHRIMP results for agate samples from South Dakota (ages in Ma and errors are 1σ)	167

1.0 INTRODUCTION

1.1 Purpose and scope and aims

This thesis uses SHRIMP (Sensitive High Resolution Ion Microprobe) to determine ages and derive interpretations of formation of opaline silica ($\text{SiO}_2 \cdot n\text{H}_2\text{O}$) deposited in several different environments/geological settings. This information can be used to better understand chronology and the mechanisms of formation of opaline silica as well as processes that govern regolith evolution.

U–Pb geochronology of hydrogenic minerals is relatively under developed compared to geochronology of igneous minerals, and has been mostly limited to carbonates. Opaline silica has been demonstrated to be a successful U–Pb and ^{230}Th –U geochronometer because of its ability to not only concentrate uranium from water and an absence lead and thorium in near-surface aqueous solutions (due to their low solubilities) during formation, but to also preserve radiogenic lead and other decay products of uranium formed during the lifespan of the mineral.

The aim of this thesis was to develop a SHRIMP technique to gain accurate geochronological data for opals of various ages formed in different environments. A second aim was to determine the limitations of this approach and identify information about depositional environments from the chronological data.

In the course of this work geochronological data were used to interpret the mechanisms and processes responsible for opal deposition and where possible link those to past changes in the climate. Widespread occurrence of opaline silica together with high U concentrations and very low non-radiogenic Pb concentrations suggest that this mineral may eventually become a widely used geochronometer as zircon is in igneous and metamorphic rocks.

This is one of the first in-depth studies into the ages of opaline silica using SHRIMP and using samples from more than one location, providing a larger age range and encompassing different environments of formation. Published studies of a similar nature are limited to samples from the same location.

The work in this thesis is summarised in the following points which demonstrate the development of the technique, through to the dating of opals with no age constraints.

- 1) Initial development and testing of U-Pb and U-series dating of opaline silica using SHRIMP. Three uraniferous hyalite opal samples (previously dated Yucca Mountain hemispheres for U-series investigation and opal from Hungary and Mexico for U-Pb investigation) were used for this purpose.
- 2) A Yucca Mt sample was used for the fine tuning and testing of the technique and gave increased confidence in the method when compared with previously obtained ages and growth rates for the same samples.
- 3) Two West Australian opal samples were used to investigate applicability of the method to dating of Australian regolith as well as providing information on opal vein orientation, growth rates and depositional conditions.
- 4) South Dakota agate samples represent opal deposition in carbonates which has never been geochronologically investigated before. These samples tested the applicability of the technique on low uranium samples tens to hundreds of millions of years old.

2 U-TH-PB ISOTOPE SYSTEMATICS AND GEOCHEMISTRY

This chapter discusses the three different decay series; ^{232}Th , ^{238}U and ^{235}U as well as the causes and repercussions of disequilibrium within these decay series and the geochemistry and transportation of these isotopes. It also discusses different opal types and environments conductive to opal formation.

2.1 Nuclides and radioactivity

In a simple model, atoms are viewed as an assembly of negatively charged electrons, which move in orbit around a central nucleus. This nucleus is made up of positively charged protons and neutral particles called neutrons bound together by strong short range forces (Figure 2.1). Most atoms (nuclides) are stable in this formation and do not change with time. However, some nuclides are radioactive (unstable) which means that at any instant they may change into a different nuclide, a process known as radioactive decay. Stability for nuclides with low mass numbers (A , total number of protons and neutrons) is achieved when the number of neutrons and protons are approximately equal. As the mass number increases (elements with the atomic numbers from 20 to 83), so does the neutron/proton ratio required for stability, until it is close to 1.5. The radioactive nuclides change in an attempt to achieve stability by emitting particles and energy, hence adopting a lower energy state. It is this process that drives radioactive decay.

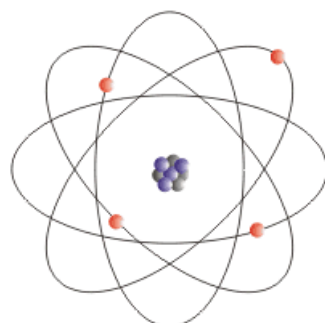


Figure 2.1 The basic structure of an atom, showing the electrons as solid red dots and the nucleus (protons and neutrons) as blue dots.

Loss of energy is achieved by emission of either a moderately light beta particle (a high energy, high speed electron or positron) or by a heavier alpha particle (2 protons and 2 neutrons). Alpha particles are positively charged nuclear particles that are identical with the nucleus of a helium atom that consists of two proton and two neutrons and is ejected at high speed in certain radioactive transformations. Highly unstable nuclides can decay by emission of an alpha particle (α), which causes a nuclide with atomic number, Z, to lose two protons and is thus transmuted into an element of atomic number $Z - 2$. An example of this is the decay of $^{238}\text{U}_{92}$ by alpha-particle emission to become $^{234}\text{Th}_{90}$. Nuclides that are more stable need to lose only a small amount of energy to become stable. This occurs by beta decay, which is the emission of a beta (β) particle. Beta particles are electrons and their emission changes the nuclide to another element of atomic number $Z + 1$. For example, $^{234}\text{Th}_{90}$ emits a beta particle to become $^{234}\text{Pa}_{91}$. Emission of a positron (positive electron) is another form of beta decay and changes the value of the nuclear Z but in the opposite sense to that for negative electron emission. For example, $^{22}\text{Ne}_{11}$ decays to $^{22}\text{Ne}_{10}$ upon emission of a positron.

2.2 Law of radioactive decay

Radioactive decay is a statistical process in which the decay rate is proportional to the number of radioactive nuclei of a particular type present at any time (t) (Rutherford and Soddy, 1902). The constant of proportionality (λ) is also known as the decay constant and is the probability of decay of a given atom per unit time interval. It is related to the half-life ($t_{1/2}$) of a radionuclide by the equation:

$$\lambda = 0.693 / t_{1/2}$$

The half-life of a radionuclide is the time required for the decay of exactly one half of the original number of its nuclei. The rates of decay of radionuclides are constant under conditions that occur at or near the surface of the earth. The decay rate can be expressed as:

$$dN/dt = -N\lambda = a$$

where N is the number of parent atoms, a is the activity of these atoms and dN/dt is the rate of depletion of the number of parent atoms which is negative because this rate decreases with time. dN/dt is equal to the activity as long as there is no new supply of radioactive atoms. The solution to the above equation can be expressed as:

$$N = N_0 e^{-\lambda t}$$

where N_0 is the initial number of radioactive atoms at $t=0$, and N is the number of remaining radioactive atoms at a later time (t).

The number of radiogenic daughter nuclei formed (D^*) is equal to the number of parent atoms consumed.

$$D^* = N_0 - N \quad (\text{but } N_0 = N e^{\lambda t})$$

$$D^* = N(e^{\lambda t} - 1)$$

If the number of daughter atoms at time $t = 0$ is D_0 , then the total number of daughter atoms after time, t , is:

$$D = D_0 + N(e^{\lambda t} - 1)$$

2.3 Decay series, equilibrium and disequilibrium

Equilibrium for a decay chain is reached when the rate of decay of each nuclide is equal to its rate of production. A number of geochronological techniques are based on disequilibrium between ^{235}U , ^{238}U , ^{232}Th and their immediate daughters. In addition, disequilibrium produced during the history of minerals and rocks can significantly bias observed relationships between these isotopes and the final products in the decay chains (^{206}Pb , ^{207}Pb and ^{208}Pb) leading to erroneous results in U-Pb dating. Therefore, an understanding of the mechanisms of disequilibrium is essential for an accurate interpretation of results for a wide range of dating techniques that use different combinations of ^{235}U , ^{238}U , ^{232}Th and their daughters.

2.3.1 Radioactive decay series

All alpha-emitting nuclides can be classified into four genetically independent decay series: ^{232}Th (thorium), ^{237}Np (neptunium), ^{238}U (uranium) and ^{235}U (actinium). The

^{237}Np series does not occur in nature and is not discussed further. Each of these decay series begins with a parent that has a half-life longer than that of all intermediate nuclides and ends with a stable isotope of lead. The intermediate nuclides range in half-lives from seconds to several hundred thousand years. The applicability of specific intermediate daughters to the studies of various processes in nature is determined by the relationship of the half-life of the parent and the length of the time interval during which the processes take place. The best results are commonly achieved when the time interval in question is between 0.1 and 5 times the half-life. This requirement limits the number of intermediate products within the U and Th decay chains applicable to geological processes to those that generally have half-lives of days or longer.

The ^{232}Th (thorium) decay series (Figure 2.2) begins with $^{232}\text{Th}_{90}$, and through a series of alpha and beta decays eventually becomes stable $^{208}\text{Pb}_{82}$. Most of the intermediate products within this chain are short-lived and therefore are of very little use in geological studies. The useful isotopes in this series are ^{232}Th ($t_{1/2} = 1.4 \times 10^{10}$ years), ^{228}Th ($t_{1/2} = 1.9$ years), and ^{208}Pb (stable).

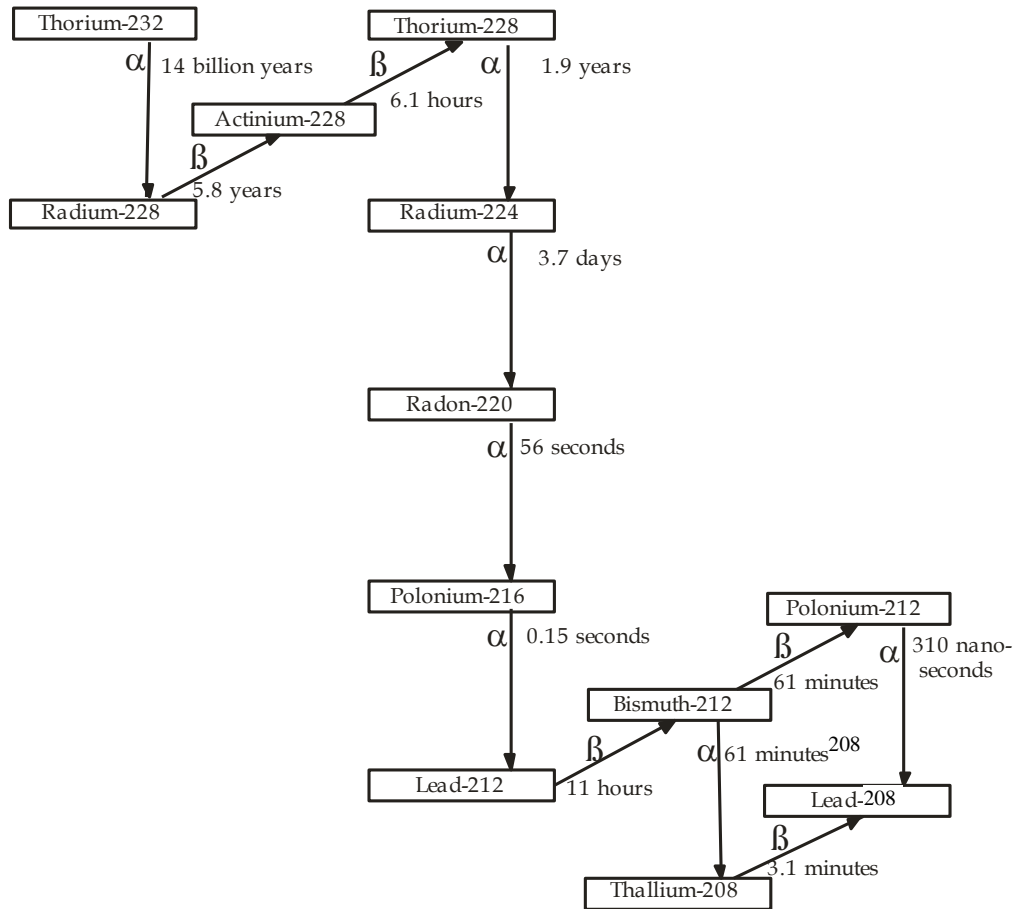


Figure 2.2 ^{232}Th decay series

The ^{238}U (uranium) decay series (Figure 2.3) begins with the isotope $^{238}\text{U}_{92}$ and decays eventually to $^{206}\text{Pb}_{82}$, which is stable. The useful isotopes are ^{238}U ($t_{1/2} = 4.45 \times 10^9$ years), ^{234}U ($t_{1/2} = 2.4 \times 10^5$ years), ^{230}Th ($t_{1/2} = 7.5 \times 10^4$ years), ^{226}Ra ($t_{1/2} = 1600$ years), ^{210}Pb ($t_{1/2} = 22$ years) and ^{206}Pb (stable). Radon-222 is also considered in this decay series because of its ability to diffuse out of the system resulting in radioactive disequilibrium.

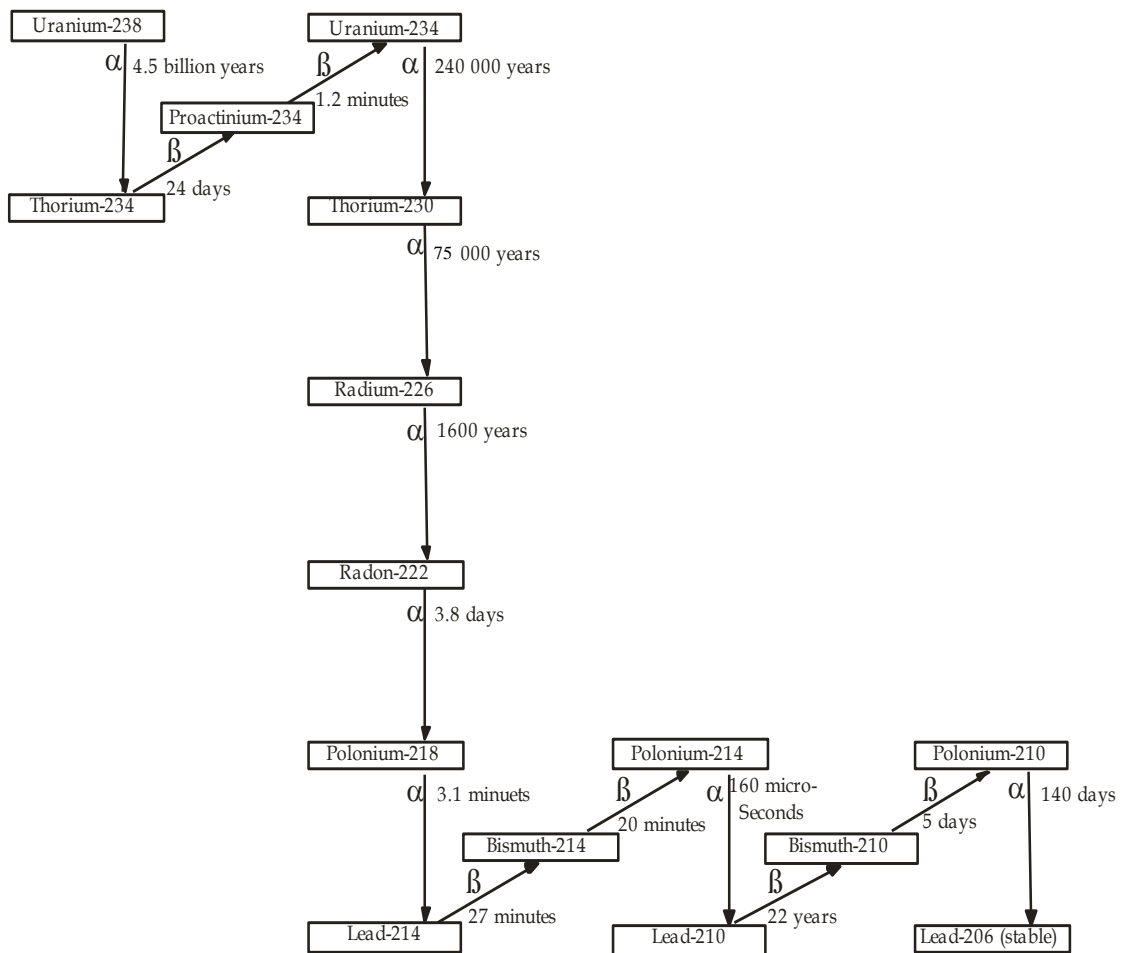


Figure 2.3 ^{238}U decay series

The primary nuclide of the ^{235}U (actinium) series (Figure 2.4), from which all other nuclides in this series are derived, is $^{235}\text{U}_{92}$, which decays through the chain of reactions ending with stable $^{207}\text{Pb}_{82}$. The useful isotopes in this system are ^{235}U ($t_{1/2} = 7.0 \times 10^8$ years), ^{231}Pa ($t_{1/2} = 3.2 \times 10^4$ years), ^{227}Ac ($t_{1/2} = 21.8$ years) and stable ^{207}Pb .

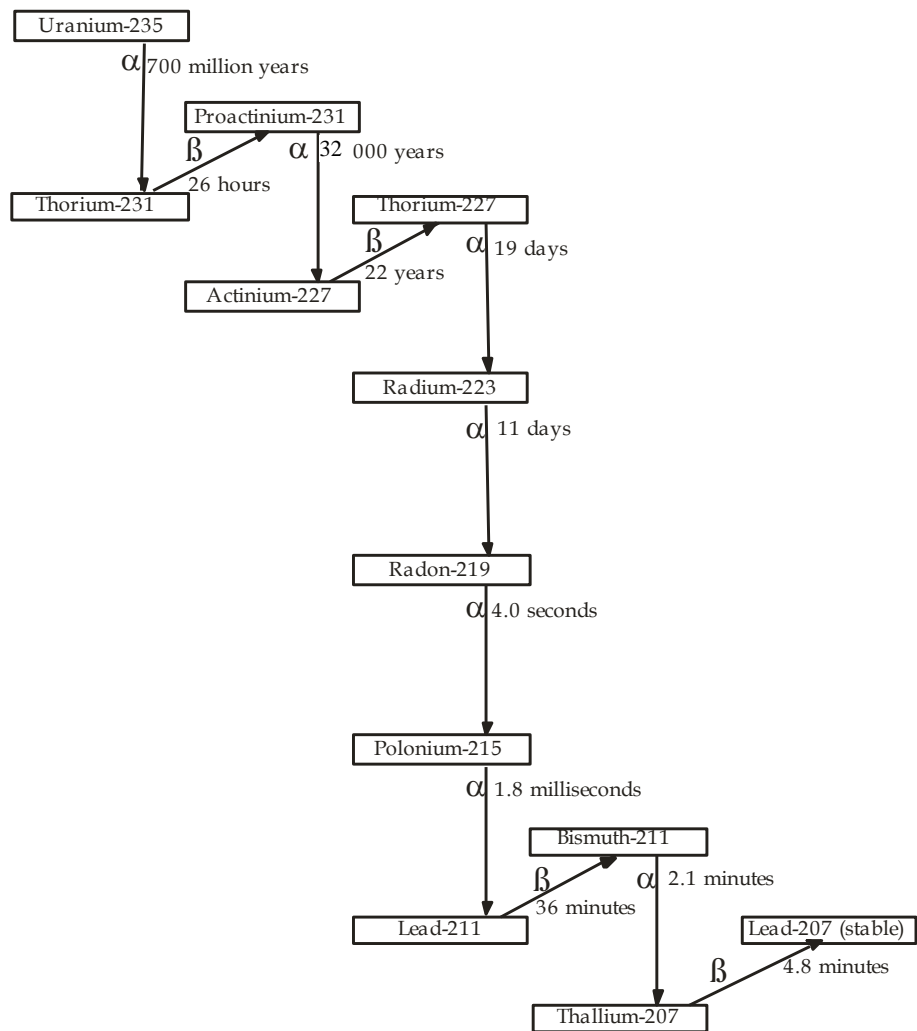


Figure 2.4 ^{235}U decay series

The selection criteria for isotopes used in dating opals is that they must have a half-life greater than several thousand years as their relatively long half-lives make the materials containing these nuclides susceptible to experiencing geological processes causing chemical fractionation between parent and daughter nuclides.

The majority of the daughter nuclides of uranium and thorium are too short lived (half-lives of less than several days) to be used successfully in describing geological processes which took place, and often continued for, thousands or even millions of years. Therefore, these daughters are not discussed any further. Several longer lived key nuclides ^{238}U , ^{234}U , ^{234}Th , ^{230}Th , ^{266}Ra , ^{231}Pa , ^{222}Rn and ^{210}Pb are discussed in detail, as an understanding of their behaviour forms a background to this study.

2.3.2 Secular equilibrium and disequilibrium

In the uranium and thorium series decay chains, the daughter products of radioactive decay (other than the three stable Pb isotopes) are themselves radioactive. Therefore, the rate of decay of such a daughter product is given by the difference between its production rate from the parent and its own decay rate:

$$dN_2/dt = N_1\lambda_1 - N_2\lambda_2$$

Where N_1 and λ_1 are the abundance and decay constant of the parent, and N_2 and λ_2 correspond to the daughter. The amount of stable daughter product at the end of the series will continue to increase with time at a decreasing rate. When the parent activity is equal to the daughter activity they are described as being in a state of secular equilibrium. For the complete chain to be in secular equilibrium the activities of all isotopes within the chain must be the same:

$$N_1\lambda_1 = N_2\lambda_2 = N_3\lambda_3 = \dots = N_n\lambda_n$$

Secular equilibrium between a daughter and a parent also implies that the parent to daughter activity ratio is one.

In order to achieve secular equilibrium the parent nuclide must have a half-life longer than that of any other nuclide in the series. In addition, a sufficiently long period of time must have elapsed after the system containing the nuclides in question was closed, i.e. several half-lives of the decay product having the longest half-life, to allow for ingrowth of the decay products. Nuclides with half-lives less than one year will re-establish equilibrium conditions with their longer lived parent nuclide rapidly, in the order of several years, while the slower decaying products will require longer periods of time to re-equilibrate. If the chain remains undisturbed for a period of six times the longest half-life of an intermediate nuclide then the chain will be within 1.5% of secular equilibrium (equal activity of all nuclides).

If the series is not in equilibrium then it is said to be in disequilibrium. Disequilibrium can be a result of elemental fractionation caused by differences in chemical behaviour or by isotope fractionation through radioactive decay. Some radioactive parents and daughters are chemically different and can be separated by ordinary geological processes producing various degrees of disequilibrium. An

activity ratio greater than one indicates an excess of daughter nuclide, whereas an activity ratio less than one indicates an excess of parent. If the system is closed after being disequilibrated and remains closed, then the state of secular equilibrium will return after a certain period of time.

The ^{234}U half-life, of about 250,000 years, is the largest among the intermediate daughters of all three decay series. As a result any system that is older than approximately 1.5 Ma must be in secular equilibrium with respect to all intermediate daughters of all three decay chains. The contribution of intermediate daughters into the final quantities of accumulated radiogenic Pb isotopes, in any system that is old enough (tens of millions of years) is insignificant and can be ignored when the ages are calculated if extreme parent-daughter fractionation has not occurred. This results in the known set of equations relating ^{207}Pb , ^{206}Pb and ^{208}Pb with their parent isotopes:

$$\left(\frac{^{207}\text{Pb}^*}{^{235}\text{U}} \right)_t = e^{\lambda_{235} t} - 1 \quad \text{equation 1}$$

$$\left(\frac{^{206}\text{Pb}^*}{^{238}\text{U}} \right)_t = e^{\lambda_{238} t} - 1 \quad \text{equation 2}$$

$$\left(\frac{^{208}\text{Pb}^*}{^{232}\text{Th}} \right)_t = e^{\lambda_{232} t} - 1 \quad \text{equation 3}$$

Where t is the age of formation, λ_{235} , λ_{238} and λ_{232} are the decay constants of ^{235}U , ^{238}U and ^{232}Th , and $^{206}\text{Pb}^*$, $^{207}\text{Pb}^*$ and $^{208}\text{Pb}^*$ are radiogenic Pb isotope abundances.

Strictly speaking, these equations assume that the activities of all radioactive intermediate daughter isotopes were equal to the activity of their parent isotopes at

the moment of formation of a system. However, for relatively young systems, contributions from the decay of intermediate daughters to the final amounts of radiogenic Pb can be significant and must be included in the relevant equations. The following equation is used for a closed system older than 1000 years and, therefore, only considers daughters with half-lives longer than 1 year.

$$\left(\frac{^{207}\text{Pb}^*}{^{235}\text{U}} \right)_t = e^{\lambda 235t} (B_1 e^{-\lambda 235t} + B_2 e^{-\lambda 231t} + B_3 e^{-\lambda 227t} + 1) \quad 4$$

$$\left(\frac{^{206}\text{Pb}^*}{^{238}\text{U}} \right)_{t(\text{total})} = R_1 (\text{from } ^{234}\text{U}) \quad 5$$

$$R_1 = e^{\lambda 238} (C_1 e^{\lambda 238t} + C_2 e^{-\lambda 234t} + C_3 e^{-\lambda 230t} + C_4 e^{-\lambda 226t} + C_5 e^{-\lambda 210t} + 1) \quad 6$$

$$R_2 = \frac{\lambda_{238}}{\lambda_{234}} e^{\lambda 238} \left(\frac{^{234}\text{U}}{^{238}\text{U}} \right)_{\text{Ao}} (D_1 e^{-\lambda 234t} + D_2 e^{-\lambda 230t} + D_3 e^{-\lambda 226t} + D_4 e^{-\lambda 210t} + 1) \quad 7$$

where λ is the decay constant of the isotope, t is the age and $(^{234}\text{U}/^{238}\text{U})_{\text{Ao}}$ is the initial activity ratio of $^{234}\text{U}/^{238}\text{U}$. The above equations assume negligible initial ^{231}Pa , ^{227}Ac , ^{230}Th , ^{226}Ra , ^{210}Pb , ^{207}Pb and ^{206}Pb . $B1$, $C1$ and $D1$ are the Bateman's coefficients (Bateman, 1910) for a chain of multiple successive decays given by the equation:

$$B_1 = \prod_{i=1}^{n-1} \lambda_i \Bigg/ \prod_{j=1}^n (\lambda_j - \lambda_i) \quad 8$$

where $i=1,2,3,\dots,n$; $j \neq i$; n = number of isotopes in the decay chain and where i and j values correspond to the order of the daughter isotopes in the ^{235}U or ^{238}U decay chain. The decay constants for the stable decay products ^{207}Pb and ^{206}Pb are $\lambda_{207} = \lambda_{206} = 0$. Therefore, the coefficients are:

$$B_1 = \frac{-\lambda_{231}\lambda_{227}}{(\lambda_{231}-\lambda_{235})(\lambda_{227}-\lambda_{235})}, B_2 = \frac{-\lambda_{235}\lambda_{227}}{(\lambda_{235}-\lambda_{231})(\lambda_{227}-\lambda_{231})}, B_3 = \frac{-\lambda_{235}\lambda_{231}}{(\lambda_{235}-\lambda_{227})(\lambda_{231}-\lambda_{227})}$$

For samples younger than 1-2 Ma and with measurable amounts of excess ^{234}U , two or more equations are used to describe the temporal evolution of the $^{234}\text{U}/^{238}\text{U}$ and $^{230}\text{Th}/^{238}\text{U}$ activity ratios (Ivanovich and Harmon, 1992).

$$\left(\frac{^{234}\text{U}}{^{238}\text{U}} \right)_{At} = \left[\left(\frac{^{234}\text{U}}{^{238}\text{U}} \right)_{Ao} - 1 \right] \bullet e^{-\lambda_{234}t} + 1 \quad 9$$

$$\left(\frac{^{230}\text{Th}}{^{234}\text{U}} \right) = \frac{1 - e^{-\lambda_{230}t}}{^{234}\text{U}/^{238}\text{U}} + \left(1 - \frac{1}{^{234}\text{U}/^{238}\text{U}} \right) \frac{\lambda_{230}}{\lambda_{230} - \lambda_{234}} \left(1 - e^{-(\lambda_{230} - \lambda_{234})t} \right) \quad 10$$

where At is the measured ratio and Ao is the initial activity ratio.

In equation 9 ($^{234}\text{U}/^{238}\text{U}$)_{Ao} is isolated and its substitution into equation 7 provides a solution for both age (t) and the $^{234}\text{U}/^{238}\text{U}$ initial activity ratio using measured values of $^{234}\text{U}/^{238}\text{U}$ and $^{206}\text{Pb}*/^{238}\text{U}$. Errors can be propagated assuming their statistical independence from the general equation:

$$\sigma_{f(x_1, \dots, x_n)}^2 = \sum_{i=1}^n \left(\frac{\partial f}{\partial x_i} \right)^2 \sigma_{x_i}^2 \quad 11$$

The $^{234}\text{U}/^{238}\text{U}$ and $^{230}\text{Th}/^{238}\text{U}$ systems provide independent age information in the range where $^{230}\text{Th}/^{238}\text{U}$ system has not reached secular equilibrium. Providing that the mineral or rock sample remained closed to the loss of intermediate daughters and initial excess or deficit of both ^{234}U and ^{230}Th is known, both $^{234}\text{U}/^{238}\text{U}$ and $^{230}\text{Th}/^{238}\text{U}$ systems are expected to define a similar age.

2.4 Geochemistry of uranium, thorium and lead

Nuclides in the near surface environment follow a cycle of mobilisation, transportation and precipitation. Disequilibrium of the chains can be produced at any stage of a cycle. Nuclides are found in four main areas relating to groundwater; in the water itself, attached to colloidal particles, in the host aquifer rock and as atoms adsorbed onto host rock surfaces. A general overview of the mobilisation, transportation and precipitation of the relevant nuclides follows.

2.4.1 Accessibility and mobilisation

U and Th do not fit well into most mineral structures due large size and because of this they tend to be enriched in late forming silica-rich alkalic rocks (Rogers and Adam, 1969).

2.4.1.1 U, Th and Pb-bearing minerals

Uranium occurs in three ways in unweathered alkalic rocks – background U (in major rock forming minerals), interstitial U (in an adsorbed form in intergranular spaces or liquid inclusions) and resistate U. Resistate U is found in two types of accessory phases – minerals which remain in the rock despite chemical weathering such as xenotime, zircon, apatite or monazite or in altered minerals (saussurtization product) (Bajo *et al.*, 1983). Several accessory minerals with high concentrations of U, Th or Pb are discussed.

Zircon (crustal) generally contains between tens to thousands of ppm of U and Th (Hoskin and Schaltegger, 2003) and typically less than 5000 ppm (Ewing *et al.*, 2003) and often shows a considerable range in U concentrations within a magmatic zircon population as well as within individual zircon grains. The Th/U ratios vary much less than the intercrystalline distribution of U and Th and is generally >0.5 (Hoskin and Schaltegger, 2003). Majority of the lead in zircon is radiogenic lead and there is very little initial lead present.

Monazite is the main source of thorium and usually contains between 3 and 9% and sometimes up to 20% ThO₂ (Langmuir and Herman, 1980). It is generally enriched in uranium (100 to 20 000 ppm) (Bea, 1999). However, there can be wide variation in U, Th and Pb and it favours incorporation of Th relative to U (Parrish, 1990).

There is some non-radiogenic lead (^{204}Pb approximately 200 ppm). Most of the radiogenic lead is from the decay of thorium resulting in a ^{206}Pb poor and ^{208}Pb rich mineral. Silver *et al.* (1980) noted that there appears to be some highly complex intergrowths of monazite and apatite. There can also be an association between monazite and thorite in some granites.

Apatite is generally enriched in uranium (5-200 ppm) (Bea, 1999). The Th/U ratio is usually a factor of 2 - 4 lower than that of the host granite, however, there are cases where it is a factor of 2 - 4 higher than the host granite suggesting that apatite has been depleted in U compared to Th. Non-radiogenic lead accounts for about half of the lead concentration and the radiogenic lead is enriched in ^{208}Pb compared to ^{206}Pb (Silver *et al.*, 1980).

Xenotime can contain up to 2000 ppm of radiogenic lead and nearly one weight percent uranium and thorium (Silver *et al.*, 1980). However, there can be large variations in concentrations of these elements in the xenotime population.

Uranium titanate can be an important mineralogical site for U in rocks which lack other high U-bearing minerals. Despite its generally low abundance, it can contain up to 40-50 percent UO_2 (Silver *et al.*, 1980). The radiogenic lead and thorium component is high, approximately 2 percent each. Although the mineral is highly radioactive there is some non-radiogenic ^{204}Pb , the concentration of which ranges between 2000 ppm and 4000 ppm (Silver *et al.*, 1980).

Coffinite shows high concentrations of uranium (average 400 000 ppm), thorium (average 150 000 ppm) and lead (average 2000 ppm) and it is assumed that all lead in coffinite is radiogenic (Silver *et al.*, 1980). Thorite is another radioactive accessory mineral which can be found in granites. It is the most Th-rich mineral and contains up to 50% thorium component (430 000 ppm on average). The average concentration for uranium is 20 000 ppm and the upper limit for lead is 3000 ppm (Silver *et al.*, 1980). Thorium is also found in allanite and uranothorite in granites (average of 9500 ppm and 440 000 ppm, respectively) (Silver *et al.*, 1980).

Most of the interstitial U is present in deuterically altered biotite and its alteration products. Background U in granites is generally found in finely fractured quartz and deuterically altered feldspar and biotite. The major rock forming minerals have very

little background U. However, there is a slightly higher concentration of U in the feldspars and biotite through saussuritisation, sericitisation and chloritisation (Guthrie and Kleeman, 1986).

There is a large fraction of radiogenic lead that appears to be located in non-radiogenic minerals and sites not normally considered as hosts for lead. Such minerals are quartz, feldspars, biotite-chlorite, magnetite, bismutite or weakly ferromagnetic opaques. Of these, feldspars hold the most non radiogenic lead and represent the most ^{204}Pb rich component in the rock. The other part of the lead is in the accessory minerals as radiogenic lead that is the product of radioactive decay of U. The amount of lead present in these accessory minerals is related to the age of the granite. Therefore, in older granites the accessory minerals will have a greater proportion of lead than uranium compared to younger granites. More radiogenic lead can also be found in Fe-rich halos around minerals such as brannerite, monazite and xenotime.

There are other minerals in granites that have high radioactivity such as titanite, epidote and allanite but these minerals are not always present in the majority of granites. Another mineral that can be present in granite is uraninite and this contains significant amounts of uranium. However, this mineral is generally seen in granites that are associated with uranium ore deposits and is not discussed further.

2.4.1.2 Weathering and release of U, Th and Pb

Input of nuclides by weathering occurs when air and water gain access to minerals resulting in a series of chemical reactions (chemical weathering) such as oxidation. It is these reactions that lead to mobilisation (e.g. through solubility) and subsequent large or small scale disequilibrium of nuclides (Figure 2.5).

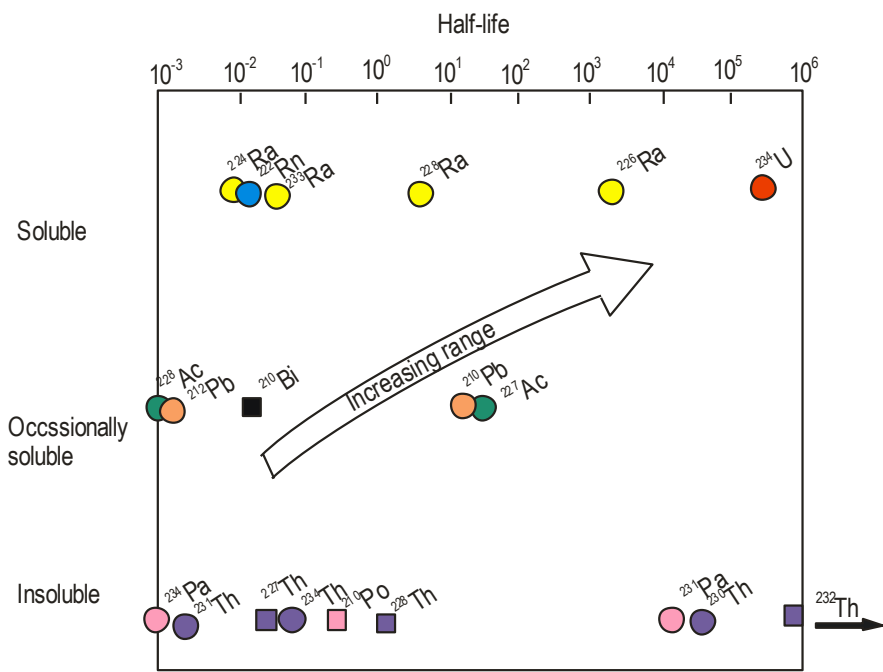


Figure 2.5 Geochemical mobility and range of radionuclides. Range is depicted as the product of both half-life and solubility of each nuclide. Nuclides represented by circles are products of alpha decay and are susceptible to mobilisation by alpha recoil (from Osmond and Cowart, 1992).

The first stage of granite weathering is typified by rapid alteration in the form of saussuritisation, sericitisation and chloritisation of plagioclase, biotite and K-feldspar (Scheepers and Rozendaal, 1993), releasing lead held within these minerals. Further alteration to clay minerals with high sorptive capacities fixes background and interstitial U by adsorption from circulation of late-stage U-rich fluids. However, with severe weathering and leaching this type of uranium can become mobile as it is weakly bonded to unstable alteration minerals and may be removed through cation exchange. These alteration minerals can also become saturated with uranium and circulating groundwater can remobilise uranium from the less stable interstitial adsorption positions and remove it from the system as UO_2^{2+} (Guthrie and Kleeman, 1986). With increased chemical weathering these clays alter to more stable phases such as kaolinite and gibbsite and are less adsorbent of uranium. Mn- and Fe-oxides also provide adsorption sites for uranium. However, leaching solutions can strip uranium and its removal into solution is commonly in the form of UO_2^{2+} .

The majority of uranium, thorium and a proportion of total lead situated in accessory minerals, as previously discussed, becomes mobilised with weathering. Weathering

does not need to continue until the whole grain is dissolved to releasing uranium, thorium and lead. Other accessory minerals such as monazite, apatite and sphene do not lose much uranium during weathering, suggesting that uranium is incorporated through crystal lattice substitution.

Input and mobilization of uranium and thorium can also be caused by alpha-recoil displacement. Alpha decay results in the recoil of the radiogenic daughter through impermeable crystalline material over a distance of 10-20 nm (Osmond and Ivanovich, 1992), leaving the daughter nuclide in a site that is susceptible to chemical alteration or being selectively removed (Figure 2.6). Ejection of an alpha particle by a ^{238}U atom near the surface of the mineral results in the short lived daughter nuclide, ^{234}Th , being recoiled into the solution surrounding the grain (i.e. groundwater). In this situation decay of ^{234}Th to highly mobile ^{234}U , via the short lived ^{234}Pa , would increase the $^{234}\text{U}/^{238}\text{U}$ ratio in the groundwater (Rosholt and Bartle, 1969). Further release of uranium occurs by migration along recoil tracks. ^{232}Th can only be released from aquifer minerals by weathering (Porcelli and Swarzenski, 2003) whereas mobilisation of ^{230}Th can occur through alpha recoil as well as weathering. The recoil displacement can cause significant disequilibria.

Direct recoil of nuclides into groundwater can also occur. The direction of recoil is random for each decay and the rate of ejection into groundwater is determined only by the fraction of parent nuclides within recoil distance of mineral surfaces or channels to the surface. The degree of vulnerability to leaching is known as the Szilard-Chalmers effect and is where alpha or beta decay disrupts the crystalline lattice along the path of recoil and in the area of the displaced daughter, however, the disruption caused by the beta decay is several magnitudes smaller than by alpha decay. The daughter radionuclide becomes lodged in the lattice site and can exhibit an unstable electronic configuration. This radionuclide becomes more vulnerable to leaching than the undecayed ^{238}U atoms. If groundwater is percolating past a mineral grain, the rate at which daughters are supplied relative to the rate at which they are removed determines the degree of disequilibrium.

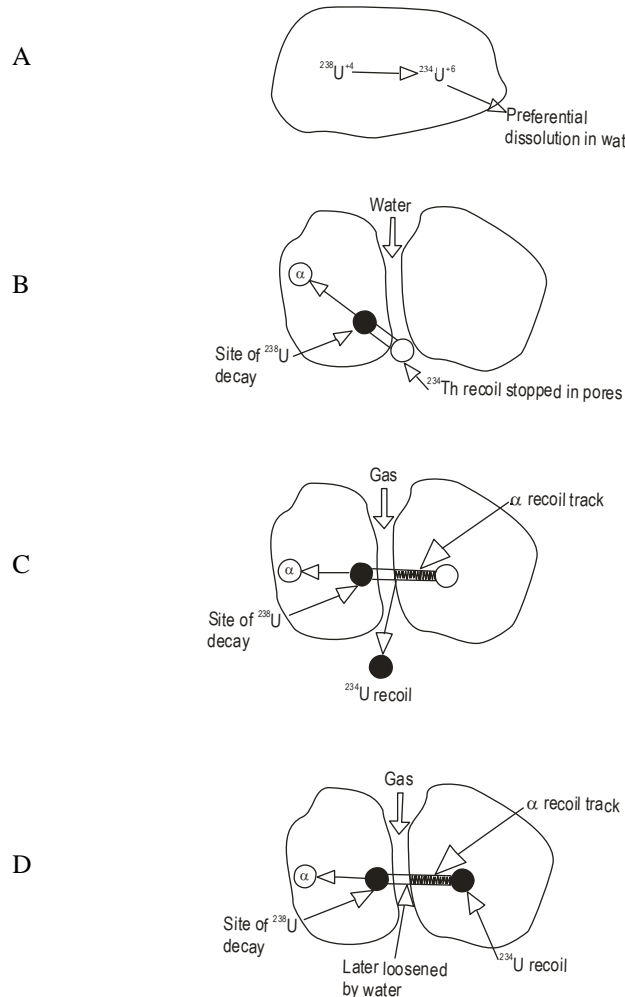


Figure 2.6 Models of recoil causing $^{238}\text{U}/^{234}\text{U}$ disequilibrium. A) The recoiling nucleus finds itself in an unusual lattice site where it acquires an unusual charge state. B) The recoiling nucleus is stopped in the intergranular material. C) The nucleus recoils into an adjacent grain from which it escapes by diffusion along the damage track. D) The same as for C except that the damage is removed chemically by intergranular liquid (from Fleischer and Rabbe 1978).

Selective leaching is the process of groundwater percolating past the solid mineral grains in an aquifer or soil and taking soluble daughters. However, some daughters are less soluble than others and the less soluble daughters are not taken up in solution. This leads to a solution with an excess of soluble daughters and a deficient solid phase. These soluble daughters produce daughters of their own which may not be as soluble and are precipitated out of the solution. This situation becomes responsible for disequilibrium. A simple example of this is selective leaching of rocks with the immediate resulting soils producing a $^{230}\text{Th}/^{234}\text{U}$ activity ratio of about

10 because ^{230}Th (daughter) is less soluble and remains in the solid material as ^{234}U and ^{238}U are dissolved in the groundwater (Osmond and Ivanovich, 1992). However, secondary cements may have $^{230}\text{Th}/^{238}\text{U}$ activity ratio greater than 1 depending on age and purity. ^{234}U is relatively soluble in oxidised waters leading to the conclusion that selective leaching can be dependant on Eh and pH. Radiogenic lead in non-radiogenic minerals can easily be leached by moderately acidic solutions, yielding major fractions of their radiogenic lead content, whereas the minerals show minor chemical dissolution (Silver *et al.*, 1980).

Uranium is lost from zircon as it begins to decay resulting in alpha recoil which causes a self-induced breakdown of the crystal structure, becoming amorphous (metamict). Radiation damage, which causes the zircon to become metamict, takes a significant amount of time to accumulate because of the natural annealing that occurs over geological timescales. However, annealing generally occurs at temperatures over 300° C (Cherniak and Watson, 2000) and, therefore, the zircons exposed to temperatures below this point will accumulate radiation damage over a shorter period of time. In low temperature acidic solutions the outer rim of the metamict zircons can be incongruently dissolved, removing uranium and thorium as well as lead. Uranium, thorium or lead atoms diffuse out of a metamict zircon by volume diffusion as there are areas of low atomic density that act as fast diffusion pathways (Geisler *et al.*, 2002) (Figure 2.7).

Geisler *et al.*, (2002) also suggest that leaching of metamict zircon (mainly U and Pb) in natural waters can be significant even at temperatures less than 200°C and that volume diffusion can occur even at low temperatures (175°C). Significant loss of U from zoned zircons suggests that a proportion of U is incorporated by adsorption and ionic exchange and becomes readily mobilised by migrating fluids (Geisler *et al.*, 2002). Cherniak and Watson (2000) suggest that most Pb loss from zircon by diffusion occurs at low temperatures and is not influenced by pressure or the presence of water.

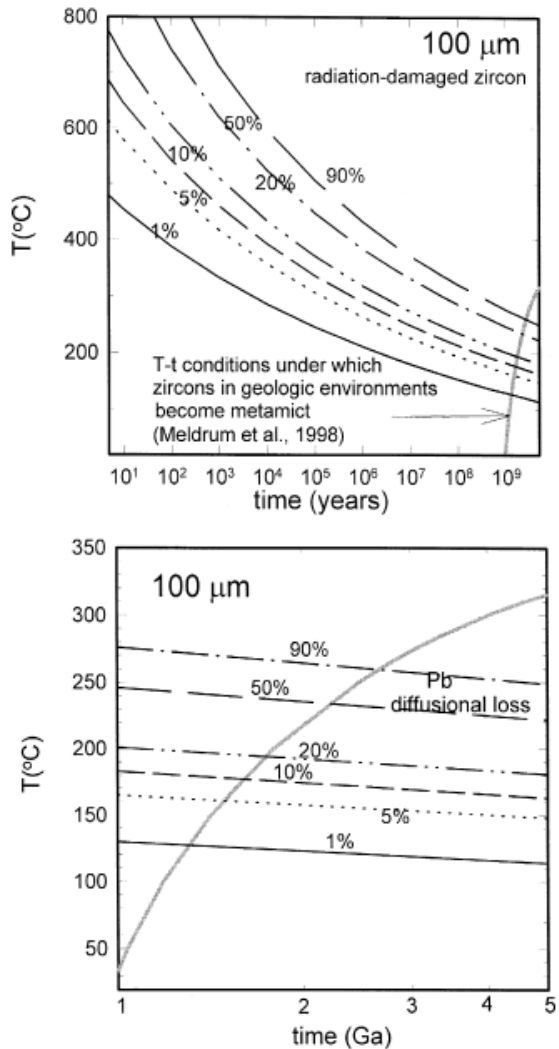


Figure 2.7 Conditions for diffusional Pb loss in metamict zircon. Curves represent time-temperature conditions under which a zircon of 100 μm radius will lose the indicated fraction of Pb. Also plotted is a curve which indicates the time-temperature conditions under zircon with 100 ppm uranium will become metamict. Times in excess of a billion years are necessary in order for the zircon to accumulate sufficient radiation damage to become metamict. Significant Pb loss will be likely only in the region below this curve (from Cherniak and Watson, 2000).

2.4.2 Transport of nuclides

Transportation of nuclides in groundwater depends on their geochemical characteristics, the characteristics of the fluid and the solid particles that make up the aquifer. Transportation of U, Th and Pb isotopes can occur by sorption (irreversible or reversible) onto natural colloids (less than 0.45 μm) in the groundwater such as precipitates, bacteria, organic and inorganic matter, mineral fragments or as inorganic constituents such as Fe or Mn oxyhydroxides and clays or as organic colloids such as humic and fulvic acids. If the sorption is irreversible then the

nuclide will not be removed from the colloid by a change in the groundwater geochemistry and will migrate with the velocity of the groundwater. Colloids can be responsible for an unsupported excess of nuclides in the groundwater rather than on surfaces or in minerals and can provide an explanation for increased migration rates. Th, due to its greater reactivity is more likely to be carried by colloids than U although colloids can carry a large fraction of U (Porcelli and Swarzenski, 2003). Uranium and thorium can also be transported as particulate matter (size fraction greater than $0.45\mu\text{m}$) which is controlled by the physical properties and flow velocity of the transporting medium, providing that no chemical interaction occurs across the phase boundary (Gascoyne, 1992). Thorium is generally transported by particulate matter because of its extremely low solubility in most natural waters. Without colloids and particulate matter less soluble elements such as Th are not readily mobilized and, therefore, not transported very far from their origins.

Uranium is a multivalent element and cycles between the weathering zone and the deep groundwater zone. It exhibits different characteristic behaviours under different near surface conditions. The degree of mobility depends on its ability to form complexes with both inorganic and organic ligands. Unsaturated rocks and soils with oxidising conditions cause uranium to have a 6+ valence, which in this state is not readily sorbed to charged solid surfaces (Langmuir, 1978; Cowart and Burnett, 1994). In aqueous solutions U^{6+} hydrolyses to become the soluble uranyl complex ion (UO_2^{2+}). Further water soluble complexes of the uranyl ion may then occur depending on pH, Eh and the presence of other dissolved ions (Langmuir, 1978). UO_2^{2+} can be complexed by F^- , OH^- , SO_4^{2-} , NO_3^- and carboxylates (Bea, 1999). Uranyl complexes are more soluble than uranous species and the dominant species will depend on the Eh-pH conditions, the concentration and availability of complexing ions and the temperature. The uranyl complex ions can be carried down into percolating groundwater and further into deeper aquifers with reducing low temperature environments. Here the uranium becomes 4+, which is insoluble and immobile and is adsorbed onto aquifer grains that are brought to the surface via the process of uplift, and over a period of time the cycle is repeated. U^{4+} can become mobile by forming a wide range of strong complexes, especially with fluorite and O– donor chelating ligands (Bea, 1999). However, generally U^{6+} is more mobile because its greater solubility. The increase in uranium concentrations in deeper

weathered zones suggests that at least part of the uranium leached from the oxidizing surface is accumulated lower in the profile where redox conditions may vary with time (i.e. temporal water saturation due to limited drainage in contact with hard rock) and allow uranium adsorption and/or precipitation. Newly liberated uranium may also be introduced later via groundwater and this new uranium can significantly increase the uranium concentration.

Thorium concentrations in natural waters are low, reflecting a combination of insolubility of thorium-bearing minerals and strong adsorption of thorium by natural materials in this pH range (Figure 2.8). Thorium resides in near surface environments at low temperatures in both oxidising and reducing conditions in the insoluble and chemically immobile tetravalent state. Because of this thorium will not be transported long distances thereby inducing an excess of ^{238}U and ^{234}U relative to ^{230}Th in groundwater. The lack of thorium removal into groundwater is related to its strong ability to adsorb onto particle surfaces and organic matter, particularly simple organic acids and fulvic and humic acids, more so than uranium. The adsorption of dissolved thorium onto clays, oxides, especially Fe oxyhydroxides (Scheepers and Rozendaal, 1993) and organic matter increases with increasing pH. Maximum amounts of thorium adsorption (95-100%) are attained at pH values above 5.5-6.5 (Langmuir and Herman, 1980) although thorium removal and mobility has been shown to occur in extremely acid environments (Brookins, 1988).

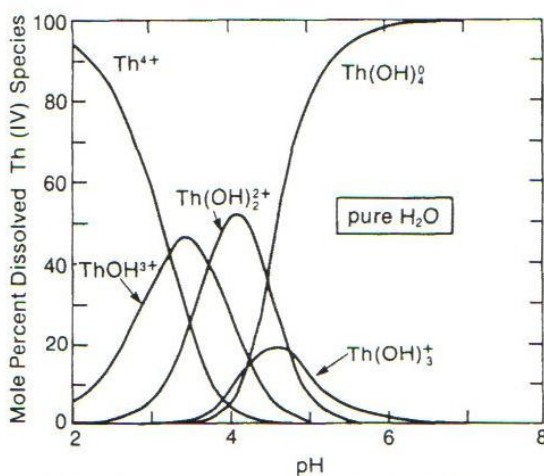


Figure 2.8 The distribution of thorium-hydroxy complexes vs pH at 25°C with $\Sigma\text{Th} = 0.01 \text{ ppb}$ in pure water (from Langmuir and Herman, 1980).

Thorium mobility is increased by the formation of complexes and this is suggested by the increase in thorium concentration with an increase in groundwater temperature (Langmuir and Herman, 1980). Thorium mobility is greatly increased by thorium complex formation and it is usually complexed with sulphate, fluorite, phosphate, hydroxide and soluble organic anions or colloidal humic/fulvic acids. In typical groundwater the most abundant thorium species in solution vary with increasing pH from $\text{Th}(\text{SO}_4)_2^0$, ThF_2^{2+} , $\text{Th}(\text{HPO}_4)_2$, $\text{Th}(\text{HPO}_4)_3^{2-}$ and $\text{Th}(\text{OH})_4$ (which is dominant at pH greater than 5) (Langmuir and Herman, 1980; Porcelli and Swarzenski, 2003). Thorium can also be mobilised in the oxidized zone of the near surface environment through hydrolysis with a pH greater than 3.2. This means that thorium leaching is enhanced in the well aerated, organic matter-rich topsoils and immobilized in horizons with low organic matter contents and slower drainage.

Thorium 228 can be leached from fresh samples as it has weaker bonds and tends to migrate into dislocation zones along recoil paths which results in its preferential removal with leaching. The relatively higher solubility of radium can also enhance $^{228}\text{Th}/^{232}\text{Th}$ disequilibrium in the weathered material with recoil ^{228}Th from ^{228}Ra in solution being emplaced on a solid phase.

Lead activities are dependant on temperature and are low in low temperature environments. The solubility of lead in aqueous fluids is very low resulting in minimal transportation. However, in the presence of complexing agents such as chloride, sulphide, carbonate and organic ligands its solubility is increased and it may be transported further. At high temperatures the stability of complexes such as lead chloride increases which in turn increases mobility (Ku *et al.*, 1992).

2.4.3 Other nuclides

Other nuclides may cause disequilibrium resulting in unsupported lead. The only protactinium isotope that causes significant diseqilibrium is ^{231}Pa because of its long half-life ($t_{1/2} = 33$ kyr). Proactinium is insoluble and generally occurs in the 5+ state. It hydrolyses more readily than thorium and like U^{6+} does not exist in solution simply as hydrated ions but as oxo ions of MO_2^n+ , where M is the metal. It is removed quickly from water once hydrolysed and is adsorbed onto particulates

(Gascoyne, 1992). Proactinium also has strong affinities for organic complexing ligands and may be more soluble in waters that are high in organic ligands.

Radium has four naturally occurring isotopes; ^{223}Ra , ^{224}Ra , ^{226}Ra and ^{228}Ra . The short lived isotopes (^{223}Ra and ^{224}Ra) are mobilised more so by recoil effects rather than weathering (Procelli and Swarzenski, 2003) whereas the longer lived isotopes (^{226}Ra and ^{228}Ra) can be mobilised by weathering as well as recoil. ^{226}Ra is often found in excess of its parent ^{230}Th in most natural waters due to its greater solubility, especially in reducing water, and resulting diffusion into the water column from the sediment (Gascoyne, 1992). However, in saline environments it can also be depleted with respect to ^{230}Th (Gascoyne and Schwarcz, 1986). It is also greatly in excess of ^{238}U due to preferential leaching of ^{238}U . ^{228}Ra is also found in excess of its parent in natural waters. The removal of radium from solution is primarily controlled by adsorption to colloids or particulates (clays or iron hydroxides) as it has a strong affinity to surfaces. High temperatures tend to increase radium concentrations in groundwater by reducing adsorption coefficients of the divalent radium ions.

There are two gaseous products of the radioactive decay of uranium and thorium - helium and radon. Helium is formed during alpha decay and will not cause disequilibrium. Radon has three naturally occurring isotopes with the most abundant and longest lived being ^{222}Rn that has a half-life of 3.8 days. Radon is a noble gas and is not readily ionised or chemically reactive and it is present as uncharged single atoms in the groundwater. It is produced by the decay of its parent ^{226}Ra and accumulates as unsupported radon (excess of parent ^{226}Ra) where it can be lost by dissolution or diffuse into intergranular water (as it is highly soluble in water) resulting in disequilibrium. However, radon is often seen in large concentrations in groundwater, despite low concentrations of its parent in groundwater, which cannot be produced from recoil from the edges of the grains. Rama and Moore (1984) propose that a major part of the Rn in the intergranular water comes from within the grains and not by recoil from the outer surface. They determine that the grains are permeated and that Rn recoils into the nanopore water and then diffuses into the intergranular water, leaving the amount of recoil from the edges to be negligible.

2.5 Opal mineralogy and environments of formation

2.5.1 Mineralogy

Opaline minerals are essentially forms of hydrous silica ($\text{SiO}_2 \cdot n\text{H}_2\text{O}$) with differing crystal structure and degrees of crystallinity and are divided into two types of opal; non-crystalline opal and microcrystalline opal. Non-crystalline opal, opal-A (highly disordered) is divided into opal-AG (amorphous gel-like) and is more commonly known as precious opal and opal-AN (amorphous network/glass like), which is commonly known as hyalite (Langer and Flörke, 1974). Jones and Segnit (1971) subdivided microcrystalline opal into opal-CT, disordered cristobalite and tridymite, and opal-C, well ordered cristobalite. Opal-C and opal-CT are part of a continuous series of intergrowths between end-member cristobalite and tridymite stacking sequences and are low temperature opaline silica polymorphs .

Cristobalite is built of layers consisting of 6-membered rings of silica tetrahedra that are vertically stacked (Figure 2.9).

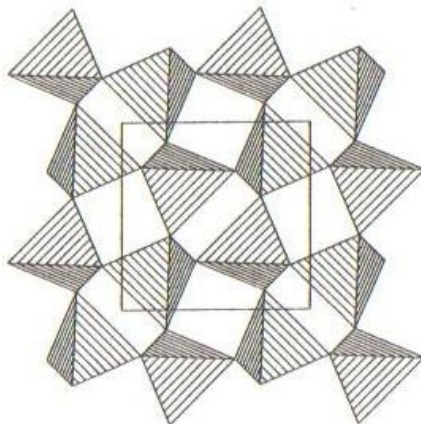


Figure 2.9 Crystal structure of cristobalite (from Heaney, 1994).

These layers are linked by the vertices of tetrahedra that alternately point up and down. This is a low energy structure and so promotes the precipitation of cristobalite over other silica polymorphs. The tridymite structure consists of stacked sheets of silicon tetrahedra, with the tetrahedra in each sheet forming six member rings. Within each ring the tetrahedra alternately point up and down (Figure 2.10). When viewed down the c-axis the rings of tetrahedra within each sheet line up one above

the other. This is the only difference between the two structures. In cristobalite the rings in adjacent sheets do not line up with each other but are offset so that the up tetrahedra in one sheet are over the centres of the rings in the sheet below.

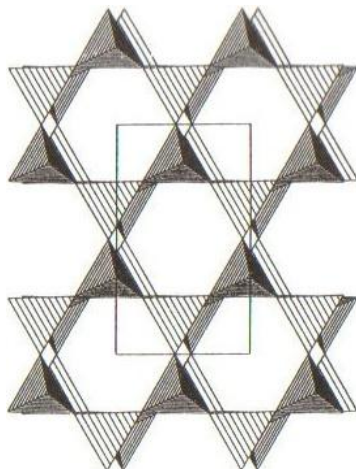


Figure 2.10 Crystal structure of tridymite (from Heaney, 1994).

Opal-C is a well ordered silica predominately in cristobalite form. The XRD (X-ray diffraction) pattern of opal-C is very similar to that of high temperature cristobalite. Opal-C is characterised by sharp (101) reflections near 4.0 Å and major reflections centred on 3.13, 2.84 and 2.47 Å (Elzea *et al.*, 1994). It is interpreted as more ordered than opal-CT because it has sharper and more intense peaks. Opal-C consists of disordered low cristobalite with minor evidence for tridymite stacking. Heating to temperatures above 1000°C gradually transforms Opal-C to a more highly ordered form of cristobalite. Figure 2.11 shows the different XRD patterns for the three main types of opal.

Opal-CT consists of cristobalite/tridymite in a matrix of amorphous silica with a strong stacking disorder. Opal-CT occurs as tiny spherical aggregates formed by thin crystal blades (Flörke *et al.*, 1975) made up of cristobalite and tridymite. Opal-CT has two broad reflections. The most intense (101) reflections can occur between 4.05 and 4.10 Å and at 2.50 Å (Elzea *et al.*, 1994). Smaller reflections are seen at 4.25 to 4.35 Å. From this it can be determined that opal-CT has a cristobalite-like structure with varying degrees of stacking disorder leading to the appearance of tridymite

reflections (Elzea and Rice, 1996). The degree of ordering increases with diagenesis and manifests itself as sharper and more intense XRD peaks.

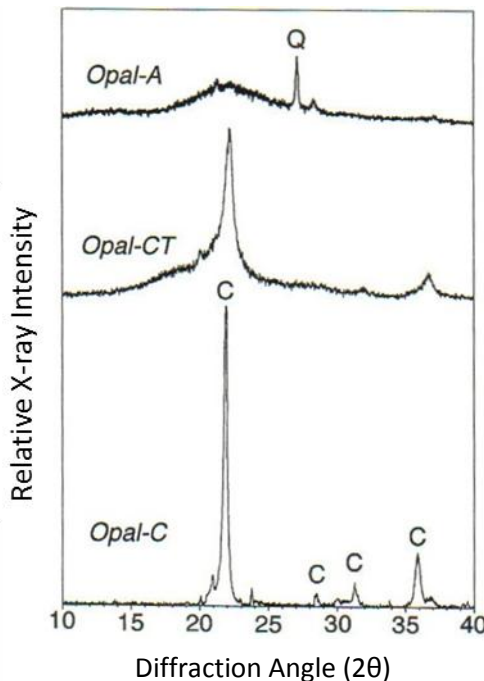


Figure 2.11 X-ray diffraction scans of opal-A, opal-CT and opal-C with quartz (Q) impurities present within opal-A (from Elzea and Rice, 1996).

Microcrystalline opal can be diagenetically transformed from opal-CT to opal-C by reductions of tridymite stacking therefore creating a more ordered low-cristobalite (Graetsch, 1994). When opal-CT is heated to 1000°C it is converted to opal-C or low cristobalite (Rice *et al.*, 1995). Opal-A can also be converted to opal-CT by diagenesis (Elzea *et al.*, 1994) and factors which affect the transformation include burial depth, time, heat flow and host rock lithology. Studies have shown that this reaction can proceed when temperatures reach ~2°C to 50°C (Williams *et al.*, 1985; Knauth, 1994).

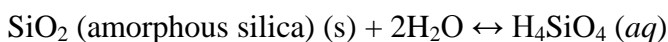
The water content in crystalline opals ranges between 1.5 and 10 wt % with opal-CT having a higher water content and opal-C having a lower water content. Graetsch (1994) suggests that most of the water is molecular water.

The XRD pattern of opal-A is characterised by a single diffuse peak centred at approximately 4.1 Å (Elzea and Rice, 1996). Opal-AG is precious opal and is not discussed as it was not used in this study due to low uranium concentrations. Opal-AN is a water-containing amorphous (network-forming) silica glass (Flörke *et al.*, 1973) and typically occurs as millimetre thick botryoidal crusts on volcanic rocks. It contains about 3-8% water both as molecular water and bound in silanol (SiOH) groups. Most of the water in non-crystalline opal is molecular water with the two main species being isolated water and liquid water (Graetsch, 1994). The isolated water molecules are trapped in the network and is highest in opal-AN, whereas the liquid water is in the voids or interstices of the microstructure. The remaining water is silanol water.

2.5.2 Environment of opal formation

There are three main environments where specific conditions allow opal deposition—hydrothermal systems, meteoric waters and environments where biogenic opal is produced. The first two systems are applicable to this study and are silica-rich systems where silica solubility and rates of dissolution and precipitation are important. Silicic acid can also be released in the weathering of igneous silicate minerals.

Silica dissolves in water by the reaction;



The solubility of silica phases increases from quartz to cristobalite to amorphous silica, with amorphous silica being the least stable and the most soluble (Dove and Rimstidt, 1994; Icenhower and Dove, 2000). The solubility of quartz and other silica phases increases with both pressure and temperature, with pH greater than 9 and with an increase in salinity, resulting in some solutions becoming supersaturated with respect to dissolved silica (Zielinski, 1982).

The presence of dissolved constituents (organic and inorganic species) that can form complexes with silica can increase silica solubility. Quartz equilibrates with

geothermal solutions rapidly above 200°C (Dove and Rimstidt, 1994). Reaction rates above this temperature are very fast and rapidly convert metastable silica phases to quartz via dissolution and precipitation. This suggests that metastable silica phases cannot exist above temperatures greater than 200°C. Dove and Crerar (1990) show that alkali cations enhances quartz and amorphous silica dissolution rates in near neutral pH solutions at lower temperatures, although the effect declines with decreasing temperature. Quartz precipitation rates increase with an increase in salinity (NaCl) as well as with an increase in KCl. This is significant because geothermal fluids contain significant concentrations of Na, Ca, K, and Mg. Cooling of a silica-saturated solution below the equilibrium temperature increases super saturation of silica, which tends to raise the precipitation rate but because the rate constant rapidly decreases, the precipitation rate is subsequently lowered. These competing effects cause a maximum rate of precipitation 25-50°C below the saturation temperature. At temperatures below that of the maximum rate, silica is often quenched into solution by very slow reaction rates (Rimstidt and Barnes, 1980). Eh conditions also need to be suitable at the time of precipitation and must be sufficient to oxidize uranium to U⁶⁺ so that it can be incorporated in the opal (Zielinski, 1982). This is also supported by the fact that U⁶⁺ is more soluble than U⁴⁺ and is, therefore, more likely to be present in solution.

Opal minerals, with perhaps the exception of opal-C, form at temperatures usually below 100°C (Elzea *et al.*, 1994). Opal-A may be precipitated from silica saturated solutions formed as a result of water interacting with silica-rich rocks causing silicic acid polymers to precipitate (Elzea *et al.*, 1994). These polymers then grow by Ostwald ripening to form colloidal sols and gels (Crerar *et al.*, 1981). The subsequent transformation by crystallographic ordering from opal-A to opal-CT to opal-C may be caused by thermal changes.

Host rocks serve as the major source of silica and uranium and it is the interaction between water (either groundwater or magmatic fluid) and the silicic rocks which produce a silica and uranium rich solution, which coprecipitate to form uraniferous opal. Silica precipitation relies upon the removal of water vapour from the depositional site and when this is achieved mineral precipitation will occur. The volume deposited will be greatest where water films curve tightly around crystal edges.

Deposition of opal is most likely from films of hydrothermal water moving down fractured footwalls or meteoric water percolating down through rock masses along fractures and porous matrix onto drawn up faces of growing crystals by surface tension and evaporated at the crystal tips (Whelan *et al.*, 2002). Slow crystallization kinetics of opal-A mean that it is precipitated late in the crystallization sequence from pore waters and can coat earlier forming minerals such as calcite and gypsum (Meijer, 2002).

In the vadose zone water probably flows down fractures as a meandering, fingering film (Whelan *et al.*, 2002). Areas where there are larger open spaces in the rock and connected fracture flow paths will facilitate separation of gases from the percolating water as well as removal of gases and deposition of silica (Whelan *et al.*, 2002). Confined areas will be filled by the percolating water but will retard the removal of gases and the precipitation of silica. Silica solubility increases with depth due to the increase in temperature and water flow is gravity driven. Shallower dipping fractures have slower downward flow velocities resulting in an increase in the ratio of gas-phase removal to percolation flux rates and an increase in the silica deposited (Whelan *et al.*, 2002). Water percolates via matrix and fracture flow and it is the water from the fracture flow that is the main fluid source (Whelan *et al.*, 2002).

2.5.2.1 Hydrothermal systems

Hydrothermal and epithermal deposits circulate hot meteoric waters, with high concentrations of CO₂ and NaCl, and it is because of this hot water that there is dissolution of silica from surrounding felsic rocks. Recharge of fluid is minimal and the heat source of the hot water can be either volcanic activity or regional metamorphism of the existing rocks. A metamorphic hydrothermal system is where there is expulsion of water from rocks that undergo regional metamorphism. The majority of the fluid released is a mixture of H₂O and CO₂. Alternatively, magmatic hydrothermal systems consist of fluids released from crystallizing magma and are common around shallow intrusions (Kesler, 2005). Confined hydrothermal systems are isolated from the surface and are driven by magmatic or metamorphic fluids, or, tectonic or sedimentary processes that isolate fluid reservoirs. Fluid from confined systems can be expelled into unconfined zones if faults breach the reservoir. Unconfined hydrothermal systems are most likely to be responsible for producing a

suitable environment for silica mobilisation and opal deposition. Cooling joints, shears, faults and fractures form a network of potential pathways that may facilitate water movement within the otherwise low-permeability volcanic rock. Active near-surface hydrothermal systems operate at temperatures less than 350°C, whereas temperatures are highest, about 600°C, in magmatic systems. In order for opal to precipitate in a hydrothermal system the temperature must be less than 100°C and at moderate depth. This temperature is achieved by decreasing magmatic activity or by increasing the distance from the magmatic activity.

2.5.2.2 Groundwater

Deposition of opal from meteoric water occurs in the cool, brittle rocks of the upper crust where precipitation (rain and melted snow) percolates downwards along a limited number of connected fracture pathways. Other waters which are involved are ephemeral surface waters, soil waters, vadose zone pore waters, perched waters and saturated zone groundwaters. Water cooling and evaporation are the main processes that control the deposition of opal. The silica is initially deposited as non-crystalline opal-A when the waters cool below 100 °C. This system is generally driven by hydrostatic pressure, which can be caused by topographically high recharge, or by near-surface evaporation caused by differences in temperature or density of the fluid (Kesler, 2005). Evapotranspiration of meteoric waters in the soil zone appears to be a very important process in the control of vadose zone pore waters, perched waters and saturated zone groundwater compositions (Meijer, 2002).

2.5.3 *Biogenic opal*

Biogenic opal is amorphous opal formed from natural sources such as the skeletons of radiolaria, diatoms and siliceous sponges. Siliceous tests (shell) are not always dissolved post mortem and accumulate on the ocean floor where they lithify and form poorly crystalline opal deposits (Heaney, 1994). Amorphous opal is also cycled through the terrestrial environment by vascular plants where there is internal silicification of plant tissue. This biogenic opal preferentially collects in the A horizon of soils and, to a lesser extent, in the B horizon (Clarke, 2003). Opal A may be dissolved and reprecipitated, as opal CT or micro-quartz lower in the soil profile, where it plays a role in cementation and silicification of regolith to form silica

hardpans and silcrete (Clarke, 2003). Clarke (2003) indicates that there is a strong correlation between high levels of biogenic opal in soils and poor drainage.

2.5.4 Previous work

Much of the published research on the geochronology of opaline silica has been focused on opal found in USA, and more specifically in Nevada, due to significant interest in the area related to the exploration for a suitable high level nuclear waste repository.

Suitability of uraniferous opal as geochronometer was first established by Ludwig *et al.*, (1980) and Zielinski (1982) and was used in the understanding of ore genesis. They determined that opal can have high uranium concentrations and low non-radiogenic Pb and ^{232}Th abundances (i.e. initial $^{230}\text{Th}/^{232}\text{Th}$ activity). Low non-radiogenic Pb abundances allow determination of initial-lead corrected $^{206}\text{Pb}*/^{238}\text{U}$ and $^{207}\text{Pb}*/^{235}\text{U}$ ratios with low errors and consequently dating samples as young as 1 Ma is possible. These original investigations showed a decrease in age from the interior to the outer edge of the opal suggesting either a continuous or episodic deposition of opal. U-series dating method was trialled by Szabo and Kyser (1985, 1990), however, all of the samples from Yucca Mountain, Nevada, were older than the detection limit of the method of about 400 kyr. Nevertheless, these studies proved that opal can be used as geochronometer.

Investigation into dating opals focussed on opal coatings from open fractures and lithophysal cavities in the unsaturated zone tuffs at Yucca Mountain as a part of a study of Yucca Mountain being a potential site for isolating high-level radioactive waste. These studies all show a systematic microstratigraphy of opal layers with U-Pb ages from the base to the outer edge determined to be 50 kyr to ~10 Ma (Neymark *et al.*, 1998; Neymark *et al.*, 2000b; Neymark *et al.*, 2002; Wilson *et al.*, 2003; Whelan *et al.*, 2008; Neymark and Amelin 2008). The age of the base of the opal layers (initial deposition) is ~10 Ma and is close to the age to the host tuffs at 13 Ma. These ages confirm that opal deposition began shortly after deposition of the tuffs and grew outward from the contact with the host rock.

The data show that the Yucca Mountain opal is consistent with the continual or semi continuous depositional model, as opposed to an instantaneous deposition model, where very thin layers of opal are added more or less continuously on a scale finer than the sampling technique can resolve. Consequently apparent ages of individual analyses will represent a mixed age depending on the number of layers and their ages included in the sample. Continuous depositional rates of about ~1 to 5 mm/Ma have been calculated for outermost opal layers from Yucca Mountain (Neymark, 1998; Neymark and Paces, 2000; Paces *et al.*, 2000, 2001; Neymark *et al* 2002).

Researchers commonly noticed that individual analyses by TIMS of individual hemispheres (especially those that are >1 Ma) show discordance between $^{207}\text{Pb}/^{235}\text{U}$ and $^{206}\text{Pb}-^{234}\text{U}-^{238}\text{U}$ ages as a result of sampling of multiple layers with different age due to the large sample size. In order to increase the spatial resolution, SHRIMP and insitu microdigestion with analysis by TIMS, were used on the outmost layers of an opal sample. Growth rates determined by SHRIMP analysis and insitu microdigestion with analysis by TIMS were ~1mm/m.y. (Paces *et al.*, 2004a; Paces *et al.*, 2010) and verified the previously determined very slow growth rate on samples less than 1 Ma and reconfirmed the validity of the continuous deposition model.

The slow growth rates are product of precipitation by evaporation from films of water, of meteoric origin, that descended slowly through fracture pathways and seeped into air filled cavities (Paces *et al.*, 2001; Whelan *et al.*, 2002; Paces *et al.*, 2010). These slow growth rates imply that the deeper parts of the unsaturated zone at Yucca Mountain maintained long term hydrological stability throughout significant periods of climate variation over the last 10 Ma.

The time framework provided by the opal ages also provides a guide for investigation carbon, oxygen and strontium isotope variations which are preserved in the mineral coatings. Isotopic variations support a descending meteoric water source that has interacted with the soil at Yucca Mountain.

Several different opal samples have been investigated for their suitability for use as a geochronological standard. Common and precious opals were analysed but the precious opal are low in U and contain high non-radiogenic Pb and, therefore, are not

suitable for U-Pb age determinations. U-Pb ages of approximately 15 Ma to ~2 Ma were determined for several common opal samples (Amelin and Back, 2006).

Authigenic and detrital opal clasts are also suitable for dating due to elevated uranium concentrations and low contents of ^{232}Th and non-radiogenic lead and can be used to establish the age of clastic sediments. Opal rich clast rinds and cements in soils near Yucca Mountain produced $^{230}\text{Th}/\text{U}$ ages ranging from several thousand years to finite ages over 500 ka (Ludwig and Paces, 2002; Neymark *et al.*, 1998) and U-Pb ages of ~1.65 (Neymark, 2011; Neymark *et al.*, 2007; Neymark and Paces, 2013) to ~6 Ma (Neymark and Paces, 2013) and yield a minimum age of the alluvium deposition. The detrital opal from erosion of silica-rich fracture coatings out of the source volcanic bedrock constrains the maximum age of the alluvium deposition. The deposition rate for authigenic opal from Midway Valley, Nevada, USA is slow and long term average growth rates were calculated to be about 0.1 mm/Ma (Neymark and Paces, 2013).

3 ANALYTICAL TECHNIQUES

3.1 Introduction

Previous work (e.g. Paces *et al.*, 2004a and b) showed that opals may be finely laminated with growth bands that have variable U concentrations and ages. This inhomogeneity, which is evident on both macro and micro scales, reflects the time sequence of silica deposition in slow growing opal and requires high spatial resolution of sampling to avoid analysing multiple layers with different ages (Neymark and Paces, 2000; Paces *et al.*, 2001). The need to minimise the sample size resulted in the application of the sensitive high resolution ion microprobe (SHRIMP) for U-series dating of opal (Paces *et al.*, 2004a and b), which allows dating of 30- μm -diameter spots on polished opal cross sections. Paces *et al.*, (2004a and b) obtained ^{230}Th - ^{238}U ages and initial $^{234}\text{U}/^{238}\text{U}$ activity ratios (U_i) for younger portions of opal samples and then used these U_i values and measured $^{234}\text{U}/^{238}\text{U}$ in older portions of the samples to calculate model ages, assuming that the U_i value was constant over the entire time of opal formation.

The aim of this study is to extend the work of Paces *et al.*, (2004a) by utilizing both U-series and U-Pb systems in combination to avoid assumptions about the U_i values. This chapter aims to demonstrate that SHRIMP dating can be applied successfully to U-enriched opals ranging in age from several hundred thousand years to several million years.

3.2 Sample collection and selection

Opal can be present in several forms, including as a network of veins as well as isolated veins of pure opal, isolated and groups of hemispheres, thin sheets or evenly distributed in a massive texture throughout the host rock. Coatings in the form of thin sheets vary in thickness from 3 mm to less than 0.5 mm, whereas, hemisphere diameters are generally between 7 mm to 3 mm and are coalescing. Veins vary greatly in size but are generally less than 2 cm thick. Opal that formed in veins was extracted for this study so that a profile of the vein was left intact. Hemispheres were

chipped off and for massive opal there was no attempt made to choose a specific orientation on the samples. Additional information on the samples is provided in each chapter. All samples were mounted in epoxy resin and polished.

Samples used for age determinations were selected on the basis of high intensity of green fluorescence under short wavelength ultraviolet light, a property generally caused by the presence of uranium in high concentrations. Ideally, a large sample (centimeter size) is preferred so that a quantifiable age range can be observed if present, and a contact with the host rock also helps to establish growth chronology.

3.3 SHRIMP

The inhomogeneity of opal makes the application of SHRIMP (Sensitive High Resolution Ion Micro Probe) for chronological work worthwhile, however, despite the apparent advantages there are several disadvantages which need to be carefully considered. All analytical work was conducted using the SHRIMP-II instrument at Curtin University of Technology. This work was built on the practical experience of Paces *et al.*, (2004a), who used SHRIMP-RG at Stanford University to establish the first working analytical procedure for the opal U-series dating.

3.3.1 Advantages

An ion probe such as the SHRIMP allows for the analysis of a small, 20-30 μm , spot on the surface of sample, giving an advantage of high spatial resolution. The advantage of this instrument is; (1) ability to minimize sample preparation, (2) no need for chemical separation and purification, and (3) the ability to analyse all required isotopes in a single run. This is particularly important since the ages of different parts of the same sample can vary significantly and fall within the ranges where either U-Pb or U-series systems are applicable for the purpose of dating. These ages are not known before the samples are analysed and the ability to measure all isotopes simultaneously and select the most appropriate system afterwards can save time and reduce the amount of unnecessary analytical work.

3.3.2 Disadvantages

Major disadvantages of using the SHRIMP for opal dating include the significant loss in precision compared to the thermal ionisation mass spectrometry (TIMS) and difficulties in analysing relatively low uranium opal samples (with less than 20-30 ppm U concentration), as samples with lower concentrations result in insufficient count rates on the least abundant isotopes such as ^{234}U and ^{230}Th . Despite this limitation, SIMS (secondary ion mass spectrometry) dating methods are applicable to a variety of deposits including silicified regolith profiles, which appear to contain significant quantities of U-rich opal.

3.3.3 Simultaneous U-Pb and U-series analysis

The uranium concentrated by opal decays to stable Pb isotopes through a chain of intermediate daughters and so the age of an opal sample can be estimated using a variety of parent-intermediate daughter pairs. The applicability of a particular pair depends on the age of the sample, compared to the half-life of the selected radioactive isotope within the U decay chain. If the age is five times larger than the half-life, the chosen isotope pair will reach a state, close to secular equilibrium and will not yield a finite date. A number of isotopes within the U-series decay chain have relatively long half-lives, making them useful for dating Quaternary materials.

The $^{230}\text{Th}/\text{U}$ dating technique is commonly used for samples younger than ~300 to ~350 ka and occasionally for samples as old as ~ 500 ka, if the analytical errors are sufficiently small. This limit is only applicable for samples analysed using isotope dilution and TIMS. SHRIMP errors are significantly larger, due to smaller ion beam intensities (compared to TIMS), making $^{230}\text{Th}/^{238}\text{U}$ activity ratios of samples older than ~200 to ~250 ka difficult to distinguish from the secular equilibrium value of one. Because opals do not concentrate significant amounts of initial Th, no correction for initial Th is necessary and both the age of a sample and the U_i value can be calculated directly from the observed amounts of ^{230}Th , ^{234}U , and ^{238}U .

In theory, $^{206}\text{Pb}-^{238}\text{U}$ and $^{207}\text{Pb}-^{235}\text{U}$ systems can be used to date opals of any age. However, limits are often imposed by the proportion of non-radiogenic (initial) Pb in the sample, especially for the $^{207}\text{Pb}-^{235}\text{U}$ system, for which very small amounts of radiogenic ^{207}Pb are generated in samples younger than ~1.5 Ma. Concentrations of

both U and non-radiogenic Pb can vary widely in different samples so that opals with high U/Pb ratios may yield reasonably precise ^{207}Pb - ^{235}U ages, as young as a few hundred thousand years, whereas others with low U/Pb ratios may have age uncertainties too large to be useful even though they may be several million years old.

The ^{206}Pb - ^{238}U age calculations are affected by the presence of the initial excess of ^{234}U , which is usually an unknown quantity. Nevertheless, for young samples with measurable ^{234}U - ^{238}U disequilibrium, the simultaneous solution of two equations describing the accumulation of ^{206}Pb from ^{238}U and ^{234}U provides a way to estimate both the age and U_i (Neymark *et al.*, 2000a). In samples where ^{230}Th has not reached equilibrium with its parent, the same calculations can be made based on the observed amounts of ^{230}Th , ^{238}U , and ^{206}Pb . In a closed system ^{206}Pb - ^{230}Th - ^{238}U and ^{206}Pb - ^{234}U - ^{238}U ages must be concordant providing that there is no initial excess of ^{230}Th . Combined U-Pb and U-series techniques have been used to date Quaternary opals (Neymark *et al.*, 2000a), significantly extending the age range beyond that of the ^{230}Th -U dating method. However, in some cases, discordant ages were calculated from different isotope pairs. This discordance was attributed to the effects of mechanical mixtures of older and younger material within a single volume of analysed material, and the non-linear effects of radioactive decay of isotopes with differing half-lives. The combined U-Pb and ^{230}Th -U ages were used to support a model of slow mineral deposition (rates of millimetres per million years) resulting in layering on a scale too fine to resolve using mechanical sampling. Refinement of the ages of such slow depositional processes is possible only by improving the spatial resolution of sampling.

3.4 ^{238}U - ^{234}U - ^{230}Th - ^{206}Pb - ^{235}U - ^{207}Pb system applied to the opal chronology

A detailed description of combined ^{238}U - ^{234}U - ^{230}Th - ^{206}Pb - ^{235}U - ^{207}Pb , four-dimensional system and as applied to the chronology of Yucca Mountain opals can be found in Neymark *et al.*, (2000a). Different parent-daughter pairs within this system are most relevant for the dating of different parts of opal coatings depending on their age. In addition to the age a factor limiting applicability of one or another pair is the amount of initial Pb and ^{234}U accumulated in the analysed volume. The latter is assumed to always be present to a varying degree in samples precipitated

from the water. This makes the use of the ^{206}Pb - ^{238}U system for geochronology of opal difficult, where ^{234}U reached secular equilibrium with ^{238}U , since the relative contribution of initial ^{206}Pb and ^{206}Pb formed by the decay of initial ^{234}U is not known. The most reliable way to determine an age of such “old” opal is to utilise the ^{207}Pb - ^{235}U pair, which is typically free of significant influence from any initial excess of intermediate daughters. This, however, reduces the precision of the estimated age due to the smaller abundance of ^{235}U relative to ^{238}U , and the larger contribution of initial Pb into the total measured ^{207}Pb , which in its turn places a lower limit on the age that can be determined using ^{207}Pb - ^{235}U system. The main source of uncertainty for ages calculated in this manner is the unknown composition of initial Pb, which is a problem common for U-Pb analysis of any mineral. On the other side of the age range are opal samples where ^{234}U and ^{230}Th are not in secular equilibrium. The ^{230}Th - ^{234}U systematics is most appropriate for these samples.

Samples with the ages younger than the limit for the ^{207}Pb - ^{235}U system but older than limit of ^{230}Th - ^{234}U system often have ^{234}U which is still not equilibrated with ^{238}U . That allows simultaneous use of ^{206}Pb - ^{238}U and ^{234}U - ^{238}U pairs to estimate ages and initial activities of ^{234}U . As in case of ^{207}Pb - ^{235}U system unknown composition of initial Pb is a main source of uncertainty.

There are two age intervals where consistency of the ^{238}U - ^{234}U - ^{230}Th - ^{206}Pb - ^{235}U - ^{207}Pb system can be tested by simultaneously applying two of the three age calculation schemes described above. The first interval is within the older part of the ^{230}Th - ^{234}U system range where use of both, ^{206}Pb - ^{238}U and ^{234}U - ^{238}U chronometers is possible. Two age estimates can be compared and must be similar providing that (i) initial Pb composition is guessed correctly or its contribution is not significant and (ii) there is no loss or gain of daughters between ^{230}Th and ^{206}Pb (such as ^{222}Rn) after the formation of sampled opal (this includes absence of initial excess of any of these daughters). The other interval is at the upper end of applicability of ^{206}Pb - ^{234}U - ^{238}U system where the results can be compared to the ^{207}Pb - ^{235}U ages, with similar requirements necessary to obtain similar ages from two estimates.

3.5 Samples

SHRIMP analyses were conducted for three opal samples. The first sample, M21277, was previously analysed by both U-series and U-Pb TIMS methods and was used to develop the SHRIMP analytical protocols and later as a SHRIMP standard. Five fractions of a sample from Mexico were analysed using TIMS to compare SHRIMP and TIMS U-Pb ages. A third sample from Hungary had not been dated previously.

3.5.1 *Opal standard M21277*

The extraction and ionisation efficiency of different elements in an ion microprobe are dissimilar, resulting in the deviation of observed element ratios from the true ratios in the analysed samples. Correction for this instrumental bias requires frequent analysis of a standard where the true ratios of interest have been determined by independent means (i.e. by isotope dilution TIMS). Paces *et al.*, (2004a) calibrated Th/U ratios in unknowns against opal M21277 from Virgin Valley, Nevada, USA. This sample is an amorphous, porcelanous opal of biogenic origin. Macroscopically, it is homogeneous; however, backscatter electron images reveal compositional heterogeneities on the scale of tens of micrometers, which are related to its diatomaceous origin (Paces *et al.*, 2004a).

3.5.2 *Opals from Guanajuato, Mexico and Hosszú Hill, Hungary*

Two opal samples from Mexico and Hungary were analysed as a part of technique development, with a view to potentially use as additional standards. The samples are old enough for the intermediate products of U decay to be in secular equilibrium. Use of the U-Pb system is, therefore, the only way to date these samples.

A sample of the Mexican opal was selected from the collection of the Department of Applied Geology at Curtin University of Technology, Western Australia. The homogenous, transparent opal (Figure 3.1) was originally collected from cavities in volcanic rocks from the basaltic plateau near Guanajuato, a part of the Trans-Mexican Volcanic Belt.

A hyalite sample, collected from Hosszú Hill in Borsod-Abaúj-Zemplén County, Hungary (Figure 3.2), formed in cavities of Miocene (Sarmatian) perlitic rhyolite.

Silicification is widely developed in the area and is associated with both volcanic and sedimentary processes of Miocene age (Papp G, 2003, personal communication, 5 May).

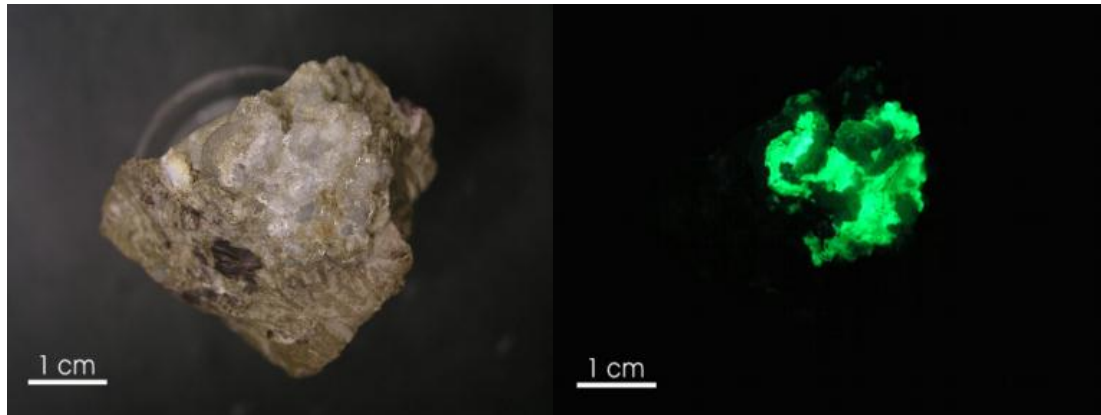


Figure 3.1 (A) Photograph of the Mexican opal and host rock from Guanajuato, Mexico. (B) Photograph of the same opal and host rock under UV light showing the green fluorescence of the opal reflecting the uranium concentration.

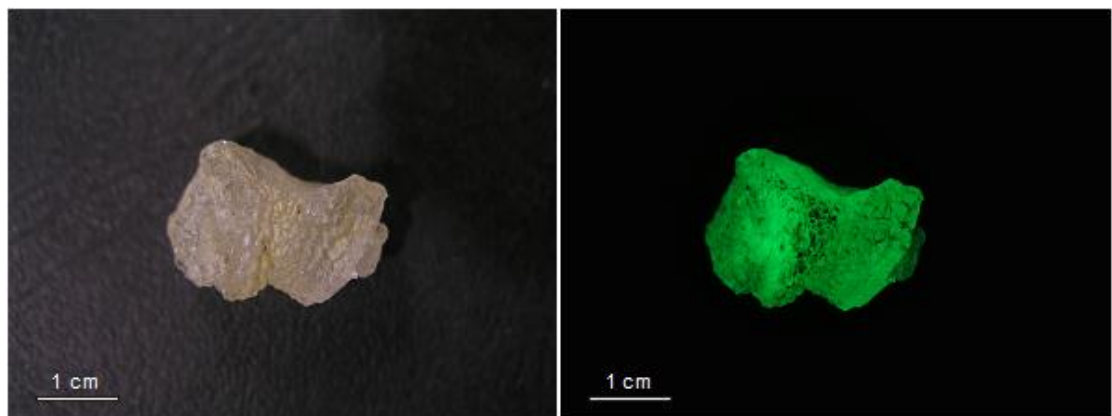


Figure 3.2 (A) Photograph of the Hungarian opal sample from Hosszú Hill, Hungary showing the homogenous and transparent nature of the opal. (B) Photograph of the same opal under UV light showing the green fluorescence of the opal.

Two chips representing different parts of the sample from Mexico were investigated during one SHRIMP session. Two additional sessions were used to analyse two chips of the sample from Hungary. Analytical procedures involving ^{238}U and

$^{238}\text{U}^{16}\text{O}$ were used during to the first session, whereas ^{235}U and $^{235}\text{U}^{16}\text{O}$ data were collected during the second session (see later discussion).

3.6 Analytical procedure – TIMS

3.6.1 *Details of the analytical procedure - TIMS*

TIMS samples were leached mildly in 3M HCl at room temperature, rinsed in ultra pure water and air dried resulting in pure opal without adhering calcite and surface contamination. Sample size was kept between 0.1 – 2.5 mg because larger samples of slowly grown opal are not likely to yield reliable results. Complete dissolution of opal samples was obtained by digestion in a mixture of HF along with a mixed ^{233}U - ^{229}Th or ^{205}Pb - ^{235}U spike in Teflon vials. U and Th were purified and separated using anion exchange chromatographic resins in Teflon microcolumns with HCl and HNO_3 media. All three elements were analysed with a VG354 isotope-ratio mass spectrometer (FISONS Instruments) at Curtin University of Technology. This instrument has a 90° magnetic sector field and was fitted with a 16 sample turret, thermal ion source and a single Daly collector which operated in analogue mode. Both U-Pb and U-Th subsamples were loaded on the central filament of triple rhenium filament assemblies. Pb was loaded using a H_3PO_4 – silica gel mixture and run as Pb^+ and UO_2^+ . U-Th was loaded using layers of colloidal graphite. Subsamples were degassed extensively before analysis. Measurements were performed manually with the operator increasing the temperature of the subsample and focusing the ion beam. The average temperature used was 1800° C for U analysis, 1700°C for Th and ~1400°C for Pb. The pressure inside the source chamber was $\sim 3 \times 10^{-6}$ Pa during analyses. Between 5 and 10 data blocks, each containing ten $^{233}\text{U}/^{235}\text{U}$, $^{234}\text{U}/^{235}\text{U}$, $^{235}\text{U}/^{235}\text{U}$ isotopic ratios. The resulting Pb and U isotopic data were reduced using the PBDAT program (Ludwig, 1987) which makes corrections for mass fractionation, procedural blanks, spike contribution and initial Pb. Disequilibrium U-Pb and U-series ages were calculated using the ISOPLOT program (Ludwig, 1999). All uncertainties are reported at 2σ level.

3.7 Results -TIMS

3.7.1 Opal standard M21277

Previous studies have indicated that M21277 opal has uranium concentrations up to 850 µg/g and an average ^{207}Pb - ^{235}U age of 2.20 Ma (Amelin and Neymark, 1999). U-series TIMS analyses of this opal showed that the ^{230}Th / ^{238}U and ^{234}U / ^{238}U activity ratios are equal to unity within the analytical uncertainty (Paces *et al.*, 2004a) hence this ‘standard’ is considered to be in secular equilibrium. A number of U-Pb TIMS analyses (Amelin and Neymark, 1999; Amelin and Back, 2006) indicate that U-Pb ages are homogeneous in different aliquots of this sample. U-Pb and U-series data for six additional chips of this opal (Table 3.1), obtained during this study by isotope dilution TIMS, are compatible with the results published for this opal by Amelin and Neymark (1999) and Paces *et al.*, (2004a).

3.7.2 Opals from Guanajuato, Mexico

Five TIMS analyses of the opal from Guanajuato, Mexico determined in this study (Table 3.1) gave a weighted average ^{207}Pb / ^{235}U age of 9.9 ± 0.3 Ma.

3.8 Analytical procedure - SHRIMP

3.8.1 General approach

There are a number of differences between SHRIMP U-Pb analysis and procedures used for opal compared to those developed for the more common U-bearing accessory minerals such as zircon, monazite, titanite etc. Most of these minerals analysed over the last two decades, with the exception of zircons studied by Reid *et al.*, (1997) and Bacon *et al.*, (2000), are significantly older than the late Tertiary and Pleistocene opals investigated in this study. Young opals have relatively small amounts of radiogenic ^{206}Pb , that consist of a mixture produced by in situ decay of ^{238}U and from the decay of excess intermediate daughter products of ^{238}U (notably ^{234}U , ^{230}Th and ^{226}Ra) that may have been incorporated at the time of opal formation. Therefore, procedures for U-Pb dating of samples younger than about 1.5 Ma need to include analysis of these intermediate daughter isotopes, even though they are

present at very low abundances. In order to achieve an acceptable level of precision for these isotopes, a sufficient number of secondary ion counts must be obtained through the combination of long integration times and high intensity of the primary beam. The latter can be attained by increasing the diameter of the analytical spot or by switching the primary beam from $^{16}\text{O}_2^-$ (most commonly used in SHRIMP analysis) to $^{16}\text{O}^-$.

Table 3.1 U-Pb and U-series TIMS data for opal sample M21277 used as a SHRIMP standard* and Mexican opal (all errors are 2σ).

Sample	U ($\mu\text{g/g}$)	$\frac{^{206}\text{Pb}}{^{204}\text{Pb}}$	$\frac{^{207}\text{Pb}}{^{235}\text{U}}$	$\frac{^{206}\text{Pb}}{^{238}\text{U}}$	Corr Coeff.	$\frac{^{207}\text{Pb}}{^{235}\text{U}}$ Age(Ma)	$\frac{^{234}\text{U}}{^{238}\text{U}}$ Act	$\frac{^{230}\text{Th}}{^{238}\text{U}}$ Act
M21277								
1	751	80.5	0.00199 ± 26	0.000405 ± 4	0.698	2.20 ± 29		
2	835	75.6	0.00199 ± 31	0.000389 ± 5	0.674	2.02 ± 31		
3	842	108.3	0.00227 ± 9	0.000437 ± 10	0.631	2.30 ± 9		
4	954						0.999 ± 6	1.015 ± 6
5	863						0.989 ± 12	1.008 ± 13
6	805						1.000 ± 6	1.003 ± 9
Mexican opal								
1	65	69.5	0.0098 ± 14	0.001726 ± 20	0.806	9.8 ± 1.4		
2	46	74.5	0.0093 ± 6	0.001545 ± 15	0.897	8.3 ± 0.6		
3	62	315.3	0.0099 ± 5	0.001654 ± 13	0.854	10.0 ± 0.5		
4	54	258.4	0.0101 ± 7	0.001794 ± 16	0.894	10.2 ± 0.6		
5	42	68.3	0.0100 ± 11	0.001664 ± 18	0.776	9.1 ± 1.1		

*Opal chips ranging from 0.1 to 0.3 mg were spiked with the mixed ^{205}Pb - ^{235}U or ^{229}Th - ^{236}U spikes and digested in HF. After evaporation salts were re-dissolved in nitric acid and loaded in a single filament configuration with silica gel or activated carbon. Samples were analysed using Daly multiplier fitted on VG354 instrument at Curtin University of Technology. Pb data were corrected for 2 picograms blank and non-radiogenic lead contribution using modern Stacey-Kramers model non-radiogenic Pb (Stacey and Kramers, 1975). Decay constants by Jaffey *et al.*, (1971) and Cheng *et al.*, (2000) were used to calculate ages and activity ratios.

These strategies have some disadvantages. For example, a large spot size reduces the spatial resolution compromising the purpose of using SHRIMP analysis for this type of dating. Also, high primary ion beam intensity results in a large number of $^{238}\text{U}^{16}\text{O}$ (mass 254) counts, very close to the upper limit of the electron multiplier for high-U samples. This condition precludes further increases in the counting rates of less abundant isotopes and therefore limits precision of the $^{234}\text{U}/^{238}\text{U}$, $^{230}\text{Th}/^{238}\text{U}$, and Pb/U . A potential solution to this problem is to measure ^{235}U and ^{235}UO (mass 251) as a proxy for ^{238}U and ^{254}UO . However, this change of analytical protocol will only give an advantage if the primary beam intensities above 30-50 nA are achieved on a day to day basis. This is not attainable with the existing duoplasmatrons even if the more intensive $^{16}\text{O}^-$ primary beam is used to extract secondary ions from the sample.

Longer integration times for the small isotopes results in an increased time required for a single analysis which, combined with an intense primary beam, can cause significant damage to the gold coat around an analytical spot, increasing the risk of drift in the secondary beam focus and the observed elemental ratios.

A usable analytical protocol must consider a combination of all of these factors which will ultimately give ratios with sufficient precision to resolve the investigated geological processes. This study attempts to discuss one of the possible combinations as well as investigating advantages and disadvantages of (i) increasing the primary beam by switching from $^{16}\text{O}_2^-$ to $^{16}\text{O}^-$, as opposed to increasing the spot size, and to some degree (ii) increasing the number of counts by using a larger primary beam as opposed to longer counting for the small isotopes.

3.8.2 *Details of the analytical procedure - SHRIMP*

During this study the primary beam was set above 10 nA to obtain sufficient counting rates for isotopes with low abundances, but below ~15 nA to keep the ^{254}UO counting rate below the saturation limit of the secondary electron multiplier. Both $^{16}\text{O}_2^-$ and $^{16}\text{O}^-$ were tested as primary beam in order to determine conditions most suitable for the opal analysis. The large number of mass stations with long integration times, compared to the traditional U-Pb analysis of zircon, results in a significantly longer time required for an analysis. Individual runs take between 25 and 40 min.

Several SHRIMP sessions were devoted to the measurements of a standard opal in order to establish the best analytical conditions for SHRIMP dating of opal. The analytical procedure was designed to accommodate both U-Pb and U-series dating systems. The individual spot analysis consisted of 5 scans over 12 peaks at masses ^{197}Au , ^{204}Pb , 204.1-background, ^{206}Pb , ^{207}Pb , ^{208}Pb , 209 (Pb hydrides), ^{238}U , ^{246}ThO , ^{248}ThO , ^{250}UO and ^{254}UO , with the exception of the first two SHRIMP sessions where 10 and 7 scan procedures were used to increase the number of collected secondary ions (Table 3.2).

Table 3.2 Run tables used for SHRIMP opal analysis.

Peak #	Mass (amu)	Species	Integration time (s)		
			(10 scans)	(7 scans)	all subsequent runs (5scans)
1	197	^{197}Au	2	2	2
2	204	^{204}Pb	10	30	30
3	204.1	Background	30	30	30
4	206	^{206}Pb	10	30	20
5	207	^{207}Pb	30	30	40
6	208	^{208}Pb	10	30	20
7	209	Pb-hydride monitor	10	10	10
8	238 (or 235)*	^{238}U (or ^{235}U)	3	3	3
9	246	$^{230}\text{Th}^{16}\text{O}$	30	na**	30
10	248	$^{232}\text{Th}^{16}\text{O}$	30	5	5
11	250	$^{234}\text{U}^{16}\text{O}$	30	na	30
12	254 (or 251)*	$^{238}\text{U}^{16}\text{O}$ (or $^{235}\text{U}^{16}\text{O}$)	3	3	1

* ^{235}U and $^{235}\text{U}^{16}\text{O}$ have been analysed instead of ^{238}U and $^{238}\text{U}^{16}\text{O}$ in a single analytical session

** not analysed

Masses ^{238}U and $^{238}\text{U}^{16}\text{O}$ were replaced with ^{235}U and $^{235}\text{U}^{16}\text{O}$ during a single analytical session. Masses 197 and 254 were used for the magnetic field calibration. Background was measured near mass 204, similar to that used in standard U-Pb zircon analyses. Both ^{234}U and ^{230}Th were analysed as oxides in order to increase the total number of counts. There is a possibility of interference from $^{232}\text{Th}^{18}\text{O}$ at mass 250 where the $^{234}\text{U}^{16}\text{O}$ peak was measured. However, even in the worst case scenario represented by the standard sample M21277, where the $^{232}\text{Th}/^{238}\text{U}$ average

value of ~ 0.0001 is largest in the group of analysed samples and $^{234}\text{U}/^{238}\text{U}$ is smallest, the contribution of $^{232}\text{Th}^{18}\text{O}$ at mass 250 is less than 0.5%, considering that ^{18}O is about 0.2% of the total oxygen. The retardation lens at $\sim 10,000$ V was employed to filter low energy ions and reduce the background. Mass 209 was included to monitor potential Pb hydrides, which were anticipated since opal contains a variable amount of water. However, the intensity of this mass never significantly exceeded that of the background and thus counts at mass 209 were never used in the data reduction.

3.8.3 Behaviour of secondary beam and calculation of isotope ratios

The traditional approach to SHRIMP data reduction, used to obtain isotope ratios, involves regression of counts versus times of particular integrations for all analysed isotopes, followed by linear extrapolation of all fits to the same point in time. The single value for each isotope is then used to calculate ratios. Errors are propagated based on counting statistics. This approach is not acceptable to data sets obtained during this study, because the secondary beam intensity for individual mass stations varies nonlinearly with time, especially for the most abundant peaks, ^{238}U and $^{238}\text{U}^{16}\text{O}$. In fact, many runs show a maximum number of counts in the middle of the run for these two masses (Figure 3.3). The less abundant isotopes (for example, ^{206}Pb , Figure 3.3) rarely show similar intensity versus time behaviour. Uncorrelated behaviour of intensities of different isotopes suggests that the changes in the count rates during the run are not determined by fluctuations in the total secondary beam and, more likely, reflect variations in the extraction efficiency of Pb and U from the sample. In any case, an attempt to fit a straight line using observed data would result in either accepting a poorly constrained fit or rejecting some counts, which are not necessarily outliers, but rather reflect the nonlinear behaviour of the count rates with time.

An alternative algorithm is traditionally used in TIMS analyses of chemically-extracted isotopically-homogenous elements to account for fluctuations in the ion beam during the run. This approach assumes a linear behaviour of the ion beam between two measurements of the same isotope in sequential scans, which allows calculation of the rate at which the ion beam is changing.

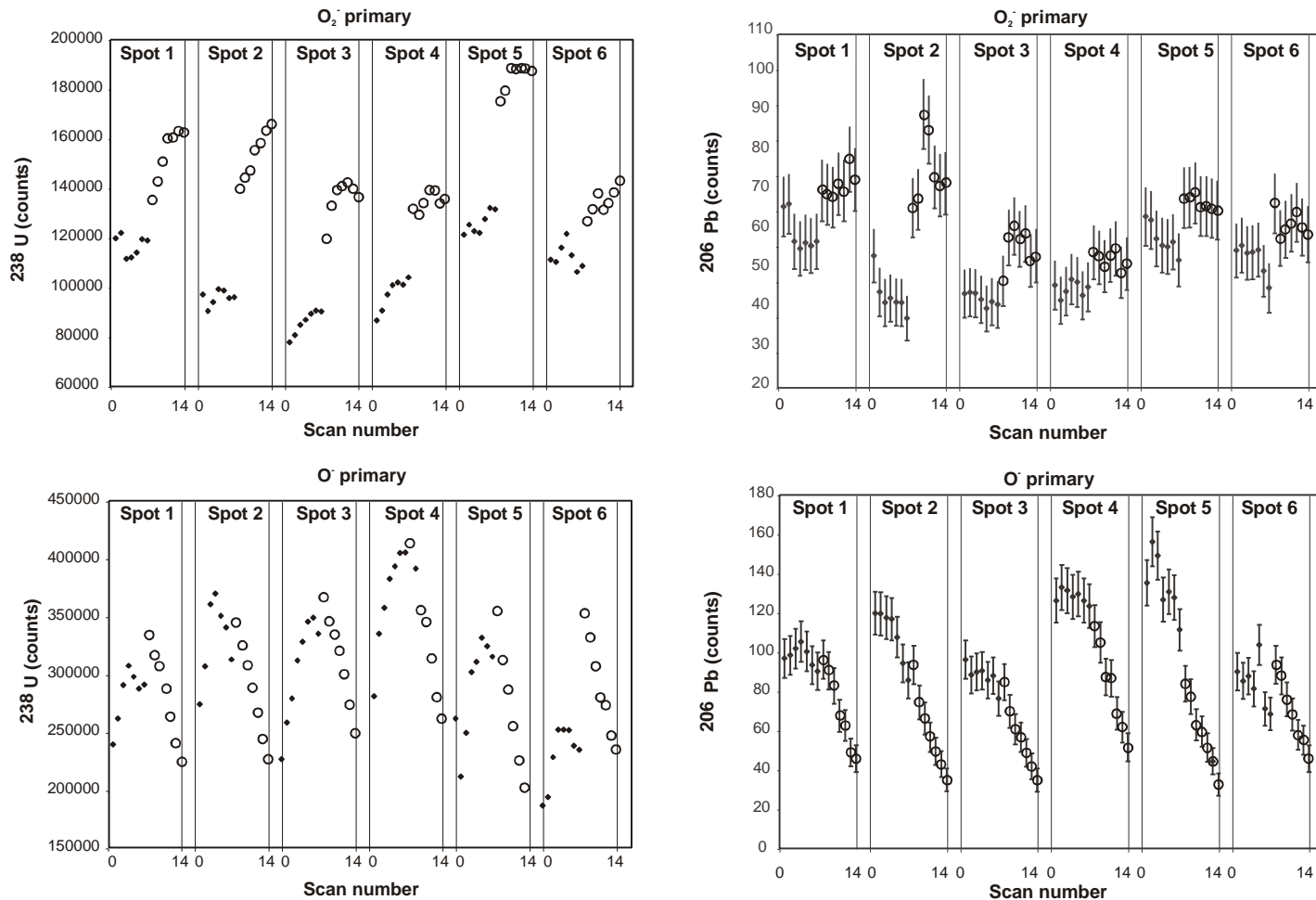


Figure 3.3 Within-run variations of ^{238}U and ^{206}Pb counts (black dots – first run of a spot; open circles – second run). All plots show non-linear behaviour prohibiting line fitting, which is commonly used for initial SHRIMP data reduction. Uncertainties are shown as 2σ error bars in this and all other figures.

This rate can then be used to apply corrections to the observed intensities of all other isotopes. However, as mentioned earlier, uncorrelated variations in the intensities of different isotopes during the SHRIMP runs prohibit application of this correction procedure to the SHRIMP data. Therefore, a third approach, which has been used by Paces *et al.*, (2004a) and involves summing counts obtained for individual masses during the run, was adopted for this study. The total counts for each mass were divided by the cumulative integration times to obtain average count rates (counts per second values) for all isotopes. These values were then used to calculate isotope ratios. Within-run uncertainties were calculated based on counting statistics. The probable weakness of this approach is the possibility of bias in the calculated ratios, when the sequential measurements of the isotopes are made while the overall secondary beam changes systematically. However, variation of the number of scans compensated by changes of integration times for different isotopes during several analytical sessions did not produce any observable difference in the isotopic ratios, suggesting that even if such bias exists it is far smaller than the other factors contributing to errors in the analysed ratios

3.9 Data reduction

The data reduction procedure was implemented as a Microsoft Excel AddIn and was designed to obtain a series of ratios relevant to all possible combinations of measured parent-daughter pairs, as well as their errors and error correlations. This included $^{234}\text{U}/^{238}\text{U}$ and $^{230}\text{Th}/^{238}\text{U}$, used for the disequilibrium-based dating techniques, as well as $^{207}\text{Pb}/^{235}\text{U}$ and $^{206}\text{Pb}/^{238}\text{U}$ corrected for initial-Pb contributions.

The initial Pb correction in the opal samples, including the standard, can be carried out using both ^{204}Pb and ^{208}Pb . The ^{204}Pb in many opal samples is hardly distinguishable above the background, which combined with the very low counting rate of ^{206}Pb in the younger samples, makes ^{204}Pb correction rather imprecise or even impossible. Alternatively, corrections based on ^{208}Pb can be applied. The opal standard (M21277) has an average $^{206}\text{Pb}/^{204}\text{Pb}$ of ~ 200 , which is low enough (i.e., the ^{204}Pb counting rate is high enough) so that initial Pb corrections based on ^{204}Pb are similar to those obtained using ^{208}Pb . The latter correction for initial Pb in opal samples differs from the approach developed for zircon analysis, and takes advantage

of the fact that ^{230}Th is analysed as a part of the analytical routine. Furthermore, because Th is largely insoluble in most aqueous solutions, ^{232}Th is typically absent in many samples of pure opal. Providing there is no initial excess of intermediate daughter products of ^{232}Th , the resulting ^{208}Pb present in opal is almost entirely non-radiogenic and can be used for the correction in exactly the same way as the ^{204}Pb is usually used.

Nevertheless, as part of a uniform data reduction procedure, radiogenic ^{208}Pb was subtracted from the total ^{208}Pb in both the standard and the unknowns before the non-radiogenic Pb corrections were made in order to determine the possible range of contributions of the radiogenic component in ^{208}Pb . During zircon analysis the proportion of radiogenic ^{208}Pb is calculated from the measured $^{208}\text{Pb}/^{206}\text{Pb}$, assuming that the U-Th-Pb system is concordant and, in the case of the standard, knowing its age. A coefficient of about 1.1 determined from multiple runs of the standard with a known $^{232}\text{Th}/^{238}\text{U}$ is commonly applied to obtain true $^{232}\text{Th}/^{238}\text{U}$ in unknown samples. This true $^{232}\text{Th}/^{238}\text{U}$ combined with an initial estimate of the age (the ^{204}Pb corrected age can be used for this initial assumption) is used to determine the radiogenic proportion in the total ^{208}Pb . $^{232}\text{Th}/^{238}\text{U}$ is not known in the opal standard, however, this standard is in a state of secular equilibrium (meaning that its $^{230}\text{Th}/^{238}\text{U}$ activity ratio is equal to one) and the true $^{232}\text{Th}/^{238}\text{U}$ in the standard can be estimated from the measured $^{230}\text{Th}/^{238}\text{U}$ and $^{232}\text{Th}/^{238}\text{U}$ as follows (expressed as activity ratios):

$$\frac{\frac{^{232}\text{Th}}{^{238}\text{U}}_{true}}{\frac{^{232}\text{Th}}{^{238}\text{U}}_{measured}} = \frac{\frac{^{232}\text{Th}}{^{238}\text{U}}_{measured}}{\frac{^{230}\text{Th}}{^{238}\text{U}}_{measured}} \times \frac{\frac{^{230}\text{Th}}{^{238}\text{U}}_{true}}{\frac{^{232}\text{Th}}{^{238}\text{U}}_{true}} = \frac{\frac{^{232}\text{Th}}{^{238}\text{U}}_{measured}}{\frac{^{230}\text{Th}}{^{238}\text{U}}_{measured}} \times 1.0$$

Coefficients (1/measured $^{230}\text{Th}/^{238}\text{U}$) relating measured and true values of $^{232}\text{Th}/^{238}\text{U}$ can also be derived from all standard analyses and the average of these coefficients can be used to estimate true $^{232}\text{Th}/^{238}\text{U}$ in unknowns. The proportion of radiogenic ^{208}Pb can be estimated from these true $^{232}\text{Th}/^{238}\text{U}$ in exactly the same way as it is usually done for zircons.

3.10 Results - SHRIMP

3.10.1 Data for opal standard M21277- Establishing optimal analytical conditions

Several SHRIMP sessions were devoted to measurements of opal standard M21277 to establish the best analytical conditions for opal SHRIMP dating. The most intense secondary ion beam for $^{238}\text{U}^{16}\text{O}^+$ during these sessions ranged from $\sim 1.8 \times 10^5$ to $\sim 7.6 \times 10^5$ counts per second (cps), with the average value of $3.5 \pm 1.3 \times 10^5$ cps, similar to that for the SHRIMP-RG average value of $3.9 \pm 1.5 \times 10^5$ cps reported for splits of the same opal (Paces *et al.*, 2004a).

A single run in the first SHRIMP session consisted of 10 scans. This setting was used in an attempt to maximise the number of counts without making the run excessively long. Nevertheless, the duration of a single analysis was more than one hour and it was discovered that in all runs the primary beam was constant only during the first seven scans and decreased towards the end of each run. Primary beam intensity could be recovered after the run by adjusting either primary or secondary steering. The observed effect was interpreted as a possible loss of conductivity near the spot due to long burning with the high primary beam. In addition, significant and systematic drift in measured $^{206}\text{Pb}/^{238}\text{U}$ was observed in all runs. Increasing the thickness of the gold coat was not considered desirable, because it usually increases the length of rastering prior to the analysis and introduces additional non-radiogenic Pb at the surface of the sample.

Unlike Pb-U ratios, the $^{234}\text{U}^{16}\text{O}/^{238}\text{U}^{16}\text{O}$ and $^{230}\text{Th}^{16}\text{O}/^{238}\text{U}^{16}\text{O}$ were relatively constant within each run. These ratios were not measured during the second analytical session. During this session, the number of scans per run was cut down to seven and each spot was analysed twice. The secondary extraction potential was readjusted by about 10% between the two analyses to recover the intensity of the secondary beam, which decreased by 10 to 20% towards the end of each run. Six spots analysed using the O_2^- primary beam was followed, after moving the stage, by another six spots analysed with the O^- beam. Both types of primary beam resulted in a very similar behaviour of the secondary beam. It was found that the $^{206}\text{Pb}/^{238}\text{U}$ calculated for the individual scans within the run decreased systematically towards the end of the run (Figure 3.4). This decrease often continued during the second

analysis of the same spot so that both analyses defined a single trend, despite the secondary beam being refocused between the runs. This observation may indicate that the decrease in measured Pb-U ratios is a function of the pit depth. The overall change in the measured $^{206}\text{Pb}/^{238}\text{U}$ can be as large as 100% and on average it is poorly correlated with the change in U/UO. The U/UO is a sensitive indicator of changes in the secondary ion extraction during the run, and fitting the line through standard analyses in $^{206}\text{Pb}/^{238}\text{U}$ versus U/UO coordinates is an essential part of the data reduction procedure for all minerals commonly analysed with ion probes. Although the proportion of non-radiogenic Pb in the standard is relatively high (the $^{206}\text{Pb}/^{204}\text{Pb}$ varies from ~100 to ~200), a subtraction of the non-radiogenic Pb component neither significantly reduces the within-run variation of Pb/U nor increases its correlation with the U/UO. Because the Pb/U drift is correlated with run duration (i.e. burning time of a spot), the analysis time was further shortened in all subsequent sessions. At the same time, integration times were adjusted so that, in spite of the reduction to five scans, total counts for small masses were not significantly impacted.

The switch from 10 to 5 scans did not result in any dramatic decrease in the number of counts. In any case it can be compensated by an increase in the integration time on some isotopes. It appears that the intensity of the primary beam during the session has more effect on the overall counting rate. The total number of cumulative counts of ^{206}Pb in the first session varied from ~3000 to ~5000, whereas this range for the third session was from ~ 5000 to 15000 counts. The smallest number of counts collected for ^{230}Th averaged ~1500 was but sometimes as low as ~1000 counts. That corresponds to ~2.5-3.5% counting statistics error. This error can be potentially improved by increasing integration time on this isotope.

Comparison of variation in the number of counts for different isotopes reveals strong correlation between ^{238}U , $^{230}\text{Th}^{16}\text{O}$ (mass 246), $^{234}\text{U}^{16}\text{O}$ (mass 250) and $^{238}\text{U}^{16}\text{O}$ (mass 254). The correlation coefficients between different pairs are above 0.9 and most commonly are more than 0.95. The correlation between the different U species is somewhat expected since their intensities appear to correlate with the dissociation of uranium-oxygen bonds during the sputtering.

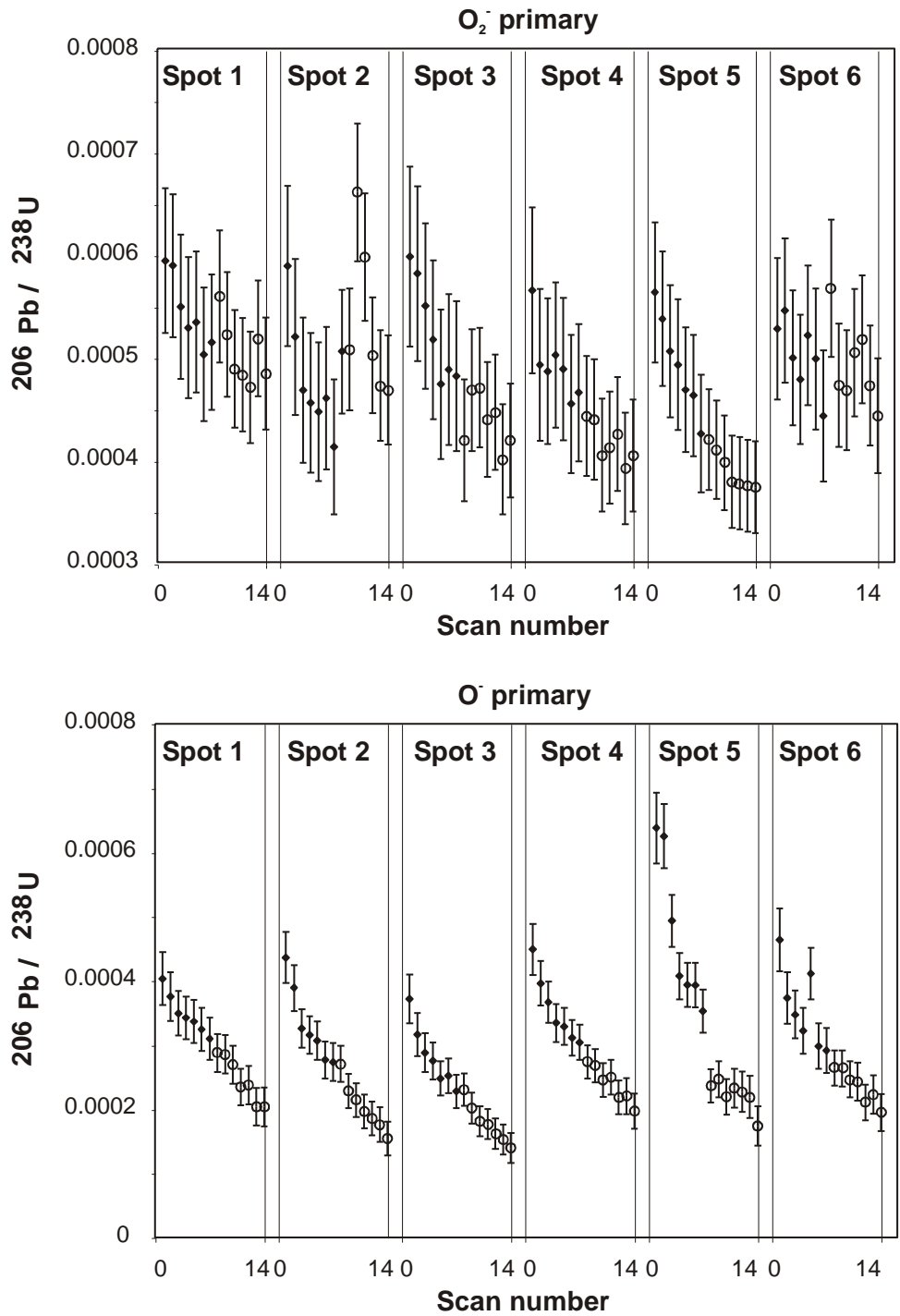


Figure 3.4 Within-run behaviour of $^{206}\text{Pb}/^{238}\text{U}$ (black dots – first run of a spot; open circles – second run). During the second analysis of the same spot, the $^{206}\text{Pb}/^{238}\text{U}$ continues to decrease despite the refocusing of the secondary beam.

Opal samples are unlikely to produce significant amounts of any molecular species other than oxides. Therefore, the sum of U^+ , UO^+ and UO_2^+ above the sputtered region must come close to 100% under any type of analytical conditions, and change in any one of them will be compensated by the proportional change in the other two. Correlation between the U isotopes and ^{246}ThO once again reiterates the point made by Paces *et al.*, (2004a), that Th/U ratios do not vary significantly during the opal SHRIMP analysis.

^{207}Pb and ^{208}Pb also show strong correlation, with the correlation coefficient in most of the sessions larger than 0.95. Contrary to that, ^{206}Pb is only weakly correlated with both ^{207}Pb and ^{208}Pb (maximum correlation coefficient is ~0.7, but usually less and sometimes near zero). These observed relationships between the Pb isotopes can be explained by the mixing of radiogenic and non-radiogenic Pb. The $^{232}\text{Th}/^{238}\text{U}$ ratios in the standard vary between $\sim 10^{-4}$ to 10^{-5} . The very low ^{232}Th abundances imply that the ^{208}Pb measured in hydrogenic opal is almost entirely derived from non-radiogenic sources. The contribution of non-radiogenic Pb in the ^{207}Pb is significantly higher than in the ^{206}Pb , resulting in a much better correlation between the ^{207}Pb and ^{208}Pb than the ^{206}Pb and ^{208}Pb or the ^{206}Pb and ^{207}Pb .

Although ^{206}Pb contains more radiogenic component than other Pb isotopes, correlation between ^{206}Pb and ^{238}U is not very strong (correlation coefficient varies between ~0.4 and 0.9). The non-radiogenic Pb contribution to the ^{206}Pb can be calculated and subtracted from the total counts assuming that all ^{208}Pb is non-radiogenic. This subtraction however, does not result in substantial improvement of the correlation between ^{206}Pb and ^{238}U , indicating that the reasons for the observed differences in behaviour of these two isotopes are other than the presence of non-radiogenic Pb. This conclusion is not new and similar observations are made for other minerals such as zircon. The complications associated with the determination of true values of U/Pb ratios appear to be a general problem of ion probe geochronology and are discussed in the following sections as applied to opal analysis.

3.10.2 Th/U and Pb/U ratios

Results obtained for the M21277 opal standard (Figure 3.5) confirm the conclusion of Paces *et al.*, (2004a), that the Th/U ratio is constant within error during the SHRIMP session and is independent of variations in $^{238}\text{U}/^{238}\text{U}^{16}\text{O}$ (Figure 3.5a). The average value of the $^{230}\text{Th}/^{238}\text{U}$ activity ratio (recalculated from the measured atomic ratio using decay constants by Jaffey *et al.*, (1971) and Cheng *et al.*, (2000) for the opal standard analysed during seven sessions is about 0.3% lower than the secular equilibrium value of one (Figure 3.5b). The 2σ relative uncertainties of $^{230}\text{Th}/^{238}\text{U}$ in individual runs (within-run errors) vary from ~5.7 to ~11.5%, with an average value of ~8.6%, whereas the within-session errors, estimated by calculating a weighted average and its associated error for all runs of the standard analysed during each SHRIMP session, range between ~2.3 and ~5.3% (Table 3.3). The MSWD exceeds one in a single session, suggesting that in all other runs the counting errors are the major source of analytical uncertainty. The external reproducibility calculated using the within-session weighted averages is equal to 0.6%, smaller than the errors obtained for individual sessions. Therefore, these within-session errors can be used (added in quadrature) to calculate errors for unknown samples.

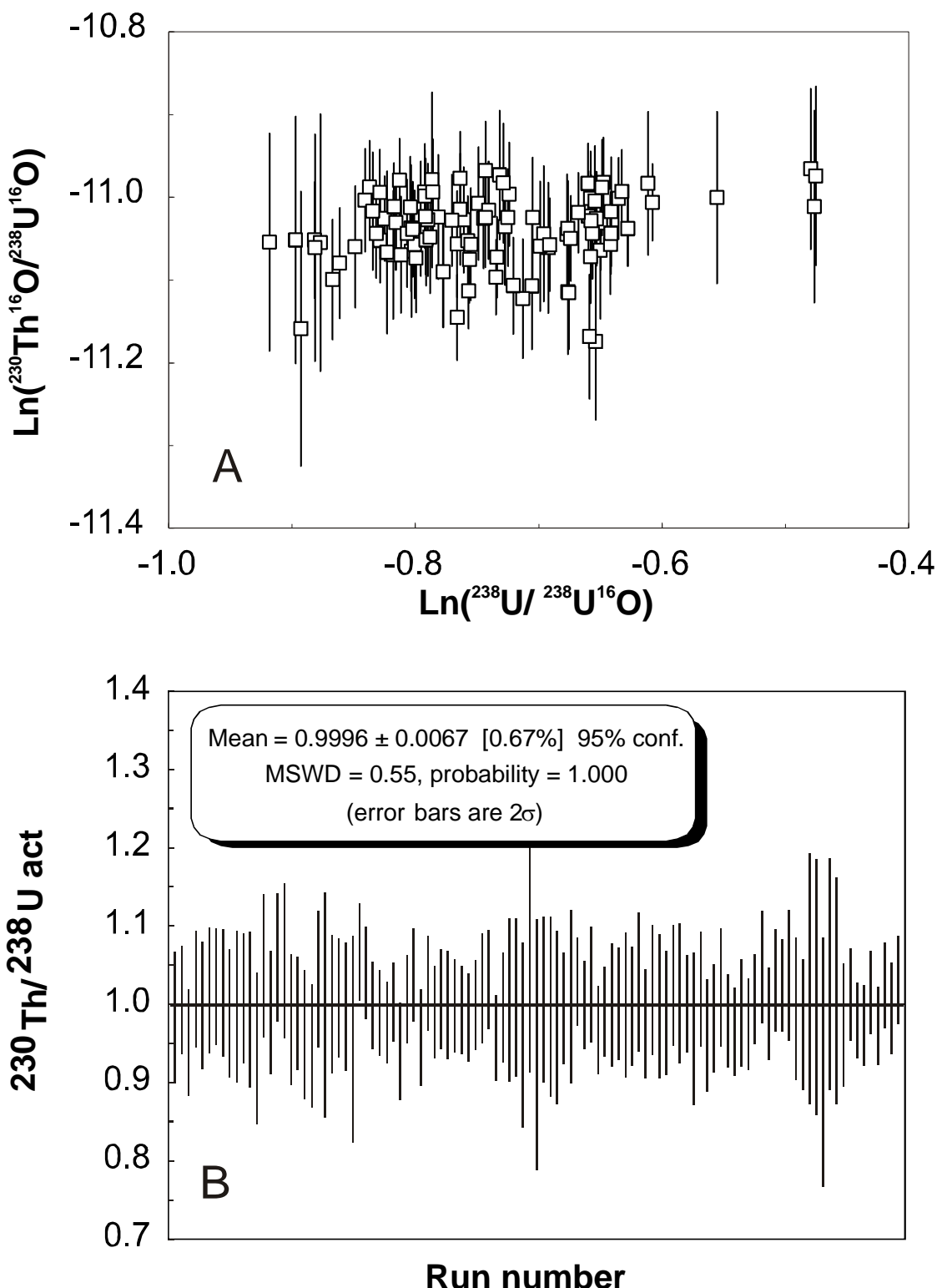


Figure 3.5 (A) Log-log plot showing session-by-session variations of $^{230}\text{Th}/^{16}\text{O}$ vs. $^{238}\text{U}/^{238}\text{U}^{16}\text{O}$ observed during analyses of opal standard M21277. (B) Weighted average of all $^{230}\text{Th}/^{238}\text{U}$ obtained for the standard during this study.

Table 3.3 The within session and external reproducibility of $^{234}\text{U}/^{238}\text{U}$, $^{230}\text{Th}/^{238}\text{U}$ and $^{206}\text{Pb}/^{238}\text{U}$ ratios in standard opal M21277; all data represent weighted averages of standard analyses collected for the individual sessions, their 95% confidence limits and MSWDs, calculated by ISOPLOT (Ludwig, 1999).

Date	Number of standards	$\frac{^{234}\text{U}}{^{238}\text{U}}$	MSWD	$\frac{^{234}\text{U}}{^{238}\text{U}} \text{act}$	$\frac{^{230}\text{Th}}{^{238}\text{U}}$	MSWD	$\frac{^{230}\text{Th}}{^{238}\text{U}} \text{act}$	$\frac{^{206}\text{Pb}}{^{238}\text{U}} (8\text{corr})^*$	MSWD	$\frac{^{206}\text{Pb}}{^{238}\text{U}} \text{true}^{**}$	MSWD
21/05/05***	8	0.0000548±7	1.1	1.001±13	0.00001684±32	0.3	0.999±19	0.000316±12	9.5	0.000401±15	7.2
23/01/04	8	0.0000540±14	0.6	0.987±26	0.00001682±69	0.3	0.997±41	0.000237±74	250	0.000402±8	1.2
11/01/04	7	0.0000553±14	1.4	1.011±26	0.00001687±40	0.5	1.000±24	0.000400±47	96	0.000395±47	70
11/12/03	9	0.0000540±15	1.6	0.986±27	0.00001684±41	0.4	0.998±25	0.000419±17	5	0.000402±21	4
21/10/03	3	0.0000559±47	1.9	1.021±85	0.00001687±76	0.1	1.000±45	0.000351±5	0.4	0.000403±8	0.2
	5	0.0000542±13	1.0	0.991±24	0.00001688±60	0.3	1.001±35	0.000314±14	2.2	0.000403±17	1.3
3/10/03	7	0.0000537±15	1.3	0.981±27	0.00001678±53	0.5	0.995±35	0.000293±32	36	0.000396±51	29
	4	0.0000528±47	5.0	0.965±86	0.00001683±61	0.2	0.997±36	0.000336±29	16	0.000448±50	16
13/09/03	7	n.d****		n.d			n.d	0.000337±39	99	0.000398±33	39
3/08/03	9	0.0000537±12	1.7	0.981±22	0.00001684±34	0.8	0.998±20	0.000391±13	15	0.000402±11	8
20/07/03	9	0.0000546±13	0.5	0.997±24	0.00001684±59	0.4	0.998±35	0.000413±30	33	0.000401±21	12
25/04/03	6	n.d		n.d			n.d	0.000293±22	26	0.000402±18	7
16/01/03	9	n.d		n.d			n.d	0.000218±39	60	0.000398±30	8.4
16/11/02	3	0.0000551±44	2.7	1.006±79	0.00001688±88	0.1	1.001±52	0.000345±76	36	0.000397±78	17
12/11/02	9	0.0000563±14	3.1	1.029±26	0.00001686±42	0.4	0.999±25	0.000396±30	34	0.000403±14	5.5
30/08/02	4	0.0000559±52	8.7	1.022±94	0.00001690±74	0.1	1.002±44	0.000244±31	9	0.000414±53	5.7
15/07/02	10	0.0000561±7	0.7	1.025±12	0.00001685±44	1.1	0.998±26	0.000300±13	15	0.000401±17	11.5
1/10/01	8	0.0000564±10	2.2	1.030±18	0.00001687±54	1.7	1.000±32	0.000320±45	2	0.000403±11	7.5
17/08/01	14	n.d		n.d			n.d	0.000432±22	64	0.000396±27	100
(O ₂ -all)											
O ₂ 1 st -run	8	n.d		n.d			n.d	0.000458±20	18	0.000448±23	23
O ₂ 2 nd -run	6	n.d		n.d			n.d	0.000413±38	80	0.000365±17	17
O-all	12							0.000239±37	657	0.000384±45	311
O ¹ 1 st -run	6	n.d		n.d			n.d	0.000309±39	185	0.000466±22	21
O ² 2 nd -run	6	n.d		n.d			n.d	0.000203±25	140	0.000334±27	42
21/07/01	15	0.0000546±4	1.1	0.998±8	0.00001686±26	0.6	0.999±15	0.000257±16	41	0.000396±24	35
External Reproducibility*****	0.0000549±5	2.8	1.004±9	0.00001685±11	0.1	0.999±7					

* Corrected for non-radiogenic Pb using ^{208}Pb .

** Projected along the line in the $\ln(\text{U}/\text{UO})$ vs. $\ln(\text{Pb}/\text{U})$ coordinates to the intercept with Y-axis.

*** Run with ^{235}U and $^{235}\text{U}^{16}\text{O}$ analysed as a proxy for ^{238}U and $^{238}\text{U}^{16}\text{O}$.

**** Not determined.

***** Weighted average of all data representing individual sessions.

The 2σ relative deviations of $^{234}\text{U}/^{238}\text{U}$ for 95% of individual spots (representing within-run errors) vary between ~ 2.9 and $\sim 7.6\%$, with an average value of $\sim 5.3\%$. The within-session errors (expressed as 95% confidence limits) for the same $^{234}\text{U}/^{238}\text{U}$ measurement have a similar range (Table 3.3) and have been used as a component of errors calculated for analyses of unknowns. The MSWDs calculated for within-session averages are slightly higher than unity for $\sim 75\%$ of the analytical sessions (range from 0.5 to 8.7) and suggests the presence of excess scatter above the counting statistics error. A similar (greater than one) MSWD=2.8 is calculated for the weighted average of all analytical sessions. The external error (95% confidence limit for this weighted average) for the $^{234}\text{U}/^{238}\text{U}$ is equal to 0.9%. Although the activity ratio itself appears to be slightly above unity (outside the 95% confidence limit) in three analytical sessions, the majority of sessions, as well as the average of all analytical sessions indicate that the $^{234}\text{U}/^{238}\text{U}$ values are in secular equilibrium in the standard.

The non-radiogenic Pb-corrected (Pb^*), $^{206}\text{Pb}^*/^{238}\text{U}$ values for M21277, calculated using both ^{208}Pb and ^{204}Pb approaches, yield similar results that plot along the 1:1 correlation line (Figure 3.6). The ^{208}Pb correction, which was used in all subsequent calculations, resulted in slightly smaller errors for $^{206}\text{Pb}^*/^{238}\text{U}$. Runs using $^{16}\text{O}_2^-$ as a primary beam, which is smaller than the $^{16}\text{O}^-$ primary beam and resulted in lower secondary ion count rates, showed a slightly larger amounts of scatter about the 1:1 line. This is indicated by the slightly larger MSWD of 4.7 determined by analyses made with $^{16}\text{O}_2^-$, as compared to MSWD of 3.3 estimated for analyses obtained with $^{16}\text{O}^-$ primary beam. However, $^{206}\text{Pb}^*/^{238}\text{U}$ data obtained using $^{16}\text{O}^-$ as primary beam displayed much greater variation and were displaced significantly further away from the true value of $^{206}\text{Pb}^*/^{238}\text{U}$ in the standard than the ratios determined using $^{16}\text{O}_2^-$ as a primary beam (Figure 3.6).

The systematic variation in $^{206}\text{Pb}^*/^{238}\text{U}$ appears to correlate with the drift in measured U/UO, which is dependent on the primary beam. All analyses fall along a poorly defined linear trend in the Pb/U versus U/UO log-log plot (Figure 3.7 and 3.8). In addition, there is a change in the Pb/U ratio, which is correlated with the overall duration of the analysis and not with changes in observed U/UO. This results in a shift of second analyses made on the same spots to lower $^{206}\text{Pb}^*/^{238}\text{U}$ values (Figure 3.7). Earlier runs of opal standard M21277, consisting of seven or even ten

scans per run, also yielded lower Pb/U ratios compared to 5-scan runs used in later analytical sessions. It was assumed, however, that if the standard is analysed under exactly the same conditions as the unknowns, then the calibration line (i.e., best-fit in $\ln(\text{Pb}/\text{U})$ versus $\ln(\text{U}/\text{UO})$ coordinates, constrained from analyses of standards obtained during the session) could be applied to correct unknowns. This assumption implies that possible matrix related effects influencing the efficiency of extraction of different species during SHRIMP analysis of opal can be ignored. A similar assumption is made in SHRIMP analysis of zircon, where crystalline zircon standards are used to analyse grains with unknown degrees of metamictness. When all standard analyses obtained with the 5-scan runs are plotted together on the Pb/U versus U/UO log-log diagram (Figure 3.8), a common trend is obtained with a slope of -2.00 ± 0.22 (MSWD=34, 95% confidence limit) and an intercept of -9.46 ± 0.17 . The maximum scatter of the individual analyses around this line is ~4 to ~5% with respect to Pb/U (Figure 3.8). This scatter places a lower limit on the precision of Pb/U in unknowns. The within-run 2σ errors of non-radiogenic Pb corrected $^{206}\text{Pb}/^{238}\text{U}$ obtained for the individual spots vary from 1.7 to 6.2%, with an average of ~3.9%. However, the within-session errors are significantly higher and the weighted average ratios for the separate SHRIMP sessions are calculated with high MSWDs (ranging between 0.4 and 657). Normalisation using Pb/U versus U/UO relationships reduces both errors and MSWDs, but they both are still in excess of what is expected from the counting statistics alone. This highlights once again the presence of additional scatter in $^{206}\text{Pb}/^{238}\text{U}$, which is not related to either variation of the U/UO ratio or the non-radiogenic Pb correction. Nevertheless, the within-session errors were included in the calculated errors for the unknowns.

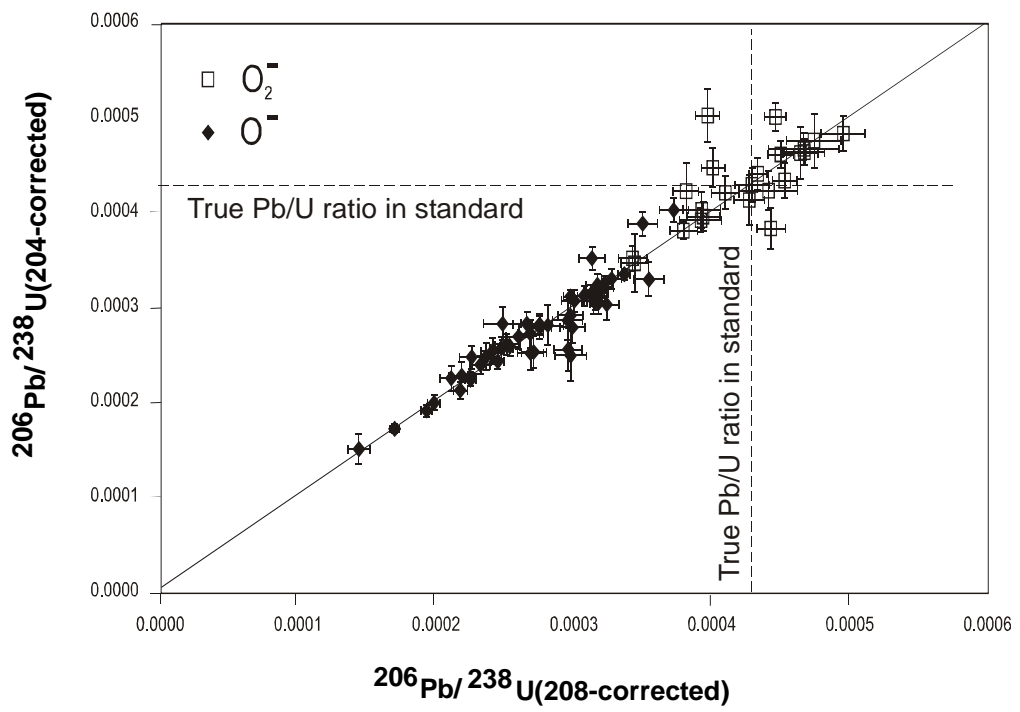


Figure 3.6 Non-radiogenic Pb corrected $^{206}\text{Pb}^*/^{238}\text{U}$ obtained during multiple runs of opal standard M21277. Both ^{204}Pb and ^{208}Pb corrections give very similar results. Larger deviation of points from the reference line for the O_2^- primary beam is a consequence of lower counting rate. The absolute value of ratios obtained with the O_2^- as a primary beam is much closer to the true value (shown as dashed lines) when compared to the ratios determined with O^- primary beam.

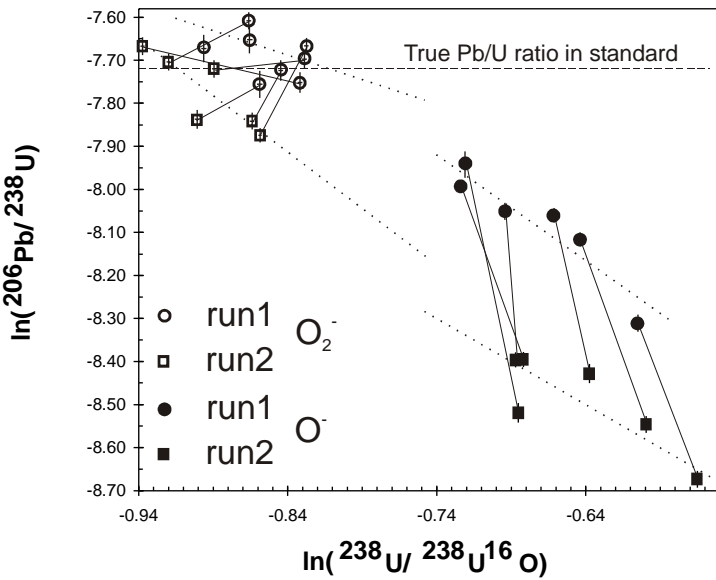


Figure 3.7 $^{206}\text{Pb}^*/^{238}\text{U}$ vs. $^{238}\text{U}/^{238}\text{U}^{16}\text{O}$ log-log plot for the single SHRIMP session where each spot was analysed twice. The data show two components present in the drift of the Pb/U. The first component is correlated with the change in $^{238}\text{U}/^{238}\text{U}^{16}\text{O}$ during the run and can be corrected by the linear extrapolation of the data to the Y-axis. The second component apparently does not correlate with the $^{238}\text{U}/^{238}\text{U}^{16}\text{O}$ and causes systematically lower Pb/U for all second analyses of all spots. (Best fits are shown as dotted lines; First and second analyses of the same spot are connected with the tie lines).

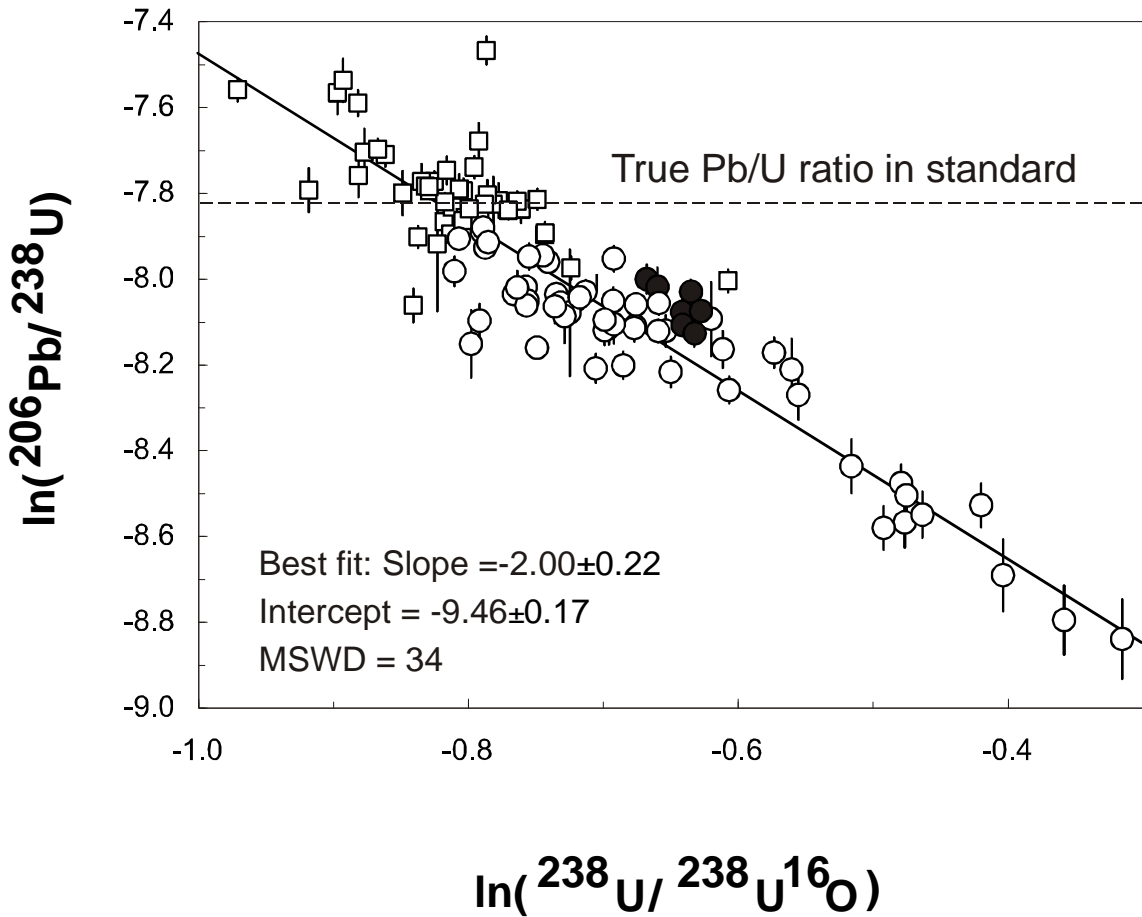


Figure 3.8 An $\ln(^{206}\text{Pb}*/^{238}\text{U})$ vs. $\ln(^{238}\text{U}/^{238}\text{U}^{16}\text{O})$ plot showing the variation of Pb-U ratios obtained during all five scan runs of opal standard M21277. Squares and circles represent analyses with O_2^- and O^- primary beam, respectively (filled circles are analyses with ^{235}U and $^{238}\text{U}^{16}\text{O}$ – based run table). The Y-axis values for this plot are calculated from the measured $^{206}\text{Pb}/^{238}\text{U}$ ratios applying the ^{208}Pb non-radiogenic Pb correction and taking natural logarithms, whereas the X-axis values are obtained by taking the natural logarithms of measured $^{238}\text{U}/^{238}\text{U}^{16}\text{O}$ ratios.

3.10.3 Opal from Guanajuato, Mexico

Precise U-Pb dating of this hyalite sample is possible because of its low non-radiogenic Pb abundance ($^{206}\text{Pb}/^{204}\text{Pb}$ ratios are relatively high, ranging between ~200 and several thousand, Table 3.4). The estimated U concentration between ~30 and ~130 $\mu\text{g/g}$ (Table 3.4), together with the relatively old age of the sample (~10 Ma), resulted in comparatively high counting rates for both ^{206}Pb and ^{207}Pb . Non-radiogenic Pb corrections using both ^{204}Pb and ^{208}Pb gave similar $^{206}\text{Pb}*/^{238}\text{U}$, and calculated $^{207}\text{Pb}*/^{235}\text{U}$ have errors ranging between 8 and 17%. The data show slight reverse discordance and a spread of $^{206}\text{Pb}*/^{238}\text{U}$ on the concordia diagram, whereas $^{207}\text{Pb}*/^{235}\text{U}$ remain constant within the errors (Figure 3.9). This behaviour appears to

be common in opals (particularly in opal less than a few tens of millions years old), where the observed reverse discordance can be attributed to unsupported ^{206}Pb present as a result of initial excess of ^{234}U (Neymark *et al.*, 2000a, 2002). The $^{207}\text{Pb}^*-\text{U}$ ages appear to be unaffected by this problem and the weighted average of these ages may be considered as the best estimate of the true opal age. The weighted average for this sample is 10.4 ± 0.8 Ma (95% confidence limit) and is similar within the error to the age of 9.9 ± 0.3 Ma obtained from the TIMS analyses. The MSWD of 1.2 is slightly elevated and is caused by a single outlier with a $^{207}\text{Pb}^*-\text{U}$ age of 14 ± 0.8 Ma. If this analysis is excluded from the calculation, the weighted average age changes insignificantly to 10.3 ± 0.6 Ma, with the MSWD reduced to 0.5. The apparent separation of $^{206}\text{Pb}^*-\text{U}$ ages into two groups is not related to the fact that two chips of opal were analysed during the session. Rather, it is interpreted as being random and caused by the small number of analyses. Both measured $^{234}\text{U}/^{238}\text{U}$ and $^{230}\text{Th}/^{238}\text{U}$ activity ratios are equal to one within the errors (Figure 3.9), suggesting that the material is currently in secular equilibrium and has remained closed with respect to the intermediate daughters at least during the past several hundred thousand years.

3.10.4 Opal from Hosszú Hill, Hungary

Two chips from a single hyalite sample were analysed. The estimated U content in this sample varies from ~15 to ~50 $\mu\text{g/g}$ (Table 3.4), which is significantly lower than in the Mexican opal discussed above. The relatively old age of the sample (~10 Ma), however, results in sufficient ^{206}Pb and ^{207}Pb counts to calculate ages with an acceptable level of precision. The data obtained for this sample illustrate that, for older opals, U concentration as low as 10-15 $\mu\text{g/g}$ can yield precise U-Pb ages, although ^{230}Th and ^{234}U would be too low for analysis by SHRIMP. The $^{206}\text{Pb}/^{204}\text{Pb}$ ratios in the sample vary from ~80 to ~2200 (Table 3.4), while the observed spread of $^{206}\text{Pb}^*-\text{U}$ and $^{207}\text{Pb}^*-\text{U}$ ages is very similar to that of the Mexican opal, with the exception of two analyses, which show distinctly older $^{207}\text{Pb}^*-\text{U}$ ages and are normally discordant (Figure 3.10). These two analyses, corresponding to spots in two different chips, have the highest non-radiogenic Pb contents, which makes the data more sensitive to a potentially inaccurate non-radiogenic Pb correction. If they are not included in the calculation, the weighted average $^{207}\text{Pb}^*-\text{U}$ age of the

samples can be estimated as 9.7 ± 1.2 Ma, with MSWD of 0.95. Additional runs of this sample where ^{238}U and $^{238}\text{U}^{16}\text{O}$ mass stations were replaced with ^{235}U and $^{235}\text{U}^{16}\text{O}$ yielded a similar average age value of 11.6 ± 1.2 Ma but did not result in any significant improvement in the precision of individual analyses (Table 3.4, Figure 3.10). Combining all the $^{207}\text{Pb}/^{235}\text{U}$ ages for this sample yields a weighted average age of 10.88 ± 0.93 Ma (MSWD=1.4) and both data points with elevated non-radiogenic Pb content are rejected as outliers by the ISOPLOT program (Ludwig, 1999).

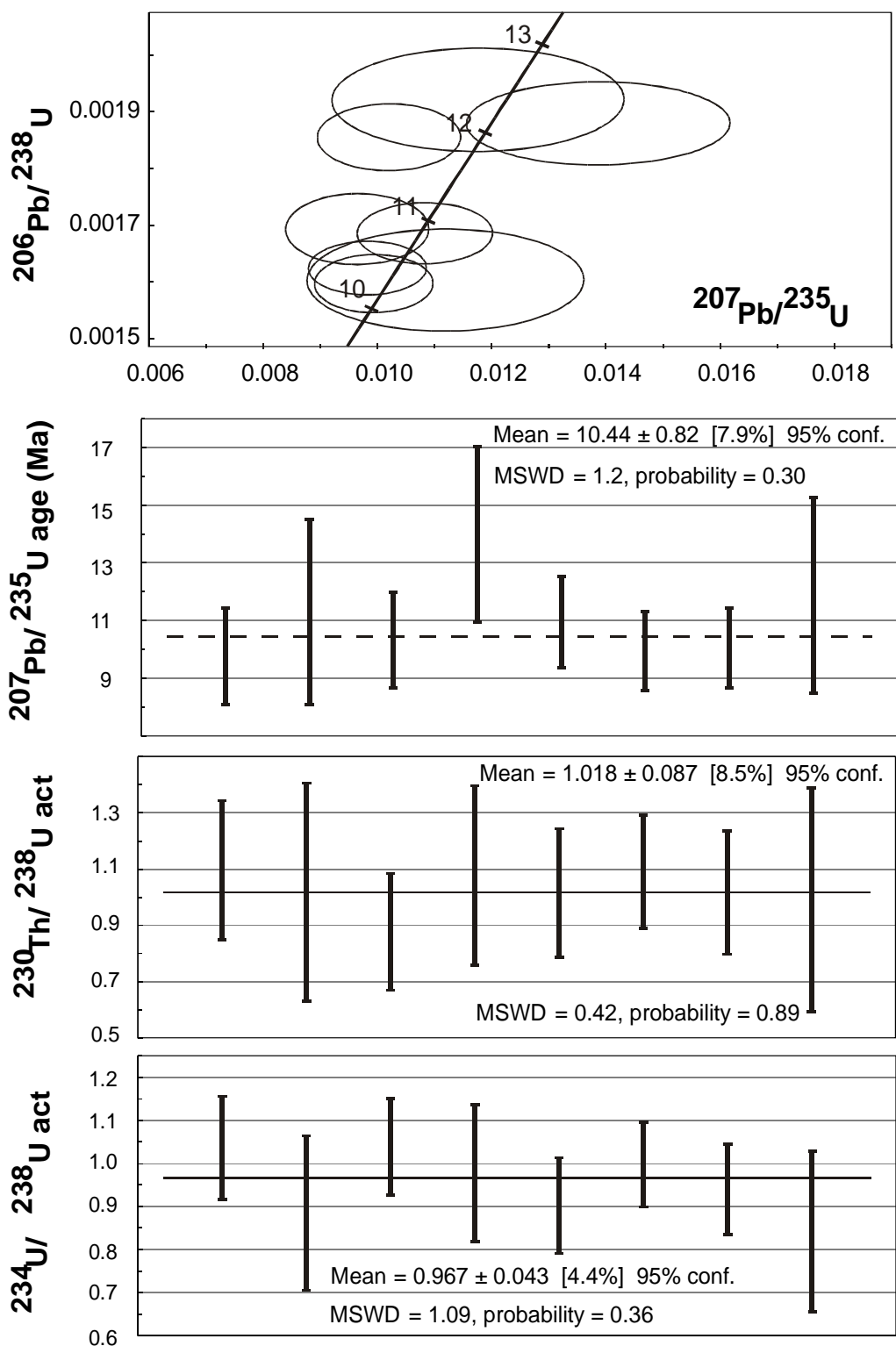


Figure 3.9 U-Pb SHRIMP (open ellipses) and TIMS (filled ellipses) data for the opal sample from Guanajuato, Mexico. The non-radiogenic Pb corrected Pb-U ratios, obtained with SHRIMP, have been normalised using sample M21277 as a standard.

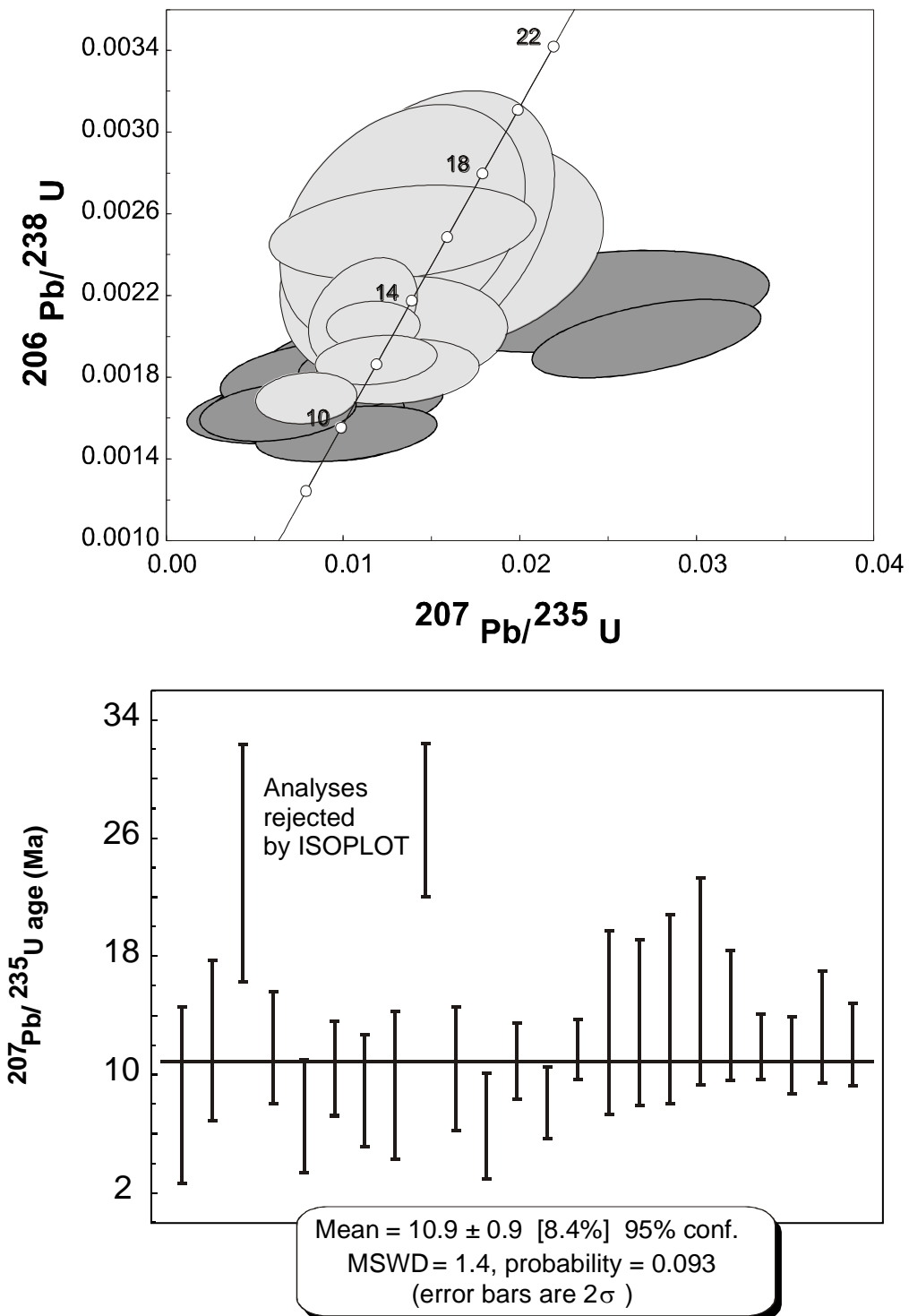


Figure 3.10 U-Pb SHRIMP data for the opal sample from Hosszú Hill, Hungary (run with ^{238}U and $^{238}\text{U}^{16}\text{O}$ masses analysed is represented by the dark grey ellipses; run with ^{235}U and $^{235}\text{U}^{16}\text{O}$ masses analysed is shown as the light grey ellipses). The non-radiogenic Pb corrected Pb-U ratios have been normalised using sample M21277 as a standard.

Table 3.4 SHRIMP data for two hyalite samples (errors are 2σ)

N	U ($\mu\text{g/g}$)*	Measured				208-corrected				^{207}Pb $\frac{^{207}\text{Pb}}{^{206}\text{Pb}}$	^{206}Pb $\frac{^{206}\text{Pb}}{^{238}\text{U}}$ act	^{234}U $\frac{^{234}\text{U}}{^{238}\text{U}}$ act	$f8^{**}$	^{206}Pb $\frac{^{206}\text{Pb}}{^{238}\text{U}}$	^{207}Pb $\frac{^{207}\text{Pb}}{^{206}\text{Pb}}$	$Error$ $Corr$	^{235}U Age (myr)	$Th\text{-}Age$ Age (kyr)	^{206}Pb $\frac{^{206}\text{Pb}}{^{238}\text{U}}$	$dist$ Age (kyr)
		$\frac{^{204}\text{Pb}}{^{206}\text{Pb}}$	$\frac{^{207}\text{Pb}}{^{206}\text{Pb}}$	$\frac{^{208}\text{Pb}}{^{206}\text{Pb}}$	$\frac{^{230}\text{Th}}{^{238}\text{U}}$ act	$f8^{**}$	^{206}Pb $\frac{^{206}\text{Pb}}{^{238}\text{U}}$	^{207}Pb $\frac{^{207}\text{Pb}}{^{206}\text{Pb}}$	^{207}Pb $\frac{^{207}\text{Pb}}{^{235}\text{U}}$											
Mexican opal																				
1	93	0.0011±16	0.054±6	0.033±8	1.10±24	1.04±12	0.016±4	0.00169±8	0.041±8	0.0096±16	0.00	9.7±1.6	n.d.	n.d.	n.d.	n.d.	n.d.			
2	38	0.0035±42	0.079±14	0.076±18	1.02±38	0.89±18	0.037±10	0.00160±12	0.051±16	0.0112±32	0.12	11.3±3.2	n.d.	n.d.	n.d.	n.d.	n.d.			
3	107	0.0002±14	0.057±6	0.043±8	0.88±20	1.04±12	0.021±4	0.00186±8	0.040±6	0.0102±16	0.04	10.3±1.6	n.d.	n.d.	n.d.	n.d.	n.d.			
4	50	0.0058±36	0.092±12	0.101±16	1.08±32	0.98±16	0.049±10	0.00188±10	0.054±12	0.0139±30	0.24	14.0±3.0	n.d.	n.d.	n.d.	n.d.	n.d.			
5	94	0.0003±16	0.053±6	0.016±6	1.02±22	0.90±12	0.008±2	0.00169±8	0.047±8	0.0108±16	0.01	10.9±1.6	n.d.	n.d.	n.d.	n.d.	n.d.			
6	131	0.0017±16	0.056±6	0.033±6	1.09±20	1.00±10	0.016±4	0.00162±6	0.044±6	0.0098±14	0.03	9.9±1.4	n.d.	n.d.	n.d.	n.d.	n.d.			
7	112	0.0000±16	0.049±6	0.009±4	1.01±22	0.94±10	0.005±2	0.00160±6	0.045±6	0.0099±14	0.04	10.0±1.4	n.d.	n.d.	n.d.	n.d.	n.d.			
8	32	0.0026±40	0.067±12	0.059±16	0.99±40	0.84±18	0.028±8	0.00192±12	0.044±14	0.0118±34	0.17	11.9±3.4	n.d.	n.d.	n.d.	n.d.	n.d.			
Hungarian opal																				
1	17	0.0000±98	0.097±24	0.156±40	0.67±56	0.77±26	0.075±20	0.00165±14	0.037±28	0.0085±58	0.37	8.6±6.0	n.d.	n.d.	n.d.	n.d.	n.d.			
2	18	0.0106±74	0.094±20	0.125±30	1.32±52	1.08±26	0.060±16	0.00191±16	0.046±22	0.0122±54	0.33	12.3±5.4	n.d.	n.d.	n.d.	n.d.	n.d.			
3	14	0.0097±94	0.137±28	0.154±38	0.65±48	0.84±28	0.074±20	0.00217±20	0.081±30	0.0242±80	0.32	24.3±8.0	n.d.	n.d.	n.d.	n.d.	n.d.			
4	25	0.0014±36	0.078±14	0.082±20	0.91±38	1.03±20	0.040±10	0.00182±12	0.047±16	0.0117±36	0.19	11.8±3.8	n.d.	n.d.	n.d.	n.d.	n.d.			
5	23	0.0000±68	0.065±16	0.088±24	0.50±42	1.13±24	0.042±12	0.00165±12	0.031±18	0.0071±38	0.25	7.2±3.8	n.d.	n.d.	n.d.	n.d.	n.d.			
6	27	0.00008±42	0.074±14	0.065±18	0.98±38	0.99±20	0.032±10	0.00153±12	0.049±16	0.0103±32	0.14	10.4±3.2	n.d.	n.d.	n.d.	n.d.	n.d.			
7	20	0.0031±56	0.072±16	0.082±24	0.83±42	0.92±22	0.040±12	0.00161±14	0.040±18	0.0088±38	0.24	8.9±3.8	n.d.	n.d.	n.d.	n.d.	n.d.			
8	16	0.0035±52	0.078±18	0.106±30	1.33±54	0.91±24	0.051±14	0.00180±16	0.037±20	0.0092±48	0.28	9.3±5.0	n.d.	n.d.	n.d.	n.d.	n.d.			
9	21	0.0118±80	0.277±26	0.499±50	0.67±54	0.88±24	0.241±34	0.00199±16	0.099±24	0.0272±52	0.53	27.2±5.2	n.d.	n.d.	n.d.	n.d.	n.d.			
10	26	0.0037±58	0.101±18	0.138±30	0.96±40	1.15±22	0.067±16	0.00152±12	0.049±22	0.0103±42	0.34	10.4±4.2	n.d.	n.d.	n.d.	n.d.	n.d.			
11	26	0.0024±51	0.072±14	0.110±24	1.46±48	1.14±22	0.053±12	0.00163±12	0.029±16	0.0064±36	0.27	6.5±3.6	n.d.	n.d.	n.d.	n.d.	n.d.			
12	46	0.0005±30	0.061±10	0.049±12	0.97±30	1.04±16	0.024±6	0.00183±10	0.043±10	0.0108±26	0.14	10.9±2.6	n.d.	n.d.	n.d.	n.d.	n.d.			

Table 3.4 (continued)

<i>N</i>	<i>U</i> ($\mu\text{g/g}$)*	$\frac{^{204}\text{Pb}}{^{206}\text{Pb}}$	$\frac{^{207}\text{Pb}}{^{206}\text{Pb}}$	$\frac{^{208}\text{Pb}}{^{206}\text{Pb}}$	$\frac{^{230}\text{Th}}{^{238}\text{U}}$ act	$\frac{^{234}\text{U}}{^{238}\text{U}}$ act	<i>f8</i> **	$\frac{^{206}\text{Pb}}{^{238}\text{U}}$	$\frac{^{207}\text{Pb}}{^{206}\text{Pb}}$	$\frac{^{207}\text{Pb}}{^{235}\text{U}}$	<i>Error</i> <i>Corr</i>	$\frac{^{207}\text{Pb}}{^{235}\text{U}}$	<i>Th-Age</i> *** <i>Age</i> (<i>myr</i>)	$\frac{^{206}\text{Pb}}{^{238}\text{U}}$ ****	<i>dist</i> ***** <i>Age</i> (<i>kyr</i>)
Measured								208-corrected							
^{235}U and $^{235}\text{U}^{16}\text{O}$ are measured as a proxy for ^{238}U and $^{238}\text{U}^{16}\text{O}$															
13	33	0.0042±34	0.062±10	0.072±14	1.08±26	0.96±18	0.035±8	0.00170±10	0.034±10	0.0080±24	0.11	8.1±2.4	n.d.	n.d.	n.d.
14	46	0.0019±24	0.059±8	0.032±8	0.95±20	0.96±16	0.016±4	0.00179±8	0.047±8	0.0116±18	0.10	11.7±2.0	n.d.	n.d.	n.d.
15	10	0.0086±80	0.077±16	0.100±26	1.18±56	1.12±40	0.048±14	0.00250±18	0.039±18	0.0134±62	0.26	13.5±6.2	n.d.	n.d.	n.d.
16	13	0.0084±52	0.078±14	0.103±22	1.03±42	1.46±34	0.050±12	0.00255±48	0.038±16	0.0134±56	0.32	13.5±5.6	n.d.	n.d.	n.d.
17	12	0.0044±54	0.079±16	0.098±22	0.45±30	1.37±36	0.047±12	0.00250±58	0.041±16	0.0142±64	0.40	14.4±6.4	n.d.	n.d.	n.d.
18	10	0.0101±82	0.091±18	0.113±28	0.49±36	1.55±44	0.055±14	0.00245±42	0.048±20	0.0162±70	0.20	16.3±7.0	n.d.	n.d.	n.d.
19	16	0.0041±36	0.086±14	0.096±22	0.91±32	0.91±24	0.047±12	0.00204±22	0.049±16	0.0139±44	0.03	14.0±4.4	n.d.	n.d.	n.d.
20	38	0.0007±16	0.055±8	0.035±8	1.00±22	1.04±18	0.017±4	0.00205±10	0.042±8	0.0117±22	0.04	11.9±2.2	n.d.	n.d.	n.d.
21	37	0.0017±16	0.057±8	0.048±10	0.78±22	1.19±18	0.023±6	0.00212±22	0.038±8	0.0112±24	0.33	11.3±2.6	n.d.	n.d.	n.d.
22	18	0.0084±56	0.087±14	0.093±20	1.24±36	1.07±26	0.045±10	0.00183±14	0.052±16	0.0131±38	0.17	13.2±3.8	n.d.	n.d.	n.d.
23	26	0.0026±28	0.069±10	0.061±14	0.99±26	1.08±20	0.029±8	0.00189±10	0.046±12	0.0119±28	0.19	12.0±2.8	n.d.	n.d.	n.d.

* U concentration is calculated as counts per second of ^{238}U in unknown divided by average counts per second of ^{238}U in the standard and multiplied by U concentration in the standard (assumed to be 800 $\mu\text{g/g}$).

**Proportion of non-radiogenic Pb calculated using ^{208}Pb correction.

*** ^{230}Th - ^{234}U - ^{238}U age.

**** ^{206}Pb - ^{234}U - ^{238}U age.

***** Distance from the outer margin of hemisphere in the sample HD2074.

3.11 Summary and conclusions

The U-Pb SHRIMP analytical procedure developed in this study was designed based on the assumption that the behaviour of U and Pb during sputtering is similar for both standard and unknown opals. A similar assumption has been applied to SHRIMP analyses of zircons and allows calculations of U/Pb ratios in unknown samples using data obtained for the standard analysed during the same SHRIMP session, without a need for detailed understanding of sputtering mechanisms.

The procedure includes measurements of all isotopes necessary for U-Pb and U-series age calculations. Abundances of ^{234}U and ^{230}Th as well as radiogenic Pb in young opals are relatively low and require a substantial increase in primary beam intensity and long integration times to obtain count rates sufficient to achieve ages with precision of about 10%. Increased primary beam intensity and long integration times result in a drift in the measured U-Pb ratios that is not correlated with U/UO ratios and, therefore, cannot be corrected for. As a consequence, the primary beam intensity and integration times are adjusted to produce high counting rates and minimise the drift.

The secondary ion beam intensity can be increased by switching from O_2^- to the more intense O^- primary beam. However, $^{206}\text{Pb}/^{238}\text{U}$ values measured using O^- as the primary beam are significantly smaller than the true value estimated using TIMS analyses, whereas ratios measured with the O_2^- primary beam are closer to the true value and are less susceptible to errors associated with extrapolation along the line in $\ln(\text{Pb}/\text{U})$ versus $\ln(\text{U}/\text{UO})$ coordinates. An increased secondary beam intensity can also be achieved by using a larger spot size, but this would reduce spatial resolution, which is undesirable when the opal growth rate is very slow. A large primary beam may also result in $^{238}\text{U}^{16}\text{O}$ secondary beams that saturate the multiplier when the high-U material is analysed. This problem can be overcome by replacing ^{238}U and $^{238}\text{U}^{16}\text{O}$ with ^{235}U and $^{235}\text{U}^{16}\text{O}$ in the run table, which does not cause any reduction in precision.

The large number of parameters influencing the quality of opal SHRIMP analyses makes it difficult to find optimum run conditions, which can vary from sample to sample depending on the age of opal and the proportion of non-radiogenic Pb, as

well as initial excess of ^{234}U . Runs consisting of 5 scans each and the primary O⁻ beam intensity between 10 and 15 nA were adopted as the best compromise during this study to demonstrate the applicability of the technique to a variety of opals.

The series of $^{234}\text{U}/^{238}\text{U}$ - $^{230}\text{Th}/^{238}\text{U}$ - $^{206}\text{Pb}/^{238}\text{U}$ - $^{207}\text{Pb}/^{235}\text{U}$ analyses of opal standard M21277 from Virgin Valley, Nevada, USA, show that the SHRIMP technique can be successfully applied to opal dating. This sample was found to be a suitable standard for the correction of $^{230}\text{Th}/^{238}\text{U}$, $^{206}\text{Pb}/^{238}\text{U}$, and $^{207}\text{Pb}/^{235}\text{U}$ ratios in unknowns. The SHRIMP technique provides an opportunity to analyse a single ~20 micron spot, on the surface of a sample thereby significantly increasing the spatial resolution of dating as compared to that achieved by TIMS analysis. An additional advantage of this method is the ability to analyse all isotopes required for combined U-Pb and U-series dating in a single run. All ratios can be analysed with precisions ranging from ~2 to ~10%, which can be improved by further optimisation of the analytical procedure.

Ages determined for opals from Guanajuato, (Mexico), and Hosszú Hill (Hungary) are consistent with the known regional geology. TIMS and SHRIMP analyses of Mexican opal are similar within the errors. These analyses demonstrate the application of the technique for dating opal samples that range in age from ~ 2 million to ~10 million years with precisions ranging between 5 and 10%. Although the method discussed is applicable to both U-series and U-Pb dating only U-Pb examples are shown in this particular chapter and U-series examples are given and discussed in detail in the following chapters.

4 OPAL FROM YUCCA MOUNTAIN, NEVADA, USA

4.1 Introduction

Yucca Mountain is located in the south-western Nevada volcanic field 145 km northwest of Las Vegas, Nevada (Byers *et al.*, 1976; Christiansen *et al.*, 1977) (Figure 4.1) and has been studied as a potential site for the isolation of high-level radioactive waste produced in the United States. The threat of radionuclides from the site into the environment by groundwater led to the need to determine and understand the rate and nature of water movement to enable predictions of groundwater behaviour in the future. Particularly evaluations of past water movement through the unsaturated zone of volcanic rocks of Yucca Mountain was needed. This required a detailed study of the chronology of cavity filling minerals precipitated from water that percolated through the repository horizon. The potential repository is 200 to 300 m beneath Yucca Mountain and 200 to 300 m above the present day water table (Tucci and Burkhardt, 1995). The area has an arid to semi arid climate with an average annual precipitation of approximately 170 mm (Hevesi *et al.*, 1992). Under present conditions, the most important site selection attributes were the thick unsaturated zone and a semi arid climate which combined were expected to limit the amount of water coming into contact with the radioactive waste packages.

Opal was selected from this site for use in this study as there is a known widespread range of ages from ~12 Ma to ~4 kyr (Neymark *et al.*, 2000a; Neymark *et al.*, 2002, Paces *et al.*, 2004a). This spread combined with the fact that all samples acquired for SHRIMP analysis in this study have been previously investigated by Neymark *et al.*, (2000a; 2002) and Neymark and Paces (2000), using TIMS, allows for a comprehensive test of the SHRIMP procedure. This chapter also examines potential sources of systematic error, which are relevant to both SHRIMP and TIMS data. One is the initial Pb correction, which is a common problem for U-Pb dating of any mineral with an intermediate proportion of common Pb and is particularly important for relatively young systems where accumulated radiogenic component is comparatively small. The three samples investigated using SHRIMP were collected

by U.S. Geological Survey investigators from the Exploratory Studies Facility (ESF) between 250 and 270 metres below the land surface and 2700–3100 metres from the ESF north portal. An 8 metre diameter tunnel was built to assess Yucca Mountain as a potential site for long-term isolation of radioactive waste.

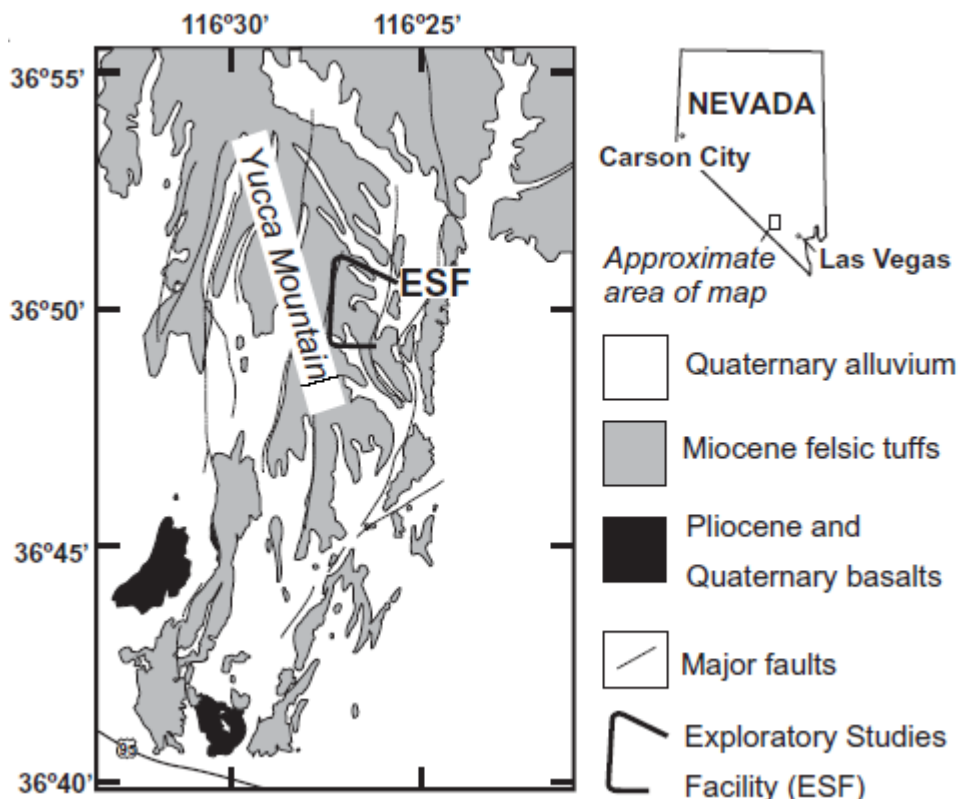


Figure 4.1 Geology of the Yucca Mountain area and location of the Exploratory Studies Facility tunnel (from Neymark and Amelin, 2008).

4.2 Geological and hydrological units

Yucca Mountain consists of 1-3 km thick sequences of alternating layers of welded and non-welded rhyolitic tuffs of Miocene-age (Byers *et al.*, 1976; Christiansen *et al.*, 1977) that range in age from 11.4 to 15.2 Ma (Sawyer *et al.*, 1994) (Figure 4.2). The Tertiary volcanic rocks of the Paintbrush Group and the Calico Hills Formation primarily compose unsaturated (vadose) zone. The Paintbrush Groups consists of four formations primarily composed of pyroclastic-flow deposits; the 380 m thick welded Topopah Spring Tuff (12.8 Ma) (Bluesch *et al.*, 1996), which is the host rock for the proposed nuclear waste repository overlain by the Pah Canyon Tuff

(composed of multiple flow units), the nonwelded Yucca Mountain Tuff and the 12.7 Ma mostly densely welded Tiva Canyon Tuff at the top of the sequence (Stuckless and Dudley, 2002). The Yucca Mountain and Pah Canyon Tuffs are thin (0-45 m), lenticular ignimbrites and volcanic ashes that are non-welded whereas, the Tiva Canyon and Topopah Spring Tuffs are thick, tabular ignimbrites made up of mostly densely welded quartz latite to high silica rhyolite (U.S. Department of Energy, 1998). The Calico Hills Formation consists of nonwelded and bedded tuffs that have been variously altered to zeolites. Below the Calico Hills Formation is the Crater Flat undifferentiated unit. The stratigraphic units of Yucca Mountain are shown in Figure 4.2.

The tuffs at Yucca Mountain are also divided into informal hydrologic units; the Paintbrush Tuff Nonwelded (PTn) and the Calico Hills Nonwelded (CHn) (Montazer and Wilson, 1984). The Paintbrush Tuff Nonwelded hydrologic unit consists of the basal parts of the Tiva Canyon, the Yucca Mountain and Pah Canyon Tuffs and the uppermost Topopah Spring Tuff (Montazer and Wilson, 1984; Moyer *et al.*, 1996). Matrix permeability dominates flow in the Paintbrush Tuff nonwelded unit unless it has been altered, in which case permeable may become dominated by fracture flow. The Calico Hills Nonwelded (CHn) unit is strongly zeolitized below much of the potential repository area. It may act to retard some radionuclides if they escape their primary containment (Stuckless and Dudley, 2002).

The unsaturated zone consists of six hydrogeological units; unconsolidated alluvium, remnants of Timber Mountain Tuff, Tiva Canyon welded unit, Paintbrush nonwelded unit, Topopah Spring welded unit, Calico Hills Nonwelded unit and the Crater Flat undifferentiated unit (CFu) (Montazer and Wilson, 1984). It is considered that the unsaturated zone formed about 11.5 million years ago, shortly after the emplacement of the Paintbrush Group. Figure 4.4 shows a typical vertical cross section of the unsaturated zone.

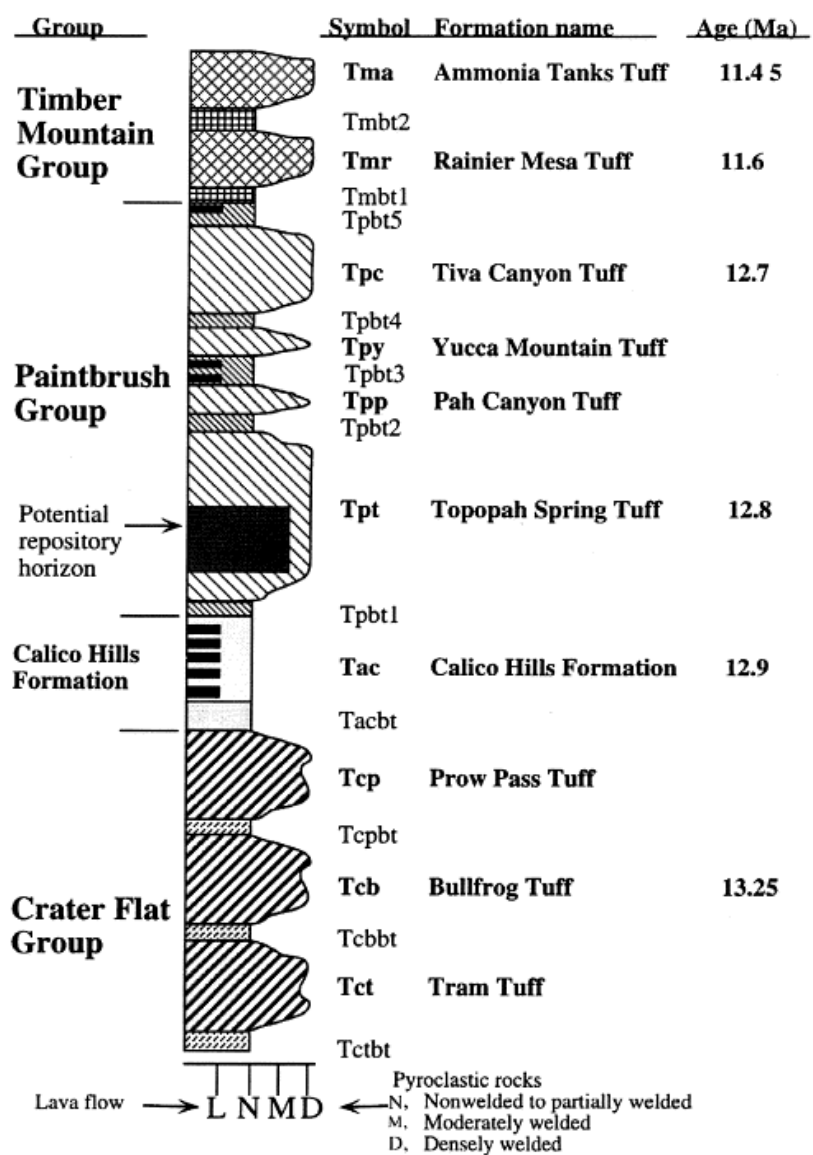


Figure 4.2 Principal stratigraphic units at Yucca Mountain (from Stuckless and Dudley, 2002 with ages from Sawyer *et al.*, 1994).

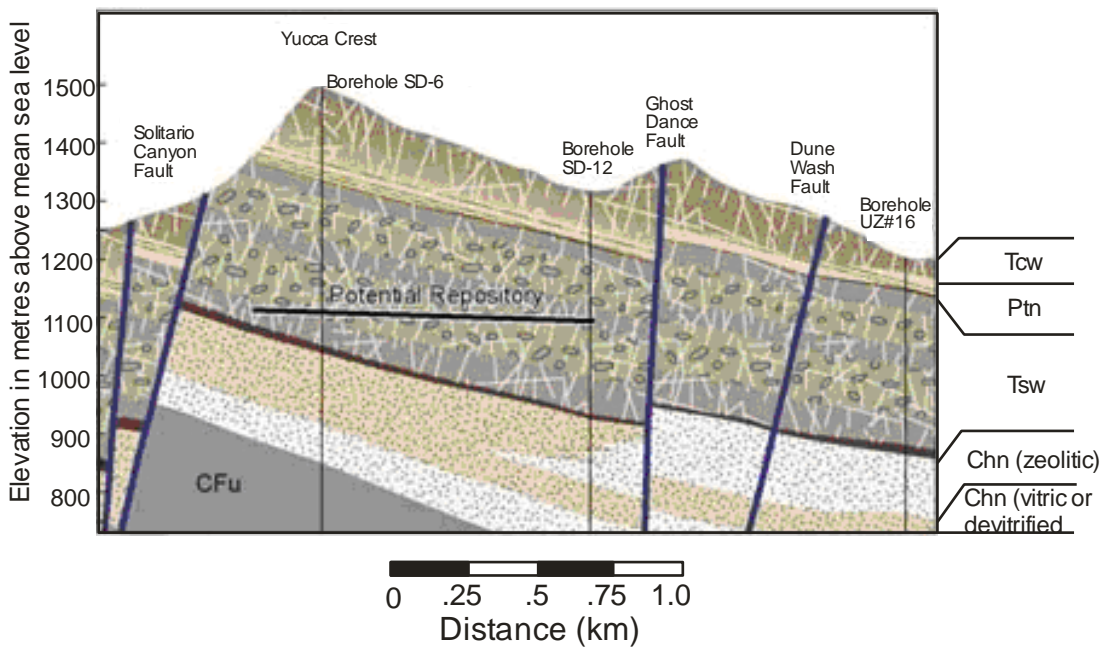


Figure 4.3 Generalised east-west section through Yucca Mountain showing hydrological units (after Zhang *et al.*, 2006).

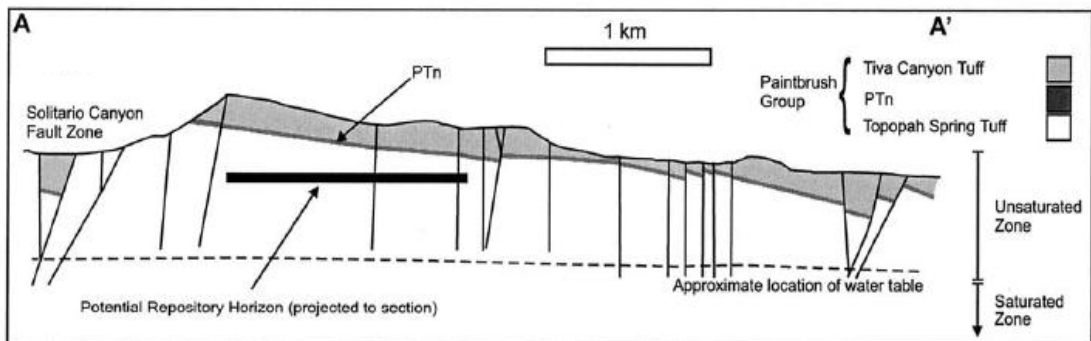


Figure 4.4 Showing the approximate location of the water table, unsaturated zone (UZ), saturated zone and the repository (from Wilson *et al.*, 2003).

4.3 Structural geology

High angle normal faults and numerous strike-slip faults with varying amounts of offset in the range of tens to hundreds of meters created a series of north trending structural blocks dipping at 5-10° east (Scott and Bonk, 1984; O’Leary, 2007). These major faults are generally vertical or near vertical and penetrate the entire unsaturated zone (Zhang *et al.*, 2006). Additional faults, fractures, and cooling joints in the welded tuffs form a partially connected network of pathways that allow

downward movement of water through the rock mass (Paces *et al.*, 2004a) but may also serve as barrier to lateral flow (Wu *et al.*, 2002).

4.4 Origin of opaline silica – two models

The origin of the calcite and silica in the open fractures and lithophysal cavities at Yucca Mountain has been the centre of discussion for several years. In particular, the discussion centres around the origin of the solution from which the silica and calcite precipitate and there are two main points of view that need to be considered. One view proposes that the solution is meteoric in origin where water descends through the unsaturated zone via interconnected fractures. The other relies on short term upwelling of deep seated hydrothermal fluids into the thick unsaturated zone to precipitate calcite and silica. This latter theory was initiated by Szymanski (1989), who postulated that calcite and silica were precipitated from water forced to the surface by earthquakes (seismic pumping). This theory was dismissed as there was no evidence that the water table had risen periodically hundreds of meters in the past (Bredehoft, 1992; National Research Council, 1992). However, Dublyansky *et al.*, (2001) reported calcite samples from the Exploratory Studies Facility tunnel at Yucca Mountain contained fluid inclusions with trapping temperatures up to 85° C and considered this depositional temperature consistent with intermittent upwelling of hydrothermal fluids and saturation of the unsaturated zone. Whelan *et al.*, (2002) proposed that the secondary mineral deposits formed from meteoric water that followed discrete fracture flow pathways down through otherwise air-filled open spaces in an unsaturated zone environment that had slowly cooled from approximately 85° C to approximately 35° C in the past but had remained at near present day ambient temperatures for the past 2 to 4 Ma. The high temperatures recorded by fluid inclusions in early-formed calcite can be explained as a consequence of slow cooling of the unsaturated zone caused by conductive heating due to thermal input from large late-Miocene plutons emplaced in the shallow crust less than 10 km north of Yucca Mountain. Elevated temperatures within the unsaturated zone existed up to 6 Ma. Although liquid water could not have percolated through the rock mass until temperatures in the tuff cooled to less than 100° C, initial dissipation of magmatic heat was probably rapid, lasting no more than several tens of years or less (Holt, 2002).

4.4.1 Evidence for meteoric model

Evidence for the meteoric theory is seen in the observation that the deposits are heterogeneously distributed and occupy less than 10% of the available fractures and lithophysal cavities and that these coatings are commonly intersected or surrounded by barren fractures and cavities (Whelan *et al.*, 2002). Further evidence for this theory is that deposits are restricted to fracture footwalls and are patchy with barren zones common both up and down dip and that in lithophysal cavities the deposits are restricted to the floors of the cavities. These observations are considered by Whelan *et al.*, (2002) to be incompatible with mineral deposition in a saturated zone environment. Dublyansky *et al.*, (2004) suggests that the open spaces were filled with fluid and mineral deposition on cavity floors resulted from crystals settling out of supersaturated solutions. However, this mechanism is inconsistent with the morphology of the mineral coating in the unsaturated zone as crystal settling would result in deposits on the lower surfaces of all opening spaces and covering all upward-facing surfaces as well as producing evenly distributed coating of late stage opal. None of these features are observed at Yucca Mountain. The absence of mineral deposition on cavity walls and ceilings indicates that selvages in these areas never became saturated and, therefore, calcite and silica were deposited only on the floors of cavities where fluids accumulated due to gravity.

4.4.2 Infiltrating waters

Net infiltration is defined as the amount of water that penetrates the ground surface to a depth where liquid water can no longer be removed and is only a small fraction of the total precipitation at the ground surface (Zhang *et al.*, 2006). It is the ultimate source of groundwater recharge and percolation through the unsaturated zone in Yucca Mountain. Present average infiltration is estimated to range between less than 1 to about 6 mm per year (Flint and Flint, 1994; Fabryka-Martin *et al.*, 1994). Infiltrating waters are likely to be saturated with silica and calcite (Whelan *et al.*, 2002) because of reactions with pedogenic calcite and silica, that are present in the soil zone as colluvial veneers over bedrock, alluvial valley fill and fractures filled with pedogenic calcite and opal in the upper 5 to 10 m of bedrock (Paces *et al.*, 2001) and with volcanic glass during percolation through the non welded tuffs. This compositional pattern supports a meteoric origin for the unsaturated zone water.

Coatings of calcite and opal deposits in fractures and lithophysal cavities and represent direct evidence of past fracture flow. Rates of water infiltration may varied in the past because of shifts in Pleistocene climate (Paces *et al.*, 2004a); however long-term deposition appears to have remained relatively constant despite major shifts in the surface–water availability (Neymark *et al.*, 2002; Paces *et al.*, 2010). Mean annual precipitation during the periods of glaciation in the past may have been two to four times greater than present day precipitation, whereas the mean annual temperatures may have been as much as 5 to 10 °C cooler (Forester and Smith, 1994; Forester *et al.*, 1999; Thompson *et al.*, 1999). Records of regional climate variation indicate that up to 80 percent of the last million years may have been characterised by cooler, wetter conditions relative to the present climate (Forester *et al.*, 1999). Despite these large variations in the presence of surface water, Paces *et al.*, (2010) found no evidence for significant variations in middle-late Pleistocene opal growth rates and postulated that infiltration at Yucca Mountain was buffered by a number of hydrogeologic processes.

Net infiltration is considered by Zhang *et al.*, (2006) to be episodic in nature over seasons and years with significant pulses occurring every few years. Initially these pulses percolate rapidly through the top part of the unsaturated zone, which is made up of the highly fractured tuffs of the Tiva Canyon Welded unit (Zhang *et al.*, 2006). However, as the rock units change from welded tuffs to nonwelded tuffs the flow behaviour changes from fracture dominated flow to matrix-dominated flow (Wu *et al.*, 2002), suggesting that the flow rate decreases as a result of damping by the underlying tuff units (Wang and Narasimhan, 1985; Wang and Narasimhan, 1993) that are highly porous and less fractured. The water is most likely to percolate through the connected fractures in the welded tuffs rather than through the low permeability matrix. Therefore, the thick unsaturated zone acts a natural barrier by slowing the rapid percolation and producing damping effects on the amount of water percolating through and thus percolation, once passed the unsaturated zone, could be approximated as a steady-state (Zhang *et al.*, 2006).

Several geological features such as lateral flow or diversion by capillary barriers can also cause the damping effects. Capillary barriers form in unsaturated zones where a layer containing relatively fine pores or fractures overlies a layer containing relatively coarse pores or fractures. Such capillary barriers within the Paintbrush

Group could promote lateral flow and retard the rate of percolation (Wu *et al.*, 2002; Pan *et al.*, 2004; Zhang *et al.*, 2006). Also adding to the damping effects is the period of no infiltration after episodic infiltration which allows the Paintbrush Group rock matrix to desaturate before it is recharged by the next infiltration event. This additional pore space in the dryer Paintbrush Group matrix provides a storage capability that prevents a rapid flow-through of water percolation (Zhang *et al.*, 2006). However, if an infiltration pulse is large and lasts long enough, the damping effect may decline and the flux below the Paintbrush Group would eventually respond to these infiltration pulses and that episodic infiltration, once crossing the Paintbrush Group, can be approximated as steady state (Zhang *et al.*, 2006).

Hydrogenic calcite and silica are present as coatings on footwall surfaces of open fractures or floors of lithophysal cavities and record past percolation, timing of flow, the thermal history of the rock mass and amount of seepage (Whelan *et al.*, 1994; Paces *et al.*, 1998; Whelan and Moscati, 1998; Whelan *et al.*, 1998; Neymark and Paces, 2000; Neymark *et al.*, 2000a; Paces *et al.*, 2001; Neymark *et al.*, 2002; Whelan *et al.*, 2002; Marshall *et al.*, 2003; Wilson *et al.*, 2003). A small proportion of the total silica is present in completely filled fractures with apertures between 1 and 5 mm (Paces *et al.*, 2001). Low temperature mineral coatings in fractures are commonly restricted to depositional sites where the apertures exceed 2 to 3 mm, and fractures with smaller apertures generally have vapour phase mineral assemblages (Paces *et al.*, 2001). The earliest mineral to be deposited from the supersaturated aqueous solution is a basal layer of massive silica with clusters of radiating quartz prisms on top (Whelan *et al.*, 1998) (Figure 4.5). Late calcite and interlayered opal may also overlie the massive silica and late forming calcite is limited to the tips of the blades of earlier calcite. Although calcite constitutes the bulk of the mineral coatings, opal is commonly present as the last mineral deposited on the outer growth surfaces of other minerals (Paces *et al.*, 2001) (Figure 4.6a and b).

Deposits of opal are present on low angle fractures where the thickness may be up to 2 cm (Paces *et al.*, 2001). Opal coatings on high angle fractures are rare and generally these coatings are between 1 to 2 mm thick. The presence of mineral deposits in open cavities and their general absence in narrow fractures implies that open void space is needed for fluid and gas exchange. The floors of primary spheroidal lithophysal cavities are typically between 5 to 50 cm in diameter and can

contain coatings of calcite and opal up to 4 cm thick, however, these mineral coatings are only present in a small number of lithophysae and only on the floors of these cavities (Paces *et al.*, 2001).

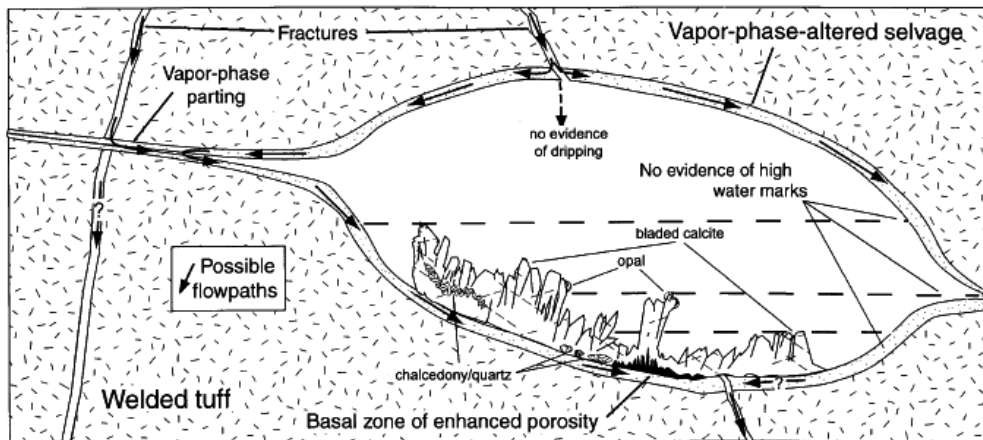


Figure 4.5 Schematic drawing of vapour phase parting and lithophysal cavity showing the high porosity, vapour-phase-altered selvage, and possible fracture flow paths intersecting both the parting, up dip from the cavity and the cavity. Flow paths are shown as arrows. Secondary calcite and silica are on the floor of the cavity, with a basal zone of enhanced porosity that may reflect later dissolution (from Whelan *et al.*, 2002).

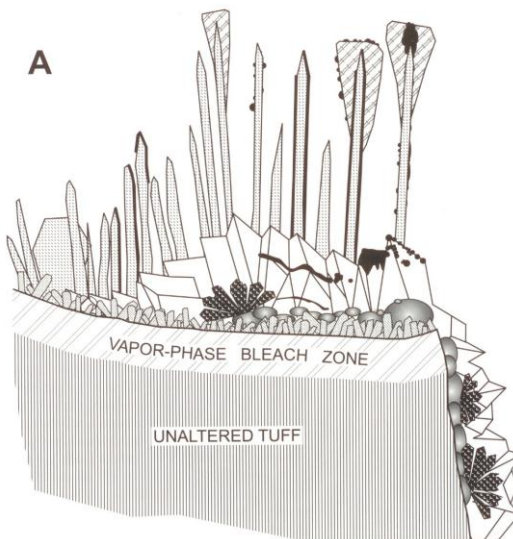


Figure 4.6a Typical mineral sequence coatings on a lithophysal cavity floor (from Whelan *et al.*, 1998).

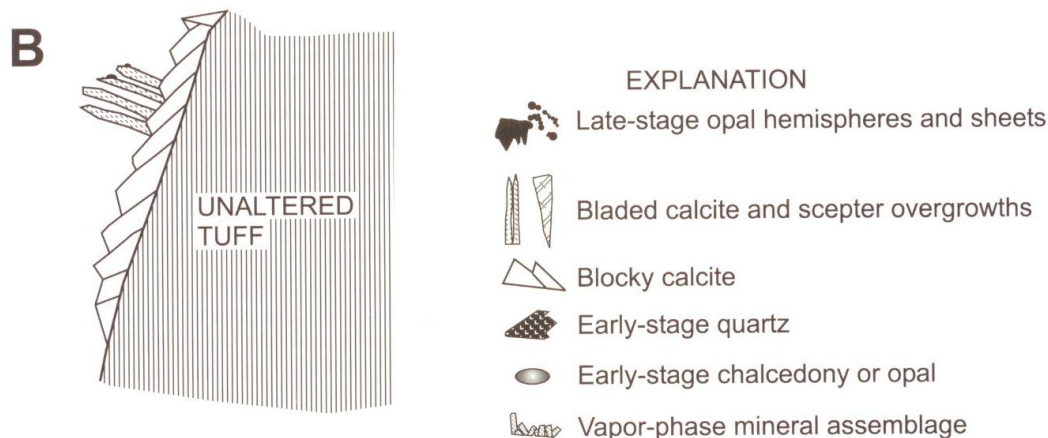


Figure 4.6b Typical mineral sequence coatings on a steeply dipping fracture surface (from Whelan *et al.*, 1998).

The deposits of opal on the lithophysal floors accumulate at the lowest elevation of the lithophysal cavity and in most cases the lithophysae are intersected by fractures that may have served as fluid pathways. These coatings are distinctly different from the vapor-phase mineral assemblages such as fine tridymite/cristobalite crystals with minor alkali feldspar, hematite and traces of garnet that coat the floors, walls and ceilings of lithophysal cavities. The vapour-phase mineral assemblages are formed at high temperatures during initial cooling and degassing of the tuffs (Paces *et al.*, 2001). The calcite and opal formed from, aqueous solutions requiring temperatures below boiling point. Deposition of secondary minerals are consistent with from percolating water at temperatures that are in equilibrium with the present day geothermal gradients or at slightly elevated temperatures caused by cooling of the tuffs or with elevated geothermal gradients in the unsaturated zone associated with regional magmatic activity. Measured temperatures, at or near the present day water table, range from 28° C to 39° C beneath Yucca Mountain (Sass *et al.*, 1988; Fridrich *et al.*, 1994). Opal formed during the latest stage of the paragenetic history at Yucca Mountain in lithophysal cavities was deposited on pre-existing secondary calcite commonly as isolated hemispheres at the tips of some calcite blades (Figure 4.6a).

The precipitation of silica gel from solution can occur in response to carbon dioxide degassing, water evaporation in the unsaturated zone (Marshall *et al.*, 2003), possible changes in pH or salinity or in a response to decrease in temperature (Zielinski, 1982). Uranium is incorporated into the matrix of the silica gel precipitates as an

adsorbed coprecipitate or uranyl-silica species. Uranium is unlikely to be lost from the opaline silica unless it is exposed to hot or very corrosive fluids over long periods of time (Ludwig *et al.*, 1980). The tuffs contain between 4 to 5 ppm of uranium and between 20 to 30 ppm of thorium (Gascoyne *et al.*, 2002). There is a deficiency of ^{234}U in the tuffs and this is caused by rapid and gradual removal of ^{234}U in the rock volume by alpha recoil and by slow removal by leaching. This leads to the preferential accumulation of ^{234}U in the pore fluid phase compared to ^{238}U . The ^{234}U is moved downwards via the pore fluid in the unsaturated zone and opal precipitated from the ^{234}U enriched fluid will incorporate this elevated $^{234}\text{U}/^{238}\text{U}$ ratio at the time of formation. Opal deposits at Yucca Mountain generally have initial $^{234}\text{U}/^{238}\text{U}$ ratios between ~4 to >10. Surface waters from Yucca Mountain have low $^{234}\text{U}/^{238}\text{U}$ values; in contrast groundwater beneath Yucca Mountain and most perched water from within Yucca Mountain have elevated $^{234}\text{U}/^{238}\text{U}$ that are consistent with opal initial ratios (Paces *et al.*, 1998; Paces *et al.*, 2001; Paces *et al.*, 2002).

Opal can be in the form of clear to light grey hemispheres, botryoidal masses or thin, lumpy or smooth sheets but generally forms as sheets or mounds of hemispheres rather than flat uniform layers (Figure 4.7).

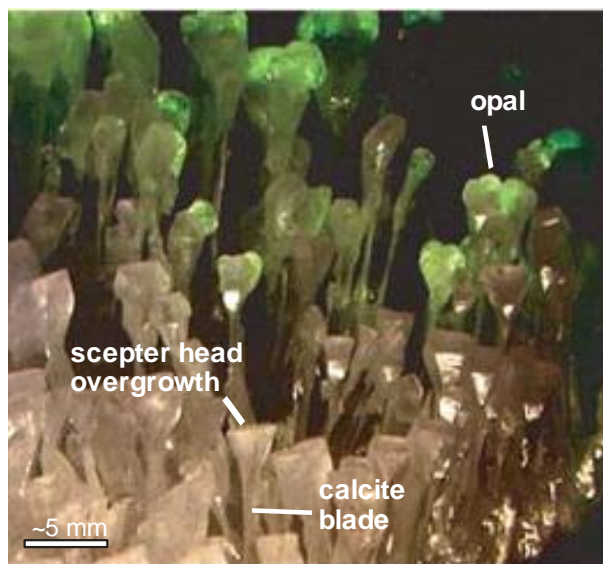


Figure 4.7 A combination of white and short-wave ultraviolet light showing thin blades of calcite (grey) with clear bulbous cluster of opal (green) on top of angular sceptre head calcite overgrowths at the tips of calcite blades (from Paces *et al.*, 2001).

Opal hemispheres experienced upward and outward growth. This observation is supported by concentric internal growth zoning observed in thin sections and with

dating of the opal. This indicates that mineral growth was progressive with material added to the upper and outermost parts of the opal hemispheres. This type of deposition is consistent with the meteoric water model (Whelan *et al.*, 2002), where tightly convex films of water have an increased vapour pressure and enhanced evaporation relative to flat films of water. Opal and chalcedony coatings range in thickness from sub millimetre to centimetre.

4.5 Previously determined ages and rates

Much of the previous work performed on opal dating has been done on the uranium rich opal coatings from fractures and cavities within the unsaturated zone in Yucca Mountain.

Yucca Mountain opal shows a high uranium concentration ranging from ~20 to ~850 ppm (Paces *et al.*, 1996; Paces *et al.*, 1998; Neymark *et al.*, 1998; Neymark and Paces 2000; Neymark *et al.*, 2000a; Paces *et al.*, 2001; Neymark *et al.*, 2002; Paces *et al.*, 2004a) and an initial $^{234}\text{U}/^{238}\text{U}$ activity ratios ranging from close to secular equilibrium (1.0) to close to 10 (Paces *et al.*, 1996; Neymark *et al.*, 1998; Neymark and Paces 2000; Paces *et al.*, 2001). Previous work also demonstrated high $^{238}\text{U}/^{232}\text{Th}$ and $^{238}\text{U}/^{204}\text{Pb}$ (up to 108) (Neymark *et al.*, 2000a). Low initial ^{230}Th and low common Pb abundances ($^{206}\text{Pb}/^{204}\text{Pb}$ ratios are greater than 100) are also characteristics of this opaline material.

Early dating of opal samples from the Yucca Mt by Szabo and Kyser (1985; 1990) produced inconclusive U-series ages greater than 400 kyr, which is older than the detection limit of the method.

The age of the outermost surfaces of the opal coatings was initially determined by Paces *et al.*, (1996), who calculated $^{230}\text{Th}/\text{U}$ ages ranging from 37 to >700 kyr. This age range is supported by U-Pb ages of 50 to 1611 ka (Neymark *et al.*, 1998) and $^{230}\text{Th}/\text{U}$ ages calculated by Neymark and Paces (2000) ranging between 40.1 to 710 ka but with most ages evenly spread between 40.1 and 447 ka. Similar conventional $^{230}\text{Th}/\text{U}$ ages were produced by Paces *et al.*, (2001). Neymark *et al.*, (2000a) reported ages for the outmost layers of opal coatings between 34.1 ± 0.6 ka to 1772 ± 40 ka using the $^{230}\text{Th}/^{238}\text{U}-^{234}\text{U}/^{238}\text{U}$, $^{206}\text{Pb}*/^{238}\text{U}-^{234}\text{U}/^{238}\text{U}$, $^{206}\text{Pb}_*/^{238}\text{U}-^{230}\text{Th}/^{238}\text{U}$,

and $^{207}\text{Pb}^*/^{235}\text{U}$ - $^{206}\text{Pb}^*/^{238}\text{U}$ projections. Use of the U-Pb technique significantly extends the age range beyond the limit of $^{230}\text{Th}/\text{U}$ dating method and provides a more accurate estimation of the time of deposition for mixed age samples as identified by Neymark and Paces (1996).

The base of the opal coatings have ages between 8 to 10 Ma (Neymark *et al.*, 1998), with relatively precise U-Pb ages being reported as 9.8 ± 3.4 Ma (Neymark *et al.*, 2002), 9.36 ± 0.41 Ma (Whelan *et al.*, 2008) and 9.10 ± 0.21 Ma (Neymark and Amelin 2008).

The discordance of some ages observed in samples from the same microstratigraphic layer and U-series disequilibrium observed in samples with U-Pb ages older than ~2 Ma may indicate either an open system or two-component mixing of older (in secular equilibrium with regard to ^{234}U) and younger (not in secular equilibrium) opal components (Neymark *et al.*, 2002). This highlighted the need for better spatial resolution in analyses as most of the previous dating was done by digestions of whole hemispheres of sheets of opal in the outer portions of the mineral coating from Yucca Mt with sample sizes up to 1000 μm thick.

Paces *et al.*, (2004a) used both ion microprobe (SHRIMP) and in situ microdigestion and TIMS methods for $^{230}\text{Th}/\text{U}$ and $^{234}\text{U}/^{238}\text{U}$ dating of opal to significantly increases the spatial resolution, resulting in U-series dates that are both younger and older than those obtained by earlier whole hemisphere digestions. The SHRIMP analyses produced $^{230}\text{Th}/\text{U}$ ages from 34.4 ± 8.0 to $560+\infty/-300$ ka and the insitu microdigestion of opal hemispheres with analyses by TIMS resulted in $^{230}\text{Th}/\text{U}$ dates from the outer part of the hemisphere between 7.3 ± 0.7 to 37.1 ± 2.3 ka. SHRIMP U-series ages were calculated on the outermost opal layers and range from 41 to 1290 ka (Paces *et al.*, 2010). These ages are similar to the ages produced by TIMS analysis.

Extremely slow and uniform long term growth rates of opal at Yucca Mountain have been estimated by Neymark *et al.*, (1998) and Paces *et al.*, (1996) to be approximately 1 to 4 mm per million years. Neymark and Paces (2000) and Paces *et al.*, (2001) calculated similar continuous deposition rates to be between 0.1 and 5.0 mm/Ma and these deposition rates are supported by deposition rates calculated by

Neymark *et al.*, (2002) who determined average growth rates to range from 1.31 ± 0.44 to 5.1 ± 0.8 mm/Ma. Growth rates between 0.58 and 0.69 mm/Ma (Paces *et al.*, 2004a) were calculated from ages using techniques with increased spatial resolution from the outerpart of opal hemisphere. Similar growth rates of ~1 to ~2 mm/Ma were reported by Neymark and Amelin (2008) and 0.42 to 1.54 mm/Ma by Paces *et al.*, (2010).

4.6 Opaline silica depositional models

Paces *et al.*, (2001) identifies two theoretical models that represent end member depositional processes. Both assume closed system behaviour after mineral formation. The first model is the episodic or instantaneous deposition model where opal layers of finite thickness form instantaneously over short time intervals, relative to the half-life of ^{230}Th and ^{234}U , and have uniform initial isotopic compositions. Ages of the individual layers reflect the time of deposition for that particular layer indicating that a single depositional event can be represented in a subsample of finite thickness. However, the presence of micrometre scale laminations in the opaline silica suggests that the model of simple instantaneous deposition is not realistic. Inconsistencies include: a positive correlation between the age and sample thickness, discordant $^{230}\text{Th}/\text{U}$ ages for samples of the outer surface of individual coatings, discordance between the range of ages obtained using isotopic systems with different half-lives ($^{207}\text{Pb}/^{235}\text{U}$, $^{230}\text{Th}/\text{U}$), a negative correlation between $^{230}\text{Th}/\text{U}$ ages and initial $^{234}\text{U}/^{238}\text{U}$ values and a paucity of ages near the limits of $^{230}\text{Th}/\text{U}$ ages (Paces *et al.*, 2004a).

The second model is the continuous deposition model where mineral growth occurs at a slow and constant rate and results in a continuum of infinitely thin layers (Figure 4.8). Several assumptions were made by Paces *et al.*, (2001) for the continuous deposition model. These include the assumption that deposition of mineral coatings continued growing outward until the present at a constant rate of deposition. Secondly, that ^{238}U is homogeneous in the opal. Thirdly, no initial ^{230}Th was inherited from the aqueous solution and that once formed the opal behaves as a closed system relative to ^{238}U and its decay products and lastly that all samples of finite size integrate multiple infinitely thin depositional layers with continuously varying ages (Paces *et al.*, 2001). The isotopic concentrations will be different for

each model and ages determined from single subsamples using isotopic systems with different half-lives will be discordant for continuous deposition and concordant for instantaneous deposition as long as both methods use material collected from the same, single layer having a single instantaneous deposition event.

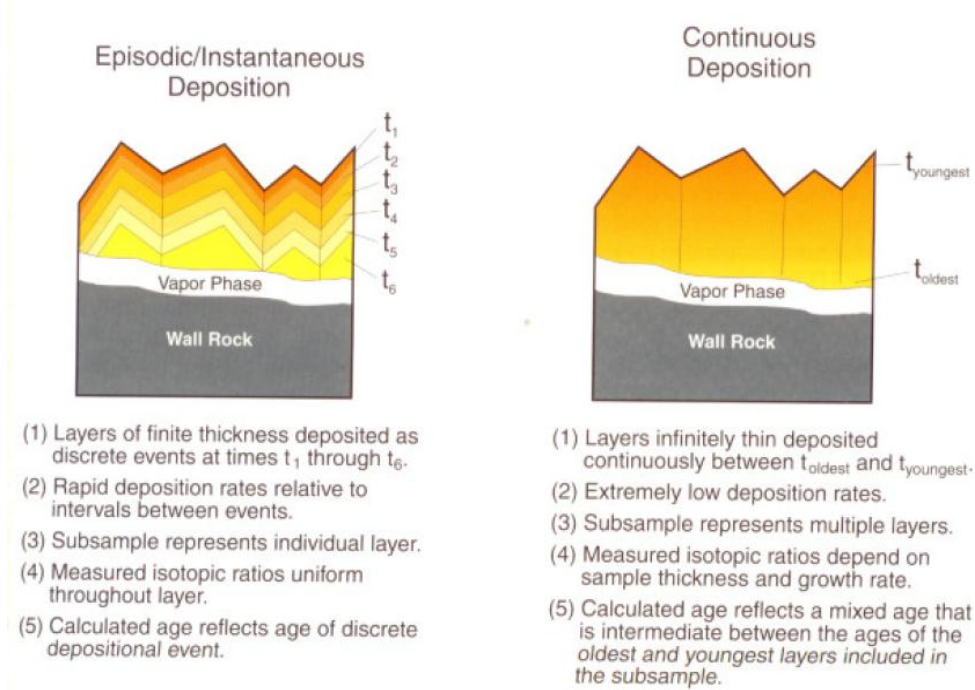


Figure 4.8 Conceptual models of episodic/instantaneous and continuous mineral deposition (from Paces *et al.*, 2001).

The age of a given layer, if considering the instantaneous deposition model, is independent of subsample thickness in so much as all the material analysed is sampled from that single instantaneously deposited layer. Whereas, for the continuous deposition model, the age is a product of sample thickness as the age for a thicker sample will be the combined age of a larger range of ages. The continuous deposition model also shows that the age of samples that are of uniform thickness are dependant on mineral growth rates, whereas, the instantaneous model ages are not affected by the growth rate.

Investigations into the age of opal and consequently the rate of deposition with an increased resolution provided by SHRIMP analysis gives clarification on the style of deposition and is discussed in later in this chapter.

4.7 Results

4.7.1 HD2059

Sample HD2059 is a thick coating of calcite and silica developed within a lithophysal cavity located from the proposed repository horizon in the Miocene-age tuffs in the unsaturated zone in Yucca Mountain. Neymark *et al.*, (2000a, 2002) studied this sample using TIMS and reported ages varying from 0.34 ± 0.04 Ma in the outer parts to 5.27 ± 0.02 Ma near the base of the opal coating.

HD2059 was the first sample to be analysed by SHRIMP (over two days) at the early stage of the technique development in this study. The primary beam intensity was relatively low during these sessions resulting in a generally low counting rate and the errors higher than in subsequent runs. Nevertheless, the data show a systematic correlation between the age and the observed microstratigraphy (Figure 4.9).

Fourteen analyses of the innermost layer of opal, which is in direct contact with the host tuff and has thickness of $\sim 1\text{-}1.5$ mm, show a range in the proportion of common lead ($^{204}\text{Pb}/^{206}\text{Pb}$ ratios vary from 0.01 to 1.49×10^{-9} , Table 4.1). The $^{232}\text{Th}/^{238}\text{U}$ ratios vary between $\sim 10^{-5}$ and 10^{-13} so that the accumulated radiogenic ^{208}Pb is negligible and ^{208}Pb was used for the initial Pb correction. Two analyses have a negative $^{207}\text{Pb}/^{235}\text{U}$ age and higher $^{206}\text{Pb}/^{238}\text{U}$ ages (Figure 4.10).

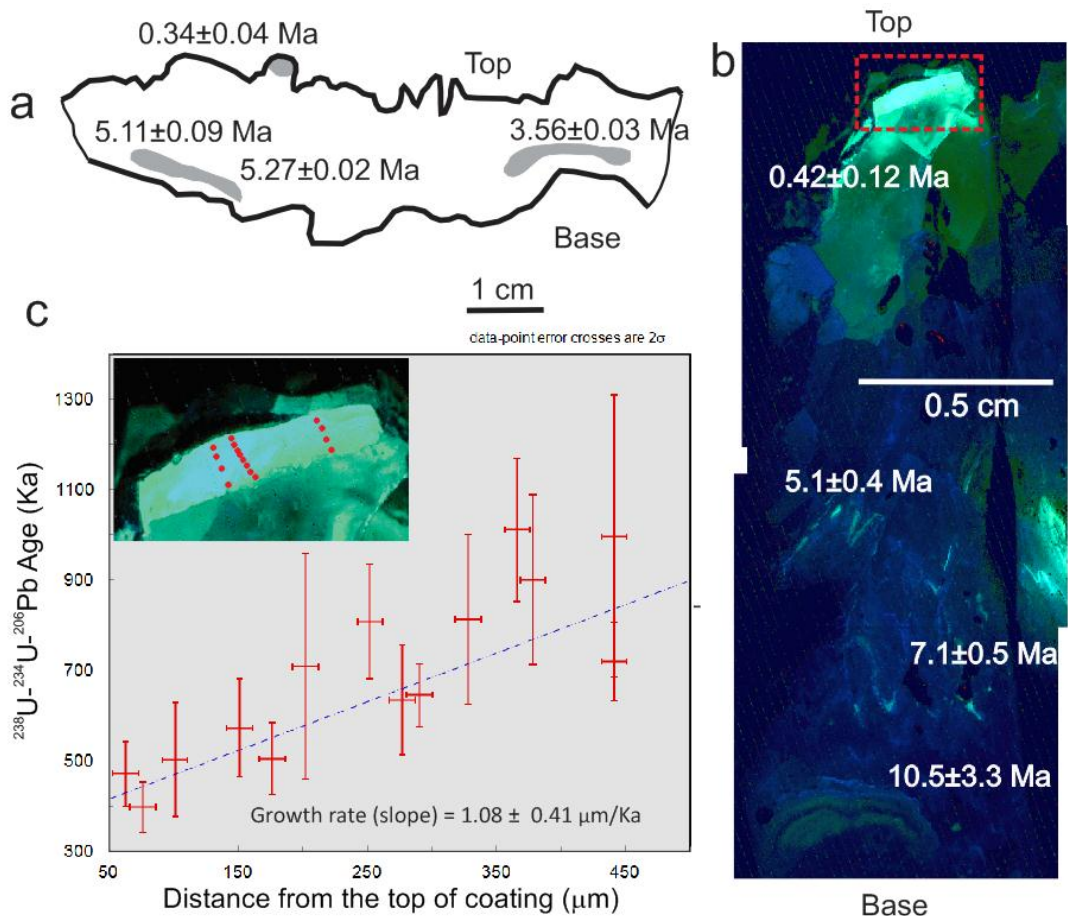


Figure 4.9. U-Pb and U-series ages of opal sample HD2059 from Yucca Mountain (Nevada, USA); (A) diagram showing areas within a slice of the sample analysed using ID-TIMS (after Neymark *et al.*, 2002); (B) UV-light image of different slice of the same sample analysed with SHRIMP with the ages of investigated opal parts (dark blue is non-luminescent calcite and green is opal); (C) distance vs. age plot for the outermost part of the opal sample (analysed spots are shown as red dots on the insert; area of the insert is shown as red square in B).

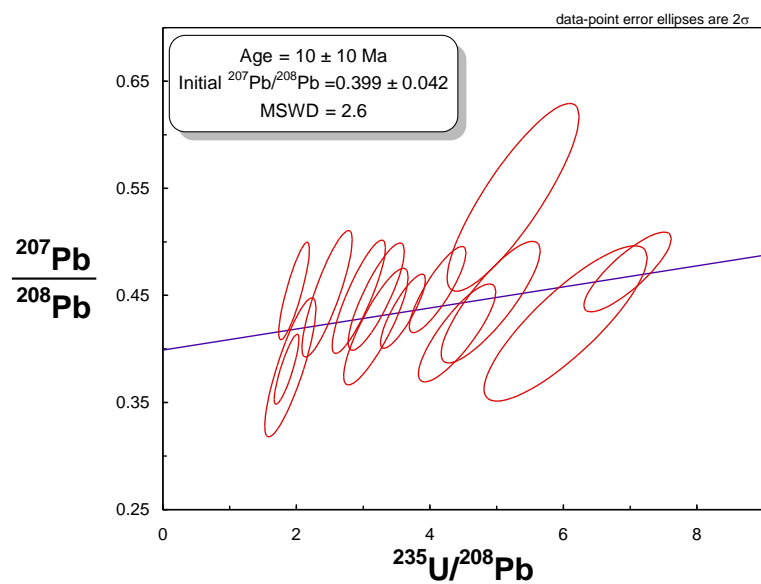
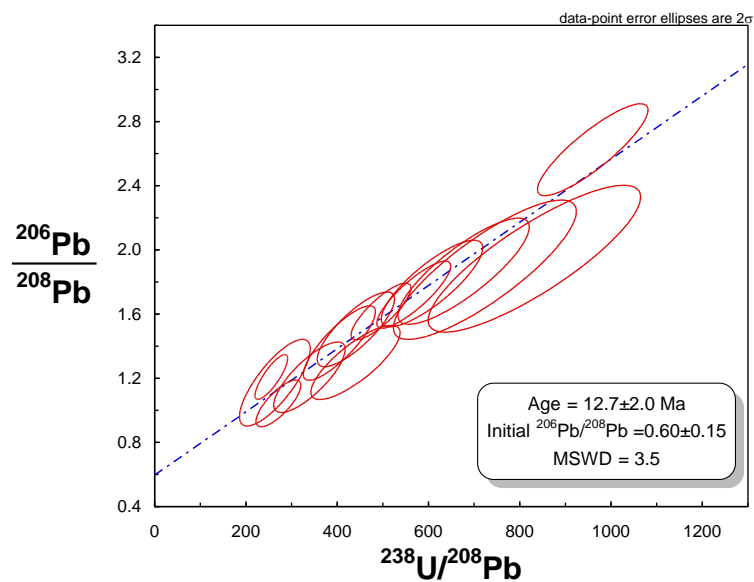


Figure 4.10. ^{206}Pb vs ^{238}U and ^{207}Pb vs ^{235}U plots for sample HD2059. Data are not corrected for the common Pb. Intercepts with the Y-axis determine initial Pb composition.

Table 4.1 SHRIMP results for opal samples from Yucca Mountain, USA (errors are 1σ).

N	U ($\mu\text{g/g}$) _a	$\frac{204}{206}\text{Pb}$	$\frac{207}{206}\text{Pb}$	$\frac{208}{206}\text{Pb}$	$\frac{232}{238}\text{Th}$	$\frac{230}{238}\text{Th}$ act	$\frac{234}{238}\text{U}$ act	$\frac{206}{238}\text{Pb}$	$\frac{207}{235}\text{Pb}$	f8b	$\frac{206}{238}\text{Pb}$	$\frac{207}{206}\text{Pb}$	$\frac{207}{235}\text{Pb}$										
								<i>common lead uncorrected</i>			^{208}Pb corrected	^{208}Pb corrected	^{208}Pb corrected										
HD2059																							
Inner part of the coating (Day 1)																							
10	5	0.0146±0.0055	0.316±0.022	0.705±0.047	2.45E-11±3.26E-06	0.96±0.44	0.69±0.17	0.00351±0.00015	0.1529±0.0085	0.3412±0.0281	0.00183±7.72E-05	0.047±0.027	0.01500±0.0081										
11	23	0.0075±0.0027	0.180±0.008	0.381±0.017	2.14E-06±4.53E-06	0.93±0.21	0.93±0.09	0.00273±0.00007	0.0678±0.0028	0.1845±0.0121	0.00178±4.08E-05	0.031±0.007	0.00966±0.0020										
12	14	0.0192±0.0038	0.269±0.013	0.619±0.028	8.96E-12±1.79E-06	0.80±0.25	1.06±0.12	0.00326±0.00010	0.1210±0.0049	0.2996±0.0198	0.00183±5.53E-05	0.027±0.010	0.00850±0.0029										
13	13	0.0124±0.0044	0.265±0.014	0.581±0.029	1.02E-11±6.41E-06	1.25±0.35	0.93±0.13	0.00303±0.00009	0.1106±0.0048	0.2814±0.0195	0.00173±5.30E-05	0.041±0.013	0.01234±0.0037										
14	7	0.0178±0.0049	0.315±0.016	0.828±0.039	4.65E-06±1.28E-05	1.08±0.50	0.57±0.16	0.00472±0.00015	0.2055±0.0086	0.4010±0.0271	0.00225±9.33E-05	-0.033±0.017	-0.01274±-0.0066										
Inner part of the coating (Day 2)																							
1	9	0.0385±0.0083	0.374±0.029	0.829±0.062	1.03E-12±3.96E-09	N.D.	N.D.	0.00356±0.00021	0.1835±0.0119	0.4015±0.0357	0.00143±7.49E-05	0.065±0.038	0.01905±0.0104										
2	17	0.0096±0.0036	0.298±0.020	0.665±0.042	1.69E-11±1.12E-06	N.D.	N.D.	0.00341±0.00016	0.1404±0.0080	0.3219±0.0257	0.00134±5.26E-05	0.043±0.023	0.01380±0.0069										
3	16	0.0146±0.0043	0.238±0.018	0.536±0.039	5.70E-13±2.19E-09	N.D.	N.D.	0.00276±0.00013	0.0904±0.0059	0.2594±0.0226	0.00134±5.20E-05	0.028±0.022	0.00795±0.0060										
4	11	0.0313±0.0083	0.218±0.022	0.514±0.049	8.68E-13±3.34E-09	N.D.	N.D.	0.00234±0.00014	0.0702±0.0062	0.2490±0.0268	0.00123±5.98E-05	0.013±0.030	0.00317±0.0071										
5	10	0.0082±0.0051	0.289±0.027	0.533±0.050	2.84E-11±1.89E-06	N.D.	N.D.	0.00259±0.00016	0.1032±0.0081	0.2581±0.0274	0.00134±6.49E-05	0.098±0.033	0.02610±0.0075										
6	24	0.0099±0.0035	0.232±0.015	0.559±0.034	1.20E-11±1.13E-06	N.D.	N.D.	0.00295±0.00013	0.0942±0.0055	0.2705±0.0212	0.00120±4.17E-05	0.008±0.018	0.00235±0.0053										
7	11	0.0267±0.0054	0.435±0.026	0.958±0.055	9.43E-06±9.43E-06	N.D.	N.D.	0.00385±0.00018	0.2310±0.0114	0.4641±0.0348	0.00160±8.85E-05	0.088±0.028	0.02515±0.0071										
8	12	0.0245±0.0062	0.324±0.025	0.770±0.056	7.73E-13±2.97E-09	N.D.	N.D.	0.00295±0.00016	0.1319±0.0085	0.3729±0.0326	0.00123±5.89E-05	0.020±0.034	0.00509±0.0084										
9	6	0.0218±0.0078	0.327±0.033	0.853±0.080	1.96E-05±1.96E-05	N.D.	N.D.	0.00445±0.00033	0.2004±0.0176	0.4131±0.0437	0.00126±7.93E-05	-0.032±0.055	-0.01145±-0.0203										
Central part of the coating (Day 1)																							
5	20	1.05E-08±0.0020	0.033±0.005	0.021±0.005	5.95E-12±9.71E-07	0.88±0.18	0.971±0.09	0.00157±5.70E-05	0.0072±0.0010	0.0102±0.0027	0.00125±4.05E-05	0.025±0.005	0.00535±0.0011										
6	83	0.0012±0.0007	0.034±0.002	0.014±0.002	1.47E-12±1.70E-07	0.87±0.08	0.953±0.04	0.00130±2.61E-05	0.0061±0.0004	0.0068±0.0011	0.00103±1.81E-05	0.029±0.003	0.00514±0.0004										

Table 4.1 continued

N	U ($\mu\text{g/g}$) _a	$\frac{204}{206}\text{Pb}$	$\frac{207}{206}\text{Pb}$	$\frac{208}{206}\text{Pb}$	$\frac{232}{238}\text{Th}$	$\frac{230}{238}\text{Th}$ act	$\frac{234}{238}\text{U}$ act	$\frac{206}{238}\text{Pb}$	$\frac{207}{235}\text{Pb}$	f8 _b	$\frac{206}{238}\text{Pb}$	$\frac{207}{206}\text{Pb}$	$\frac{207}{235}\text{Pb}$
								common lead uncorrected			^{208}Pb corrected	^{208}Pb corrected	^{208}Pb corrected
7	91	2.61E-09±0.0008	0.042±0.003	0.009±0.002	1.37E-12±8.62E-07	0.98±0.09	1.062±0.04	0.00142±2.45E-05	0.0082±0.0005	0.0043±0.0009	0.00112±1.82E-05	0.038±0.003	0.00748±0.0005
8	180	1.49E-09±0.0003	0.041±0.002	0.006±0.001	6.81E-13±3.01E-07	1.01±0.06	0.979±0.03	0.00125±1.93E-05	0.0070±0.0003	0.0031±0.0005	0.00100±1.22E-05	0.038±0.002	0.00657±0.0003
9	69	3.86E-09±0.0013	0.051±0.003	0.024±0.003	6.39E-06±2.57E-06	0.87±0.11	1.038±0.05	0.00128±3.93E-05	0.0090±0.0006	0.0116±0.0017	0.00099±1.93E-05	0.042±0.004	0.00728±0.0006
15	185	1.61E-09±0.0004	0.041±0.002	0.007±0.001	7.08E-13±3.16E-07	0.91±0.06	0.987±0.03	0.00114±1.75E-05	0.0064±0.0003	0.0036±0.0006	0.00090±1.14E-05	0.038±0.002	0.00597±0.0003
16	75	3.63E-09±0.0009	0.044±0.003	0.021±0.003	1.72E-06±1.42E-06	1.11±0.10	0.928±0.05	0.00124±2.48E-05	0.0076±0.0005	0.0104±0.0016	0.00097±1.85E-05	0.036±0.003	0.00610±0.0005
17	181	1.51E-09±0.0005	0.042±0.002	0.005±0.001	9.19E-08±5.11E-07	1.03±0.06	0.970±0.03	0.00123±1.66E-05	0.0071±0.0003	0.0024±0.0005	0.00098±1.21E-05	0.040±0.002	0.00681±0.0003
Central part of the coating (Day 2)													
10	50	0.0018±0.0018	0.060±0.007	0.067±0.010	1.75E-06±2.13E-06	N.D.	N.D.	0.00099±3.77E-05	0.0082±0.0009	0.0327±0.0050	0.00080±2.83E-05	0.034±0.008	0.00448±0.0010
11	91	0.0009±0.0006	0.042±0.004	0.017±0.003	9.66E-14±3.71E-10	N.D.	N.D.	0.00110±3.02E-05	0.0064±0.0006	0.0084±0.0017	0.00088±2.26E-05	0.035±0.004	0.00533±0.0006
12	40	0.0011±0.0011	0.053±0.007	0.061±0.010	2.26E-13±8.69E-10	N.D.	N.D.	0.00119±5.11E-05	0.0088±0.0011	0.0295±0.0052	0.00078±3.11E-05	0.030±0.008	0.00472±0.0012
13	130	5.20E-09±0.0003	0.039±0.003	0.018±0.003	2.10E-12±1.40E-07	N.D.	N.D.	0.00114±2.78E-05	0.0062±0.0005	0.0086±0.0016	0.00079±1.80E-05	0.032±0.004	0.00504±0.0005
14	131	0.0006±0.0008	0.044±0.003	0.025±0.004	5.41E-07±8.34E-07	N.D.	N.D.	0.00110±2.56E-05	0.0067±0.0005	0.0122±0.0018	0.00085±1.85E-05	0.034±0.004	0.00511±0.0005
15	142	4.52E-09±0.0003	0.038±0.003	0.017±0.003	6.27E-07±7.63E-07	N.D.	N.D.	0.00108±2.44E-05	0.0057±0.0004	0.0082±0.0014	0.00084±1.77E-05	0.032±0.003	0.00471±0.0005
16	82	0.0011±0.0008	0.044±0.004	0.026±0.005	1.10E-13±4.23E-10	N.D.	N.D.	0.00110±3.31E-05	0.0066±0.0006	0.0125±0.0023	0.00081±2.28E-05	0.034±0.005	0.00502±0.0007
17	60	0.0019±0.0013	0.061±0.005	0.057±0.007	3.92E-12±3.70E-07	N.D.	N.D.	0.00106±3.36E-05	0.0089±0.0007	0.0278±0.0035	0.00125±3.24E-05	0.039±0.005	0.00551±0.0007
18	26	0.0045±0.0026	0.059±0.009	0.076±0.014	4.05E-06±4.05E-06	N.D.	N.D.	0.00111±5.55E-05	0.0091±0.0013	0.0368±0.0068	0.00090±4.16E-05	0.030±0.010	0.00436±0.0014
19	19	0.0078±0.0039	0.040±0.008	0.071±0.015	4.81E-13±1.85E-09	N.D.	N.D.	0.00140±8.06E-05	0.0076±0.0015	0.0342±0.0074	0.00093±4.94E-05	0.012±0.010	0.00214±0.0018
Outer part of the coating (Day 1)													
1	99	0.0009±0.0017	0.015±0.003	0.019±0.004	1.33E-12±2.16E-07	2.80±0.14	2.18±0.06	0.00050±1.39E-05	0.0010±0.0002	0.0093±0.0020	0.00039±1.02E-05	0.007±0.003	0.00048±0.0002
2	136	0.0008±0.0012	0.029±0.003	0.047±0.006	1.83E-07±3.81E-07	2.41±0.10	2.19±0.05	0.00040±1.02E-05	0.0016±0.0002	0.0226±0.0029	0.00031±7.65E-06	0.010±0.004	0.00057±0.0002

Table 4.1 continued

<i>N</i>		<i>U</i> ($\mu\text{g/g}$) _a	$\frac{^{204}\text{Pb}}{^{206}\text{Pb}}$	$\frac{^{207}\text{Pb}}{^{206}\text{Pb}}$	$\frac{^{208}\text{Pb}}{^{206}\text{Pb}}$	$\frac{^{232}\text{Th}}{^{238}\text{U}}$	$\frac{^{230}\text{Th}}{^{238}\text{U}}$ act	$\frac{^{234}\text{U}}{^{238}\text{U}}$ act	$\frac{^{206}\text{Pb}}{^{238}\text{U}}$	$\frac{^{207}\text{Pb}}{^{235}\text{U}}$	<i>f8b</i>	$\frac{^{206}\text{Pb}}{^{238}\text{U}}$	$\frac{^{207}\text{Pb}}{^{206}\text{Pb}}$	$\frac{^{207}\text{Pb}}{^{235}\text{U}}$
<i>common lead uncorrected</i>														
3	59	0.0010±0.0034	0.053±0.007	0.118±0.015	2.29E-12±3.41E-07	3.38±0.22	2.99±0.09	0.00038±1.61E-05	0.0028±0.0004	0.0573±0.0076	0.00028±1.06E-05	0.005±0.009	0.00026±0.0004	
4	75	0.0105±0.0040	0.035±0.006	0.131±0.015	1.82E-12±2.10E-07	4.19±0.26	3.78±0.09	0.00032±1.35E-05	0.0015±0.0002	0.0633±0.0078	0.00023±8.46E-06	-0.019±0.008	-0.00078±-0.0003	
18	50	1.68E-08±0.0022	0.024±0.005	0.097±0.014	2.55E-12±2.94E-07	3.97±0.21	3.54±0.11	0.00040±1.67E-05	0.0014±0.0003	0.0470±0.0070	0.00031±1.21E-05	-0.016±0.007	-0.00084±-0.0004	
19	39	2.12E-08±0.0014	0.025±0.006	0.047±0.010	1.11E-06±1.35E-06	3.35±0.22	2.67±0.10	0.00041±1.91E-05	0.0014±0.0003	0.0229±0.0052	0.00032±1.44E-05	0.006±0.007	0.00034±0.0004	
20	68	0.0025±0.0013	0.020±0.003	0.026±0.005	7.87E-07±7.87E-07	2.23±0.15	1.90±0.07	0.00053±1.77E-05	0.0015±0.0002	0.0124±0.0025	0.00041±1.26E-05	0.010±0.004	0.00073±0.0003	
21	91	0.0017±0.0012	0.020±0.003	0.035±0.005	3.68E-07±5.68E-07	1.52±0.10	1.50±0.05	0.00059±1.49E-05	0.0016±0.0002	0.0169±0.0025	0.00046±1.14E-05	0.006±0.003	0.00049±0.0003	
Outer part of the coating (Day 2)														
22	50	7.21E-09±0.0013	0.004±0.002	0.010±0.003	2.12E-06±2.31E-06	4.33±0.68	3.74±0.14	0.00181±0.00011	0.0010±0.0004	0.0047±0.0015	0.00123±3.30E-05	0.000±0.002	-0.00001±-0.0005	
23	85	2.31E-08±0.0031	0.009±0.005	0.014±0.007	2.41E-12±2.78E-07	3.90±0.40	3.11±0.10	0.00030±1.80E-05	0.0004±0.0002	0.0067±0.0034	0.00022±1.07E-05	0.004±0.005	0.00015±0.0002	
24	26	3.75E-08±0.0043	0.010±0.006	0.010±0.008	8.04E-12±7.58E-07	3.50±0.44	2.77±0.17	0.00060±4.12E-05	0.0008±0.0005	0.0048±0.0040	0.00045±2.78E-05	0.006±0.007	0.00049±0.0005	
25	21	3.39E-08±0.0045	0.027±0.009	0.064±0.016	1.10E-11±1.27E-06	2.47±0.38	2.22±0.18	0.00069±4.42E-05	0.0026±0.0008	0.0312±0.0081	0.00061±3.50E-05	0.001±0.010	0.00010±0.0010	
26	156	9.35E-09±0.0012	0.010±0.003	0.008±0.003	1.45E-12±1.67E-07	2.67±0.18	2.22±0.06	0.00033±1.21E-05	0.0005±0.0001	0.0041±0.0016	0.00030±9.20E-06	0.006±0.003	0.00030±0.0001	
27	121	0.0041±0.0019	0.014±0.003	0.012±0.004	1.71E-12±1.14E-07	1.98±0.19	1.83±0.06	0.00047±2.00E-05	0.0009±0.0002	0.0057±0.0018	0.00035±1.12E-05	0.010±0.003	0.00061±0.0002	
28	134	0.0020±0.0010	0.008±0.002	0.009±0.003	5.18E-14±1.99E-10	2.45±0.21	1.95±0.06	0.00058±2.25E-05	0.0006±0.0001	0.0043±0.0013	0.00044±1.20E-05	0.004±0.002	0.00034±0.0002	
29	49	1.44E-08±4.302E-07	0.012±0.003	0.017±0.005	3.63E-06±2.57E-06	1.92±0.20	1.60±0.09	0.00072±2.89E-05	0.0012±0.0003	0.0084±0.0025	0.00062±2.34E-05	0.005±0.004	0.00052±0.0004	
HD2019														
1	94	0.0072±0.0018	0.178±0.007	0.363±0.014	1.62E-05±4.16E-06	0.92±0.11	0.960±0.05	0.00134±2.76E-05	0.0327±0.0011	0.1756±0.0109	0.00110±2.29E-05	0.037±0.004	0.00569±0.0006	
2	81	0.0050±0.0018	0.145±0.007	0.251±0.013	2.64E-06±2.16E-06	0.92±0.11	0.986±0.06	0.00125±3.31E-05	0.0251±0.0012	0.1216±0.0088	0.00110±2.78E-05	0.050±0.007	0.00754±0.0010	
3	99	0.0022±0.0011	0.126±0.006	0.197±0.010	1.25E-05±3.49E-06	0.95±0.10	0.922±0.05	0.00112±2.48E-05	0.0196±0.0008	0.0956±0.0069	0.00102±2.15E-05	0.051±0.006	0.00720±0.0008	

Table 4.1 continued

N		<i>U</i>	$\frac{204}{206}Pb$	$\frac{207}{206}Pb$	$\frac{208}{206}Pb$	$\frac{232}{238}Th$	$\frac{230}{238}Th$ act	$\frac{234}{238}U$ act	$\frac{206}{238}Pb$	$\frac{207}{235}Pb$	f8b	$\frac{206}{238}Pb$	$\frac{207}{206}Pb$	$\frac{207}{235}Pb$
		($\mu g/g$) _a	$\frac{206}{206}Pb$	$\frac{206}{206}Pb$	$\frac{238}{U}$	$\frac{238}{U}$	$\frac{238}{U}$	$\frac{238}{U}$	$\frac{238}{U}$	$\frac{238}{U}$	$\frac{238}{U}$	$\frac{208}{208}Pb$ corrected	$\frac{208}{208}Pb$ corrected	$\frac{208}{208}Pb$ corrected
4	40	0.0148±0.0038	0.168±0.012	0.336±0.023	3.22E-05±8.85E-06	0.97±0.16	0.912±0.08	0.00115±4.03E-05	0.0265±0.0016	0.1628±0.0136	0.00096±3.10E-05	0.038±0.013	0.00504±0.0016	
5	451	0.0010±0.0004	0.050±0.002	0.039±0.003	3.75E-07±3.23E-07	0.94±0.05	1.023±0.03	0.00084±1.55E-05	0.0058±0.0002	0.0188±0.0015	0.00082±1.51E-05	0.035±0.002	0.00398±0.0002	
6	311	0.0041±0.0008	0.166±0.005	0.297±0.009	1.83E-06±7.96E-07	1.02±0.06	0.987±0.03	0.00088±1.69E-05	0.0201±0.0006	0.1437±0.0083	0.00075±1.49E-05	0.054±3.69E-05	0.00556±1.76E-07	
7	400	0.0011±0.0005	0.063±0.003	0.053±0.003	1.73E-07±2.67E-07	1.03±0.06	1.025±0.03	0.00076±1.66E-05	0.0067±0.0003	0.0257±0.0021	0.00074±1.61E-05	0.043±0.003	0.00441±0.0003	
8	640	0.0008±0.0004	0.054±0.002	0.036±0.002	7.23E-07±3.86E-07	1.03±0.05	1.001±0.02	0.00071±1.10E-05	0.0053±0.0002	0.0174±0.0014	0.00070±1.07E-05	0.040±0.002	0.00388±0.0002	
9	518	0.0011±0.0005	0.063±0.002	0.069±0.003	2.63E-06±7.50E-07	1.04±0.06	1.014±0.02	0.00074±1.50E-05	0.0065±0.0003	0.0332±0.0023	0.00072±1.44E-05	0.037±0.002	0.00365±0.0002	
10	631	0.0013±0.0004	0.067±0.002	0.067±0.003	8.61E-07±3.99E-07	1.05±0.05	1.041±0.02	0.00077±1.37E-05	0.0071±0.0002	0.0326±0.0022	0.00075±1.32E-05	0.041±0.002	0.00420±0.0002	
11	832	0.0011±0.0004	0.053±0.002	0.032±0.002	6.95E-07±3.20E-07	0.98±0.04	1.049±0.02	0.00073±1.05E-05	0.0054±0.0002	0.0155±0.0012	0.00072±1.03E-05	0.041±0.002	0.00406±0.0002	
12	343	0.0018±0.0006	0.065±0.003	0.060±0.004	3.00E-06±9.18E-07	0.94±0.05	1.010±0.03	0.00071±1.13E-05	0.0064±0.0003	0.0290±0.0023	0.00069±1.08E-05	0.042±0.003	0.00398±0.0003	
13	324	0.0039±0.0008	0.112±0.004	0.169±0.006	6.91E-06±1.43E-06	0.95±0.05	1.026±0.03	0.00085±1.27E-05	0.0131±0.0004	0.0820±0.0050	0.00078±1.15E-05	0.047±0.003	0.00509±0.0003	
14	365	0.0025±0.0007	0.082±0.003	0.099±0.005	1.89E-06±7.53E-07	1.00±0.05	1.037±0.03	0.00082±1.27E-05	0.0093±0.0003	0.0479±0.0032	0.00078±1.19E-05	0.045±0.003	0.00480±0.0003	
15	236	0.0019±0.0008	0.097±0.004	0.108±0.006	3.39E-06±1.23E-06	0.98±0.07	1.005±0.04	0.00083±1.50E-05	0.0110±0.0004	0.0522±0.0038	0.00078±1.39E-05	0.056±0.004	0.00603±0.0004	
16	844	0.0015±0.0003	0.062±0.002	0.050±0.002	1.99E-06±4.98E-07	0.96±0.04	0.971±0.02	0.00086±9.36E-06	0.0073±0.0002	0.0242±0.0015	0.00084±9.08E-06	0.042±0.002	0.00494±0.0002	
17	61	0.0121±0.0025	0.379±0.014	0.888±0.032	1.81E-05±5.57E-06	1.18±0.15	1.029±0.07	0.00155±4.12E-05	0.0809±0.0024	0.4299±0.0259	0.00088±3.81E-05	0.034±5.55E-05	0.00413±0.0003	
18	535	0.0020±0.0005	0.067±0.002	0.067±0.003	8.55E-06±1.25E-06	0.92±0.04	0.967±0.02	0.00076±9.93E-06	0.0071±0.0002	0.0323±0.0022	0.00074±9.49E-06	0.041±0.002	0.00422±0.0002	
19	406	0.0020±0.0006	0.073±0.003	0.076±0.004	1.82E-06±6.90E-07	1.08±0.06	0.993±0.03	0.00073±1.24E-05	0.0073±0.0003	0.0369±0.0026	0.00070±1.18E-05	0.044±0.003	0.00424±0.0003	
20	440	0.0030±0.0007	0.075±0.003	0.079±0.004	2.66E-06±7.69E-07	0.99±0.05	0.995±0.03	0.00066±9.29E-06	0.0068±0.0002	0.0380±0.0027	0.00063±8.78E-06	0.044±0.003	0.00388±0.0002	
21	322	0.0018±0.0006	0.060±0.003	0.050±0.003	2.13E-06±8.48E-07	1.01±0.06	0.964±0.03	0.00087±1.35E-05	0.0072±0.0003	0.0245±0.0020	0.00085±1.30E-05	0.040±0.003	0.00471±0.0003	
22	412	0.0010±0.0004	0.073±0.003	0.089±0.004	5.75E-13±7.66E-08	0.96±0.05	0.985±0.03	0.00081±1.12E-05	0.0081±0.0003	0.0431±0.0028	0.00078±1.06E-05	0.038±0.002	0.00408±0.0002	
23	428	0.0051±0.0008	0.116±0.003	0.199±0.006	4.78E-06±1.07E-06	1.03±0.05	1.000±0.03	0.00093±1.55E-05	0.0149±0.0004	0.0961±0.0055	0.00084±1.41E-05	0.040±3.50E-05	0.00463±1.46E-07	

Table 4.1 continued

<i>N</i>	<i>U</i> ($\mu\text{g/g}$) _a	$\frac{^{204}\text{Pb}}{^{206}\text{Pb}}$	$\frac{^{207}\text{Pb}}{^{206}\text{Pb}}$	$\frac{^{208}\text{Pb}}{^{206}\text{Pb}}$	$\frac{^{232}\text{Th}}{^{238}\text{U}}$	$\frac{^{230}\text{Th}}{^{238}\text{U}}$ act	$\frac{^{234}\text{U}}{^{238}\text{U}}$ act	$\frac{^{206}\text{Pb}}{^{238}\text{U}}$	$\frac{^{207}\text{Pb}}{^{235}\text{U}}$	<i>f8b</i>	$\frac{^{206}\text{Pb}}{^{238}\text{U}}$	$\frac{^{207}\text{Pb}}{^{206}\text{Pb}}$	$\frac{^{207}\text{Pb}}{^{235}\text{U}}$	
<i>common lead uncorrected</i>														
HD2074														
1	108	9.85E-09±0.0017	0.015±0.003	0.005±0.003	2.74E-07±8.65E-07	1.15±0.10	1.259±0.06	0.00045±1.47E-05	0.0009±0.0002	0.0025±2.25E-06	0.00045±1.47E-05	0.013±0.003	0.00077±0.0002	
2	201	0.0004±0.0014	0.024±0.003	0.017±0.004	2.42E-06±1.16E-06	1.50±0.09	1.281±0.04	0.00042±1.12E-05	0.0014±0.0002	0.0084±3.29E-06	0.00042±1.11E-05	0.017±0.003	0.00097±0.0002	
3	231	6.26E-09±0.0010	0.020±0.003	0.007±0.002	5.66E-07±5.45E-07	1.88±0.09	1.499±0.04	0.00032±8.71E-06	0.0009±0.0001	0.0033±1.35E-06	0.00032±8.58E-06	0.018±0.003	0.00078±0.0001	
4	113	0.0099±0.0037	0.297±0.020	0.608±0.040	5.80E-05±6.71E-06	2.78±0.16	2.407±0.08	0.00025±1.05E-05	0.0103±0.0008	0.2947±0.0006	0.00018±9.55E-06	0.072±0.033	0.00176±0.0008	
5	224	6.39E-09±0.0011	0.032±0.003	0.037±0.005	4.27E-06±1.38E-06	1.36±0.08	1.342±0.04	0.00036±9.62E-06	0.0016±0.0002	0.0177±6.85E-06	0.00035±9.40E-06	0.017±0.004	0.00083±0.0002	
6	106	3.64E-08±0.0060	0.016±0.010	0.027±0.015	3.51E-12±5.83E-07	2.03±0.14	1.416±0.06	0.00029±1.83E-05	0.0007±0.0004	0.0132±5.01E-05	0.00029±1.82E-05	0.005±0.010	0.00022±0.0004	
7	126	5.15E-08±0.0087	0.054±0.015	0.046±0.019	3.35E-12±4.10E-07	2.25±0.14	1.789±0.07	0.00021±1.58E-05	0.0016±0.0005	0.0225±8.80E-05	0.00021±1.56E-05	0.036±0.016	0.00104±0.0005	
8	38	0.0098±0.0245	0.044±0.028	0.074±0.043	9.87E-06±6.91E-06	3.86±0.31	2.863±0.15	0.00021±2.57E-05	0.0013±0.0008	0.0356±0.0004	0.00020±2.52E-05	0.015±0.029	0.00041±0.0008	
9	46	1.64E-07±0.0164	0.025±0.027	0.246±0.077	1.78E-06±3.67E-06	4.30±0.31	4.151±0.17	0.00018±2.31E-05	0.0006±0.0007	0.1191±0.0014	0.00015±2.14E-05	-0.085±0.032	-0.00181±-0.0007	
10	406	1.06E-08±0.0014	0.022±0.004	0.002±0.002	1.06E-06±7.07E-07	1.48±0.06	1.385±0.03	0.00031±1.09E-05	0.0009±0.0002	0.0008±9.94E-07	0.00031±1.08E-05	0.021±0.004	0.00090±0.0002	
11	356	1.15E-08±0.0015	0.020±0.004	0.024±0.006	2.04E-06±9.90E-07	1.72±0.07	1.438±0.03	0.00030±1.09E-05	0.0008±0.0002	0.0115±7.57E-06	0.00030±1.07E-05	0.010±0.004	0.00042±0.0002	
12	412	1.04E-08±0.0013	0.023±0.004	0.012±0.004	5.52E-07±4.86E-07	1.70±0.06	1.428±0.03	0.00024±8.33E-06	0.0008±0.0001	0.0058±3.58E-06	0.00024±8.21E-06	0.019±0.004	0.00062±0.0001	
13	247	2.18E-08±0.0021	0.027±0.006	0.026±0.008	1.50E-12±1.06E-07	2.21±0.09	1.905±0.05	0.00021±1.01E-05	0.0008±0.0002	0.0127±1.58E-05	0.00021±9.96E-06	0.017±0.006	0.00048±0.0002	
14	196	0.0023±0.0067	0.046±0.012	0.039±0.015	1.88E-12±1.63E-07	2.36±0.11	1.994±0.05	0.00012±8.55E-06	0.0008±0.0002	0.0190±5.63E-05	0.00012±8.43E-06	0.031±0.012	0.00052±0.0002	
15	76	1.35E-07±0.0131	0.128±0.036	0.162±0.053	4.91E-12±3.47E-07	3.30±0.20	2.831±0.10	0.00011±1.30E-05	0.0020±0.0006	0.0785±0.0007	0.00010±1.24E-05	0.068±0.039	0.00096±0.0006	
16	90	0.0264±0.0148	0.079±0.022	0.172±0.044	4.80E-12±2.40E-07	4.49±0.23	4.001±0.12	0.00017±1.70E-05	0.0019±0.0005	0.0833±0.0005	0.00016±1.60E-05	0.010±0.024	0.00022±0.0005	
17	17	0.0273±0.0353	0.197±0.071	0.803±0.221	8.80E-06±1.01E-05	4.21±0.50	6.280±0.34	0.00025±4.68E-05	0.0069±0.0028	0.3890±0.0118	0.00016±3.98E-05	-0.210±0.121	-0.00450±-0.0028	
18	225	0.0036±0.0024	0.035±0.006	0.029±0.007	6.01E-07±6.92E-07	1.90±0.09	1.552±0.04	0.00032±1.36E-05	0.0016±0.0003	0.0142±1.28E-05	0.00032±1.35E-05	0.024±0.006	0.00103±0.0003	
19	86	5.09E-080±.0025	0.059±0.013	0.099±0.024	5.33E-06±3.22E-06	2.08±0.15	1.867±0.08	0.00029±2.10E-05	0.0023±0.0006	0.0481±0.0001	0.00028±2.03E-05	0.019±0.014	0.00073±0.0005	

Table 4.1 continued

N	U ($\mu\text{g/g}$) ^a	$\frac{204}{206}\text{Pb}$	$\frac{207}{206}\text{Pb}$	$\frac{208}{206}\text{Pb}$	$\frac{232}{238}\text{Th}$	$\frac{230}{238}\text{Th}$ act	$\frac{234}{238}\text{U}$ act	$\frac{206}{238}\text{Pb}$	$\frac{207}{235}\text{Pb}$	f8b	$\frac{206}{238}\text{Pb}$	$\frac{207}{206}\text{Pb}$	$\frac{207}{235}\text{Pb}$
		common lead uncorrected						^{208}Pb corrected		^{208}Pb corrected		^{208}Pb corrected	
20	429	0.0006±0.0006	0.022±0.003	0.012±0.003	3.36E-07±3.36E-07	2.39±0.07	1.993±0.04	0.00028±9.04E-06	0.0009±0.0001	0.0056±2.55E-06	0.00028±8.90E-06	0.018±0.003	0.00069±0.0001
21	29	1.44E-07±0.0072	0.014±0.014	0.050±0.030	4.64E-06±5.34E-06	2.33±0.27	2.118±0.14	0.00029±3.46E-05	0.0006±0.0006	0.0244±0.0002	0.00028±3.41E-05	-0.006±0.015	-0.00024±-0.0006
22	17	0.0272±0.0196	0.122±0.039	0.265±0.083	1.75E-05±1.24E-05	3.75±0.44	3.685±0.24	0.00033±4.69E-05	0.0055±0.0019	0.1285±0.0016	0.00028±4.31E-05	0.017±0.046	0.00068±0.0018
23	111	0.0757±0.0372	0.359±0.074	0.724±0.145	5.03E-07±7.75E-07	2.40±0.15	6.412±0.12	3.38E-05±4.41E-06	0.0017±0.0004	0.3508±0.0052	0.00002±3.77E-06	0.102±0.116	0.00031±0.0004
24	16	0.1875±0.1252	0.344±0.147	0.859±0.303	1.15E-05±8.69E-06	4.04±0.51	5.702±0.30	8.47E-05±2.02E-05	0.0040±0.0020	0.4162±0.0220	0.00005±1.72E-05	-0.007±0.255	-0.00005±-0.0017
25	104	0.0061±0.0074	0.069±0.015	0.194±0.033	1.20E-06±1.04E-06	4.55±0.25	5.347±0.11	0.00013±9.57E-06	0.0013±0.0003	0.0941±0.0003	0.00012±8.95E-06	-0.011±0.017	-0.00018±-0.0003
26	93	0.0201±0.0143	0.190±0.033	0.480±0.074	6.22E-07±9.59E-07	4.83±0.24	5.040±0.12	8.54E-05±7.54E-06	0.0022±0.0004	0.2324±0.0014	0.00007±6.62E-06	-0.006±0.045	-0.00005±-0.0004
27	35	0.0449±0.0160	0.289±0.040	0.690±0.089	1.80E-06±2.19E-06	4.84±0.38	4.079±0.16	0.00027±2.27E-05	0.0106±0.0017	0.3341±0.0021	0.00018±1.95E-05	0.014±0.063	0.00035±0.0015
28	71	0.0142±0.0123	0.137±0.024	0.342±0.051	3.84E-07±1.22E-06	4.41±0.26	4.202±0.12	0.00016±1.22E-05	0.0031±0.0006	0.1654±0.0007	0.00013±1.10E-05	-0.001±0.029	-0.00002±-0.0005
29	109	0.0281±0.0074	0.117±0.014	0.205±0.026	6.69E-14±2.57E-10	4.20±0.20	3.900±0.10	0.00019±1.05E-05	0.0031±0.0004	0.0993±0.0002	0.00017±9.78E-06	0.037±0.016	0.00090±0.0004
30	27	0.0837±0.0162	0.567±0.050	1.402±0.119	2.97E-06±2.97E-06	3.58±0.35	3.532±0.18	0.00055±3.67E-05	0.0428±0.0048	0.6788±0.0044	0.00018±3.81E-05	-0.001±0.178	-0.00002±-0.0043
31	33	0.0222±0.0101	0.123±0.023	0.333±0.054	2.33E-06±2.33E-06	4.43±0.37	2.684±0.14	0.00028±2.40E-05	0.0048±0.0010	0.1614±0.0008	0.00024±2.16E-05	-0.014±0.028	-0.00045±-0.0009
32	85	0.0222±0.0065	0.094±0.012	0.186±0.025	9.23E-07±9.23E-07	3.17±0.20	2.952±0.09	0.00026±1.47E-05	0.0034±0.0005	0.0899±0.0002	0.00024±1.38E-05	0.021±0.014	0.00069±0.0005
33	27	0.0397±0.0136	0.189±0.029	0.430±0.064	2.51E-13±9.65E-10	2.77±0.31	2.319±0.15	0.00035±2.92E-05	0.0091±0.0016	0.2085±0.0011	0.00028±2.58E-05	0.018±0.039	0.00070±0.0015

a - U concentration is calculated as counts per second of ^{238}U in unknown divided by average counts per second of ^{238}U in the standard and multiplied by U concentration in the standard (assumed to be 800 $\mu\text{g/g}$).

b - Proportion of common Pb calculated using ^{208}Pb correction.

N.D - not determined.

The average $^{207}\text{Pb}/^{235}\text{U}$ age of the innermost opal is 10.5 ± 3.3 Ma (MSWD=1.4), if the two negative $^{207}\text{Pb}/^{235}\text{U}$ age analyses are excluded, and the common Pb is corrected assuming the modern Stacey-Kramers model lead composition. The average $^{206}\text{Pb}/^{238}\text{U}$ age is not much older, 13.7 ± 0.7 Ma (MSWD=3.8) although the difference is likely attributed to large amount of initial ^{234}U excess.

If the initial $^{234}\text{U}/^{238}\text{U}$ activity ratio, estimated as 5.74 ± 1.15 (Paces *et al.*, 2010) for the outer parts of opal coatings in the other Yucca Mountain samples, is assumed to be valid for the inner layers of opal, then $^{206}\text{Pb}/^{238}\text{U}$ ages corrected for the initial presence of ^{234}U can be calculated and the average of twelve corrected analyses is equal to 11.6 ± 0.7 Ma (MSWD=3.8). This later age is only slightly younger than the age of the host tuff, 12.8 Ma (Sawyer *et al.*, 1994), and is similar within the errors to the $^{207}\text{Pb}/^{235}\text{U}$ age discussed earlier, although the absolute values of $^{206}\text{Pb}/^{238}\text{U}$ ages calculated that way are still larger than $^{207}\text{Pb}/^{235}\text{U}$ ages. This suggests the possibility that the initial $^{234}\text{U}/^{238}\text{U}$ activity ratio for the inner coating of opal in this sample is larger than 7.37 ± 0.20 estimated for the outer parts of the coatings by Paces *et al.*, (2004a). Alternatively, the initial Pb composition in the sample has a larger proportion of ^{206}Pb than the assumed modern model Pb, which may be attributed to the slight gain of radon. The latter can be tested by the estimation of initial Pb composition from the common Pb uncorrected data obtained from the sample. As mentioned earlier, the ^{208}Pb is considered to be free of a radiogenic component and, therefore, the $^{208}\text{Pb}/^{204}\text{Pb}$ ratio in the initial Pb can be calculated as an average of measured $^{208}\text{Pb}/^{204}\text{Pb}$ ratios for four analyses of the inner coating. The initial $^{207}\text{Pb}/^{208}\text{Pb}$ and $^{206}\text{Pb}/^{208}\text{Pb}$ ratios can be obtained by the fitting line through fourteen analyses in the $^{235}\text{U}/^{208}\text{Pb}$ vs. $^{207}\text{Pb}/^{208}\text{Pb}$ and $^{238}\text{U}/^{208}\text{Pb}$ vs. $^{206}\text{Pb}/^{208}\text{Pb}$ coordinate systems respectively (Figure 4.10) giving $^{206}\text{Pb}/^{204}\text{Pb}$ of 25 ± 4 and $^{207}\text{Pb}/^{204}\text{Pb}$ of 17.0 ± 1.8 . An assumption of similar initial $^{234}\text{U}/^{238}\text{U}$ activity ratios in all samples is necessary for the $^{206}\text{Pb}/^{208}\text{Pb}$ calculation. The results indicate that the initial Pb is in fact enriched in ^{206}Pb compared to the model Pb. The average $^{207}\text{Pb}/^{235}\text{U}$ age calculated using this initial Pb composition is 9.0 ± 2.6 Ma (MSWD=0.9). The $^{206}\text{Pb}/^{238}\text{U}$ ages are still older (analyses are reverse discordant) with the average of 12.7 ± 0.7 Ma (MSWD=2.3). Even if analyses are corrected for the initial ^{234}U using data from Paces *et al.*, (2004a), the average $^{206}\text{Pb}/^{238}\text{U}$ age is 10.4 ± 0.7 Ma. An alternative option for the initial Pb correction is to use Pb isotope composition

obtained for Mn-oxides developed within the vein system of Yucca Mountain (Neymark and Amelin, 2008). Using $^{206}\text{Pb}/^{204}\text{Pb}$ of 18.24 ± 0.18 , $^{207}\text{Pb}/^{204}\text{Pb}$ of 15.589 ± 0.013 and $^{208}\text{Pb}/^{204}\text{Pb}$ of 39.132 ± 0.022 determined for the Mn-oxides results in the $^{207}\text{Pb}/^{235}\text{U}$ age of 11.8 ± 3.4 Ma and excess ^{234}U corrected $^{206}\text{Pb}/^{238}\text{U}$ age of 11.9 ± 0.7 Ma.

The above discussion highlights potential difficulties when calculating ages of the opals showing relative enrichment in the common Pb ($^{206}\text{Pb}/^{204}\text{Pb}$ ratios ~ 100). The significant correction for an unknown initial Pb composition has a strong impact on the confidence of $^{207}\text{Pb}/^{235}\text{U}$ age estimates. The age limits for the inner layer of silica developed in the sample HD2059 can be at best defined as 9.0 ± 2.6 to 11.8 ± 3.4 Ma, based on the three different kinds of assumptions regarding the composition of initial Pb. The $^{206}\text{Pb}/^{238}\text{U}$ ratios, which are less sensitive to the common Pb correction, have another inherited problem associated with the unknown quantity of initial ^{234}U incorporated by the opal during its growth. Correction for this initial ^{234}U , using $^{234}\text{U}/^{238}\text{U}$ initial activity ratios obtained from the other samples, consistently results in the $^{206}\text{Pb}/^{238}\text{U}$ ages that are older than $^{207}\text{Pb}/^{235}\text{U}$ ages. This indicates the possibility that the $^{234}\text{U}/^{238}\text{U}$ initial activity ratio was larger at the time of formation of opal's inner layers compared to the more recent depositions of silica.

In spite of all the indicated uncertainties, it is evident that the inner part of the coating was formed between 9 and 14 Ma and the $^{207}\text{Pb}/^{235}\text{U}$ age of 11.8 ± 3.4 Ma obtained by correcting data using the Pb composition of Mn-oxides is included in this range. Therefore, this age was taken as the best current estimate of the time of opal precipitation near the base of the sample.

The next stratigraphic layer of silica (central part of the coating) is represented by thin (~100-200 microns) veinlets developed over the inner layer of calcite crystals (Figure 4.11). A total of eighteen spots were analysed within this layer (Table 4.1). The uranium concentration varies from 19 to 184 $\mu\text{g/g}$ with an average uranium concentration of 92 $\mu\text{g/g}$. This is a significantly increased concentration of uranium compared to the inner part of the coating, which has a range between 5 and 24 $\mu\text{g/g}$ and an average of 12.7 $\mu\text{g/g}$.

The spots targeted three veinlets; 8 spots concentrated in a veinlet 1, 4 spots concentrated in a separate veinlet (veinlet 2) and 6 concentrated in another separate veinlet (veinlet 3). The veinlets are separated into two groups based on their thickness and location within the mineral coating. The two thinner veinlets (veinlet 1 and 2) are treated as one group and the thicker vein (veinlet 3) is a separate group as it is closer to the base of the coating.

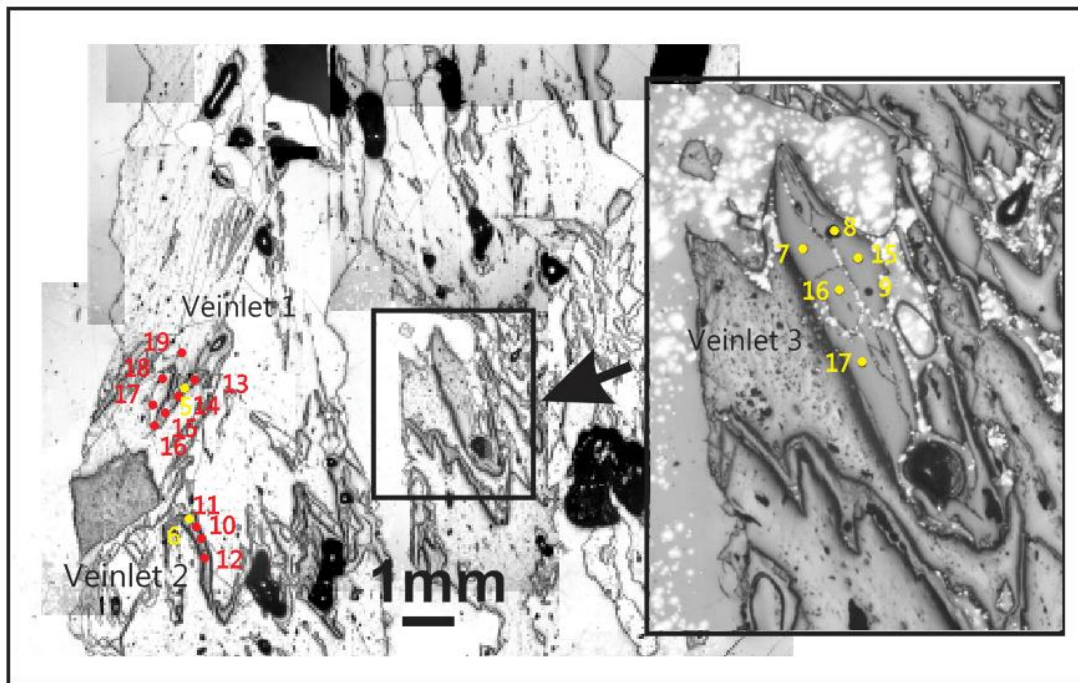


Figure 4.11 Central part of the coating showing the location of the three veinlets and analyses in each of the veinlets. Yellow spots in are from day 1 and red spots are from day 2.

This central part of the coating shows a much smaller proportion of common lead compared to the inner coating. In fact, the amount of ^{204}Pb appears to be so small that it is most likely not being measured properly. Therefore, care needs to be taken with the ^{204}Pb correction. However, there is very little difference between the ^{204}Pb and the ^{208}Pb corrections and if our standard assumption that all ^{208}Pb is common (considering that ^{232}Th is also not existent) then we can estimate $^{206}\text{Pb}/^{204}\text{Pb}$ from $^{206}\text{Pb}/^{208}\text{Pb}$, and assuming modern Stacey-Kramers model common Pb, the ratio will vary from about 500 to about 8000 (with 75% of analysed spots above 1500). This makes the calculation of U/Pb* less sensitive to the common Pb correction and, therefore, $^{207}\text{Pb}/^{235}\text{U}$ should be considered as a best estimate of age.

The $^{207}\text{Pb}/^{235}\text{U}$ ages of the thinner veinlets (veinlets 1 and 2) range from 2.2 ± 1.8 Ma to 5.6 ± 0.74 Ma and have an average age of 5.1 ± 0.4 Ma if corrected using the modern model Pb composition. The thicker vein (veinlet 3) has an age range of 6.0 ± 0.3 Ma to 7.5 ± 0.5 Ma and an average age of 7.1 ± 0.5 Ma. The thicker vein is significantly older than the other veins and so it can be proposed that initial precipitation would have occurred in the thicker veins and then progresses to the thinner veins. This vein is also significantly closer to the base of the opal coating and this is reflected in the older age.

The concordia diagram (Figure 4.12) shows the three veinlets comprising the central coating in different colours (red ellipses denote veinlet 1, blue ellipses denote veinlet 2 and green ellipses denote veinlet 3) and clearly shows all spots sitting above the concordia line suggesting an excess of ^{206}Pb (i.e. excess initial ^{234}U). It also shows that there is a range of ages within each vein.

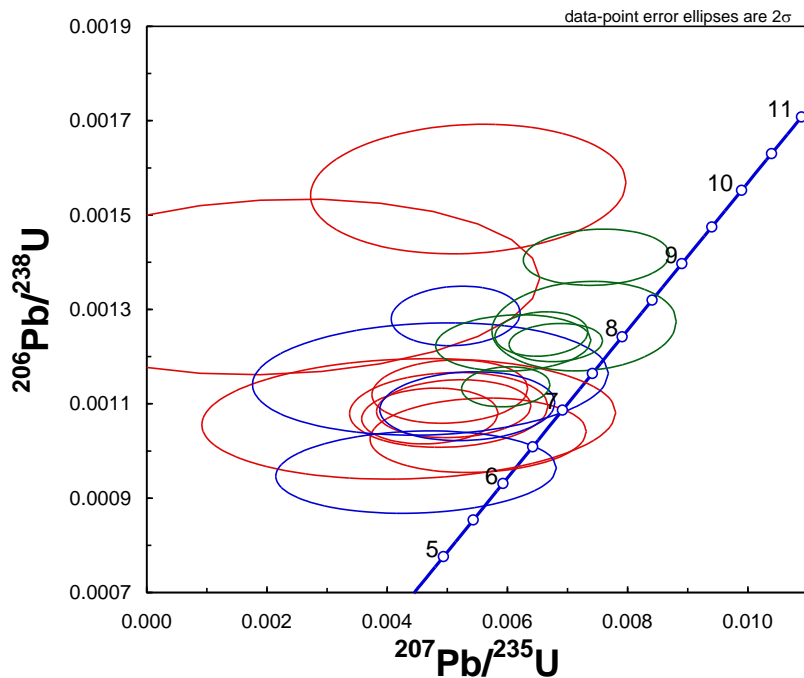


Figure 4.12 The $^{206}\text{Pb}/^{238}\text{U}$ vs. $^{207}\text{Pb}/^{235}\text{U}$ concordia plot of the central veins. Red ellipses denote veinlet 1; blue ellipses denote veinlet 2; green ellipses denote veinlet 3.

Figure 4.13 shows the same concordia but with $^{206}\text{Pb}/^{238}\text{U}$ ratios corrected for the initial $^{234}\text{U}/^{238}\text{U}$ activity ratio as estimated by Paces *et al.*, (2004a). It shows that the

position of all analyses remain the same respective to each other but are shifted down, suggesting that the initial $^{234}\text{U}/^{238}\text{U}$ activity ratio does not significantly change over a period of 10 Ma during opal precipitation.

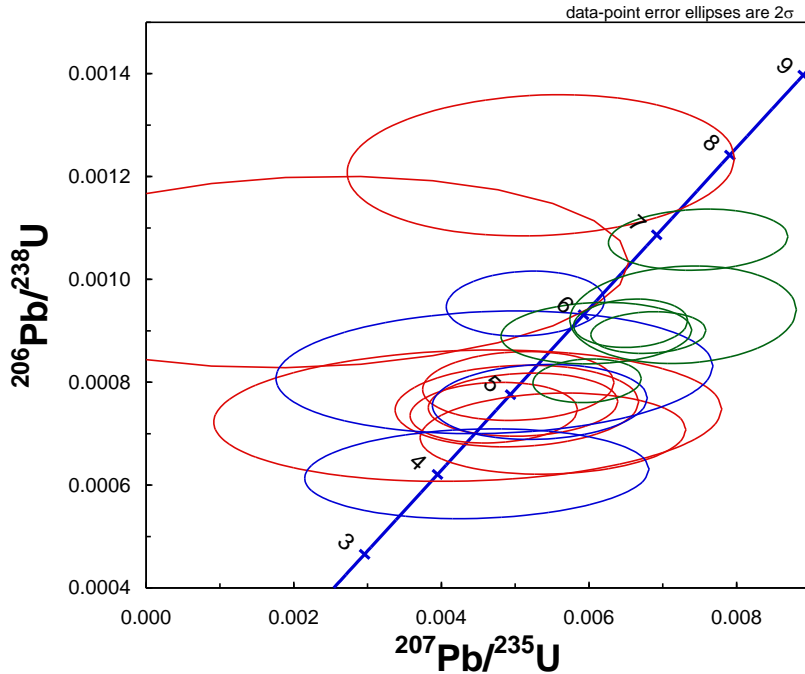


Figure 4.13 The $^{206}\text{Pb}/^{238}\text{U}$ vs. $^{207}\text{Pb}/^{235}\text{U}$ concordia plot of the central veins corrected for the initial $^{234}\text{U}/^{238}\text{U}$ activity ratio as estimated by Paces *et al.*, (2004a). Red ellipses denote veinlet 1; blue ellipses denote veinlet 2; green ellipses denote veinlet 3.

Sixteen analyses, forming three profiles across outermost layer of silica (~1 mm) indicate a variable degree of disequilibrium (Figure 4.9, Table 4.1 and 4.2), which is correlated with the distance of the analytical spots from the surface of coating. The analysed areas are relatively young reducing the applicability of $^{207}\text{Pb}/^{235}\text{U}$ ages. The average age calculated on the basis of $^{207}\text{Pb}/^{235}\text{U}$ ratios is 0.42 ± 0.12 Ma (MSWD=0.5) which is very similar to the $^{207}\text{Pb}/^{235}\text{U}$ TIMS age of 0.34 ± 0.04 Ma determined by Neymark *et al.*, (2000a, 2002). On the other hand, the coating is too old to make use of ^{230}Th ages. As a result of relatively large errors of SHRIMP analysis in general and in the described run, the data points cannot be reliably separated from the equilibrium line in the $^{234}\text{U}/^{238}\text{U}$ activity vs. $^{230}\text{Th}/^{238}\text{U}$ activity coordinate system. This means that the most appropriate way to calculate ages is to use measured $^{206}\text{Pb}/^{238}\text{U}$ and $^{234}\text{U}/^{238}\text{U}$ ratios. This approach allows calculating both age and initial activity of $^{234}\text{U}/^{238}\text{U}$. The potential problem in using this system is

once again, the unknown composition of initial Pb. The calculated $^{206}\text{Pb}/^{238}\text{U}$ ages change systematically from 397 ± 14 kyr to 1012 ± 39 kyr and are systematically older than $^{207}\text{Pb}/^{235}\text{U}$ ages even though the errors in the latter are very large and the former is calculated with the ^{234}U taken into account. An average initial $^{234}\text{U}/^{238}\text{U}$ activity ratio is equal to 9.2 ± 0.6 (MSWD=2) when calculated on the basis of observed $^{234}\text{U}/^{238}\text{U}$ and $^{206}\text{Pb}/^{238}\text{U}$ ratios or 11.1 ± 2.6 (MSWD=0.45) based on $^{207}\text{Pb}/^{235}\text{U}$ ages and the observed $^{206}\text{Pb}/^{238}\text{U}$ ratios. Both are larger than 7.37 ± 0.20 estimated by Paces *et al.*, (2004a). The use of Pb composition of Mn-oxides discussed earlier for the initial Pb correction does not result in any significant difference in calculated ages or activities.

The growth rate for the outer coating has been calculated to be 1.08 ± 0.41 mm per Ma. Two outlier spots were excluded in the rate calculation.

4.7.2 HD2019a

HD2019a is a calcite and silica coating from Yucca Mountain and has been also described by Neymark *et al.*, (2002). Their isotope dilution results suggest that the age of subsamples located at ~4 - 5 mm beneath the top of the coatings have ages ranging between 3.9 ± 0.03 Ma to 4.71 ± 0.05 Ma, whereas the older ages of 5.95 ± 0.05 and 7.67 ± 0.25 Ma are observed closer to the base of the coatings.

SHRIMP analysis of 19 spots (Table 4.1 and 4.2) within the strongly fluorescent area situated ~4 mm from the outermost surface (Figure 4.14) show common-Pb corrected $^{207}\text{Pb}/^{235}\text{U}$ ages (assuming modern Stacey-Kramers model common-Pb) ranging from 3.70 ± 0.24 to 6.10 ± 0.41 Ma with an average of 4.43 ± 0.27 Ma (MSWD=5.4). Despite the slight scatter of analyses, which is evident from the high MSWD, no systematic change in the ages correlated with the stratigraphy can be established. The $^{206}\text{Pb}/^{238}\text{U}$ ages estimated for these analytical spots, with the exception of three, are older than $^{207}\text{Pb}/^{235}\text{U}$ ages (reversely discordant points on the concordia diagram, consistent with initial excess of ^{234}U). However, if the $^{206}\text{Pb}/^{238}\text{U}$ ratios are calculated with an assumption of initial $^{234}\text{U}/^{238}\text{U}$ activity ratio of 7.37 ± 0.20 (Paces *et al.*, 2004a), the points become discordant on the concordia diagram, suggesting overcorrection for initial ^{234}U . The initial $^{234}\text{U}/^{238}\text{U}$ activity ratios calculated using $^{206}\text{Pb}/^{238}\text{U}$ ratios in combination with the $^{207}\text{Pb}/^{235}\text{U}$ ages vary

between 1.7 ± 0.6 and 5.6 ± 1.2 , with the most of analyses giving values between 2 and 4 (Figure 4.14) and an overall average for 16 reversely discordant points of 2.92 ± 0.47 (MSWD=1.6).

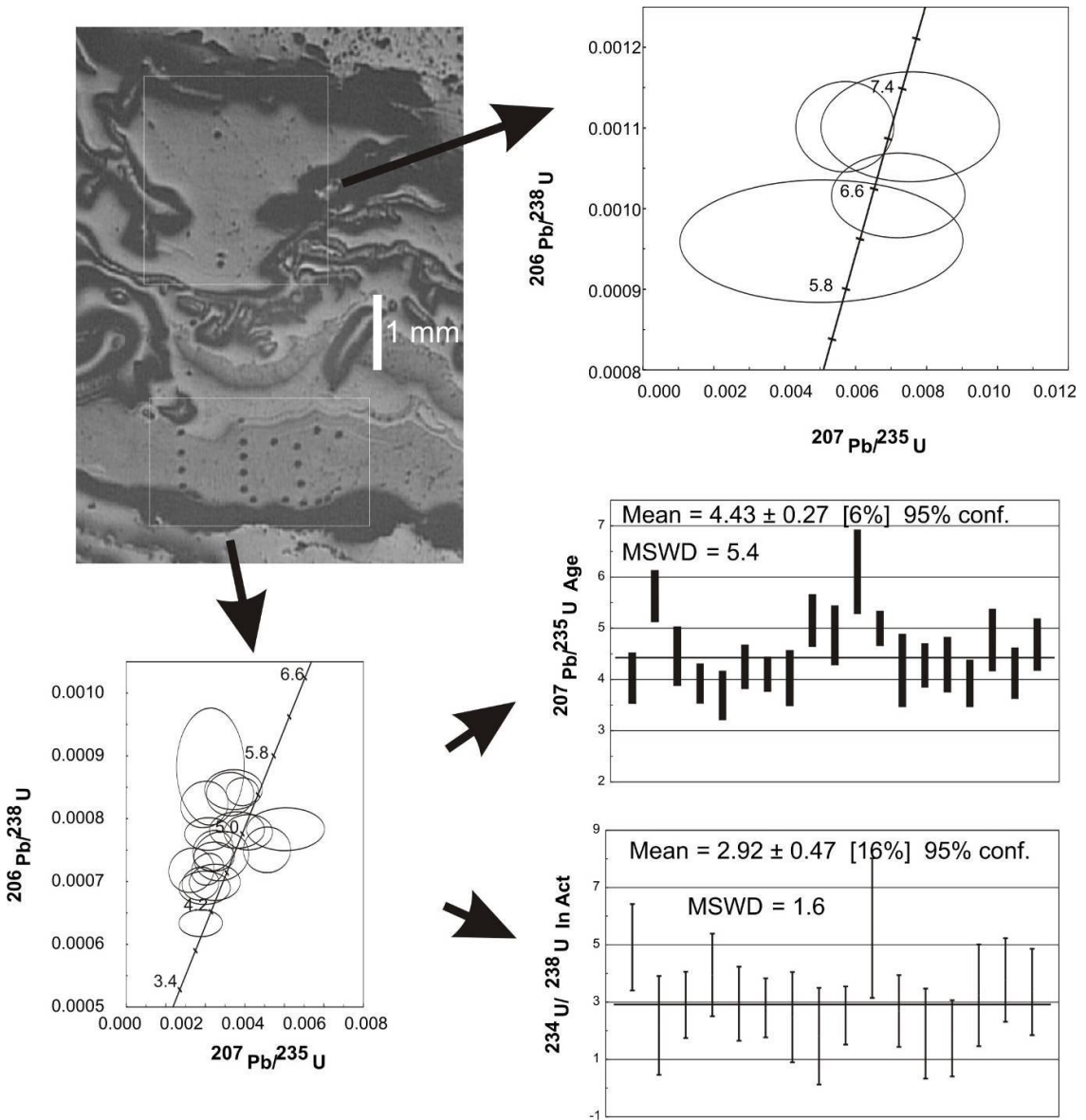


Figure 4.14 SHRIMP data for sample HD2019a; also showing a close-up of analysed areas.

$^{207}\text{Pb}/^{235}\text{U}$ ages do not deviate outside the errors, if initial Pb is corrected using composition determined from the Mn-oxides, formed early during secondary mineral formation at Yucca Mountain, with opal within the coatings, as opposed to the modern model common Pb. The $^{207}\text{Pb}/^{235}\text{U}$ age calculated by fitting the line through the data that are not corrected for the common Pb in $^{207}\text{Pb}/^{208}\text{Pb}$ vs. $^{235}\text{U}/^{208}\text{Pb}$

coordinate system is 4.07 ± 0.33 Ma (MSWD=2.4). This age is also indistinguishable from the modern Pb corrected average of $^{207}\text{Pb}/^{235}\text{U}$ ages.

Four additional analyses have been made within the part of the coating situated 1-2 mm closer to the base (Figure 4.14). The average $^{207}\text{Pb}/^{235}\text{U}$ age for these four analyses is 6.4 ± 1.6 Ma (age determined by the line in $^{207}\text{Pb}/^{208}\text{Pb}$ vs. $^{235}\text{U}/^{208}\text{Pb}$ coordinates is 8.8 ± 3.8 Ma; MSWD=0.5). This area has relatively low U concentration, which resulted in large uncertainties, specifically in $^{207}\text{Pb}/^{235}\text{U}$ ratios and apparent concordance of all analyses within the error.

The growth rate as calculated from $^{207}\text{Pb}/^{235}\text{U}$ ages of the 23 spots and the stratigraphic position of the analytical spots is 0.63 ± 0.45 mm/Ma.

4.7.3 HD2074

Sample HD2074 is opal from a 1 to 4 cm thick mineral coating on the floor of a large lithophysal cavity 270 m below land surface, where opal hemispheres are present on the tips of thin calcite blades and range from 1 to 2 mm in diameter. The outermost ~1 mm thick opal growths, have been described by Paces *et al.*, (2004a), Neymark *et al.*, (2002) and Paces *et al.*, (2001).

Paces *et al.*, (2004a) previously analysed this sample by two methods of in situ isotope analysis; SHRIMP-RG (Sensitive High Resolution Ion Microprobe – Reverse Geometry) and by microdigestion-TIMS analysis. Two 1 mm diameter opal hemispheres (HD2074-g1 and HD2074-g2) were analysed using SHRIMP-RG with 7 and 10 spots across the outer 305 and 740 μm of the two opal hemispheres, respectively. $^{230}\text{Th}/\text{U}$ dates calculated for the SHRIMP-RG spots range from 34.4 ± 8.8 to $560^{\text{infinity}}/_{-300}$ ka (Paces *et al.*, 2004a), however, large errors are present for spots older than 200-300 ka due to large uncertainties in the measured $^{230}\text{Th}/^{238}\text{U}$ activity ratio and the reduced dating resolution as the $^{230}\text{Th}/\text{U}$ age approaches about five half lives of ^{230}Th . For spots with $^{230}\text{Th}/\text{U}$ ages older than 200 ka, $^{234}\text{U}/^{238}\text{U}$ ages were calculated to be between 277 and 1430 ka by assuming that the initial $^{234}\text{U}/^{238}\text{U}$ AR value determined on the youngest spots remained constant through time (Paces *et al.*, 2004a). Growth rates using both, $^{230}\text{Th}/\text{U}$ and $^{234}\text{U}/^{238}\text{U}$ ages,

were determined to be 0.58 ± 18 mm/Ma (HD2074-g1) and 0.69 ± 0.07 mm/Ma (HD2074-g2).

The microdigestion of opal equalling 2 to 4 μm per analysis followed by TIMS analysis resulted in $^{230}\text{Th}/\text{U}$ dates ranging from 4.0 ± 1.9 to 37.1 ± 2.3 kyr. Eight sequential microdigestions on HD2074-g2 displayed a growth rate of 0.68 ± 22 mm/Ma (Paces *et al.*, 2004a).

In this study, thirty three spots were analysed on a hemisphere from HD2074 forming five profiles of various lengths across the hemisphere perpendicular to the layering (Figure 4.15). The uranium concentration in this sample varies between 17 and 429 $\mu\text{g/g}$. Additional analyses for this hemisphere, obtained in this study, include Pb isotopes which allows the calculation of $^{206}\text{Pb}/^{238}\text{U}$ ages corrected for initial excess of $^{234}\text{U}/^{238}\text{U}$ as well as initial $^{234}\text{U}/^{238}\text{U}$ activity ratio. Such calculation can be done using measured $^{234}\text{U}/^{238}\text{U}$ or $^{230}\text{Th}/^{238}\text{U}$ ratio. Both ways give $^{206}\text{Pb}/^{238}\text{U}$ ages indistinguishable within the errors. The $^{230}\text{Th}/^{238}\text{U}$ ages calculated for the outermost third of hemisphere are as young as 48 ± 7 kyr (spot 23, which is the outermost spot, Table 4.2). These ages appear to be similar to the $^{238}\text{U}-^{234}\text{U}-^{206}\text{Pb}$ ages. Both indicate comparable growth rate when plotted against the distance from the surface of hemisphere. The $^{206}\text{Pb}/^{238}\text{U}$ ages can be compared to the $^{207}\text{Pb}/^{235}\text{U}$ ages for the inner two thirds of sample and are also similar within the errors, although the precision in the latter is very poor. The $^{206}\text{Pb}/^{238}\text{U}$ ages for the inner hemisphere range show the oldest age to be 2906 ± 186 kyr.

The growth rate calculated for the outermost third of the hemisphere based on the $^{230}\text{Th}/^{238}\text{U}$ ages and the stratigraphic position of the analytical spots is equal to 0.78 ± 0.14 mm/Ma. Combining all of the $^{206}\text{Pb}/^{238}\text{U}$ ages and plotting them as a function of distance from the surface of hemisphere results in a line characterising the hemisphere's growth rate (Figure 4.15). This growth rate is estimated as 0.99 ± 0.08 mm/Ma (the slope of the line in Figure 4.15). The intercept of this line with the age axis (point where value for the distance is zero) indicates an age when the last layer within the hemisphere was formed. This age is estimated as 82 ± 23 kyr.

The initial $^{234}\text{U}/^{238}\text{U}$ activity ratios for the individual spots can be calculated using either measured $^{234}\text{U}/^{238}\text{U}$ or measured $^{230}\text{Th}/^{238}\text{U}$ ratios and the corresponding

$^{206}\text{Pb}/^{238}\text{U}$ ages. Both ways give results indistinguishable within the errors. The average initial $^{234}\text{U}/^{238}\text{U}$ activity for the outer part of the hemisphere calculated on the basis of measured $^{234}\text{U}/^{238}\text{U}$ and $^{206}\text{Pb}/^{238}\text{U}$ ages is 7.37 ± 0.28 (MSWD=1.3) which is identical to the 7.37 ± 0.20 value of Paces *et al.*, (2004a), obtained for the same area, however, the inner part of hemisphere shows smaller initial $^{234}\text{U}/^{238}\text{U}$ activity ratios with an average of 4.99 ± 0.44 (MSWD=3.5).

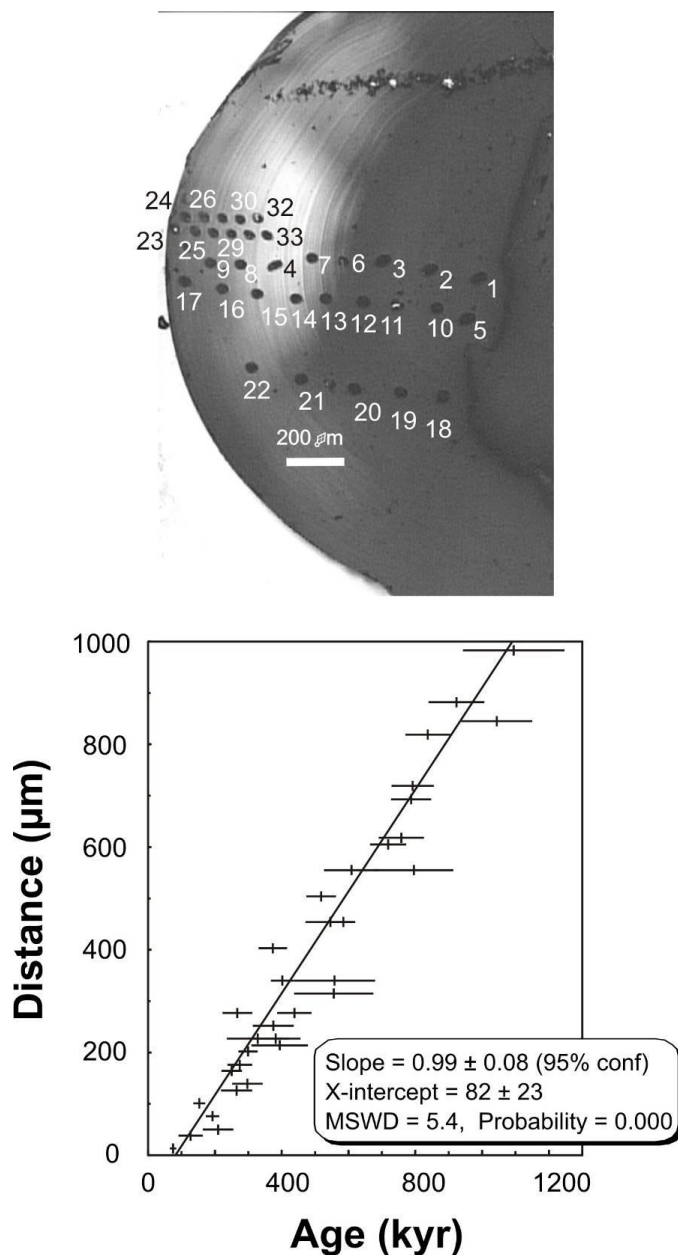


Figure 4.15 Polished cross section of an opal hemisphere from sample HD2074, showing thin, concentric layering. SHRIMP results are shown as a distance vs. age plot.

Table 4.2 SHRIMP results for opal samples from Yucca Mountain (ages in kyr and initial $^{234}\text{U}/^{238}\text{U}$, errors are 2σ).

<i>N</i>	$\frac{^{206}\text{Pb}}{^{238}\text{U}}$ Age	$\frac{^{207}\text{Pb}}{^{235}\text{U}}$ Age	$\frac{^{234}\text{U}}{^{238}\text{U}}$ Init*	Age($^{238}\text{U}-^{234}\text{U}-^{230}\text{Th}$)	$\frac{^{234}\text{U}}{^{238}\text{U}}$ Init**	Age($^{238}\text{U}-^{234}\text{U}-^{206}\text{Pb}$)	Age($^{238}\text{U}-^{230}\text{Th}-^{206}\text{Pb}$)	$\frac{^{234}\text{U}}{^{238}\text{U}}$ Init***
HD2059								
Inner part of the coating (Day 1)								
10	14880±1265	15115±16224	ND	ND	ND	ND	ND	ND
11	14357±727	9757±4077	13.0±11.7	ND	ND	ND	ND	ND
12	14696±955	8590±5804	17.3±16.7	ND	ND	ND	ND	ND
13	14029±864	12452±7335	4.5±20.9	ND	ND	ND	ND	ND
14	18216±1516	-13023±13480	ND	ND	ND	ND	ND	ND
Inner part of the coating (Day 2)								
1	13701±1625	19159±20774	ND	ND	ND	ND	ND	ND
2	14902±1352	13914±13884	2.8±39.5	ND	ND	ND	ND	ND
3	13153±1165	8041±12087	14.5±34.4	ND	ND	ND	ND	ND
4	11308±1243	3213±14467	23.0±30.8	ND	ND	ND	ND	ND
5	12390±1370	26157±14826	ND	ND	ND	ND	ND	ND
6	13842±1123	2379±10795	32.5±30.8	ND	ND	ND	ND	ND
7	13285±1607	25223±13971	ND	ND	ND	ND	ND	ND
8	11918±1283	5156±17024	19.2±48.4	ND	ND	ND	ND	ND
9	16816±2471	-11693±-41795	ND	ND	ND	ND	ND	ND
Central part of the coating (Day 1)								
5	10018±723	5417±2166	13.0±6.5	ND	ND	ND	ND	ND
6	8286±332	5206±887	8.7±2.7	ND	ND	ND	ND	ND
7	9086±314	7566±1001	4.3±3.0	ND	ND	ND	ND	ND

Table 4.2 continued

<i>N</i>	$\frac{^{206}Pb}{^{238}U} Age$	$\frac{^{207}Pb}{^{235}U} Age$	$\frac{^{234}U}{^{238}U} Init^*$	<i>Age</i> ($^{238}U - ^{234}U - ^{230}Th$)	$\frac{^{234}U}{^{238}U} Init^{**}$	<i>Age</i> ($^{238}U - ^{234}U - ^{206}Pb$)	<i>Age</i> ($^{238}U - ^{230}Th - ^{206}Pb$)	$\frac{^{234}U}{^{238}U} Init^{***}$
8	8040±248	6646±637	3.9±1.9	ND	ND	ND	ND	ND
9	8147±499	7361±1264	2.2±3.9	ND	ND	ND	ND	ND
15	7319±224	6048±607	3.6±1.8	ND	ND	ND	ND	ND
16	7916±314	6174±1066	4.9±3.2	ND	ND	ND	ND	ND
17	7923±214	6887±642	2.9±1.9	ND	ND	ND	ND	ND
Central part of the coating (Day 2)								
10	6155±460	4540±1928	4.6±5.6	ND	ND	ND	ND	ND
11	7055±383	5401±1202	4.7±3.6	ND	ND	ND	ND	ND
12	7425±627	4781±2445	7.5±7.2	ND	ND	ND	ND	ND
13	7254±353	5107±1069	6.1±3.2	ND	ND	ND	ND	ND
14	7020±322	5173±1060	5.2±3.1	ND	ND	ND	ND	ND
15	6920±310	4771±936	6.1±2.8	ND	ND	ND	ND	ND
16	7003±417	5089±1362	5.4±4.0	ND	ND	ND	ND	ND
17	6657±415	5583±1485	3.0±4.4	ND	ND	ND	ND	ND
18	6882±673	4416±2844	7.0±8.3	ND	ND	ND	ND	ND
19	8682±981	2174±3637	18.5±10.7	ND	ND	ND	ND	ND
Outer part of the coating (Day 1)								
1	3232±178	492±416	13.4±9.7	ND	ND	720±44	703±59	10.1±1.5
2	2557±128	583±411	9.1±5.2	304±112	3.8±0.8	645±35	689±53	8.4±1.0
3	2335±190	265±908	18.3±76.6	298±150	5.6±1.8	504±40	537±66	9.3±1.2
4	1934±158	-794±694	ND	264±102	6.9±1.6	397±28	425±54	9.6±0.9

Table 4.2 continued

<i>N</i>	$\frac{^{206}Pb}{^{238}U} Age$	$\frac{^{207}Pb}{^{235}U} Age$	$\frac{^{234}U}{^{238}U} Init^*$	<i>Age</i> ($^{238}U - ^{234}U - ^{230}Th$)	$\frac{^{234}U}{^{238}U} Init^{**}$	<i>Age</i> ($^{238}U - ^{234}U - ^{206}Pb$)	<i>Age</i> ($^{238}U - ^{230}Th - ^{206}Pb$)	$\frac{^{234}U}{^{238}U} Init^{***}$
18	2506±199	-858±833	ND	277±105	6.6±1.5	471±36	506±54	10.7±1.3
19	2614±238	344±771	15.2±36.6	596±1399	10.0±35.2	572±54	571±72	9.4±1.7
20	3406±226	749±540	10.4±4.9	476±698	4.5±6.6	808±64	823±94	9.9±2.1
21	3762±188	503±520	15.5±13.2	281±157	2.1±0.4	1012±79	1105±136	9.7±2.6
Outer part of the coating (Day 2)								
22	11718±1464	-11±991	ND	ND	ND	955±95	949±177	34.9±10.7
23	1954±232	155±431	31.8±133.1	ND	ND	502±63	447±88	7.7±1.6
24	3879±530	504±1093	15.9±28.4	ND	ND	856±186	674±138	11.1±7.0
25	4367±545	103±1974	135.7±4326.8	170±124	3.9±0.9	709±125	858±206	14.1±6.2
26	2164±156	303±256	14.4±14.2	ND	ND	634±61	596±73	7.1±1.5
27	3007±257	626±411	10.3±5.1	391±530	3.3±3.2	813±94	842±141	8.6±2.7
28	3756±290	345±326	21.9±21.8	ND	ND	901±94	811±110	10.4±3.3
29	4608±370	531±717	18.3±19.2	474±1285	3.6±8.8	997±156	1015±168	12.4±6.8
HD2019								
1	7154±297	5811±1157	5.0±3.4	ND	ND	ND	ND	ND
2	7153±362	7687±2103	ND	ND	ND	ND	ND	ND
3	6601±279	7344±1575	ND	ND	ND	ND	ND	ND
4	6233±403	5141±3336	4.3±9.5	ND	ND	ND	ND	ND
5	5344±197	4064±501	4.8±1.5	ND	ND	ND	ND	ND
6	4874±193	5676±1023	ND	ND	ND	ND	ND	ND

Table 4.2 continued

<i>N</i>	$\frac{^{206}Pb}{^{238}U} Age$	$\frac{^{207}Pb}{^{235}U} Age$	$\frac{^{234}U}{^{238}U} Init^*$	<i>Age</i> ($^{238}U - ^{234}U - ^{230}Th$)	$\frac{^{234}U}{^{238}U} Init^{**}$	<i>Age</i> ($^{238}U - ^{234}U - ^{206}Pb$)	<i>Age</i> ($^{238}U - ^{230}Th - ^{206}Pb$)	$\frac{^{234}U}{^{238}U} Init^{***}$
7	4809±209	4499±580	2.1±1.7	ND	ND	ND	ND	ND
8	4524±139	3960±389	2.8±1.2	ND	ND	ND	ND	ND
9	4662±187	3727±479	3.9±1.5	ND	ND	ND	ND	ND
10	4866±171	4286±429	2.8±1.3	ND	ND	ND	ND	ND
11	4673±134	4145±342	2.7±1.0	ND	ND	ND	ND	ND
12	4481±140	4069±545	2.4±1.6	ND	ND	ND	ND	ND
13	5056±150	5194±514	0.8±1.5	ND	ND	ND	ND	ND
14	5079±154	4903±583	1.7±1.7	ND	ND	ND	ND	ND
15	5087±181	6154±825	ND	ND	ND	ND	ND	ND
16	5474±118	5041±342	2.4±1.0	ND	ND	ND	ND	ND
17	5735±495	4217±714	5.5±2.5	ND	ND	ND	ND	ND
18	4804±123	4314±431	2.6±1.3	ND	ND	ND	ND	ND
19	4538±154	4330±539	1.8±1.6	ND	ND	ND	ND	ND
20	4115±114	3966±461	1.6±1.3	ND	ND	ND	ND	ND
21	5497±169	4813±611	3.1±1.8	ND	ND	ND	ND	ND
22	5038±137	4164±503	3.7±1.5	ND	ND	ND	ND	ND
23	5451±183	4725±1023	3.2±2.9	ND	ND	ND	ND	ND
	ND							
	HD2074							
1	2906±186	790±406	8.4±3.0	218±131	1.5±0.2	1094±159	ND	6.8±3.6
2	2717±138	990±378	6.6±1.8	ND	ND	1044±109	984±120	6.4±2.4

Table 4.2 continued

<i>N</i>	$\frac{^{206}Pb}{^{238}U} Age$	$\frac{^{207}Pb}{^{235}U} Age$	$\frac{^{234}U}{^{238}U} Init^*$	<i>Age</i> ($^{238}U - ^{234}U - ^{230}Th$)	$\frac{^{234}U}{^{238}U} Init^{**}$	<i>Age</i> ($^{238}U - ^{234}U - ^{206}Pb$)	<i>Age</i> ($^{238}U - ^{230}Th - ^{206}Pb$)	$\frac{^{234}U}{^{238}U} Init^{***}$
3	2078±108	795±251	5.6±1.5	ND	ND	787±60	737±70	5.7±1.1
4	1148±89	1796±1015	-0.6±2.9	351±209	4.8±2.1	402±34	409±51	5.4±0.6
5	2305±117	851±379	6.0±2.1	299±175	1.8±0.3	923±85	1008±144	5.7±1.6
6	1885±229	221±862	18.5±95.9	ND	ND	796±120	665±104	5.0±1.8
7	1353±195	1062±923	2.2±3.1	ND	ND	546±75	520±86	4.7±1.0
8	1294±312	418±1709	5.9±25.7	ND	ND	382±75	353±91	6.5±1.5
9	1002±239	-1852±2118	ND	220±84	6.9±1.2	265±47	279±72	7.7±1.1
10	2002±135	919±317	4.7±1.5	380±246	2.1±0.7	838±68	875±91	5.1±1.0
11	1930±132	426±349	8.9±7.2	ND	ND	792±63	760±70	5.1±1.0
12	1559±101	630±265	4.8±1.9	ND	ND	719±54	687±61	4.3±0.7
13	1345±125	493±380	5.2±4.1	434±308	4.1±2.5	518±45	525±57	4.9±0.6
14	787±106	528±434	2.5±2.7	486±480	4.9±5.1	373±43	363±54	3.9±0.5
15	662±146	979±1068	0.3±3.2	339±199	5.8±2.4	267±45	254±61	4.9±0.7
16	1029±188	230±1229	9.5±68.2	273±95	7.5±1.5	274±37	275±53	7.5±0.9
17	1009±301	-4614±8322	ND	101±38	8.0±0.9	210±47	284±105	10.6±1.8
18	2050±167	1052±546	4.3±2.1	ND	ND	758±68	725±76	5.7±1.2
19	1789±248	749±1224	4.9±7.1	352±300	3.4±1.8	609±83	637±110	5.9±1.5
20	1817±109	701±268	5.3±1.8	552±511	5.7±6.7	584±33	586±41	6.2±0.6
21	1811±430	-241±1436	ND	307±325	3.7±2.2	558±123	594±173	6.4±2.4
22	1851±478	696±4098	5.4±27.5	215±135	5.9±1.6	394±85	444±133	9.2±2.5
23	143±30	317±596	0.5±2.8	48±7	7.2±0.4	75±10	101±28	7.7±0.5

Table 4.2 continued

<i>N</i>	$\frac{^{206}Pb}{^{238}U}$ Age	$\frac{^{207}Pb}{^{235}U}$ Age	$\frac{^{234}U}{^{238}U}$ Init*	Age($^{238}U - ^{234}U - ^{230}Th$)	$\frac{^{234}U}{^{238}U}$ Init**	Age($^{238}U - ^{234}U - ^{206}Pb$)	Age($^{238}U - ^{230}Th - ^{206}Pb$)	$\frac{^{234}U}{^{238}U}$ Init***
24	321±119	-48±3674	ND	127±61	7.0±1.1	127±37	127±65	7.0±1.4
25	784±104	-179±684	ND	130±26	7.9±0.5	193±20	226±38	9.2±0.8
26	426±63	-54±887	ND	197±49	7.7±0.7	153±18	138±26	7.0±0.6
27	1148±164	359±2940	6.1±57.2	426±515	10.6±13.0	297±46	281±57	7.6±1.4
28	876±115	-24±1217	ND	251±98	7.2±1.4	250±31	250±43	7.2±0.9
29	1133±112	918±797	2.0±2.8	267±92	6.9±1.2	299±29	307±39	7.5±0.8
30	1141±390	-19±5947	ND	264±196	5.8±2.1	328±94	343±121	6.8±2.0
31	1545±230	-462±2232	ND	629±2258	15.4±90.3	375±62	359±71	8.0±1.8
32	1552±161	707±1013	4.3±5.9	367±284	5.8±3.4	438±52	447±63	6.8±1.2
33	1799±256	718±3060	5.1±19.0	ND	ND	556±123	529±120	6.4±2.7

* Initial activity ratio calculated from $^{207}Pb/^{235}U$ disequilibrium age and measured $^{206}Pb/^{238}U$ or $^{234}U/^{238}U$ assuming closed behaviour.

** Calculated from measured $^{230}Th/^{238}U$ and $^{234}U/^{238}U$ activity ratios

*** Calculated from measured $^{206}Pb/^{238}U$ and $^{234}U/^{238}U$.

ND, not determined.

Correction for initial Pb using the composition obtained for the Mn-oxides does not result in any significant change in Pb/U ratios. The difference in $^{206}\text{Pb}/^{238}\text{U}$ ages for most of analyses is about 1 kyr with a few analyses where the change is about 3-5 kyr and only one where it is 18 kyr (or 5% which is significantly smaller than the analytical error). The resulting difference in the $^{207}\text{Pb}/^{235}\text{U}$ ages is also about 10 times smaller than the analytical errors.

4.8 Discussion

4.8.1 Summary of SHRIMP opal chronology

The overall apparent consistency of ages determined with various ^{238}U - ^{234}U - ^{230}Th - ^{206}Pb - ^{235}U - ^{207}Pb chronometers in a number of samples with the ages varying from tens of thousands years to ~12 million years confirms that SHRIMP can be used to date U-rich opals of various ages. Samples younger than ~300 kyr can be dated using ^{238}U - ^{234}U - ^{230}Th relationships which are free of potential problems associated with disequilibrium present at the time of opal formation. Low Th concentrations in opals eliminates the necessity to correct for initial ^{230}Th while an estimate of initial ^{234}U is a by-product of the age calculation. While ~300 kyr is the limit for the application of ^{238}U - ^{234}U - ^{230}Th system in Yucca Mountain opals, which in general show relatively high U concentrations (>50 ppm), other opals having lower concentrations or lower initial $^{234}\text{U}/^{238}\text{U}$ may be reduced due to smaller ^{234}U and ^{238}Th beam intensities with larger analytical uncertainties.

The chronology of older opals involves either ^{206}Pb or ^{207}Pb and, therefore, requires initial Pb, ^{234}U and loss-gain of other intermediate daughters to be taken into account. The ^{235}U - ^{207}Pb system appears to be unaffected by the loss or gain of intermediate daughters. The only long lived isotope in the ^{235}U decay chain is ^{231}Pa . The geochemical behaviour of Pa is considered to be similar to that of Th (e.g. Bourdon *et al.*, 2003) and, therefore, it is likely to be insoluble under near surface conditions. This leaves the uncertainty in initial Pb composition as the major source of possible inaccurate estimate of desired age. However, as illustrated by the sample HD2059, the certainty and accuracy of ^{235}U - ^{207}Pb ages reduces significantly with increasing proportion of common Pb and decreasing age of samples.

4.8.2 Observed age discordance

Further insights into behaviour of ^{238}U - ^{234}U - ^{230}Th - ^{206}Pb - ^{235}U - ^{207}Pb can be made by studying samples where comparison can be made between the results of ^{238}U - ^{234}U - ^{206}Pb and ^{235}U - ^{207}Pb or ^{238}U - ^{234}U - ^{206}Pb and ^{238}U - ^{234}U - ^{230}Th systems.

The ^{238}U - ^{234}U - ^{206}Pb and ^{238}U - ^{234}U - ^{230}Th systems can be compared in the outermost part of sample HD2074. As mentioned earlier, both have been determined to have similar opal growth rates and the ages are similar within 2σ errors. Detailed investigation however, reveals that nine out of twelve points (Figure 4.16) have slightly older ^{238}U - ^{234}U - ^{206}Pb ages (four outside the 1 sigma error). The observed difference is hardly detectable at the levels of precision produced by this method. Nevertheless, the difference is not correlated with either the U concentration (proportional to the observed number of counts of ^{238}U) or proportion of common Pb or of ^{234}U / ^{238}U ratio, suggesting a possibility of slight disequilibrium (i.e. gain) of ^{238}U daughters after the ^{230}Th . There is no difference above the errors between ^{238}U - ^{234}U - ^{206}Pb and ^{235}U - ^{207}Pb ages in the inner part of the same sample.

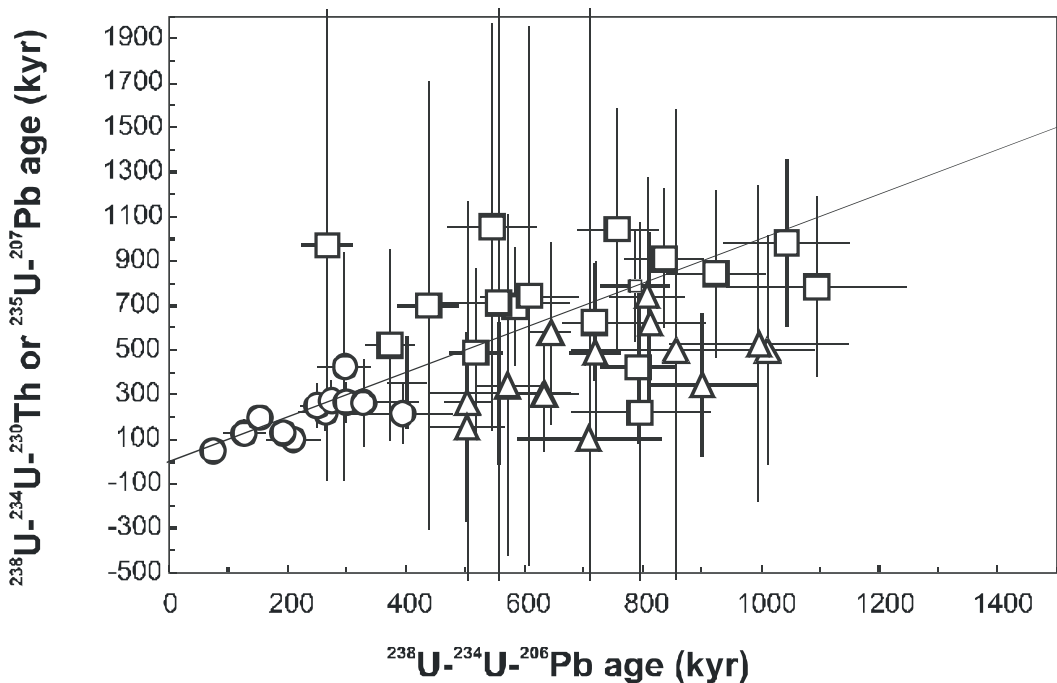


Figure 4.16 SHRIMP analyses within the samples HD2074 and HD2059 for the areas, where ^{234}U is not equilibrated with ^{238}U . Circles correspond to the outermost analyses of hemisphere (sample HD2074, ^{238}U - ^{234}U - ^{230}Th age is plotted against the ^{238}U - ^{234}U - ^{206}Pb age); squares are the inner parts of the same hemisphere (^{235}U - ^{207}Pb age is plotted against the ^{238}U - ^{234}U - ^{206}Pb age); triangles are the outer opal coating of sample HD2059 (^{235}U - ^{207}Pb age is plotted against the ^{238}U - ^{234}U - ^{206}Pb age).

Despite the fact that the discussed differences are hardly recognisable above the errors, the ^{238}U - ^{234}U - ^{206}Pb and ^{238}U - ^{230}Th - ^{206}Pb ages appear to be slightly older than corresponding ^{235}U - ^{207}Pb or ^{238}U - ^{234}U - ^{230}Th ages. In addition ^{238}U - ^{206}Pb ages in all analysed spots greater than 1 Ma are older than corresponding ^{235}U - ^{207}Pb ages. A discordance pattern observed in the series of samples, including three analysed in this study, was discussed by Neymark *et al.*, (2000a, 2002). These authors recognized the general discordance pattern $\text{T}(\text{U}-\text{Pb}) > \text{T}(\text{U}-\text{Pb}) > \text{T}(\text{U}-\text{Th}-\text{Pb}) > \text{T}(\text{U}-\text{Th}-\text{Pb})$ when samples were analysed using TIMS. They explained this pattern in terms of slow continuous growth model, where opal deposited at uniform rate accumulates U and its decay products. As a result of such deposition, each sub-sample analysed with TIMS represents a mixture of multi-age materials. Such mixture is expected to show older ages for a system based on the isotopes with the longer half-lives. A SHRIMP spot is significantly smaller than sub-samples used in TIMS analysis and is expected to represent smaller range of ages within the model of Neymark *et al.*, (2000a). Therefore, the age discordance between the different systems is also predicted to be smaller. In fact, relationships observed by Neymark *et al.*, (2000a) are not visible in the SHRIMP analyses, probably due to discordance not exceeding the analytical errors. Considering that the estimated deposition rates are in the range of 0.7-1 mm/Ma and an average size of a SHRIMP spot is ~20-30 μm , the area covered by the spot corresponds to the deposition interval of about 20-40 kyr. Any difference between discussed systems will be insignificant as illustrated by Figure 7 in Neymark *et al.*, (2000a). As a result of relatively large SHRIMP errors, comparison of ^{235}U - ^{207}Pb and ^{238}U - ^{234}U - ^{230}Th ages is impossible. However, as opposed to the samples analysed with TIMS, results of this study indicate that $\text{T}(\text{U}-\text{Pb}) = \text{T}(\text{U}-\text{Th}-\text{Pb}) > \text{T}(\text{U}-\text{Th}-\text{Pb})$ and $\text{T}(\text{U}-\text{Pb}) = \text{T}(\text{U}-\text{Th}-\text{Pb}) > \text{T}(\text{U}-\text{Pb})$. This observed pattern indicates that at the SHRIMP spot scale, slow continuous growth of opal has no detectable impact on the relationships between U and its daughters and that the potential excess of ^{206}Pb , which is not supported by in-situ decay of ^{238}U and ^{234}U , becomes a feature controlling these relations. The simplest interpretation of this excess is presence of ^{222}Rn in the groundwater or in the gas phase migrating through the unsaturated zone. Opal precipitating from such groundwater may have incorporated insoluble products of ^{222}Rn decay, increasing observed $^{206}\text{Pb}/^{238}\text{U}$ ratios. If this interpretation is correct, an attempt can be made to place limits for the Rn

impact on the U-Pb system and resulting ages. Defining these limits is important, since Pashenko and Dublyansky (2002a; 2002b; 2006) and Dublyansky *et al.*, (2003) argued that U-Pb ages of Yucca Mountain opals could be significantly overestimated as a result of ignoring Rn contribution.

4.8.3 Deposition rates

Average continuous deposition rates for opal at Yucca Mountain have previously been determined to range between 0.1 and 5.0 mm/Ma (Paces *et al.*, 1996; Neymark *et al.*, 1998; Neymark and Paces, 2000; Paces *et al.*, 2001; Neymark *et al.*, 2002 and Neymark and Amelin, 2008) indicating extremely slow and uniform long term deposition. Deposition rates calculated in this chapter are within this range.

Initial calculated deposition rate for HD2059 was 2.60 ± 0.09 mm/Ma (Neymark *et al.*, 2002). This growth rate was calculated using TIMS data from three analyses representing the inner, central and outer sections of the hemisphere (Neymark *et al.*, 2002). A slower growth rate of 1.54 ± 0.10 mm/Ma was calculated by Paces *et al.*, (2010) using $^{230}\text{Th}/\text{U}$ and model $^{234}\text{U}/^{238}\text{U}$ ages from SHRIMP analyses. This rate is in excellent agreement with deposition rate of 1.08 ± 0.41 mm/Ma calculated for HD2059 in this research. Both rates (Paces *et al.*, 2010 and this research) were calculated from the outermost ~ 400 μm of sample HD2059.

The growth rate of 0.63 ± 0.45 mm/Ma was calculated for HD2019 based on $^{207}\text{Pb}/^{235}\text{U}$ ages of the 23 spots and the stratigraphic position of the analytical spots. This rate is slower than the rate calculated by Neymark *et al.*, (2002) of 1.31 ± 0.44 mm/Ma, using $^{207}\text{Pb}/^{235}\text{U}$ ages from TIMS analyses, however, only a few layers of opal were analysed to produce this rate.

Initial calculations of the growth rate for samples HD2074 using $^{207}\text{Pb}/^{235}\text{U}$ ages derived from TIMS data resulted in a rate of 5.1 ± 0.8 mm/Ma (Neymark *et al.*, 2002). Significantly slower growth rates of 0.58 ± 0.18 mm/Ma and 0.69 ± 0.07 mm/Ma were calculated for the outermost section of the hemisphere using $^{230}\text{Th}/\text{U}$ and $^{234}\text{U}/^{238}\text{U}$ model ages from SHRIMP data and 0.68 ± 0.22 mm/Ma for TIMS data (Paces *et al.*, 2004a). These rates are similar to the growth rate of 0.78 ± 0.14 mm/Ma determined

in this study based on the $^{230}\text{Th}/^{238}\text{U}$ ages for the outermost third of the hemisphere for HD2074.

The growth rate defining the complete traverse of the HD2074 hemisphere is 0.99 ± 0.08 mm/Ma based on $^{206}\text{Pb}/^{238}\text{U}$ ages and is similar to the 0.906 ± 0.088 mm/Ma growth rate calculated by Paces *et al.*, (2010) for the outermost 800 μm hemisphere using $^{230}\text{Th}/\text{U}$ and model $^{234}\text{U}/^{238}\text{U}$ ages from SHIMP data. The growth rates appear to show a decrease from the innermost to outermost layers of the opal, however, more data is required to confirm this trend.

This slow and uniform deposition rate is a result of an increasingly arid climate with low precipitation limiting the supply of water and dissolved silica to the deposition site in the unsaturated zone. Water supplied to the unsaturated zone is further reduced by runoff and down slope diversions at contacts between different rock types, evaporation and upward flux of shallow fracture water and long percolation times to the unsaturated zone. The water is limited to seepage through fracture pathways and despite major changes in surface moisture and shallow infiltration, slow and uniform deposition rates suggest that mineral deposition in the unsaturated zone was buffered from large changes in percolation flux by these limitations. Within the unsaturated zone the reduction of deep fracture flux by evaporation and imbibitions, and liquid vapour exchange (evaporation, CO_2 loss) in open cavities contribute to this long term hydrologic stability that existed over the past 10 Ma despite significant climate variations (Paces *et al.*, 1996; Neymark *et al.*, 1998; Neymark and Paces, 2000; Paces *et al.*, 2001; Neymark *et al.*, 2002 and Neymark and Amelin, 2008).

4.9 Conclusions

The $\text{U}-^{234}\text{U}-^{230}\text{Th}-^{206}\text{Pb}-^{235}\text{U}-^{207}\text{Pb}$ SHRIMP analyses of three samples from the Yucca Mountain show an excellent agreement with the published TIMS analyses (e.g. Neymark *et al.*, 2000a, 2002), supporting the applicability of ion probes to the dating of opaline silica with the ages ranging from several thousand to several million years. Ages change systematically and correlate with the internal stratigraphy of analysed samples.

In spite of larger errors as compared to the TIMS analysis, SHRIMP gives a significant gain in the spatial resolution. One of the outcomes of this increase in the spatial resolution is the apparent absence of discordance between the ages calculated using different pairs of isotopes within the decay chains. This discordance was noted by Neymark *et al.*, (2000a) in the larger sub-samples used for the TIMS and interpreted to be a result of slow continuous growth of opal.

Discordance patterns of SHRIMP data is characterised by systematic differences such that $T(^{238}\text{U}-^{234}\text{U}-^{206}\text{Pb})=T(^{238}\text{U}-^{230}\text{Th}-^{206}\text{Pb})>T(^{238}\text{U}-^{234}\text{U}-^{230}\text{Th})$ and $T(^{238}\text{U}-^{234}\text{U}-^{206}\text{Pb})=T(^{238}\text{U}-^{230}\text{Th}-^{206}\text{Pb})>T(^{235}\text{U}-^{207}\text{Pb})$ in the younger opal samples, where the ^{234}U is not in secular equilibrium with ^{238}U . In the older samples where this equilibrium is reached $T(^{238}\text{U}-^{206}\text{Pb})$ is older than $T(^{235}\text{U}-^{207}\text{Pb})$. Both confirm an initial excess of ^{234}U discussed in the previous studies. In addition, $T(^{238}\text{U}-^{234}\text{U}-^{206}\text{Pb})$ which are marginally older than both $T(^{238}\text{U}-^{234}\text{U}-^{230}\text{Th})$ and $T(^{235}\text{U}-^{207}\text{Pb})$ support initial presence of nuclides after ^{230}Th , such as ^{222}Rn . However, the estimated contribution of this excess to the total ^{206}Pb , appears to be relatively small and cannot increase calculated ^{206}Pb - ^{238}U ages by more than ~20-100 kyr. Therefore, ^{206}Pb - ^{238}U ages are accurate within these limits even if the contribution from isotopes such as ^{222}Rn is not taken into account. Since an impact of intermediate decay products on $^{235}\text{U}-^{207}\text{Pb}$ system is expected to be significantly smaller, than those in the ^{206}Pb - ^{238}U chain, $^{235}\text{U}-^{207}\text{Pb}$ ages can place accurate timing constraints on the relatively older microstratigraphically deeper parts of analysed opal samples.

Both TIMS and ion probe data show a change in age of opal consistent with the deposition sequence from the base to the top of the coating. Multiple analyses made along the profiles in the outermost opal layer indicate a decrease of $^{238}\text{U}-^{234}\text{U}-^{206}\text{Pb}$ ages consistent with deposition order and enable estimation of opal deposition rates close to 1 mm/Ma for this layer. This rate is confirmed by the analysis of other Yucca Mountain samples (Paces *et al.*, 2004a; 2010) where the youngest identified opal forming hemispheres capping calcite crystals shows $^{238}\text{U}-^{234}\text{U}-^{230}\text{Th}$ and $^{238}\text{U}-^{234}\text{U}-^{206}\text{Pb}$ ages suggesting uninterrupted growth during the last million years with a similar rate of about 1 mm/Ma. This very slow growth of secondary hydrogenic minerals over a long time interval of about 10 Ma was used to argue for precipitation in water unsaturated rocks above the water table and ultimately hydrological stability of the site and its suitability for the radioactive waste repository (Neymark *et al.*,

2000a; Paces *et al.*, 2004a; 2010). The slow opal growth also allowed high spatial resolution investigation of U variations across the growth zones, which was found to exhibit periodicity linked to the major cycling of Earth's orbital and rotational parameters defining the cycle of long term climate variations (Paces *et al.*, 2010).

5 OPAL FROM RIVER VALLEY CALCRETES IN THE YILGARN CRATON, WESTERN AUSTRALIA

5.1 Introduction

The silicification process has played a significant role in the evolution of the deeply weathered profile in Australia, particularly within the Yilgarn Craton, Western Australia. Several distinct types of silica-rich materials are recognized in the Yilgarn Craton and characteristic differences include their habit, origin and time of formation (Anand and Paine, 2002). The chronological constraints of the weathering profile in the Yilgarn Craton have been based on geological observations of cross-cutting relationships and, so far, there has been no attempt to determine the absolute age of silicification events. The most recent geologically distinct silicification event in the regolith of the Yilgarn Craton is the formation of opaline silica veins in river valley (groundwater) calcretes (Anand and Paine, 2002). These veins are temporally distinct from the other types of silicification found within the Craton, such as silcretes and hardpans.

This chapter discusses U-series ages of silica-filled cavities and veins within river valley calcretes from Yalgoo, situated in the northern Yilgarn Craton (Figure 5.1). The ^{230}Th - ^{234}U - ^{238}U ages (U-series ages) from two samples of opaline silica veins that cross-cut the calcrete matrix have been investigated by Sensitive High Resolution Ion Microprobe (SHRIMP) in order to determine the timing of the silicification event in the area and to investigate opal growth rates during most of the late Pleistocene.

5.2 Location and geological setting of samples

The two samples discussed in this chapter, Yalgoola Well and Nangcarrong Spring, are from locations close to the town of Yalgoo, which lies within the Yalgoo-Singleton Greenstone Belt in the Murchison Domain which is part of the Youanmi Terrane in the Yilgarn Craton, Western Australia (Figure 5.1).

5.2.1 Precambrian Geology

The Yilgarn Craton is a large Archean granite-greenstone terrain consisting of mafic and felsic metavolcanics and metasedimentary rocks, granites and granitic gneisses. It is divided into four tectonic units – Narryer Terrane, South West Terrane, Eastern Goldfields Super-terrane and the Youanmi Terrane which is subsequently divided into the Murchison Domain and Southern Cross Domain.

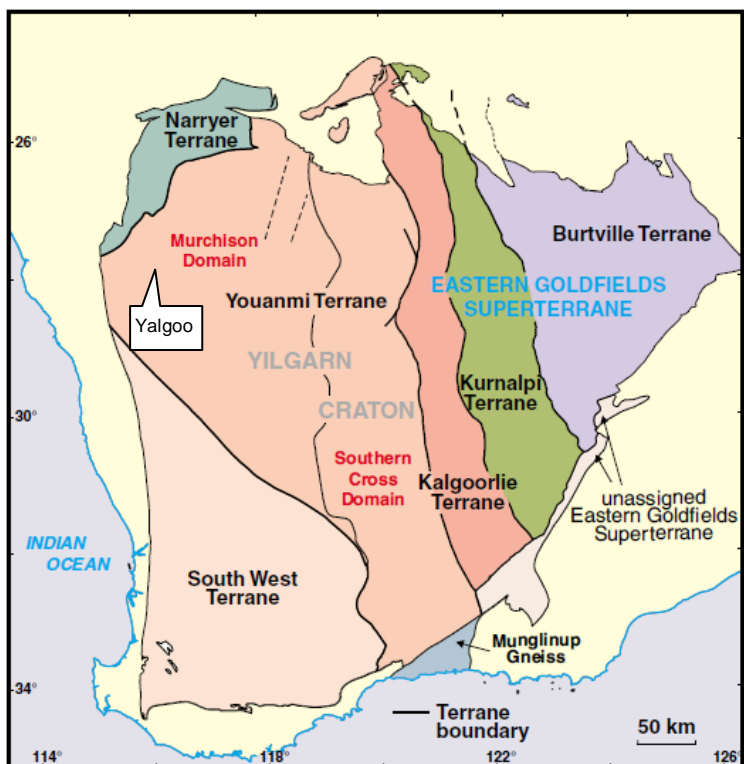


Figure 5.1 Tectonic division of the Yilgarn Craton, showing subdivision into terranes and showing the location of Yalgoo (modified from Cassidy *et al.*, 2006).

The Murchison Domain comprises a series of northwest trending elongated greenstone belts intruded by granite plutons and separated by large areas of massive to gneissic granitoids. The eruption of the first widespread greenstone and associated granites was at 2.95 Ga, predominantly in the southern Murchison Domain, followed by a 110 Ma hiatus in magmatism. A series of nearly continuous magmatic events occurred between 2820 Ma to 2600 Ma, resulting in a thick autochthonous greenstone succession and widespread crustal growth (Van Kranendonk *et al.*, 2013).

The greenstones of the Murchison Domain are dominated by metamorphosed mafic rocks but include metamorphosed ultramafic, sedimentary, and volcanic sequences

that vary in abundance and character from belt to belt. Greenstone rocks range in age from 2950 Ma to 2700 Ma (Van Krandendonk and Ivanic, 2009).

Granitic rocks in the Murchison Domain are dominated by monzogranites, including porphyritic, banded, and even-grained varieties, showing variable degrees of recrystallization and foliation development (Spaggiari, 2006). Most of the granitic rocks of the Murchison Domain appear to have formed between c. 2750 and 2610 Ma (Schiøtte and Campbell, 1996; Mueller *et al.*, 1996 Wiedenbeck and Watkins, 1993; Pidgeon and Hallberg, 2000; Champion and Cassidy, 2002; Spaggiari, 2006) although some granitic plutons have ages of c. 2800 Ma (Van Kranendonk *et al.*, 2013).

Metamorphic grades for the Murchison Domain range from lower prehnite-pumpellyite to granulite facies, however, most rocks are at greenschist or lower amphibolite facies (Van Kranendonk *et al.*, 2013).

The Yalgoo-Singleton Greenstone Belt is bounded to the north, east and west by granitic rocks dominated by biotite monzogranite. The major rock types in the Yalgoo-Singleton Greenstone Belt are ultramafic rocks, mafic rocks (mainly high-Mg basalts but also olivine adcumulates and orthocumulates, ultramafic cumulates from layered sills and undifferentiated ultramafic schists), felsic volcanic rocks, granitoids, Proterozoic dykes and sedimentary rocks consisting of graphitic shale, polymictic conglomerate and banded iron formation, overlain by Tertiary to Recent aged rocks. The northern part of the belt is composed of a south-plunging anticline (Noongal Anticline) containing mafic rocks and interbedded banded iron formation and is extensively intruded by granitoids.

Mineral assemblages suggest that pressure and temperature conditions peaked at lower amphibolite facies with localised areas metamorphosed to middle or upper amphibolite facies (Watkins and Hickman, 1990). Contact metamorphism is evident up to 800 m from the contact with granitic rocks and these zones are typified by dark coloured amphiboles, however, a widespread occurrence of andalusite in sedimentary rocks up to 4 km from the granite contact, suggests that the affected area is much greater (Muhling and Low, 1977).

It is inferred that the uranium in the opaline silica investigated in this study originates from local granites. As the granite weathers and is eroded, uranium is released based on the fact that uranium within the calcretes is acquired through shallow groundwater flowing through the granite (Mann and Horwitz, 1979).

5.2.2 Permian and Cainozoic rocks

Permian rocks in the Yalgoo area are mainly formations of sandstones, shales, siltstones and limestone and the aggregate thickness of these formations may exceed 2000 m in some areas (Muhling and Low, 1977). The base of the Permian sequence is the Nangetty Formation which is composed of tillite, shale, tillitic sandstone and poorly sorted conglomerate. It is conformably overlain by the Holmwood Shale, which is mainly grey-green shale and siltstone with thin beds of limestone. The Fossil Cliff Formation is a sequence of interbedded richly fossiliferous limestone, siltstone and shale, conformably overlain by the High Cliff Sandstone, which shows bedding and cross bedding in quartz sandstones, pebble conglomerates and thin beds of siltstone, indicative of a beach deposit. Conformably overlying this formation is the Irwin River Coal Measure, which is a sequence of interbedded sandstone, conglomerate, siltstone, carbonaceous claystone and intercalated lenses of coal. The Carynginia Formation overlies the Irwin River Coal Measure, and comprises micaceous siltstone and shale with interbedded sandstone and minor conglomerate and overlain by the white, fine to medium grained clayey sandstone of the Wagina Sandstone.

Cainozoic regolith types present in the Yalgoo area include the Victoria Plateau sandstone, sandplain units, laterite, chalcedony, colluvium, hardpans, calcretes and eolian sands. They are the product of erosion, weathering and sedimentation and are often representative of the underlying bedrock. The Victoria Plateau sandstone consists of poorly sorted sandstone with minor siltstone and conglomerate. It is flat lying and rests with angular unconformity on Permian rocks (Muhling and Low, 1977). The sandplain units are either red-brown sands that occur as isolated gently sloping remnants in topographically high areas and overlie laterite or weathered rock, or as yellow sand with iron gravel and patches of colluvial quartz-feldspar sand. This latter sand plain overlies surfaces of weathered granite. Laterite occurs as

massive or pisolithic rock composed of iron oxides and quartz and overlies weathered rocks.

Chalcedony can be variations of red, white or brown in colour and occurs on top of weathered ultramafic rocks and more specifically weathered tremolite or tremolite-chlorite rocks (Muhling and Low, 1977). The colluvial units are commonly derived from erosion of the sand plain units and form sloping areas between sandplain areas and drainages. These units include grit, which is poorly bedded coarse sand mixed with iron gravel and generally occurs over weathered granitic rock, hardpan, calcrete and eolian sands. The hardpan is dark red-brown to pale red-brown indurated and poorly bedded deposits of sand, silt and clay with minor lenses of gravel, and merges downslope into calcrete in some main drainages. The fine eolian sands form either irregular deposits over other colluvial deposits or layers and dunes over hardpan on the edge of saline lakes and drainages.

Salt lake chains are remnants of palaeodrainages or ancient river systems that were last active during the early Tertiary, although abnormally high rainfall can temporarily rejuvenate these drainages in the present time (Muhling and Low, 1977).

5.2.3 Timing of regolith development

Absolute ages of many regolith units cannot be determined, therefore, we rely on the understanding of regolith as a product of climate processes for classification and as an interpretation of their age. The following summary provides a broad stratigraphy for the regolith of Western Australia as well as major trends in the climate since the Late Mesozoic.

Western Australia's undulating duricrust surface, as well as the formation of ferricrete and silcrete in the interior of Western Australia was well developed by the Late Cretaceous to the Palaeocene (c. 95–55 Ma) (Van de Graaff *et al.*, 1977; Jackson and van de Graaff, 1981). Inland drainage systems, including chains of playa lakes were also active (Hocking *et al.*, 2001). During the Palaeocene through to the Eocene (c. 60–35 Ma) the climate varied between moist and temperate, to tropical with warmer and wetter condition compared to the present (Churchill, 1973). The sea level was 300 metres above present day (Hocking *et al.*, 2001) and rain-

bearing westerly winds from the Indian Ocean penetrated deep in to the continental interior ensuring active major drainages.

By the latest Eocene (~35 Ma) Hocking *et al.*, (2001) suggested that Western Australia was beginning to dry out and that major drainages in the interior had stopped flowing regularly. Eocene deposits in palaeovalleys were dominated by fluvial, estuarine, marine and lacustrine sediments (Clarke, 1993). Two main facies have been recognized, a sand facies sequence (Wollubar Sandstone), which represents fluvial basal units, and a clay facies sequence (Perkolilli Shale) (Kern and Commander, 1993). After the deposition of the sand facies a major change in either climate or sea-level occurred causing drying out of Western Australia and the deposition of a thick clay in lacustrine or swampy shallow environments (Anand and Paine, 2002).

The Oligocene (c. 35-25 Ma) had a seasonally moist climate and saw the formation of ferricrete and silcrete along the west coast and in the Pilbara (Hocking *et al.*, 2001). The sea level was lower at this time but changed with the onset of the last major transgression in the Miocene (c. 25-12 Ma) during which the climate became more seasonally extreme with significant variations in temperatures although cooling occurred in the late Miocene (c. 12-5 Ma). During the mid to late Tertiary widespread weathering of Eocene sediments and underlying bedrock occurred, resulting in formation of silcretes and ferruginous duricrusts (Hocking *et al.*, 2001). This weathering indicates a shift in the climate towards a more seasonally variable rainfall.

The Late Tertiary to Quaternary is marked by erosion, caused by tectonic uplift, along with a change in climatic conditions to semi-arid or arid (Bowler, 1976). Sediments deposited in this period are the result of fluvial, colluvial and aeolian processes, as the regolith at this time was soft and unconsolidated, and erosion by water and wind was prolific. However, there were certain regolith units that were formed by irreversible dehydration or by the introduction and precipitation of cements such as silica and Fe-oxides producing silcrete, calcrete and ferricrete (Anand and Paine, 2002).

The Quaternary is generally regarded as a period of alternating humidity and aridity due to a series of glacial maxima and minima (Cockbain and Hocking, 1989). In the Pliocene (5-2 Ma) there was significant pedogenic calcrete development. Continual calcrete development and dissection of pre-existing calcrete occurred in the Early to Middle Pleistocene when the climate was predominately dry with intermittent wet periods. In the Late Pleistocene (between about 126,000 and 40 000 years BP) the climate became cooler and drier. However, the onset of the last major glacial advance between 40,000 and 30,000 years BP, climate in southwest Australia shifted to significantly wetter conditions. This produced high water levels in lakes and increased fluvial activity. The last glacial maximum occurred at 25 000 to 15 000 years BP resulting in completely dried lakes and the formation of unconsolidated dunefields in Western Australia. The climate continued to change between 15 000 and 10 000 years BP with rising temperatures causing an increase in precipitation (Bowler, 1976) and a transition from intense arid conditions to humid conditions with higher temperatures and greater rainfall than present. Regolith processes occurring at this time were mainly erosional. Maximum aridity was between 17 500 and 16 000 years BP (Bowler, 1976), however, Rognon and Williams (1977) place maximum aridity between 17 000 and 12 000 BP. The onset of more arid conditions resulted in reduced recharge and the precipitation of elements leached from the upper parts of the regolith profile in topographic lows resulting in enrichment of Fe, Si and Ca to form ferricrete, ferruginous saprolite, silcrete and red-brown hardpan. Drainage also became limited due to the aridity and groundwaters became saline.

The Yilgarn Craton has a hot mediterranean to semi-arid climate at present and the gently undulating land surface forms a partial etchplain. The topography is largely controlled by bedrock lithologies. There is a complex history of valley development and aggradation. Deep weathering has affected most lithologies and geological provinces across the Craton.

5.2.4 Opaline silica veins in calcrete deposits of the Yilgarn Craton

Silica-indurated material such as silcrete, silicified saprolite, opaline silica veins, silica cemented colluvium and alluvium, and siliceous red brown hardpan are very common in the Yilgarn Craton. There are two main types of silcrete – pedogenic

silcrete, which form dominantly from soil processes, and groundwater silcrete that forms from groundwater. Only the latter is considered in this thesis.

Groundwater silcretes are generally massive, quartz-rich silcretes formed in the subsurface as a result of increased silica in the groundwater or a decrease in the volume of groundwater. Both result in the supersaturation of silica causing precipitation at seepages, water tables and porosity barriers (Taylor and Butt, 1998). The process of silicification is defined by the release of silica by chemical weathering often induced by heavy rainfall followed by the precipitation of the silica, at either the surface or at depth most likely due to evaporation. Therefore, silicification is proposed to have occurred during transitional periods between humid and arid phases (Butt, 1985). With the change to more arid conditions in the Late Miocene or Pliocene the cementing processes in the regolith shifted towards calcretisation and silicification at the expense of ferruginisation processes (Anand and Paine, 2002). Consequently, silica mobilisation and precipitation is considered the cause of extensive hardpan development of younger late Neogene to Quaternary sediments. Silcretes in the Yilgarn Craton generally form over granitic rocks (Anand and Paine, 2002) and the detailed mechanisms for the dissolution and precipitation of siliceous cements in silcrete remain poorly understood.

Calcrete is near surface material mainly composed of cemented calcium carbonate. Two genetic types of calcrete deposits are recognized within the Yilgarn Craton; groundwater calcrete, which is found in the phreatic zone and pedogenic calcrete, which is found in the vadose zone (Sanders, 1974; Butt *et al.*, 1977; Arakel, 1982; Anand and Paine, 2002). Only groundwater (river valley) calcretes are discussed in this study. Groundwater calcretes are surficial limestone deposits in major, past or present drainages (Anand and Paine, 2002) and can vary in width from a few hundred meters to several kilometres and may be over a hundred kilometres in length. Their thickness typically varies between 5-10 m but can exceed 30 metres (Anand and Paine, 2002). Calcrete distribution (Figure 5.2) south of the Menzies Line is limited (Butt *et al.*, 1977). North of the Menzies Line and west of the Meckering Line the calcretes are usually cut by modern river systems and exist as terraces above the river level, whereas, east of the Meckering Line they are mostly intact (Anand and Paine, 2002). It is believed that calcrete deposition in the northern Yilgarn Craton is related to summer rainfall, where rapid infiltration and high

evaporation rates limit prolonged periods of soil dampness (Anand and Paine, 2002). Dissolved Ca, Mg and bicarbonate are concentrated by evaporation and precipitate in the drainage depressions forming groundwater calcrete.

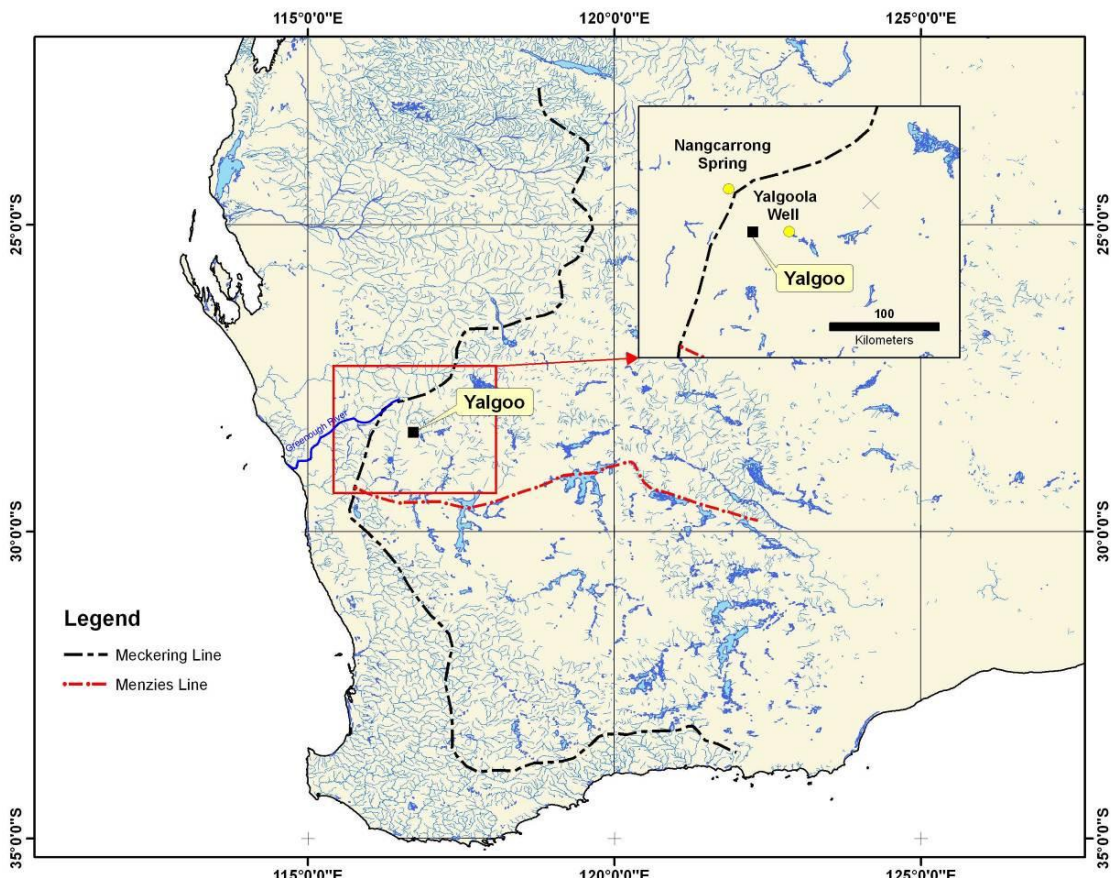


Figure 5.2 Drainage map of southern Western Australia showing the location of the Meckering and Menzies lines (after Butt *et al.*, 1977) and the location of Yalgo and the Greenough River.

Opaline silica filled cavities and veins in groundwater calcrites are commonly enriched in uranium (e.g. Butt *et al.*, 1977). The surrounding granite bedrock contains 5-10 ppm of uranium (Butt *et al.*, 1977) and is most likely the main source of this element. It is mobilised in the oxidized form by groundwater within valleys and at seepage sites along valleys, where the groundwater experiences high evaporation. The uranium can co-precipitate with calcrites, often forming significant concentrations of carnotite. Significant amounts of uranium in the groundwater also results in enrichment of this element in the veins of opaline silica within the calcrete. The uranium is leached from granites during weathering, concentrated in the drainage channels and then precipitated into the calcrete along with silica as uraniferous opaline silica. The veins are considered to have formed

after the formation of the groundwater calcrete due to the nature of the crosscutting relationships.

5.3 Yalgoo Well, Western Australia

This sample was collected from near Yalgoo Well at Wagga Wagga Station, approximately 22 km east of Yalgoo ($116^{\circ}53'E$ and $28^{\circ}22'S$, 497 km north of Perth in Western Australia). Yalgoo Well is situated on the granite bedrock near the Yalgoo-Singleton Greenstone belt, and is approximately 5 km from a granite-greenschist contact (Figure 5.3).

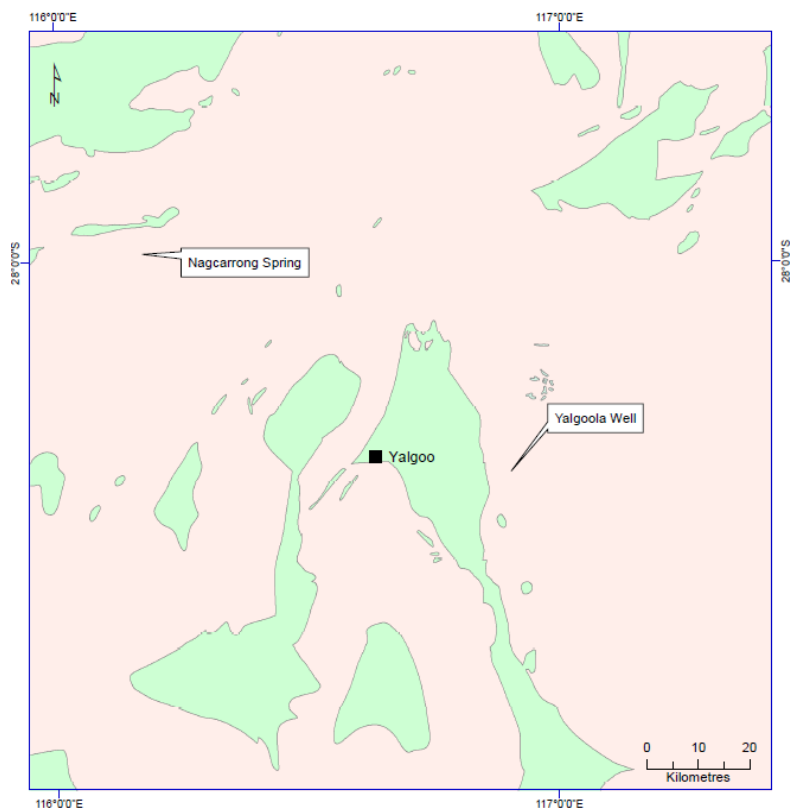


Figure 5.3 The location of Yalgoo Well, Nangcarrong Spring and the town of Yalgoo. Pink colour represent the granites of the Murchison Domain and green is the greenstones of the Murchison Domain (modified from Watkins and Hickman, 1990).

In this sample, the calcrete is crosscut by a network of veins and cavities of massive opaline silica varying in width from less than 1 mm to several millimetres (Figure 5.4). Fist size samples have been cut into several slabs approximately perpendicular to the elongation of the silica veins to approximate true thickness as close as possible. An area containing two silica veins at about 3 mm thick with a series of

thinner branching veins was cut from the Yalgoolah Well sample for the SHRIMP analysis and was mounted into epoxy resin with the standard opal and polished. All of the veins appeared macroscopically homogeneous.

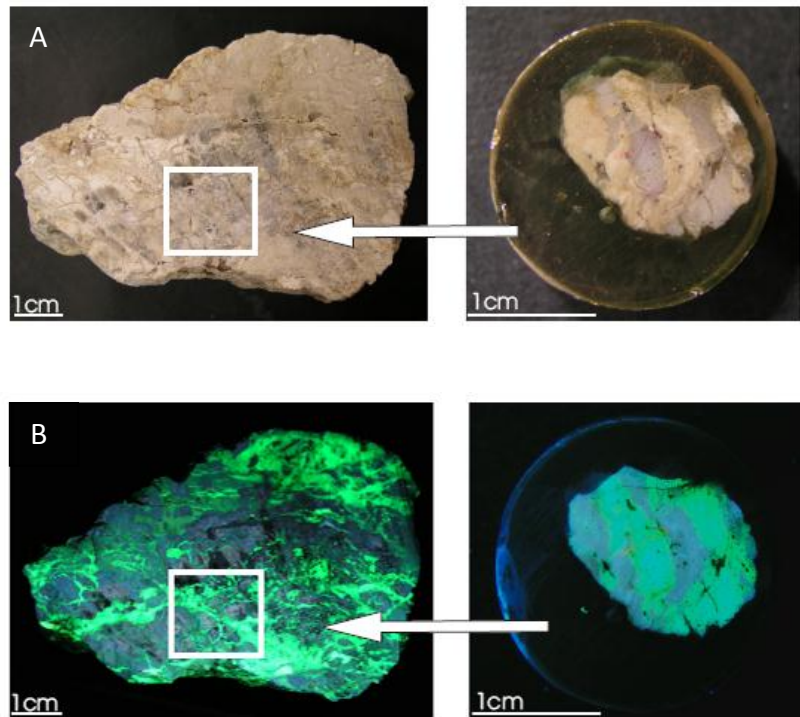


Figure 5.4 Images showing the slab and mount under plain light (A) and under UV light (B). White squares show part of the slab that was used for SHRIMP analyses.

5.4 Nangarrong Spring, Western Australia

This sample is from Nangarrong Spring, located 64 km north-west of Yalgoo ($116^{\circ}10'E$ $27^{\circ}59'S$) (Figure 5.3). Calcretes in this location are flat lying and form the bed, banks and terraces of the Greenough River. The calcrete units are 3 to 15 m thick and overlie sandy clays and lateritized granitic bedrock. Approximately 3 m of soft calcrete and calcareous earths overlying 30 cm of white opaline silica are exposed in the river bed (Butt *et al.*, 1977). The uranium enrichment is specific to the silicified zone in and near the river (Butt *et al.*, 1977). Water in bores near Nangarrong Spring has been reported to have between 35-115 ppb uranium and the water from Nangarrong Spring has between 35-50 ppb uranium (Butt *et al.*, 1977).

Calcretes samples 1.5 km north-east of Nangcarrong Spring gave a range of 100 to 500 ppm of U₃O₈ with a maximum of 1220 ppm U₃O₈ (Morete, 1977). The granites in the Nangcarrong Ranges (10 km north of Nangcarrong Spring) contain 20 to 30 ppm U₃O₈ and are considered as a source for uranium (Morete, 1977). Water from Nangcarrong Spring has a pH between 6.2 and 7.0 and the water table is reasonably shallow, between the surface and 2.6 m below the surface (Morete, 1977).

The internal structure of this sample is more complex than that of the Yalgoola Well sample, which displays a simple network of silicified veins. The opal in this sample is distributed in oval lenses varying from several millimetres to 1cm in size within the carbonate matrix. An area containing one of these lenses was selected for the SHRIMP analysis (Figure 5.5) and appears to contain at least three generations of opal based on cross-cutting textures. The main linear vein varies in thickness from about 2 to 3 mm, is filled with relatively porous opal and comprises nearly half of the analysed section. It is bound by the more compact opal that forms 200-300 µm thick bands at both contacts of the main fracture. More compact opal is also formed in the irregular network throughout the other half of the section.

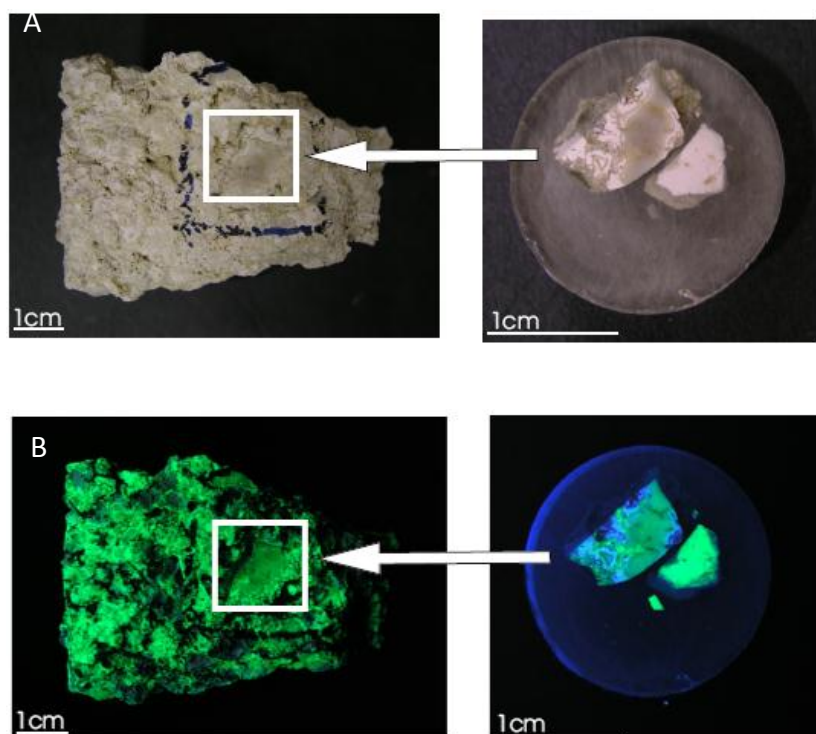


Figure 5.5 Images showing the slab and mount under plain light (A) and under UV light (B). White squares show part of the slab that was used for SHRIMP analyses. Opal is the white mineral that fluoresces bright green under UV light.

5.5 SHRIMP analytical protocol and initial data reduction

The detailed description of analytical technique is presented in Chapter 3 and is given by Nemchin *et al.*, (2006). A SHRIMP analysis of an individual spot in the present study was shortened to include only isotopes relevant to the U-series dating and consisted of 5 scans over 8 peaks at masses ^{197}Au (2 sec integration time), 204.1-background (30 sec), ^{234}U (30 sec), ^{238}U (3 sec), $^{230}\text{Th}^{16}\text{O}$ (30 sec), $^{232}\text{Th}^{16}\text{O}$ (5 sec), $^{234}\text{U}^{16}\text{O}$ (30 sec) and $^{238}\text{U}^{16}\text{O}$ (1 sec). Mass calibration was done using masses 197 and 254. The retardation lens was used to reduce the background during all runs. The primary beam of $^{16}\text{O}_2$ was kept between 5 and 10 nA in order to contain sufficient counting rates for the isotopes with low abundances.

The Th/U ratios in unknown samples were calibrated against the opal M-21277 from Virgin Valley, Nevada (USA). The U concentrations in unknown samples have been calculated based on average U concentration in the standard equal to 800 ppm, although the standard is known to be highly inhomogeneous with respect to the U content (Paces *et al.*, 2004a), which makes the obtained concentrations in unknowns very imprecise. U-series TIMS analyses of the standard opal show that the $^{230}\text{Th}/^{238}\text{U}$ and $^{234}\text{U}/^{238}\text{U}$ ratios are within analytical uncertainty of secular equilibrium values (Paces *et al.*, 2004a; Amelin and Back, 2006).

True $^{230}\text{Th}/^{238}\text{U}$ activity ratios in unknowns were obtained by multiplying the measured ratios by a correction coefficient. This coefficient was derived from the theoretical secular equilibrium $^{230}\text{Th}/^{238}\text{U}$ activity ratio based on known decay constants divided by the average of $^{230}\text{Th}/^{238}\text{U}$ activity ratios in the standard obtained during a SHRIMP session (Figure 5.6 and 5.7). The same coefficient was also used to correct the $^{232}\text{Th}/^{238}\text{U}$ activity ratios in the unknowns. This is based on the assumption that both ^{230}Th and ^{232}Th behave similarly.

Corrections were made for detrital Th, using Th^{232} as the index isotope assuming that the detrital Th and U had $(^{232}\text{Th}/^{238}\text{U})_{\text{atomic}} = 3.8 \pm 2.0$, $(^{234}\text{U}/^{238}\text{U})_{\text{activity}} = 1.0 \pm 0.1$ and $(^{230}\text{Th}/^{238}\text{U})_{\text{activity}} = 1.0 \pm 0.1$ (Ludwig and Paces, 2002). Data corrected for detrital Th did not result in any significant differences compared to the uncorrected data, suggesting that the detrital ^{230}Th is negligible.

Although $^{234}\text{U}/^{238}\text{U}$ ratios do not need to be corrected, their accuracy was monitored during the runs using the standard where they do not deviate beyond the analytical uncertainties from the secular equilibrium in all runs (Figure 5.6 and 5.7).

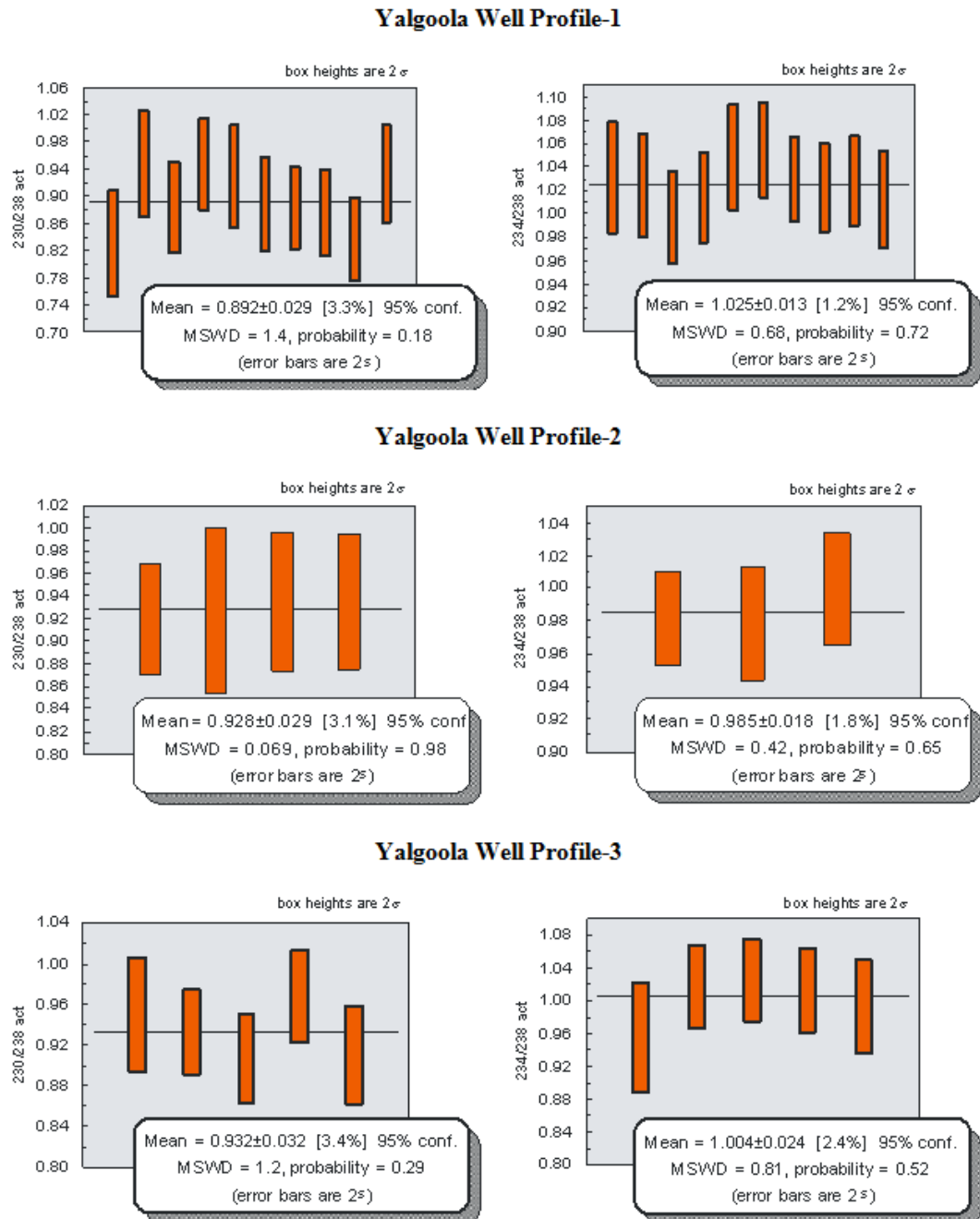


Figure 5.6 $^{230}\text{Th}/^{238}\text{U}$ and $^{234}\text{U}/^{238}\text{U}$ activity ratios measured in the standard opal M-21277 during three runs of Yalgoolo Well sample.

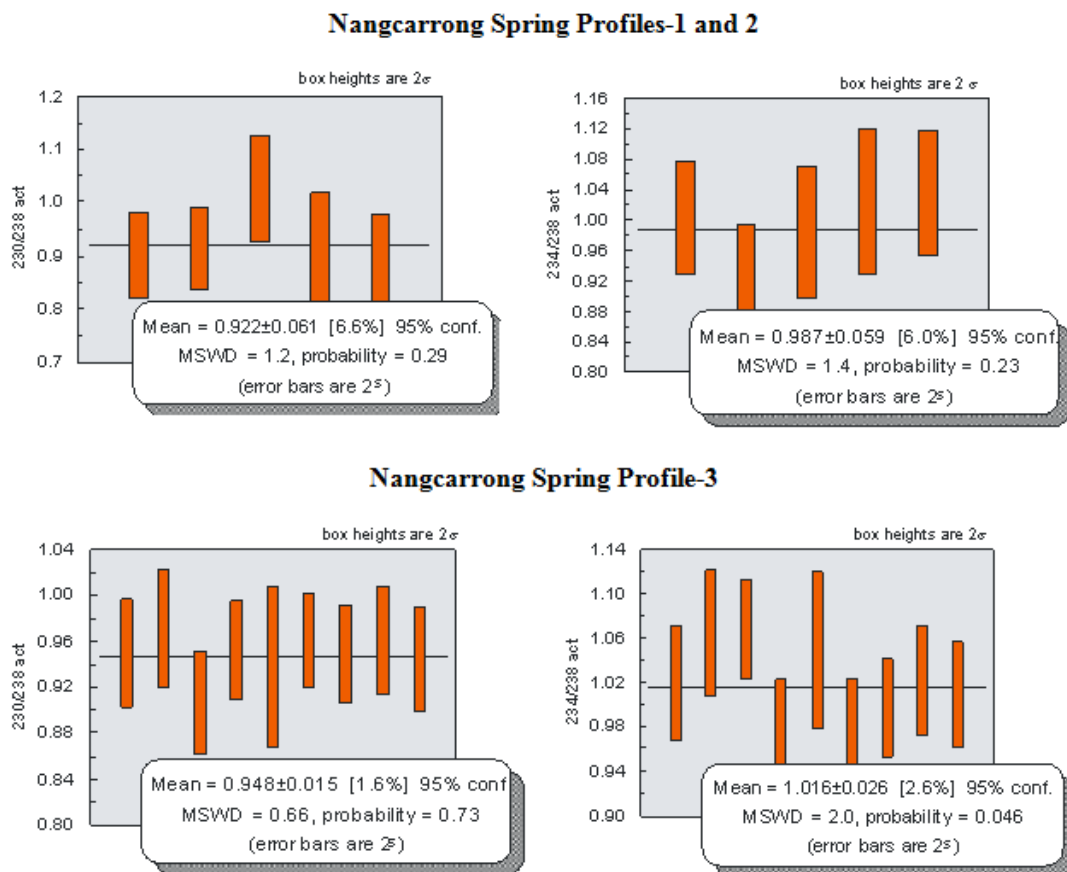


Figure 5.7 $^{230}\text{Th}/^{238}\text{U}$ and $^{234}\text{U}/^{238}\text{U}$ activity ratios measured in the standard opal M-21277 during two runs of Nangcarrong Spring sample.

All errors for individual analyses, calculated by combining counting statistics error obtained during these analyses and external error derived from the reproducibility of the standard, are reported in the table at 1σ level, while the error bars in all figures are shown as 2σ . The average values obtained from the combination of several analyses are given as 95%-confidence limits and do not take into account the errors in ^{234}U and ^{230}Th decay constants.

5.6 Results

The first run of the samples was done using the full U-Pb and U series analytical protocol, but it is evident that all Pb is non-radiogenic (Table 5.1 and Figure 5.8) and, therefore, U-Pb system would not work as geochronometer as the samples appear to be too young. Consequently U-Pb analysis was abandoned in all subsequent runs.

Table 5.1 U/Pb SHRIMP data from the first run for opal samples from Yalgooloo Well, Western Australia (errors are 1σ)

Sample	$\frac{^{204}Pb}{^{206}Pb}$	$\frac{^{207}Pb}{^{206}Pb}$	$\frac{^{208}Pb}{^{206}Pb}$	$\frac{^{206}Pb}{^{238}U}$
Ylg-1-1	0.069 ± 0.007	0.773 ± 0.030	1.86 ± 0.07	0.0006 ± 0.00002
Ylg-1-2	0.055 ± 0.009	0.875 ± 0.042	1.94 ± 0.09	0.0004 ± 0.00001
Ylg-1-3	0.075 ± 0.012	0.892 ± 0.052	1.96 ± 0.11	0.0003 ± 0.00001
Ylg-1-4	0.062 ± 0.010	0.795 ± 0.044	1.77 ± 0.09	0.0004 ± 0.00002
Ylg-1-5	0.040 ± 0.014	0.804 ± 0.061	1.77 ± 0.13	0.0002 ± 0.00001
Ylg-1-6	0.071 ± 0.012	0.775 ± 0.051	1.77 ± 0.11	0.0002 ± 0.00001
Ylg-1-7	0.071 ± 0.013	0.755 ± 0.050	1.71 ± 0.11	0.0002 ± 0.00001
Ylg-1-8	0.093 ± 0.012	0.824 ± 0.046	2.03 ± 0.11	0.0003 ± 0.00001
Ylg-1-9	0.048 ± 0.013	0.831 ± 0.056	1.86 ± 0.12	0.0002 ± 0.00001
Ylg-1-10	0.073 ± 0.011	0.836 ± 0.048	1.92 ± 0.11	0.0003 ± 0.00001
Ylg-1-11	0.061 ± 0.011	0.800 ± 0.050	1.92 ± 0.12	0.0002 ± 0.00001
Ylg-1-12	0.057 ± 0.011	0.940 ± 0.059	2.10 ± 0.13	0.0002 ± 0.00001
Ylg-1-13	0.034 ± 0.015	0.757 ± 0.059	1.82 ± 0.14	0.0002 ± 0.00001
Ylg-1-14	0.076 ± 0.011	0.716 ± 0.040	1.52 ± 0.08	0.0004 ± 0.00002
Ylg-2-1	0.078 ± 0.013	0.828 ± 0.052	1.88 ± 0.11	0.0003 ± 0.00001
Ylg-2-2	0.067 ± 0.007	0.828 ± 0.031	1.94 ± 0.07	0.0005 ± 0.00002
Ylg-2-3	0.065 ± 0.007	0.858 ± 0.034	1.95 ± 0.08	0.0005 ± 0.00002
Ylg-2-4	0.074 ± 0.007	0.902 ± 0.032	2.04 ± 0.07	0.0006 ± 0.00002
Ylg-2-5	0.099 ± 0.014	0.905 ± 0.054	1.89 ± 0.11	0.0003 ± 0.00002
Ylg-2-6	0.061 ± 0.008	0.828 ± 0.039	1.87 ± 0.09	0.0004 ± 0.00001
Ylg-2-7	0.071 ± 0.007	0.789 ± 0.030	1.88 ± 0.07	0.0006 ± 0.00002
Ylg-2-8	0.061 ± 0.007	0.800 ± 0.033	1.91 ± 0.08	0.0005 ± 0.00002
Ylg-2-9	0.069 ± 0.008	0.973 ± 0.041	2.10 ± 0.09	0.0005 ± 0.00002

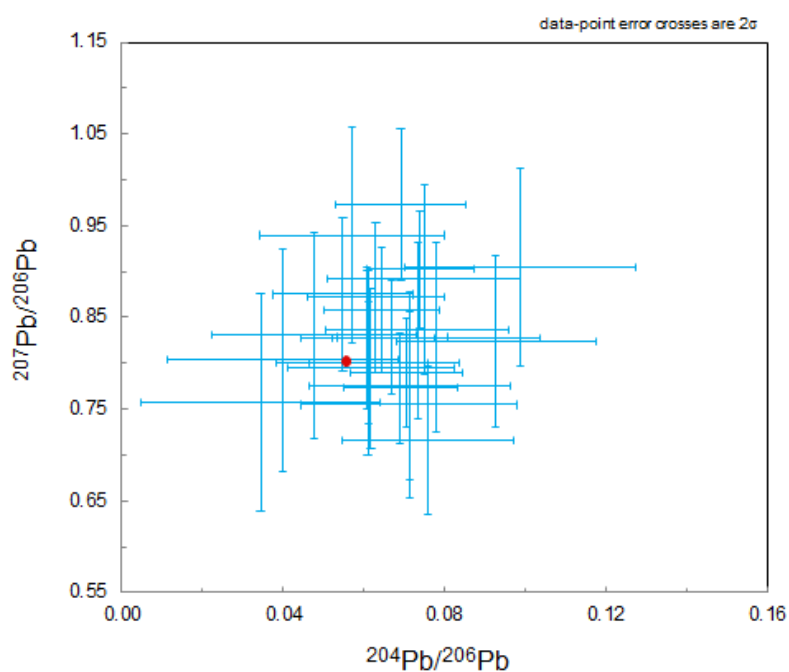


Figure 5.8 $^{207}\text{Pb}/^{206}\text{Pb}$ vs. $^{204}\text{Pb}/^{206}\text{Pb}$ plot of the first run for opal samples from Yalgooloo Well, Western Australia. The red dot is modern Stacey-Kramers Pb composition.

5.6.1 Yalgoolaa Well

A total of 55 SHRIMP spots have been analysed in three traverses across a major (3 mm) opal infilled fracture. The first fifteen analyses comprise Yalgoolaa Well 1 (Figure 5.9 and Table 5.2), a profile that forms a series of groups of analyses in the central, intermediate and contact parts of the vein. The rest of the analyses are located across the vein with the distance between the spots equal to 1-2 spot sizes (Yalgoolaa Well 2 and 3 in Table 5.2 and Figure 5.9).

Estimated uranium concentrations vary from 51 to 122 ppm with errors close to 15% as determined by the highly variable uranium content in the M21277 opal standard. The variation in uranium concentration throughout these traverses does not show any systematic change. All analyses indicate that ^{234}U and ^{230}Th are not in secular equilibrium and that both of these intermediate daughters are not equilibrated with their parent ^{238}U , making it possible to calculate $^{230}\text{Th}/^{238}\text{U}$ - $^{234}\text{U}/^{238}\text{U}$ ages. As a result of the comparatively low U contents in the sample, the errors of these ages for individual analytical spots are relatively large. Despite the large errors the data appear to show a systematic decrease of $^{230}\text{Th}/^{238}\text{U}$ - $^{234}\text{U}/^{238}\text{U}$ ages from the maximum of about 130-150 kyr in the centre of the vein to about 60-70 kyr near the contact (Table 5.2, Figure 5.9).

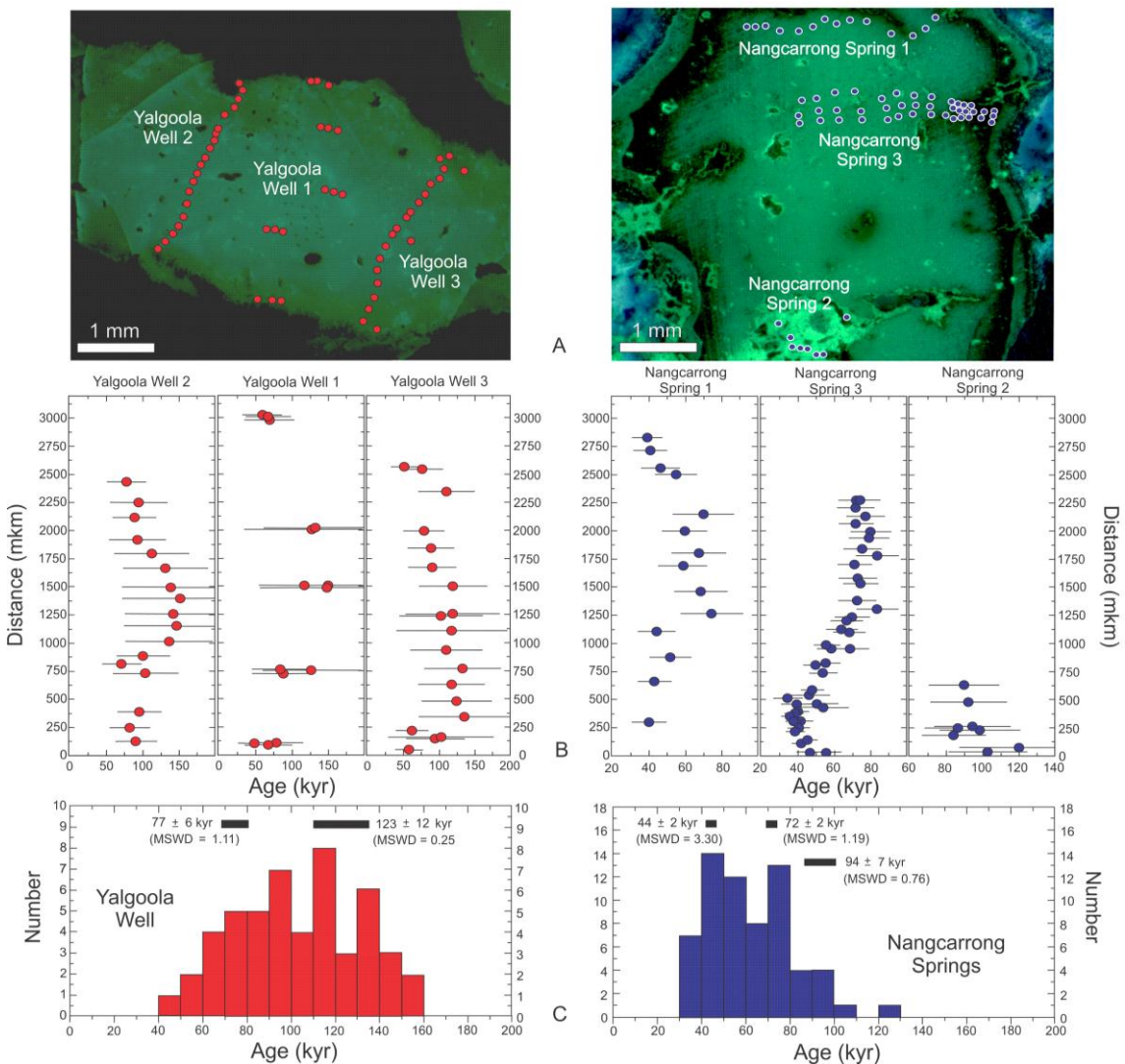


Figure 5.9 Results of U-series analyses of opal samples from Yalgoola Well and Nangcarrong Spring. A - analysed areas shown under the UV light (indicative of increase U concentration in the opal samples) with the location of analytical spots shown as circles of different colour. B - Th-ages along the individual profiles in the samples (error bars are 2σ). C - age distribution histograms for two analysed samples with average ages calculated for the identified maximums.

Table 5.2 SHRIMP results for opal samples from Yalgoo Well and Nangcarrong Spring, Western Australia (errors are 1σ)

Sample	U (ppm)	Measured		Corrected for Standard			Distance from the edge (μm)	Th age	$\frac{^{234}\text{U}}{^{238}\text{U}}$ act(init)				
		$\frac{^{230}\text{Th}}{^{238}\text{U}}$	$\frac{^{232}\text{Th}}{^{238}\text{U}}$	$\frac{^{234}\text{U}}{^{238}\text{U}}$	$\frac{^{232}\text{Th}}{^{238}\text{U}}$ act	$\frac{^{234}\text{U}}{^{238}\text{U}}$ act							
Yalgoo Well													
Profile 1													
Ylg-1-1	92	0.0000088±14	0.0000255±54	0.0000610±34	0.58±8	1.11±6	104.372±10	80±18	1.14±8				
Ylg-1-2	101	0.0000076±14	0.0000073±31	0.0000588±33	0.51±8	1.07±6	85.458±10	69±16	1.09±7				
Ylg-1-3	96	0.0000066±13	0.0000289±57	0.0000650±35	0.44±7	1.19±6	98.429±10	49±11	1.22±7				
Ylg-1-4	75	0.0000135±20	0.0000037±28	0.0000636±39	0.89±12	1.16±7	1502.484±10	151±47	1.25±10				
Ylg-1-5	84	0.0000115±21	0.0000000±17	0.0000617±41	0.76±10	1.13±7	1502.097±10	118±31	1.18±9				
Ylg-1-6	79	0.0000136±23	0.0000014±22	0.0000653±49	0.90±12	1.18±7	1482.77±10	150±46	1.27±9				
Ylg-1-7	90	0.0000077±14	0.0000056±29	0.0000581±44	0.51±8	1.06±6	2974.257±10	70±17	1.07±7				
Ylg-1-8	92	0.0000071±13	0.0000085±33	0.0000594±34	0.47±8	1.09±6	3019.468±10	61±14	1.10±7				
Ylg-1-9	93	0.0000088±15	0.0000004±17	0.0000673±36	0.58±9	1.23±7	3004.5±10	69±15	1.28±8				
Ylg-1-10	92	0.0000114±16	0.0000114±37	0.0000592±34	0.75±9	1.08±6	746.949±10	127±33	1.12±8				
Ylg-1-11	87	0.0000096±15	0.0000041±25	0.0000613±36	0.63±9	1.12±7	719.118±10	89±21	1.15±8				
Ylg-1-12	84	0.0000101±16	0.0000065±31	0.0000662±38	0.67±10	1.21±7	755.052±10	85±20	1.27±8				
Ylg-1-13	72	0.0000114±28	0.0000037±44	0.0000654±55	0.76±13	1.08±7	2002.696±10	129±47	1.11±10				
Ylg-1-14	78	0.0000131±18	0.0000016±19	0.0000654±39	0.87±11	1.19±7	2013.235±10	133±36	1.28±9				
Profile 2													
Ylg-2-1	113	0.0000109±11	0.0000025±14	0.0000663±27	0.70±7	1.21±5	128.801±10	90±14	1.27±6				
Ylg-2-2	98	0.0000096±11	0.0000000±1	0.0000628±28	0.62±6	1.15±5	247.67±10	82±14	1.19±6				
Ylg-2-3	111	0.0000111±11	0.0000011±9	0.0000653±26	0.71±7	1.19±5	390.029±10	95±15	1.25±6				
Ylg-2-4	94	0.0000152±16	0.0000026±16	0.0000604±31	0.97±9	1.11±5	524.576±10	210±66	1.20±8				
Ylg-2-5	72	0.0000106±13	0.0000044±21	0.0000597±31	0.68±8	1.09±6	736.045±10	104±22	1.12±7				
Ylg-2-6	82	0.0000087±12	0.0000001±9	0.0000626±30	0.55±7	1.14±5	815.842±10	71±14	1.18±6				
Ylg-2-7	98	0.0000106±12	0.0000016±12	0.0000606±27	0.68±7	1.11±5	882.114±10	100±18	1.14±6				
Ylg-2-8	85	0.0000125±13	0.0000014±12	0.0000601±29	0.80±8	1.10±5	1007.342±10	136±30	1.14±7				
Ylg-2-9	77	0.0000132±15	0.0000006±10	0.0000613±32	0.84±9	1.12±6	1147.528±10	146±36	1.18±8				
Ylg-2-10	88	0.0000123±13	0.0000012±12	0.0000584±28	0.78±8	1.07±5	1251.356±10	142±33	1.10±7				
Ylg-2-11	82	0.0000123±15	0.0000021±15	0.0000557±32	0.79±8	1.04±5	1389.389±10	151±39	1.06±8				
Ylg-2-12	81	0.0000124±15	0.0000007±13	0.0000594±30	0.79±9	1.08±5	1489.246±10	138±34	1.13±8				
Ylg-2-13	83	0.0000125±14	0.0000000±3	0.0000612±30	0.80±8	1.12±5	1658.636±10	131±29	1.17±7				
Ylg-2-14	73	0.0000111±14	0.0000007±10	0.0000594±32	0.71±8	1.09±6	1787.26±10	112±26	1.12±8				
Ylg-2-15	79	0.0000101±13	0.0000000±3	0.0000607±31	0.64±8	1.11±6	1907.495±10	93±19	1.14±7				

Table 5.2 continued

Sample	U (ppm)	Measured		Corrected for Standard				Distance from the edge (μm)	Th age	$\frac{^{234}U}{^{238}U}$ act(init)
		$\frac{^{230}Th}{^{238}U}$	$\frac{^{232}Th}{^{238}U}$	$\frac{^{234}U}{^{238}U}$	$\frac{^{232}Th}{^{238}U}$ act	$\frac{^{234}U}{^{238}U}$ act				
Ylg-2-16	101	0.0000105±11	0.0000000±1	0.0000644±27	0.67±7	1.18±5	2113.027±10	89±15	1.23±6	
Ylg-2-17	79	0.0000110±14	0.0000000±4	0.0000651±33	0.70±9	1.19±6	2240.44±10	95±19	1.25±7	
Ylg-2-18	81	0.0000128±14	0.0000000±2	0.0000592±31	0.82±9	1.08±6	2322.917±10	148±37	1.12±8	
Ylg-2-19	100	0.0000102±12	0.0000000±2	0.0000685±29	0.65±7	1.25±5	2422.384±10	78±13	1.31±6	
Profile 3										
Yal-3-1	101	0.0000111±15	0.0000053±21	0.0000735±58	0.70±7	1.34±10	2539.425±10	78±14	1.43±11	
Yal-3-2	95	0.0000117±11	0.0000026±18	0.0000625±43	0.75±6	1.14±7	2338.849±10	111±19	1.20±9	
Yal-3-3	74	0.0000099±14	0.0000090±32	0.0000649±49	0.63±6	1.19±8	1991.027±10	80±14	1.23±9	
Yal-3-4	75	0.0000103±12	0.0000098±30	0.0000626±50	0.65±6	1.14±8	1837.278±10	90±16	1.18±10	
Yal-3-5	69	0.0000112±14	0.0000004±19	0.0000669±53	0.71±7	1.22±8	1668.066±10	92±17	1.29±10	
Yal-3-6	70	0.0000132±15	0.0000028±23	0.0000670±50	0.84±7	1.22±8	1498.911±10	120±23	1.31±10	
Yal-3-7	72	0.0000124±22	0.0000043±40	0.0000635±83	0.78±10	1.16±13	1104.937±10	118±38	1.22±17	
Yal-3-8	66	0.0000110±15	0.0000081±32	0.0000592±55	0.70±7	1.08±8	932.595±10	111±25	1.11±11	
Yal-3-9	81	0.0000139±13	0.0000010±17	0.0000664±50	0.88±7	1.21±8	768.741±10	134±27	1.31±10	
Yal-3-10	84	0.0000128±14	0.0000035±23	0.0000653±49	0.81±7	1.19±8	626.976±10	118±23	1.27±10	
Yal-3-11	85	0.0000132±13	0.0000029±20	0.0000654±49	0.84±6	1.19±8	477.561±10	126±24	1.28±10	
Yal-3-12	78	0.0000122±13	0.0000010±17	0.0000588±50	0.78±6	1.07±8	339.445±10	136±31	1.11±11	
Yal-3-13	79	0.0000079±12	0.0000010±17	0.0000615±53	0.50±5	1.12±8	216.291±10	64±11	1.15±10	
Yal-3-14	78	0.0000077±12	0.0000010±18	0.0000632±46	0.49±5	1.15±7	47.025±10	59±10	1.18±8	
Yal-3-15	76	0.0000096±13	0.0000041±24	0.0000569±52	0.61±6	1.04±8	143.309±10	96±20	1.05±10	
Yal-3-16	68	0.0000083±13	0.0000012±20	0.0000477±60	0.52±6	0.87±9	1236.48±10	104±29	0.83±13	
Yal-3-17	70	0.0000074±12	0.0000004±17	0.0000654±51	0.47±5	1.20±8	2558.506±10	53±9	1.23±9	
Yal-3-18	58	0.0000102±16	-0.0000005±19	0.0000533±59	0.65±7	0.97±9	1252.019±10	120±32	0.96±12	
Yal-3-19	76	0.0000080±15	0.0000152±46	0.0000467±77	0.51±6	0.85±12	156.261±10	103±36	0.80±17	

Nangcarrong Spring**Profile 1**

NS-1-1	415	0.0000089±9	0.0006207±157	0.0000982±42	0.57±5	1.79±8	301.371±10	40±5	1.89±8
NS-1-2	482	0.0000090±8	0.0005748±143	0.0000943±38	0.58±5	1.72±7	649.291±10	43±5	1.82±7
NS-1-3	408	0.0000104±9	0.0006690±167	0.0000935±41	0.66±5	1.71±7	865.274±10	52±6	1.82±8
NS-1-4	451	0.0000096±9	0.0006980±173	0.0000982±40	0.62±5	1.79±7	1096.815±10	44±5	1.90±8
NS-1-5	456	0.0000126±10	0.0007896±179	0.0000862±37	0.81±6	1.57±7	1256.633±10	74±9	1.71±8

Table 5.2 continued

Sample	U (ppm)	Measured		Corrected for Standard				Distance from the edge (μm)	Th age	$\frac{^{234}U}{^{238}U}$ act(init)
		$\frac{^{230}Th}{^{238}U}$	$\frac{^{232}Th}{^{238}U}$	$\frac{^{234}U}{^{238}U}$	$\frac{^{232}Th}{^{238}U}$ act	$\frac{^{234}U}{^{238}U}$ act				
NS-1-6	458	0.0000130±9	0.0008271±175	0.0000938±38	0.83±5	1.71±7	1452.289±10	68±7	1.87±8	
NS-1-7	448	0.0000113±9	0.0007855±172	0.0000915±39	0.72±5	1.67±7	1679.537±10	59±6	1.79±8	
NS-1-8	451	0.0000119±9	0.0008490±179	0.0000875±38	0.76±5	1.60±7	1791.358±10	67±7	1.72±8	
NS-1-9	469	0.0000122±9	0.0008780±180	0.0000977±39	0.78±5	1.78±7	1987.171±10	60±6	1.93±8	
NS-1-10	418	0.0000120±10	0.0007872±184	0.0000857±39	0.77±6	1.56±7	2137.017±10	70±8	1.69±8	
NS-1-11	438	0.0000116±9	0.0008093±181	0.0000994±41	0.74±5	1.82±7	2494.048±10	55±6	1.95±8	
NS-1-12	423	0.0000095±9	0.0007623±176	0.0000940±41	0.61±5	1.72±7	2549.172±10	46±5	1.82±8	
NS-1-13	425	0.0000089±8	0.0007625±175	0.0000971±41	0.57±5	1.77±7	2707.995±10	41±5	1.87±8	
NS-1-14	548	0.0000084±7	0.0009595±175	0.0000949±36	0.53±4	1.73±7	2819.87±10	39±4	1.82±7	
Profile 2										
NS-2-1	172	0.0000165±10	0.0000612±47	0.0000918±40	1.05±6	1.68±7	220.327±10	99±11	1.90±8	
NS-2-2	199	0.0000169±10	0.0002481±89	0.0000917±37	1.08±6	1.67±7	36.95±10	103±11	1.90±8	
NS-2-3	138	0.0000178±12	0.0003832±133	0.0000878±43	1.14±7	1.60±8	63.317±10	121±17	1.85±9	
NS-2-4	182	0.0000151±10	0.0001246±66	0.0000934±39	0.96±6	1.71±7	172.023±10	84±9	1.90±8	
NS-2-5	166	0.0000160±10	0.0002282±92	0.0000968±41	1.02±6	1.77±8	239.833±10	87±9	1.98±8	
NS-2-6	168	0.0000161±10	0.0001067±62	0.0000923±40	1.03±6	1.69±7	253.932±10	95±11	1.90±8	
NS-2-7	174	0.0000148±10	0.0001212±65	0.0000864±38	0.95±6	1.58±7	469.304±10	93±11	1.75±8	
NS-2-8	171	0.0000161±10	0.0000356±36	0.0000952±41	1.03±6	1.74±7	621.024±10	90±10	1.95±8	
Profile 3										
NS-3-1	379	0.0000098±5	0.0011825±98	0.0000943±39	0.62±3	1.72±7	25.585±10	47±4	1.83±8	
NS-3-2	374	0.0000115±5	0.0011254±95	0.0000957±38	0.72±3	1.75±7	25.936±10	56±4	1.88±7	
NS-3-3	502	0.0000098±4	0.0007457±67	0.0000936±34	0.61±2	1.71±6	27.657±10	47±3	1.81±7	
NS-3-4	524	0.0000092±4	0.0007019±64	0.0000957±33	0.58±2	1.75±6	114.272±10	42±3	1.84±6	
NS-3-5	517	0.0000097±4	0.0006239±60	0.0000954±32	0.61±2	1.74±6	129.173±10	45±3	1.85±6	
NS-3-6	463	0.0000087±4	0.0007545±70	0.0000970±34	0.54±2	1.77±6	218.063±10	39±3	1.86±7	
NS-3-7	402	0.0000088±4	0.0010944±92	0.0000948±38	0.55±3	1.73±7	245.828±10	41±3	1.82±7	
NS-3-8	419	0.0000087±4	0.0008467±77	0.0000992±32	0.54±2	1.81±6	308.936±10	38±3	1.90±6	
NS-3-9	451	0.0000090±4	0.0006357±65	0.0000970±33	0.56±2	1.77±6	395.176±10	40±3	1.87±6	
NS-3-10	443	0.0000082±4	0.0006712±68	0.0000968±35	0.51±2	1.77±6	349.863±10	36±3	1.85±7	
NS-3-11	282	0.0000091±5	0.0005897±78	0.0000958±41	0.57±3	1.75±7	307.73±10	42±3	1.84±8	
NS-3-12	259	0.0000089±6	0.0006003±86	0.0000986±44	0.56±3	1.80±8	379.724±10	39±3	1.90±9	
NS-3-13	158	0.0000096±8	0.0006438±107	0.0000824±54	0.60±4	1.50±10	431.956±10	54±7	1.59±11	
NS-3-14	154	0.0000087±7	0.0005420±100	0.0000954±51	0.54±4	1.74±9	460.554±10	40±4	1.83±10	

Table 5.2 continued

Sample	U (ppm)	Measured		Corrected for Standard				Distance from the edge (μm)	Th age	$\frac{234}{238}U$ act(init)
		$\frac{230}{238}Th$	$\frac{232}{238}Th$	$\frac{234}{238}U$	$\frac{232}{238}Th$ act	$\frac{234}{238}U$ act				
NS-3-15	154	0.0000092±7	0.0006609±109	0.0000886±56	0.57±4	1.62±10	543.732±10	46±5	1.71±11	
NS-3-16	166	0.0000079±7	0.0005618±98	0.0000966±52	0.49±4	1.77±9	514.024±10	35±4	1.84±10	
NS-3-17	174	0.0000100±7	0.0005374±93	0.0000896±53	0.63±4	1.64±10	459.252±10	51±6	1.74±10	
NS-3-18	456	0.0000103±4	0.0005383±60	0.0000965±32	0.65±3	1.76±6	583.095±10	48±3	1.87±6	
NS-3-19	431	0.0000111±5	0.0005749±64	0.0000945±32	0.69±3	1.73±6	741.379±10	54±4	1.85±6	
NS-3-20	426	0.0000103±5	0.0005722±64	0.0000927±33	0.64±3	1.69±6	807.421±10	50±4	1.80±7	
NS-3-21	420	0.0000112±5	0.0006049±66	0.0000928±32	0.70±3	1.69±6	828.87±10	55±4	1.81±6	
NS-3-22	413	0.0000117±5	0.0006849±71	0.0000962±29	0.73±3	1.76±5	985.943±10	56±4	1.89±6	
NS-3-23	401	0.0000115±5	0.0006631±71	0.0000918±32	0.72±3	1.68±6	955.176±10	59±4	1.80±6	
NS-3-24	409	0.0000129±5	0.0006642±71	0.0000914±33	0.81±3	1.67±6	955.308±10	69±5	1.81±7	
NS-3-25	409	0.0000132±5	0.0006899±72	0.0000938±28	0.83±3	1.71±5	1099.066±10	68±4	1.87±6	
NS-3-26	399	0.0000126±5	0.0007150±74	0.0000936±30	0.79±3	1.71±6	1125.511±10	64±4	1.85±6	
NS-3-27	413	0.0000129±5	0.0007118±73	0.0000929±30	0.81±3	1.70±5	1198.165±10	67±4	1.84±6	
NS-3-28	402	0.0000134±5	0.0007538±76	0.0000910±30	0.84±3	1.66±5	1383.645±10	73±5	1.81±6	
NS-3-29	387	0.0000153±6	0.0009758±88	0.0000938±29	0.96±3	1.71±5	1307.592±10	83±6	1.90±6	
NS-3-30	404	0.0000131±5	0.0007084±73	0.0000912±28	0.82±3	1.67±5	1228.57±10	70±5	1.81±6	
NS-3-31	401	0.0000145±5	0.0007229±75	0.0000961±27	0.91±3	1.76±5	1533.137±10	74±5	1.93±5	
NS-3-32	385	0.0000136±5	0.0007746±79	0.0000920±31	0.85±3	1.68±6	1576.749±10	73±5	1.84±6	
NS-3-33	412	0.0000142±5	0.0006990±72	0.0000972±30	0.89±3	1.78±5	1700.64±10	71±5	1.95±6	
NS-3-34	413	0.0000142±5	0.0007396±75	0.0000904±28	0.89±3	1.65±5	1940.149±10	79±5	1.82±6	
NS-3-35	391	0.0000137±5	0.0007642±78	0.0000902±28	0.86±3	1.65±5	1841.756±10	75±5	1.80±6	
NS-3-36	386	0.0000149±6	0.0007715±79	0.0000913±29	0.93±3	1.67±5	1782.663±10	83±6	1.85±6	
NS-3-37	385	0.0000148±6	0.0008093±81	0.0000935±29	0.93±3	1.71±5	1991.673±10	80±5	1.89±6	
NS-3-38	393	0.0000139±5	0.0007743±78	0.0000945±28	0.87±3	1.73±5	2065.165±10	72±5	1.89±6	
NS-3-39	392	0.0000145±6	0.0008329±81	0.0000937±29	0.91±3	1.71±5	2128.565±10	77±5	1.89±6	
NS-3-40	381	0.0000136±5	0.0008242±82	0.0000927±28	0.85±3	1.69±5	2270.027±10	72±5	1.85±6	
NS-3-41	376	0.0000133±5	0.0008209±82	0.0000890±32	0.83±3	1.63±6	2273.278±10	74±5	1.77±6	
NS-3-42	376	0.0000133±5	0.0007896±81	0.0000909±29	0.83±3	1.66±5	2208.62±10	72±5	1.81±6	

Profile 1, which traverses the thickest section of the main vein (3.6 mm), comprises 14 analyses placed across the vein in groups of three. These groups are placed symmetrically in the middle, near the contacts and at the mid distance between the centre of the vein and its contacts. Profile 1 show ages ranging from ~150 kyr, limited to the middle of the vein, to ages as low as ~50 kyr which are in close proximity to the contacts.

Profile 2 and 3 both traverse the main vein, however, both traverses have the analyses evenly distributed evenly over 3 mm between the two contacts and show a range of ages from ~150 kyr in the middle to about 50 kyr in the outer parts of the vein.

5.6.2 *Nangcarrong Spring*

A total of 56 SHRIMP analyses of the Nangcarrong Spring sample form two traverses within the main fracture filled by porous opal (Table 5.2, Figure 5.9). One traverse is located across the vein with the distance between the spots equal to 1-2 spot sizes (Nangcarrong Spring 1), where as the other traverse across the main vein (Nangcarrong Spring 3) is represented by groups of three spots located approximately parallel to the boundaries of the fracture. Eight analyses (Nangcarrong Spring 2) were placed in a smaller vein (0.6 mm).

The uranium concentration in this sample varies greatly from 0.06 to 622 ppm with errors close to 15%. These concentrations are significantly higher than those observed in the Yalgoola Well opal. As a result individual ^{230}Th - ^{238}U - ^{234}U / ^{238}U ages have smaller errors than those from Yalgoola Well opal which allow increased confidence in recognition of age variations across the vein where ages in the middle are in the range of 70-80 kyr and decrease towards 40-50 kyr near the boundaries. The oldest ages in this sample ranging from 117 to 82 kyr are obtained where the opal forms an irregular network of small veins and patches.

5.7 Discussion

The SHRIMP data obtained for Yalgoola Well and Nangcarrong Spring samples suggest that opal deposition within calcrete deposits in the Northern Yilgarn Craton

continued for tens of thousands of years (between 150 and 40 kyr). The average ages observed in the Yalgoola Well sample are slightly older than those displayed by the Nangcarrong Spring sample, although ages between about 70 and 100 kyr are found in both samples. A detailed discussion on the opal vein orientation, growth rates and relationship to climate follows.

5.7.1 Opaline silica vein orientation and formation

The symmetrical decrease of ages from the centres of the main veins towards the contacts with the calcrete, suggests that the precipitation of opal did not take place as an open space filling, but rather as replacement of carbonate possibly along microscopic fractures, in what is determined to be antitaxial growth. In other words, the growth from the centre of the vein requires simultaneous dissolution of calcrete and precipitation of opaline silica.

A number of studies suggested that although silica is mobile under variety of pH conditions, significant proportion of silica carrying groundwater is acidic. Milnes and Twidale (1983) described association of bleached kaolin rich zones formed in arid conditions of central and southern Australia. According to these authors, acid solutions within the bleached zones can be in equilibrium with most minerals except quartz leading to dissolution and resorption of this mineral and transfer of silica into the groundwater. More recently Lee and Gilkes (2005) investigated the geochemistry of groundwater near Merredin, Western Australia, and found that the acid, moderately saline groundwater was near equilibrium with amorphous silica, whereas more neutral water corresponded to undersaturated conditions. Associations of silica-rich solutions and suggested acidity of these solutions can facilitate dissolution of carbonate and precipitation of opal inferred from the U-series analyses of opal samples from Yalgoola Well and Nangcarrong Spring. It is likely that carbonate dissolution under the acid conditions opens the space for opal precipitation, neutralising groundwater at the same time. However, according to Milnes and Twidale (1983) the solubility limits of silica are not influenced substantially by pH of the groundwater, at least when pH is lower than pH=9. Therefore, change in pH on its own probably cannot drive precipitation of opal and additional concentration of silica in the solution by evaporation is required to initiate deposition of silica in the veins.

Observed symmetrical distribution of ages relative to the axes of veins also suggests a sub-vertical orientation of fractures during the opal deposition despite replacement processes being a consequence of chemical gradients which are not likely influenced by gravity. Horizontal arrangement is influenced by gravitational field and will result in systematic change of ages from one contact of a vein to another. Even when considering a carbonate replacement mechanism, the first layer of precipitated opal is expected to change permeability. As a result precipitation conditions above and below this layer are expected to be different, which would probably lead to asymmetry in the opal growth rates and U-series ages. Horizontal alignment of some groundwater silcrete veins suggests possible water table control over silicification (Anand and Paine, 2002).

5.7.2 Interpolation of data for individual profiles

Comparison of growth rate variations along the individual profiles in the same sample is complicated to some degree by the absence of perfect layering of opal parallel to the elongation of the veins. As a result ideal correlation of opal growth rates parallel to the vein boundaries is not possible. However, most of the major peaks can be recognised in all profiles when the growth rate is plotted against the age (Figure 5.10). Under the circumstances the best available way of characterising growth rate variations in the individual opal samples is to average the data obtained for the three profiles or constrain a combined cumulative growth curve similar to that described in the previous section, but based on all data for the sample. Both approaches result in a similar combined growth rate vs. time curves for individual samples (Figure 5.13).

Consequently, the better way of comparing and combining data obtained for individual profiles within the samples is to investigate cumulative probabilities where accumulated thickness of opal is plotted against the age as illustrated by Figure 5.11. To produce these plots, mid points between the nearby SHRIMP spots have been determined for all profiles and it has been assumed that the opal between each of pairs of mid points has grown instantaneously at the time defined by the relevant SHRIMP analysis (Figure 5.9). The best fit curve was then determined for each profile using cubic spline interpolation. Taking first derivative of these curves

with respect to the age defines growth rate of opal at any time, giving an opportunity to investigate opal growth rate variations in time.

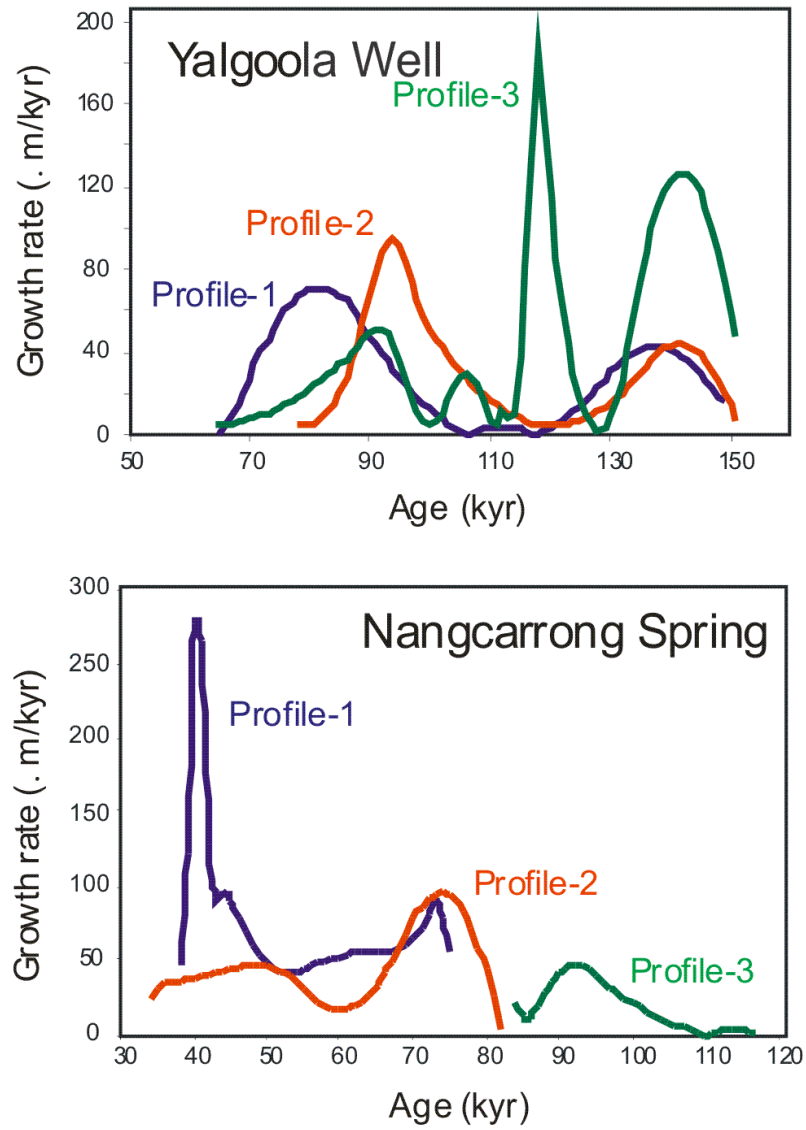


Figure 5.10 Variation of opal growth rate in time determined from individual profiles for Yalgoolaa Well and Nangcarrong Spring samples.

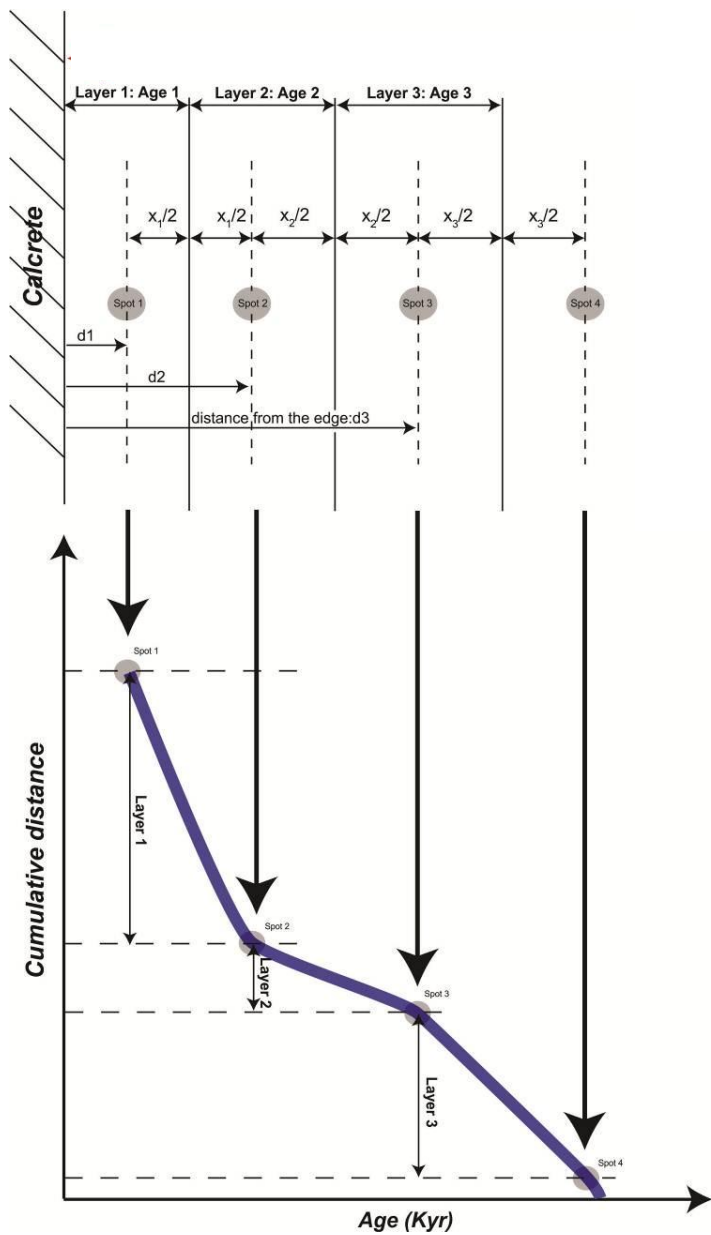


Figure 5.11 Constraining growth curves for the analytical profiles; top diagram shows an idealised sketch of a profile across the opal sample with the SHRIMP spots where lengths bound by boundaries half way between the spots are assumed to have an age similar to a SHRIMP spot between these boundaries; bottom diagram illustrates transformation of these length and age information to construct an average cumulative growth curve (shown in blue).

5.7.3 Continuous or episodic growth rates?

Consistent decrease of ages from the middle of veins to their outer parts displayed by all profiles in all samples shows that this variation is not a result of random analytical variation. In addition, the presence of a visible change in curvature of the profiles

(Figure 5.9) indicates that the opal growth rate was not constant during the entire time interval between 150 and 40 kyr recorded by the two samples.

The observed patterns can be interpreted to represent several episodes of very fast growth of opal interrupted by the periods of absence of silica precipitation. If that is the case, calculating average ages from the middle and outer parts of the veins suggests two episodes of deposition at 123 ± 12 and 77 ± 6 kyr for the Yalgoolah Well sample and three episodes at 94 ± 7 , 72 ± 2 and 44 ± 2 kyr recorded by the Nangcarrong Spring sample. However, some maximums visible in the age distribution pattern are shifted slightly relative to these average age estimates, while others are not recorded at all. In addition, the youngest average age for the Nangcarrong Spring sample is determined with a high MSWD (low probability), indicating that the groups of analyses used to estimate this age do not represent a single population.

These observations favour continuous rather than episodic silica precipitation, which can be expressed by constraining cumulative deposition curves (Figure 5.12). Differentiating the equation for each curve and combining the results from different profiles yields the overall variation of the silica precipitation rate in time. The estimated precipitation rate variation obtained from both opal samples shows three maxima with one near 90 kyr that is visible in both samples. Additionally, the data from the Yalgoolah Well opal reveals an increased precipitation rate at about 130-140 kyr and at about 115-120 kyr, while those for the Nangcarrong Spring sample show high precipitation rates at about 70 and 45 kyr (Figure 5.13). Considering the similarity of precipitation rates obtained from both samples near 90 kyr, the combined precipitation rate curve, representing the entire time interval recorded by the two analysed samples, can be determined by averaging all results obtained for these samples (Figure 5.14). A similar result suggesting periodic increases in opal growth is obtained when using a different approach to the analysis of growth rate variations in the studied samples, indicating that observed periodicity is not an artifact related to the analytical issues or specific choice of data treatment procedure. In this approach relationships between age and location of analytical spots are determined by folding each profile at a point in the middle of vein. Position of this point is determined by minimising difference between two curves fitted through the analytical spots at each shoulder of the profile. Combining these profiles allows testing of analytical data against theoretical models predicting possible variations of

opal growth rates. Testing three of these models, which assume either: (i) constant growth rate, (ii) periodic growth rate or (iii) periodic growth rate with variable oscillation amplitude, supports periodicity recorded in the samples. Statistical comparison of these models indicates that the periodic growth rate with variable oscillation amplitude gives the best description of the data. It also defines the period of oscillation equivalent to 25.8 kyr.

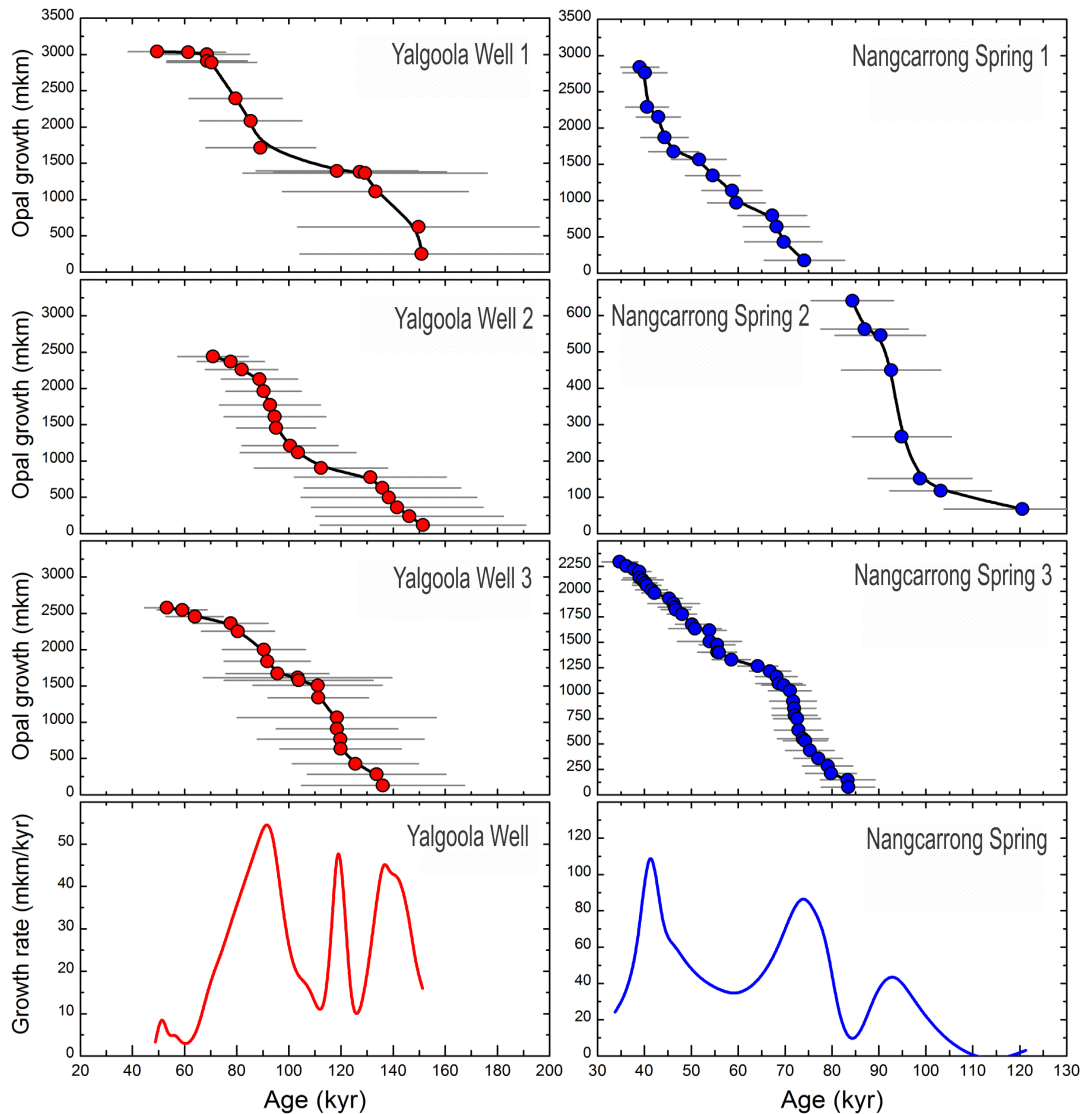


Figure 5.12 Cumulative precipitation curves that describe silica precipitation with time for the three profiles from the Yalgoolaa Well (left) and Nangcarrong Spring (right), respectively.

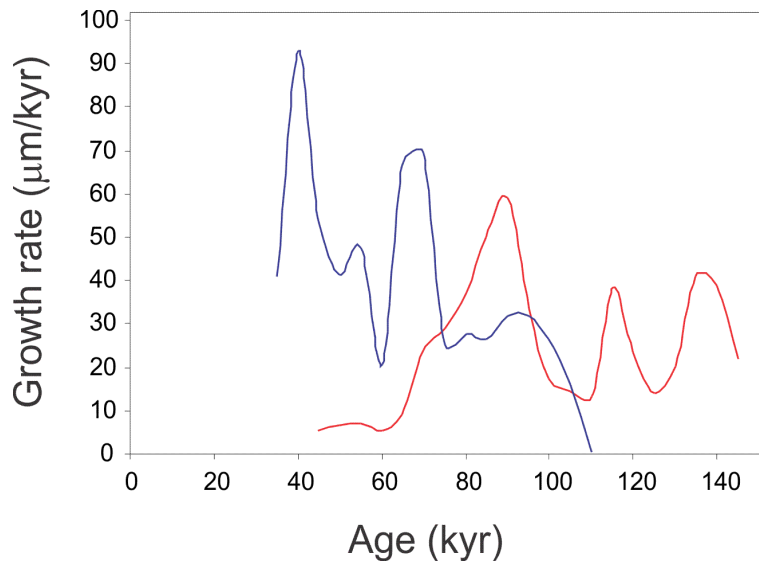


Figure 5.13 Average growth rate variation in time for Yalgooloo Well (red) and Nangarrong Spring (blue) samples.

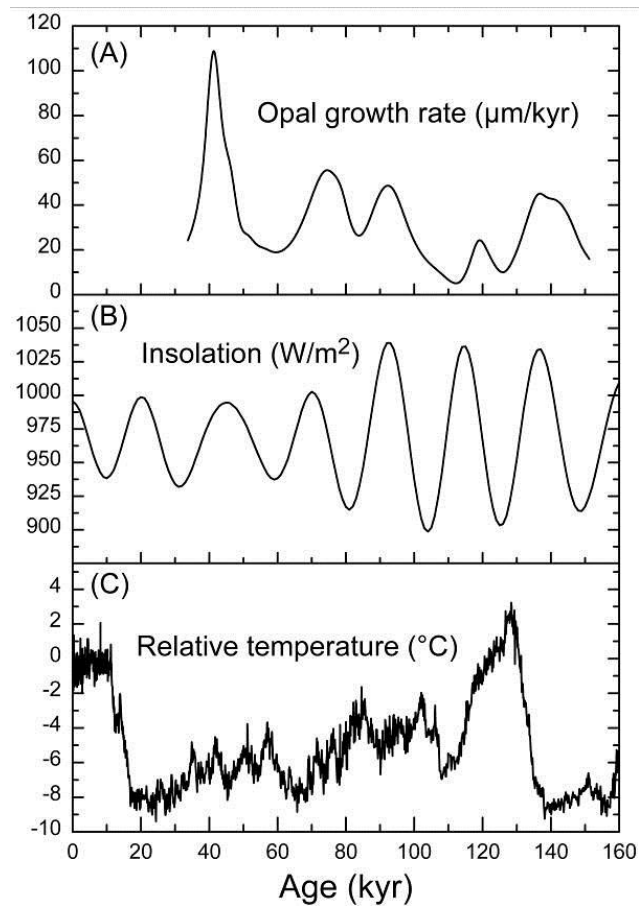


Figure 5.14 Correlation between the recorded opal growth rate and the global climate variation. A. opal growth rate variations; B. Southern Hemisphere summer (December–February) insolation pattern (Berger and Loutre, 1991); C. Temperature variation during the last 160 kyr, recorded by the Vostok ice core (from Jouzel *et al.*, 1987).

5.7.4 Opal deposition rates compared to Yucca Mountain

The overall variation of the opal growth rate closely follows the Southern Hemisphere insolation pattern, indicating that opal precipitation is linked to the Earth's climate cycle. Further understanding of this link can be gained from the comparison of Western Australian opals with the extensively studied example of opal precipitation at Yucca Mountain in Nevada (USA). Modern climate conditions in Nevada and Western Australia are very similar and characterised by relatively low rainfall and high evaporation rates. It is also likely that these conditions were similar in the two areas during the last 100-200 kyr. However, silica precipitation rates recorded at Yucca Mountain are very low, close to 1mm/Ma (or 1 μ m/kyr) (e.g. Neymark *et al.*, 2000a, Paces *et al.*, 2004a, 2010) compared to the 10-100 μ m/kyr rates estimated from Yalgoola Well and Nangcarrong Spring samples. This difference is likely to be related to the supply of silica to the precipitation sites. At Yucca Mountain opal precipitates in the water undersaturated zone, by evaporating droplets of water seeping through the pores and cavities in the rocks. This limited amount of water restricts opal precipitation also resulting in relatively constant growth rate at least during the past 1 myr. Even though these conditions appear to buffer the growth rate to a constant value independent of possible variations in rainfall in the area, they also result in a highly variable U concentration across the growth profile, which is reflected in the strong zoning visible in cathodoluminescence images (Paces *et al.*, 2010). Contrary to the Yucca Mountain opals, investigated opal samples from Yilgarn Craton have formed near the top of the saturation zone, where water (and consequently silica) supply is significantly larger. In addition, variations in water supply are more likely to be influenced significantly by the variations in rainfall, resulting in visible variability of opal growth rates.

5.7.5 Opal deposition and global climate

The variation in the observed opal growth may be correlated to regional palaeoclimatic changes, specifically fluctuations in rainfall and temperature which consequently affect subsurface conditions and processes.

This variation appears to exhibit periodicity that can be linked to the Earth's orbital variations (Paces *et al.*, 2010). Yilgarn opals show opposite characteristics with the

variable growth rates (with periodicity that is probably determined by the astronomical forcing) and relatively constant U concentrations. The observed divergence in variability of growth rate and U concentrations in opals from Yucca Mountain and Yilgarn Craton has been determined by the difference in the silica precipitation mode under water unsaturated and water saturated conditions. In both locations silica deposition is determined by the supply of silica saturated solution and any observed variations are likely to be linked to the long term changes in the rainfall. In both cases decreased rainfall should result in the reduction of supply. However, in the water unsaturated conditions already characterised by extremely slow silica precipitation rates, possible further reduction associated with the limited rainfall could be very difficult to detect with the given spatial resolution of in situ analyses on a relatively short time scale of a few thousand years, while the change to slow growth is readily recognizable when contrasted with the fast deposition rates characterising periods of precipitation in the water saturated conditions. On the other hand reduction in the rainfall, accompanied by the higher evaporative concentration of U in the groundwater would have a larger effect on variability of U content in the water from unsaturated zone and hence silica precipitating in this environment, while the effect will be softened in the larger volume of groundwater from the saturated zone.

Apparent link between the opal growth rate and rainfall allows placing constraints on the climate variations in Western Australia during the late Pleistocene between 150 and 40 kyr. Modern rainfall patterns in northern to central Yilgarn Craton are determined by low-pressure systems pushed into the continent from the North-West during the winter time (June-August). However, northern parts of the continent are dominated by the equatorial systems with the maximum rainfall during the summer time (December-February). It is possible that in the past Southern Hemisphere insolation maximums increased the temperature gradient between polar and equatorial regions helping to extend the influence of these systems further south resulting in much a wetter climate with higher rainfall within the northern to central Yilgarn Craton and increased precipitation rate of opal in the region. It is also notable that the precipitation rate recorded in the analysed opal samples appears to show gradual increase of both maximums and minimums in the growth rate curve (Figure 5.14) from older to younger parts of the samples. This is negatively

correlated with the general trend of global temperature showing a decrease from the interglacial at about 120-130 kyr towards the minimum temperature during the glacial at the end of Pleistocene. This negative correlation could be a consequence of increasing temperature contrast where the combination of increasing ice cover in the polar areas as a result of decreasing global temperature and higher temperature closer to the equator during the insolation maximums results in the gradual amplification of rainfall in the central Yilgarn Craton towards the end of Pleistocene.

This investigation of opals from the Yilgarn Craton, as well as previous studies of Yucca Mountain samples, indicate that the opals formed by precipitation of silica from the groundwater preserve record of past climate variations. It is possible that growth of Australian precious opal is also controlled by similar mechanisms, although a direct proof of this is not possible as a result of very low U concentrations commonly observed in these opals.

6 AGATE FROM SOUTH DAKOTA, USA

6.1 Introduction

Agates are classified as gemstones despite being made of chalcedony and are greatly sought after because of their striking colours and geometry. Fairburn agates are found in southwestern South Dakota, USA, especially around the town of Fairburn, but have been found as far south as northwestern Nebraska. They differ from most agates from around the world due to their intricate banding and range of bright colours.

Three thin slabs of Fairburn agate from in and around the Black Hills area of South Dakota (Figure 6.1) were considered for possible age determination using SHRIMP. The samples fluoresced brightly under UV light indicating potential high uranium concentration and subsequent suitability for SHRIMP dating.

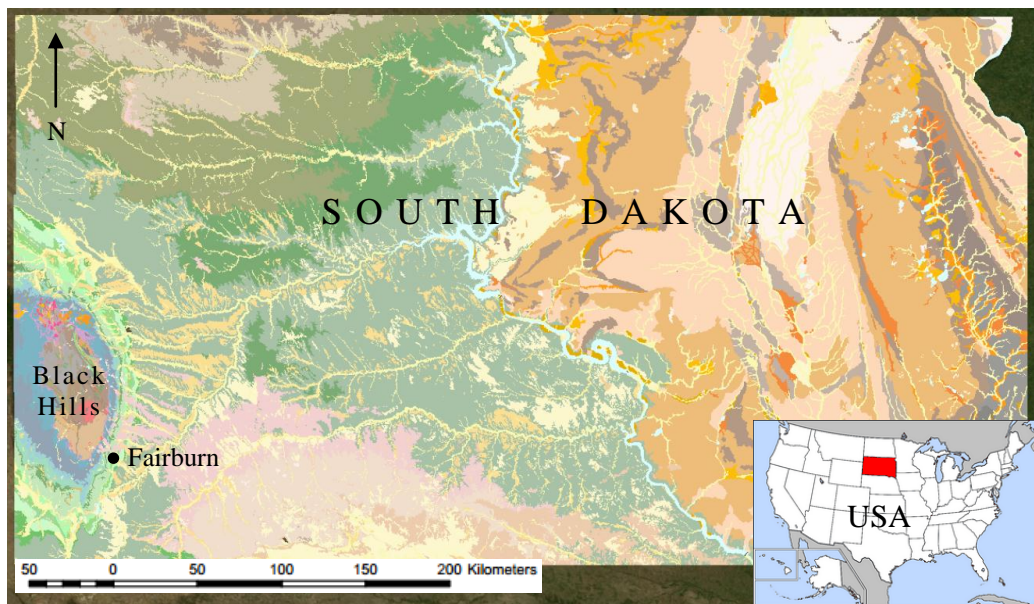


Figure 6.1 Location of the Black Hills and Fairburn, South Dakota, USA with the geology (from Martin *et al.*, 2004) with inset showing location of South Dakota (in red) within the USA.

A review of the literature on South Dakota agate suggest the age of the agate to be younger than ~300 Ma (the age of the host rock). Subsequently, ages were estimated

to be over the limit for U-series dating and so short lived isotopes of U and Th were not measured and only U-Pb ages were calculated. The calculated ages for samples within this study range from ~35 Ma to ~640 Ma and provide an interesting contribution to the depositional history of the agates, as well as significantly extend the limit of datable silica samples to Phanerozoic and perhaps even to Late Proterozoic. This is particularly surprising, considering that silica samples are expected to experience aging, i.e. change of crystallographic state in time associated with some chemical modifications, including reduction in U concentration (Moxon and Rios, 2004; Götze *et al.*, 2012).

6.2 Geology of South Dakota – Black Hills area

The Black Hills, located in southwestern South Dakota, constitutes a Laramide domal uplift that defines the eastern cratonic margin of the Archaean Wyoming Craton. The Precambrian basement consists of metasedimentary rocks intruded by the ~2550 Ma Little Elk gneissic granite and a similar aged granite at Bear Mountain (Gosselin *et al.*, 1988; Ratte and Zartman, 1970). It is overlain by two nonconformable rift successions of Paleoproterozoic sedimentary and igneous rocks. Episodic mafic magmatism associated with rift-basin sedimentation in the Black Hills occurred between ~2480 Ma (Dahl *et al.*, 2003) and ~1880 Ma (Redden *et al.*, 1990). Intrusion of the Harney Peak granite at ~1.7 Ga (Redden *et al.*, 1990) caused domal structures and late faulting leading contact metamorphism of the surrounding country rock. Exposure of the entire Precambrian complex occurred at ~520 Ma and during the 80–50 Ma Laramide orogeny (Lisenbee, 1978).

The Black Hills have at least three periods of Paleoproterozoic deformation and at least two phases of metamorphism (Redden *et al.*, 1990). The deformation events folded turbidites and volcanic rocks into east-northeast trending nappes and thrusts which were then refolded into north-northwest trending upright folds. The nappes and thrusts formed during a thrusting event (Redden *et al.*, 1990) associated with docking of a Central Plains arc terrane south of the Black Hills at ~1780 Ma (Dahl *et al.*, 1999). The second set of folds were accompanied by a widespread regional metamorphic event (DeWitt *et al.*, 1986; DeWitt *et al.*, 1989) that resulted from tectonic burial associated with Wyoming–Superior continental collision between

~1770 and 1715 Ma, during the assembly of western Laurentia (Dahl and Frei, 1998; Dahl *et al.*, 1999).

By the end of the Precambrian the South Dakota area had been eroded to a relatively flat plain with low mounds of granite and resistant quartzite ridges (Gries, 1996). Periods of transgression and regression, and associated weathering and erosion, occurred for most of the Palaeozoic depositing sequences of sandstone, shale and limestone. At the start of the Pennsylvanian period, seas transgressed from the south and reworked a red soil that had accumulated on the Mississippian limestone terrain. Alternating beds of fine sand and dolomite were deposited on the red soil (Gries, 1996). Regression occurred followed by another transgression leading to the deposition of thin layers of red to yellow cross-stratified sandstone, dolomite, limestone and shales of the lower Minnelusa Formation (Strobel *et al.*, 1999) in a shallow marine environment. Near the end of the Pennsylvanian (~325 to ~299 Ma) the sea regressed long enough for another red soil to form and the upper Minnelusa Formation was deposited and contains gypsum and fine sands. The upper part of the Minnelusa Formation also may contain anhydrite, which generally has been leached resulting in collapsed breccias (Braddock, 1963).

Erosion continued until the Triassic and shallow continental seas submerged parts of western South Dakota in the Jurassic. The end of the Cretaceous marks the final retreat of the continental seas from South Dakota. The Tertiary was dominated by erosional processes and by the Early Oligocene streams could no longer carry away their erosion products and deposition began on the plains adjacent to the Black Hills. Consequently, the lower two-thirds of the Black Hills became buried by clays and sands. Local volcanic activity contributed large volumes of windblown volcanic ash to the sediments. At the end of the Eocene the climate dried and alluvial material, known as the White River Group, consisting of mostly volcanic ash, was deposited in fluvial, lacustrine and eolian environments (Gries, 1996).

6.3 Agate composition and structure

Agates are defined as rounded bodies, 1 to 100 cm in size, of concentric, regularly spaced, millimetre to centimetre-thick layers of microcrystalline chalcedony intergrown with opal-A, opal-CT and/or moganite, an inner layer of coarse-grained

low-defect quartz crystals and a central void which can be wholly or partially filled with macrocrystalline quartz or fluorite (Wang and Marino, 1990; Wang and Merino, 1995; Götze *et al.*, 2009). The layers have sharp boundaries and are usually parallel to the walls of the cavity in which they are deposited/formed but gravity controlled horizontal banding (geopetal structures) can occur, although this is rare. The band in contact with the wall is generally thicker than comparable bands in the inner regions of the agate (Moxon, 2002). Agate have very high silica purity with non volatile impurities being generally <1% (Flörke *et al.*, 1982). The major impurity in agate is the total water (free H₂O and defect site silanol Si-OH) with a concentration of up to 2% (Graetsch *et al.*, 1985).

The different microstructural and compositional characteristics of the silica polymorphs, produces the rhythmic concentric banding such as the fibres in every alternate band being twisted, fine and catholuminescent as opposed to untwisted, coarse and non-luminescent in the adjacent bands (Wang and Merino, 1995). The fibre twisting is caused by trace element substitution for Si⁴⁺ where fibres that grow through a decreasing trace element gradient incorporate a high content of the trace elements along their edges and since the cations are larger than the Si⁴⁺ the fibres have to grow twisted to accommodate the additional peripherical trace element content (Merino *et al.*, 1995).

The colouring in the bands can be caused by trace elements, textural changes (Moxon and Reed, 2006) and porosity (Götze *et al.*, 2012) Reddish bands are attributed to iron oxides, mostly hematite, although other trace elements (Mn, Co, As and Cr) contained in iron oxides can be present acting as pigments (Götze *et al.*, 2001; 2009). Variation of shades within the reddish bands is the result of changes in elemental ratios, densities or grainsize of mineral or elemental impurities (Götze *et al.*, 2012). Blueish-grey colours and white can be the result of light scattering off the fine chalcedony fibres and generally have higher porosity than the coloured bands (Götze *et al.*, 2012).

The banding in agate shows repetitive textures and compositions including alternating layers consisting of twisted and untwisted fibrous chalcedony, respective high and low cation concentration, alternations in crystal size, banding of water inclusions, chevron interferences and micrometer scale concentric bands with

alternating high and low OH content (Wang and Merino, 1990). Agate has not been produced synthetically under laboratory conditions and consequently numerous models have been proposed to explain the banded texture produced by the rhythmic segregation of silica polymorphs.

6.4 Different types of agates – volcanic-hosted vs. sedimentary-hosted

Agates frequently occur in vesicular volcanic rocks but the agates from South Dakota are of interest as they are found in sedimentary host rocks. Little work has been done on sedimentary hosted agates, however, a moderate amount of research has been done on agates from a volcanic host rock and although this work cannot be directly applied to agates of sedimentary origin it may provide some understanding of the conditions required for sedimentary agate formation.

6.4.1 Volcanic-hosted agate

Mechanisms that produce agates in volcanic environments are not completely understood, however, volcanic-hosted agates are thought to have formed in vugs created by the vesiculation of the volcanic host by either precipitation from convecting siliceous hydrothermal fluids and gases (Götze *et al.*, 2012) or by in situ crystallization of a silica gel to chalcedony. Both mechanisms require a large silica concentration.

In the hydrothermal fluid model the type of mineral deposited is dependent on significant amounts of available fluids and gases (e.g. CO₂ and HF), the level of silica saturation and trace element concentration (Heaney and Davis, 1995; Götze *et al.*, 2001; 2012). Highly concentrated siliceous fluids can precipitate amorphous silica and less siliceous fluids precipitate quartz, producing the concentric banding. Silica supersaturated hydrothermal magmatic solutions are the most probable source of the silica for agate genesis although Götze *et al.*, (2012) suggests that the fluids may also include meteoric water, which is often heated to temperatures of up to several 100 °C during volcanic activities. The silica supersaturation of the solution can occur by boiling, rapid cooling or reactions with fresh volcanic glass as well as solution mixing. The silica source could be mobilised during the alteration of the volcanic wall rocks by hydrothermal solutions or from events such as a late magma

deposition. Large volumes of siliceous fluid would be required to flow in and out of a cavity to produce an agate in this way requiring sufficient free liquid paths in the host rock (Götze *et al.*, 2012).

The second theory of deposition, crystallisation from a hydrous silica gel with trace elements, produces banding by chalcedony fibres growing due to morphological instability at the crystallisation front caused by the presence of cations which increase the crystal growth (Wang and Merino, 1995) and producing alternating bands of high and low cation concentration. The repetitive banding and oscillatory profile suggest self organisational crystallisation, a process in which systematically repetitive textures and compositions are produced by the internal dynamics of the growth and not by changing outside conditions (Wang and Merino, 1990). A proposed origin of the silica gel is trapped surface water under basalt flows (Merino *et al.*, 2001).

There is a general decrease in trace element concentration from rim to core and trace element content in the macrocrystalline quartz is less than in chalcedony, except for the high concentrations of B, Ge and U which can be higher in macrocrystalline quartz compared to chalcedony (Götze *et al.*, 2012). Volcanic hosted agates are also characterised by enriched light REE and low heavy REE trends (Götze *et al.*, 2001). Different agate bands can show a change in REE indicating that physio-chemical conditions can change during agate formation (Götze *et al.*, 2001). There is a similarity between the REE patterns of the agates and the parent volcanic rock suggesting that elements may be mobilised by circulating fluids from volcanic wall rocks (Götze *et al.*, 2001).

Uranium concentration in agate is higher than in the surrounding host rocks and is probably bound on microinclusions or adsorbed as uranyl complexes in the agate since no structural incorporation is possible Götze *et al.*, 2001). The high content of uranium in comparison to thorium indicates transport and accumulation by oxydising, hydrous fluids Götze *et al.*, 2001).

Another characteristic feature of volcanic-hosted agates is high $\delta^{18}\text{O}$ values which require the fluids to be enriched in ^{18}O relative to meteoric water. Variations in the oxygen isotope ratios between adjacent chalcedony bands indicate that the isotope

fractionation between quartz and water in some cases took place under non-equilibrium conditions, as may be explained by formation of agate from a noncrystalline precursor (e.g., chemically controlled self-organization from initially homogeneous gels as suggested by Wang and Merino, 1990).

Temperatures for formation have been determined to be between 50 and 120°C (Harris, 1989; Heaney, 1993) using oxygen isotope studies. Although the silica source, temperature and mechanism of crystallisation are yet to be thoroughly understood, the majority of research concludes that genesis starts with the polymerisation of siliceous fluids at temperatures <100°C (Heaney, 1993). Moxon (2002) suggests that the entry of the silica into the gas vesicle in a volcanic host is penecontemporaneous with the formation of the host rock, however, the initial formation of fibrous chalcedony from the silica source could possibly block the incoming silica solution.

As the agate ages, it undergoes changes in composition, such as decreasing moganite and internal water content, increasing quartz crystallinity and density (Moxon, 2002; Moxon and Rios, 2004, Moxon *et al.*, 2013). Moxon and Rios (2004) found no moganite in agate with a host rock of pre Silurian age and suggest that agate genesis would be penecontemporaneous with the formation of the host rock. Moxon *et al.*, (2006) showed that agate from metamorphosed host rocks shows an advanced crystallisation, zero moganite and occasional partial breakdown in the fibrous chalcedony. Post depositional changes in temperature will also produce different silica phases (Moxon and Carpenter, 2009).

6.4.2 Sedimentary-hosted agate

Sedimentary-hosted agates are rare. They are almost exclusively found in limestone (Götze *et al.*, 2009) and the most plausible theories of genesis are; the successive precipitation from groundwater or hydrothermal solution in an empty space, crystallisation of a silica-rich lump already accumulated in that space (Wang and Marino, 1990) or as a product of silica digenesis where carbonate is replaced by silica on a volume-for-volume basis (Knauth, 1994). ‘Holly-leaf’ patterned banding in agates from sedimentary hosts is common suggesting that genesis is different from the wall-lining banding of agates in igneous rocks (Moxon and Reed, 2006).

Trace element concentrations are similar to those in volcanic-hosted agate and show lower concentrations in macrocrystalline quartz compared to chalcedony. The uranium concentration has been reported to be as high as 71 ppm suggesting that uranium-bearing fluids, were involved. Uranium concentrations in sediment-hosted agate are significantly higher than determined in volcanic-hosted agate and was measured to be relatively constant over the agate unlike most elements which showed fluctuation (Götze *et al.*, 2009).

Götze *et al.*, (2009) propose that agate crystallized in a rapid continuous process under non-equilibrium conditions from a silica gel but with interactions from hydrothermal fluids, at least during the formation of the outer agate layer. Rare earth element data from sedimentary-hosted agate and the surrounding rock shows distribution patterns suggesting that the mineralising fluids do not originate directly from the surrounding rocks and that REE patterns are similar to those of quartz from hydrothermally overprinted rocks. The presence of REE carbonates also support the participation of hydrothermal fluids in the agate formation or that a later hydrothermal overprint of the sedimentary rocks took place (Götze *et al.*, 2009). The temperature of formation was calculated to be <120°C and that the layers of chalcedony and quartz are from the same silica source which is most likely a non-crystalline medium such as silica gel or a direct deposit of amorphous silica (Götze *et al.*, 2009).

6.5 Dating results for South Dakota agates

This chapter focuses on Fairburn agates from South Dakota, USA, which are valuable due to their sharp parallel banding and bright colours. They are found within the limestone Minnelusa Formation in south-western South Dakota, specifically around the Black Hills (Figure 6.1). It is unclear if the agate was precipitated in voids in Minnelusa Formation, or if were they formed in older rocks and transported as clastic material into the Minnelusa Formation.

Three thin slabs of Fairburn agates were sourced for the purpose of this study. Their specific location of origin is not known, however, all samples are from locations within 100 km radius of the Black Hills, South Dakota (Moxon T, 2004, personal communication, 26 June).

U-series data was collected in the first SHRIMP session, however, once the data was processed it was realised that the samples were in secular equilibrium (Table 6.1). Consequently, only U-Pb data was collected and interpreted.

6.5.1 SG7

The sample for SHRIMP analysis was cut from a 5 cm by 2 cm slab of agate (Figure 6.2). Both plain and UV light images of the slab show regular concentric banding highlighted by the change of colour from white to grey, as well as minor variations shown by fluorescence under the short wave UV-light. The thickness of the bands varies from approximately 1 to 5 mm and the banding is colloform in nature. The agate shows strong even fluorescence and is easily distinguished from the host rock via a sharp contact.

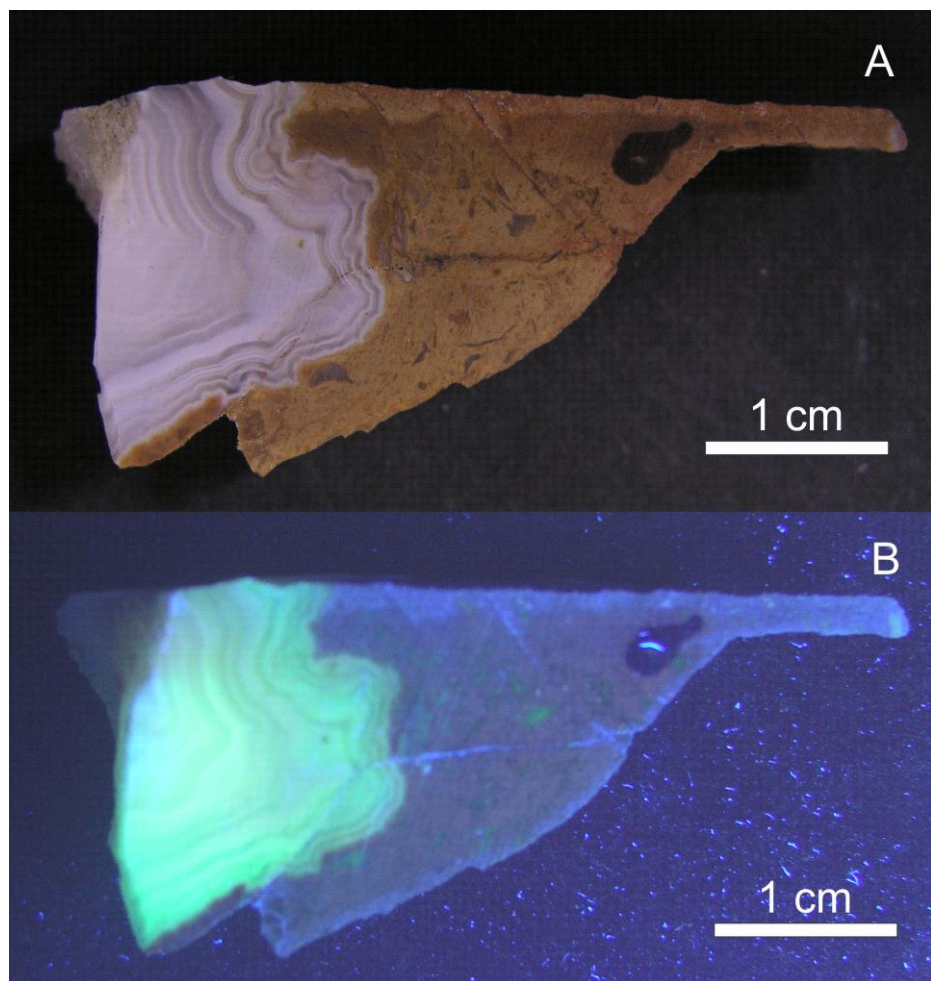


Figure 6.2 A) SG7 in plain light and B) under UV light.

SHRIMP analyses of 25 spots within the sample revealed a variable uranium concentration between 0.02 to 18 ppm with an average of 7.5 ppm (Table 6.1). The old age of the sample results in sufficient ^{206}Pb and ^{207}Pb counts to calculate ages with an acceptable level of precision.

$^{206}\text{Pb}/^{204}\text{Pb}$ ratios could not be analysed for spots with very low U concentration. Those spots also show very low ^{204}Pb counts, which are often comparable to the background, but in the spots with U above 5 ppm $^{206}\text{Pb}/^{204}\text{Pb}$ still appears to be rather low from 30 to 192. Consequently, analyses with less than 5 ppm uranium are not considered any further (analyses 3, 5, 6, 9, 13 to 18 and 20). As a result of a comparatively low U content in the sample, the errors of these ages for individual analytical spots are relatively large. The $^{232}\text{Th}/^{238}\text{U}$ ratio ranges between 0.001 and 3.5×10^{-5} indicating that the radiogenic ^{208}Pb contribution is negligible, making the $^{208}\text{Pb}/^{206}\text{Pb}$ non-radiogenic lead correction more reliable than the $^{204}\text{Pb}/^{206}\text{Pb}$ non-radiogenic lead correction.

Concordia diagrams for $^{207}\text{Pb}/^{235}\text{U} - ^{206}\text{Pb}/^{238}\text{U}$ corrected for ^{208}Pb (Figure 6.3) is used to examine the U-Pb system and shows an age of 42.3 ± 2.2 Ma. This age is supported by both the $^{206}\text{Pb}/^{238}\text{U}$ and $^{207}\text{Pb}/^{235}\text{U}$ weighted average ages of 42.1 ± 1.9 Ma and 42.3 ± 6.7 Ma respectively (Figures 6.4 and 6.5).

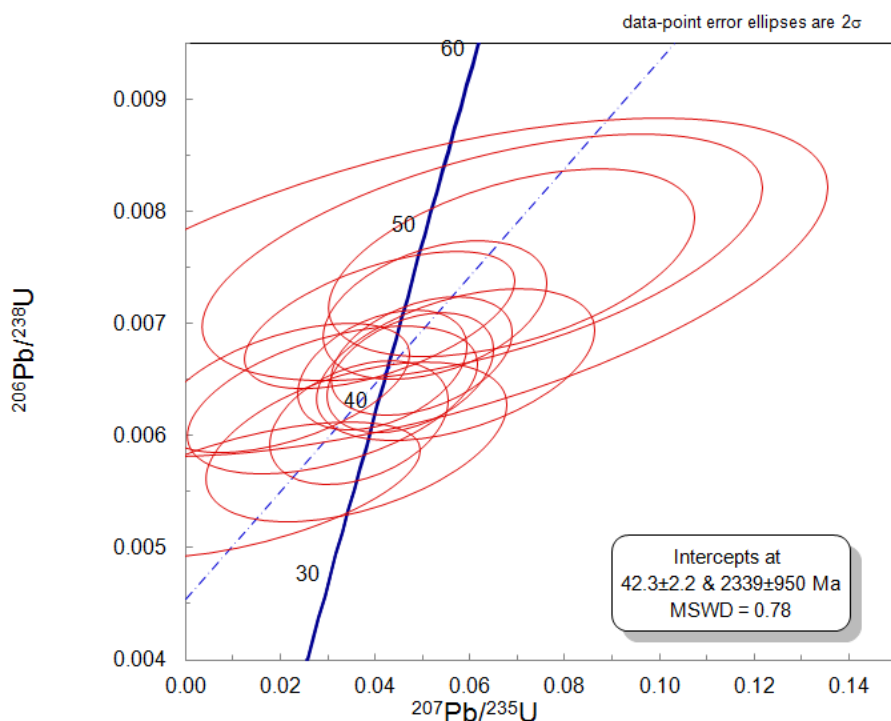


Figure 6.3 $^{207}\text{Pb}/^{235}\text{U}$ vs. $^{206}\text{Pb}/^{238}\text{U}$ concordia corrected for ^{208}Pb .

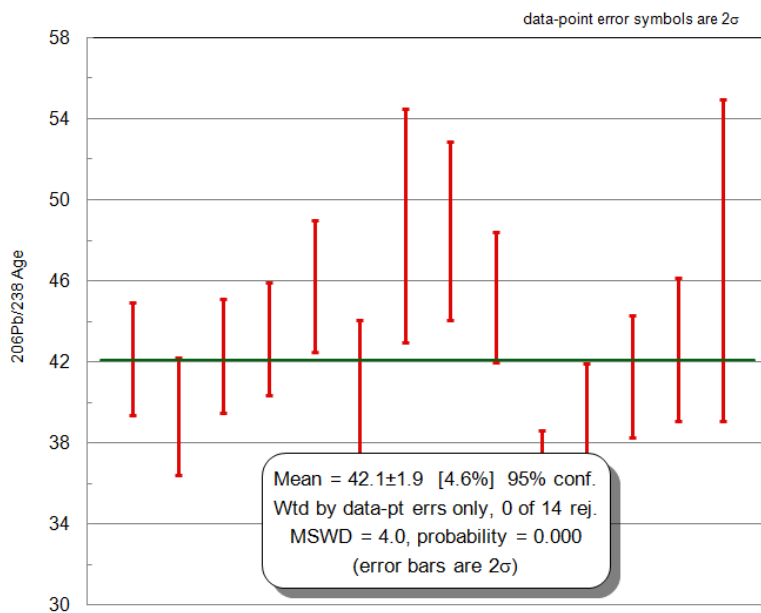


Figure 6.4 $^{206}\text{Pb}/^{238}\text{U}$ weighted average age corrected for ^{208}Pb .

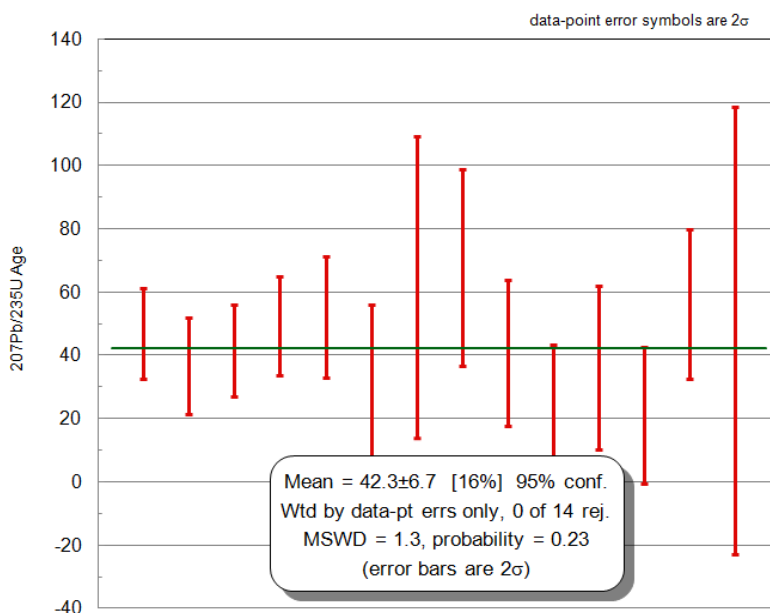


Figure 6.5 $^{207}\text{Pb}/^{235}\text{U}$ weighted average age corrected for ^{208}Pb .

The $^{206}\text{Pb}/^{238}\text{U}$ ages show some scatter, which is reflected in a relatively high MSWD possibly indicating a degree of incomplete resetting (i.e. an older component) present in the sample or may attributed to differences in growth. This, however, is difficult to investigate any further as the errors are rather large (especially in $^{207}\text{Pb}/^{235}\text{U}$) so if there is an upper intercept of the concordia it cannot be defined with any degree of precision.

Table 6.1 SHRIMP results for agate samples, South Dakota, USA (errors are 1σ).

N	U ($\mu\text{g/g}$) _a	$\frac{^{206}\text{Pb}}{^{204}\text{Pb}}$	$\frac{^{207}\text{Pb}}{^{206}\text{Pb}}$	$\frac{^{208}\text{Pb}}{^{238}\text{U}}$	$\frac{^{232}\text{Th}}{^{238}\text{U}}$	$\frac{^{230}\text{Th}}{^{238}\text{U}}$ act	$\frac{^{234}\text{U}}{^{238}\text{U}}$ act	$\frac{^{206}\text{Pb}}{^{238}\text{U}}$	$\frac{^{207}\text{Pb}}{^{235}\text{U}}$	f8b	$\frac{^{206}\text{Pb}}{^{238}\text{U}}$	$\frac{^{207}\text{Pb}}{^{206}\text{Pb}}$	$\frac{^{207}\text{Pb}}{^{235}\text{U}}$	
						<i>non-radiogenic lead</i>						^{208}Pb corrected	^{208}Pb corrected	^{208}Pb corrected
Sg7														
Sg7-1	17	149±41	0.176±0.009	0.327±0.017	0.00021±0.00005	1.558±0.432	1.279±0.309	0.008±0.0003	0.190±0.009	0.158±0.011	0.007±0.0002	0.052±0.00876	0.047±0.00719	
Sg7-2	14	192±64	0.144±0.009	0.261±0.017	0.00021±0.00005	2.000±0.506	1.569±0.360	0.007±0.0003	0.139±0.008	0.126±0.010	0.007±0.0002	0.043±0.00977	0.037±0.00767	
Sg7-4	17	104±22	0.168±0.009	0.319±0.017	0.00022±0.00005	1.366±0.382	1.357±0.304	0.008±0.0003	0.180±0.009	0.155±0.011	0.007±0.0002	0.046±0.00874	0.042±0.00729	
Sg7-7	19	85±18	0.154±0.009	0.265±0.016	0.00024±0.00005	1.433±0.411	1.485±0.316	0.008±0.0003	0.164±0.009	0.128±0.010	0.006±0.0002	0.054±0.00929	0.050±0.00785	
Sg7-8	15	123±35	0.143±0.010	0.237±0.017	0.00011±0.00004	1.582±0.458	1.000±0.277	0.008±0.0003	0.159±0.010	0.115±0.010	0.006±0.0002	0.054±0.01070	0.053±0.00965	
Sg7-10	13	173±92	0.142±0.013	0.275±0.025	0.00026±0.00007	1.347±0.533	1.515±0.389	0.007±0.0003	0.143±0.012	0.133±0.014	0.004±0.0001	0.036±0.01512	0.031±0.01248	
Sg7-11	5	114±57	0.191±0.021	0.350±0.039	0.00037±0.00012	2.023±0.905	1.724±0.610	0.009±0.0006	0.241±0.023	0.169±0.021	0.004±0.0002	0.060±0.02528	0.063±0.02420	
Sg7-12	11	111±42	0.167±0.015	0.271±0.026	0.00055±0.00011	2.059±0.651	1.046±0.331	0.009±0.0004	0.200±0.016	0.131±0.014	0.004±0.0002	0.066±0.01684	0.069±0.01579	
Sg7-19	14	92±23	0.207±0.012	0.429±0.025	0.00138±0.00014	0.848±0.347	1.629±0.364	0.009±0.0003	0.253±0.013	0.208±0.016	0.005±0.0002	0.042±0.01293	0.041±0.01165	
Sg7-21	9	94±35	0.200±0.016	0.459±0.034	0.00025±0.00007	1.274±0.601	0.889±0.381	0.007±0.0003	0.195±0.014	0.222±0.020	0.005±0.0002	0.018±0.01966	0.014±0.01458	
Sg7-22	8	184±92	0.152±0.014	0.281±0.027	0.00007±0.00004	1.457±0.596	0.733±0.328	0.007±0.0004	0.144±0.012	0.136±0.015	0.005±0.0002	0.044±0.01695	0.036±0.01299	
Sg7-23	15	81±20	0.155±0.011	0.334±0.023	0.00100±0.00012	1.627±0.470	0.846±0.255	0.008±0.0003	0.163±0.010	0.161±0.013	0.005±0.0001	0.024±0.01257	0.021±0.01072	
Sg7-24	13	134±50	0.155±0.013	0.248±0.022	0.00076±0.00011	1.628±0.515	0.866±0.274	0.008±0.0003	0.161±0.012	0.120±0.012	0.004±0.0001	0.062±0.01451	0.057±0.01203	
Sg7-25	6	28±11	0.178±0.030	0.341±0.058	0.00033±0.00013	0.512±0.512	1.653±0.585	0.009±0.0008	0.215±0.032	0.165±0.029	0.002±0.0001	0.048±0.03790	0.048±0.03569	
Badlands														
Badl-1	20	4649±4026	0.076±0.002	0.040±0.002	0.00016±0.00005	n.d.	n.d.	0.096±0.0031	1.002±0.039	0.019±0.001	0.094±0.0011	0.061±0.00184	0.788±0.03313	
Badl-2	20	1115±227	0.080±0.002	0.058±0.002	0.00010±0.00003	n.d.	n.d.	0.104±0.0022	1.140±0.030	0.028±0.002	0.105±0.0010	0.058±0.00124	0.804±0.02213	
Badl-3	27	2370±888	0.062±0.001	0.020±0.001	0.00005±0.00002	n.d.	n.d.	0.067±0.0010	0.571±0.014	0.010±0.001	0.073±0.0007	0.054±0.00142	0.495±0.01355	
Badl-4	28	1567±455	0.062±0.001	0.023±0.001	0.00003±0.00002	n.d.	n.d.	0.062±0.0014	0.525±0.016	0.011±0.001	0.063±0.0006	0.053±0.00149	0.447±0.01501	
Badl-5	12	1399±553	0.073±0.002	0.044±0.002	0.00008±0.00004	n.d.	n.d.	0.068±0.0016	0.681±0.025	0.021±0.002	0.071±0.0010	0.056±0.00239	0.516±0.02275	
Badl-6	16	1730±599	0.070±0.002	0.034±0.002	0.00014±0.00004	n.d.	n.d.	0.075±0.0015	0.720±0.022	0.017±0.001	0.079±0.0009	0.057±0.00185	0.577±0.02005	
Badl-7	10	881±308	0.084±0.002	0.072±0.003	0.00006±0.00004	n.d.	n.d.	0.081±0.0020	0.935±0.033	0.035±0.002	0.090±0.0013	0.057±0.00230	0.613±0.02618	
Badl-8	14	676±156	0.074±0.002	0.054±0.002	0.00003±0.00002	n.d.	n.d.	0.078±0.0018	0.794±0.025	0.026±0.002	0.089±0.0010	0.053±0.00179	0.559±0.02083	
Badl-9	9	587±219	0.097±0.004	0.100±0.005	0.00012±0.00005	n.d.	n.d.	0.052±0.0013	0.692±0.027	0.048±0.003	0.056±0.0010	0.059±0.00342	0.403±0.02266	
Badl-10	16	578±104	0.090±0.002	0.089±0.003	0.00003±0.00002	n.d.	n.d.	0.081±0.0020	1.010±0.031	0.043±0.002	0.092±0.0010	0.057±0.00131	0.608±0.01857	
Badl-11	10	390±90	0.167±0.004	0.282±0.007	0.00012±0.00005	n.d.	n.d.	0.070±0.0016	1.617±0.046	0.136±0.007	0.066±0.0010	0.061±0.00003	0.512±0.00561	
Badl-12	10	670±296	0.103±0.003	0.115±0.005	0.00005±0.00004	n.d.	n.d.	0.059±0.0014	0.839±0.030	0.056±0.004	0.064±0.0010	0.060±0.00294	0.461±0.02222	

Table 6.1 continued

N	U ($\mu\text{g/g}$) _a	$\frac{206}{204}\text{Pb}$	$\frac{207}{206}\text{Pb}$	$\frac{208}{206}\text{Pb}$	$\frac{232}{238}\text{Th}$	$\frac{230}{238}\text{Th}$	$\frac{234}{238}\text{U}$	$\frac{206}{238}\text{Pb}$	$\frac{207}{235}\text{Pb}$	$f8b$	$\frac{206}{238}\text{Pb}$	$\frac{207}{206}\text{Pb}$	$\frac{207}{235}\text{Pb}$
		$\frac{204}{206}\text{Pb}$	$\frac{206}{208}\text{Pb}$	$\frac{206}{208}\text{Pb}$	$\frac{238}{U}$	$\frac{act}{U}$	$\frac{act}{U}$	$\frac{238}{U}$	$\frac{238}{U}$	$\frac{235}{U}$		$\frac{208}{238}\text{Pb corrected}$	$\frac{208}{206}\text{Pb corrected}$
Badl-13	18	834±177	0.089±0.002	0.082±0.002	0.00005±0.00003	n.d.	n.d.	0.100±0.0016	1.234±0.028	0.040±0.002	0.105±0.0010	0.059±0.00101	0.776±0.01542
Badl-14	18	823±172	0.092±0.002	0.092±0.003	0.00012±0.00004	n.d.	n.d.	0.099±0.0025	1.261±0.038	0.044±0.002	0.097±0.0010	0.058±0.00100	0.755±0.02056
Badl-15	17	1632±480	0.079±0.002	0.048±0.002	0.00008±0.00003	n.d.	n.d.	0.107±0.0020	1.157±0.029	0.023±0.001	0.120±0.0012	0.061±0.00140	0.874±0.02385
Badl-16	11	490±118	0.079±0.002	0.061±0.003	0.00001±0.00002	n.d.	n.d.	0.068±0.0016	0.745±0.027	0.030±0.002	0.076±0.0011	0.056±0.00243	0.513±0.02288
<i>Prairie</i>													
Pr6-1	9	216±22	0.116±0.002	0.150±0.003	0.00036±0.00006	1.276±0.405	0.790±0.263	0.074±0.0010	1.178±0.024	0.072±0.004	0.071±0.0008	0.060±0.00003	0.539±0.00002
Pr6-2	10	296±37	0.102±0.002	0.145±0.003	0.00021±0.00004	0.462±0.358	0.616±0.276	0.068±0.0008	0.959±0.020	0.070±0.004	0.066±0.0007	0.046±0.0003	0.399±0.00001
Pr6-4	12	382±49	0.087±0.002	0.080±0.002	0.00028±0.00005	1.236±0.346	1.128±0.262	0.066±0.0008	0.793±0.017	0.039±0.002	0.066±0.0006	0.057±0.00118	0.502±0.00285
Pr6-5	13	707±103	0.070±0.001	0.043±0.001	0.00028±0.00004	0.855±0.247	1.232±0.242	0.083±0.0009	0.796±0.016	0.021±0.001	0.084±0.0007	0.053±0.00117	0.594±0.00608
Pr6-6	13	815±127	0.080±0.001	0.062±0.002	0.00219±0.00013	0.589±0.233	1.063±0.237	0.088±0.0016	0.969±0.023	0.030±0.002	0.090±0.0007	0.057±0.00096	0.711±0.00002
Pr6-7	10	925±169	0.070±0.001	0.041±0.001	0.00025±0.00005	0.635±0.273	0.589±0.204	0.090±0.0023	0.872±0.027	0.020±0.001	0.094±0.0008	0.055±0.00130	0.743±0.01693
Pr6-8	13	567±76	0.079±0.001	0.050±0.002	0.00027±0.00004	0.936±0.260	1.422±0.260	0.078±0.0012	0.851±0.019	0.024±0.001	0.080±0.0007	0.060±0.00124	0.661±0.00989
Pr6-9	12	268±33	0.094±0.002	0.100±0.003	0.00022±0.00004	1.243±0.335	0.737±0.214	0.050±0.0006	0.648±0.015	0.048±0.003	0.049±0.0005	0.056±0.00125	0.352±0.00175
Pr6-10	21	349±35	0.087±0.002	0.087±0.002	0.00030±0.00004	0.865±0.194	1.030±0.172	0.050±0.0006	0.602±0.011	0.042±0.002	0.051±0.0004	0.054±0.00003	0.366±0.00001
Pr6-11	20	293±28	0.100±0.002	0.114±0.002	0.00030±0.00005	1.192±0.235	1.294±0.197	0.051±0.0009	0.704±0.015	0.055±0.003	0.051±0.0004	0.057±0.00003	0.403±0.00001
Pr6-12	21	239±21	0.109±0.002	0.134±0.003	0.00050±0.00007	1.108±0.231	1.086±0.183	0.048±0.0006	0.725±0.013	0.065±0.003	0.047±0.0004	0.059±0.00003	0.374±0.00001
Pr6-13	23	331±32	0.089±0.001	0.090±0.002	0.00037±0.00006	1.022±0.208	1.043±0.169	0.050±0.0005	0.608±0.010	0.043±0.002	0.050±0.0004	0.055±0.00003	0.363±0.00001
Pr6-14	25	154±9	0.141±0.002	0.218±0.003	0.00109±0.00009	1.007±0.202	0.927±0.154	0.056±0.0011	1.087±0.023	0.106±0.005	0.053±0.0005	0.059±0.00004	0.439±0.00838
Pr6-15	26	321±27	0.099±0.001	0.113±0.002	0.00267±0.00013	0.876±0.190	1.118±0.165	0.053±0.0020	0.726±0.029	0.055±0.003	0.054±0.0004	0.057±0.00003	0.473±0.01017
Pr6-16	27	250±18	0.111±0.001	0.133±0.002	0.00023±0.00003	0.693±0.156	0.862±0.140	0.058±0.0011	0.884±0.018	0.065±0.003	0.057±0.0004	0.061±0.00003	0.486±0.00531
Pr6-17	32	660±70	0.068±0.001	0.055±0.001	0.00019±0.00003	1.166±0.194	0.864±0.134	0.061±0.0008	0.568±0.010	0.027±0.001	0.062±0.0004	0.047±0.00009	0.397±0.00001
Pr6-18	30	288±21	0.096±0.001	0.105±0.002	0.00020±0.00003	0.876±0.172	0.581±0.114	0.057±0.0006	0.755±0.011	0.051±0.003	0.057±0.0004	0.056±0.00003	0.428±0.00001
Pr6-19	33	280±20	0.088±0.001	0.105±0.002	0.00021±0.00003	1.237±0.195	0.979±0.138	0.053±0.0010	0.642±0.014	0.051±0.003	0.053±0.0003	0.048±0.00003	0.356±0.00338
Pr6-20	34	284±20	0.133±0.002	0.150±0.002	0.00014±0.00002	0.906±0.158	1.012±0.135	0.052±0.0007	0.958±0.016	0.073±0.004	0.051±0.0004	0.078±0.00003	0.547±0.00564
Pr6-21	24	74±3	0.266±0.003	0.507±0.005	0.00017±0.00003	1.147±0.211	0.799±0.141	0.061±0.0012	2.220±0.046	0.245±0.012	0.048±0.0008	0.080±0.00004	0.549±0.02683
Pr6-22	21	168±11	0.152±0.002	0.266±0.004	0.00012±0.00002	0.870±0.195	1.265±0.191	0.061±0.0008	1.278±0.020	0.129±0.006	0.056±0.0005	0.051±0.0004	0.387±0.00921
Pr6-23	28	183±11	0.116±0.001	0.157±0.002	0.00019±0.00003	0.771±0.162	0.962±0.145	0.057±0.0012	0.921±0.021	0.076±0.004	0.056±0.0004	0.057±0.00003	0.454±0.00665
Pr6-24	37	210±12	0.124±0.001	0.405±0.004	0.000015±0.00002	1.091±0.171	0.937±0.127	0.053±0.0007	0.898±0.014	0.196±0.010	0.044±0.0006	-0.049±0.00004	-0.300±0.00001
Pr6-25	33	313±24	0.084±0.001	0.107±0.002	0.00011±0.00002	1.092±0.180	0.882±0.130	0.050±0.0008	0.577±0.012	0.052±0.003	0.050±0.0003	0.043±0.00003	0.299±0.00222

Table 6.1 continued

N	U ($\mu\text{g/g}$) ^a	$\frac{^{206}\text{Pb}}{^{204}\text{Pb}}$	$\frac{^{207}\text{Pb}}{^{206}\text{Pb}}$	$\frac{^{208}\text{Pb}}{^{238}\text{U}}$	$\frac{^{232}\text{Th}}{^{238}\text{U}}$	$\frac{^{230}\text{Th}}{^{238}\text{U}}$ act	$\frac{^{234}\text{U}}{^{238}\text{U}}$ act	$\frac{^{206}\text{Pb}}{^{238}\text{U}}$	$\frac{^{207}\text{Pb}}{^{235}\text{U}}$	f8b	$\frac{^{206}\text{Pb}}{^{238}\text{U}}$	$\frac{^{207}\text{Pb}}{^{206}\text{Pb}}$	$\frac{^{207}\text{Pb}}{^{235}\text{U}}$
						non-radiogenic lead						^{208}Pb corrected	^{208}Pb corrected
Pr6-26	23	218±16	0.108±0.002	0.245±0.003	0.00015±0.00002	1.439±0.256	0.925±0.161	0.055±0.0018	0.817±0.029	0.119±0.006	0.052±0.0005	0.010±0.00004	0.079±0.00398
Pr6-28	21	83±4	0.206±0.003	0.496±0.006	0.00015±0.00002	1.139±0.269	0.850±0.171	0.057±0.0022	1.609±0.064	0.240±0.012	0.035±0.0006	0.006±0.00004	0.038±0.00658
Pr6-29	25	194±15	0.110±0.002	0.160±0.003	0.00017±0.00002	1.490±0.287	0.970±0.163	0.050±0.0027	0.760±0.041	0.077±0.004	0.038±0.0003	0.049±0.00003	0.312±0.01652
Pr6-30	17	160±14	0.137±0.002	0.203±0.004	0.00016±0.00002	0.627±0.249	1.159±0.225	0.051±0.0013	0.965±0.028	0.098±0.005	0.037±0.0004	0.061±0.00004	0.385±0.00951
Pr6-31	14	296±39	0.087±0.002	0.101±0.003	0.00013±0.00002	0.495±0.293	0.986±0.246	0.057±0.0020	0.679±0.027	0.049±0.003	0.044±0.0004	0.048±0.00106	0.359±0.01394
Pr6-32	11	278±39	0.103±0.002	0.156±0.004	0.00011±0.00002	1.115±0.375	0.961±0.262	0.058±0.0012	0.829±0.023	0.076±0.004	0.043±0.0005	0.043±0.00003	0.321±0.00405
Pr6-33	11	263±37	0.103±0.002	0.145±0.004	0.00015±0.00002	0.770±0.374	0.947±0.278	0.056±0.0016	0.794±0.027	0.070±0.004	0.042±0.0005	0.048±0.00003	0.344±0.00746
Pr6-34	14	123±9	0.170±0.003	0.539±0.007	0.00014±0.00002	0.270±0.270	0.825±0.233	0.069±0.0020	1.603±0.051	0.261±0.013	0.041±0.0008	-0.065±0.0004	-0.457±-0.00001
Pr6-35	15	94±6	0.235±0.003	0.269±0.005	0.00017±0.00002	0.920±0.265	1.375±0.243	0.068±0.0018	2.215±0.061	0.130±0.007	0.048±0.0005	0.145±0.00004	1.192±0.03204
Pr6-36	20	224±22	0.100±0.002	0.128±0.003	0.00025±0.00003	1.018±0.280	0.716±0.179	0.051±0.0013	0.696±0.021	0.062±0.003	0.038±0.0003	0.051±0.00003	0.334±0.00758
Pr6-37	21	366±44	0.101±0.002	0.111±0.003	0.00023±0.00004	1.039±0.246	1.165±0.192	0.053±0.0014	0.737±0.023	0.054±0.003	0.040±0.0003	0.060±0.00003	0.412±0.01019
Pr6-38	21	161±13	0.130±0.002	0.232±0.004	0.00012±0.00002	1.269±0.259	0.801±0.157	0.050±0.0016	0.899±0.031	0.112±0.006	0.036±0.0004	0.041±0.00004	0.249±0.00897
Pr6-39	17	209±21	0.123±0.002	0.207±0.004	0.00018±0.00003	0.944±0.244	1.368±0.222	0.051±0.0013	0.866±0.026	0.100±0.005	0.037±0.0004	0.044±0.00004	0.278±0.00723

^a - U concentration is calculated as counts per second of ^{238}U in unknown divided by average counts per second of ^{238}U in the standard and multiplied by U concentration in the standard (assumed to be 800 $\mu\text{g/g}$).

b - Proportion of non-radiogenic Pb calculated using ^{208}Pb correction.

n.d - not determined.

Table 6.2 SHRIMP results for agate samples from South Dakota (ages in Ma and errors are 1σ).

N	$\frac{^{207}Pb}{^{235}U}$ Age	$\frac{^{206}Pb}{^{238}U}$ Age	$\frac{^{207}Pb}{^{235}U}$ Age	$\frac{^{206}Pb}{^{238}U}$ Age
	204 Pb-corrected	204 Pb-corrected	208 Pb-corrected	208 Pb-corrected
Sg7				
Sg7-1	75.40 ± 5.738	43.82 ± 2.23	46.97 ± 6.97	42.17 ± 1.40
Sg7-2	59.49 ± 15.087	40.64 ± 2.08	36.51 ± 7.51	39.32 ± 1.44
Sg7-4	19.74 ± 0.001	41.10 ± 2.36	41.35 ± 7.10	42.32 ± 1.41
Sg7-7	1E-09 ± 3.521	38.64 ± 2.64	49.37 ± 7.59	43.14 ± 1.39
Sg7-8	18.64 ± 13.730	43.86 ± 2.69	52.09 ± 9.30	45.76 ± 1.63
Sg7-10	51.94 ± 38.861	41.81 ± 3.14	31.02 ± 12.29	40.62 ± 1.74
Sg7-11	68.01 ± 67.978	49.11 ± 5.44	61.68 ± 23.12	48.74 ± 2.88
Sg7-12	32.32 ± 43.366	46.43 ± 3.98	67.64 ± 15.00	48.46 ± 2.21
Sg7-19	46.93 ± 4.613	45.53 ± 3.23	40.75 ± 11.37	45.18 ± 1.61
Sg7-21	33.67 ± 39.045	36.56 ± 3.64	13.91 ± 14.60	35.45 ± 1.59
Sg7-22	62.45 ± 32.946	39.73 ± 2.94	35.97 ± 12.74	38.21 ± 1.86
Sg7-23	1E-09 ± 0.001	37.89 ± 3.09	21.02 ± 10.66	41.27 ± 1.51
Sg7-24	39.77 ± 31.053	41.66 ± 3.00	56.26 ± 11.55	42.61 ± 1.78
Sg7-25	1E-09 ± 922.216	19.94 ± 13.97	47.86 ± 34.57	47.01 ± 3.98
Badlands				
Badl-1	682.22 ± 26.946	590.02 ± 18.82	588.67 ± 20.24	579.99 ± 19.82
Badl-2	672.64 ± 7.583	599.31 ± 12.45	625.68 ± 14.06	618.81 ± 13.64
Badl-3	418.23 ± 13.534	408.23 ± 9.21	414.90 ± 6.34	414.13 ± 6.08
Badl-4	370.21 ± 11.267	375.09 ± 10.53	382.15 ± 8.89	382.52 ± 8.77
Badl-5	462.24 ± 23.802	422.48 ± 15.24	417.80 ± 10.35	414.62 ± 9.89
Badl-6	493.73 ± 17.378	462.23 ± 12.91	461.74 ± 9.59	459.15 ± 9.24
Badl-7	561.41 ± 28.992	485.14 ± 16.49	489.43 ± 13.34	482.90 ± 12.25
Badl-8	441.52 ± 5.929	451.20 ± 13.56	472.63 ± 11.83	473.40 ± 11.14
Badl-9	413.08 ± 34.913	343.78 ± 16.40	315.06 ± 9.36	309.78 ± 8.15
Badl-10	543.25 ± 0.013	482.45 ± 11.73	487.17 ± 13.22	482.02 ± 12.50

Table 6.2 continued

N	$\frac{^{207}Pb}{^{235}U}$ Age	$\frac{^{206}Pb}{^{238}U}$ Age	$\frac{^{207}Pb}{^{235}U}$ Age	$\frac{^{206}Pb}{^{238}U}$ Age
	204 Pb-corrected	204 Pb-corrected	208 Pb-corrected	208 Pb-corrected
Badl-11	813.80 ± 4.584	419.76 ± 3.76	417.48 ± 11.11	379.78 ± 9.18
Badl-12	508.43 ± 42.314	384.94 ± 15.44	359.56 ± 10.31	349.55 ± 8.73
Badl-13	691.49 ± 2.114	583.08 ± 8.82	601.59 ± 10.77	591.38 ± 9.95
Badl-14	704.98 ± 9.759	571.23 ± 11.89	595.11 ± 15.93	582.49 ± 15.27
Badl-15	711.85 ± 14.988	637.64 ± 12.92	646.30 ± 13.40	639.10 ± 12.71
Badl-16	374.41 ± 6.370	420.19 ± 15.36	409.20 ± 10.89	412.70 ± 9.96
<i>Prairie</i>				
Pr6-1	360.04 ± 63.422	403.91 ± 7.34	431.71 ± 82.08	409.89 ± 5.66
Pr6-2	380.44 ± 50.359	392.65 ± 6.65	334.14 ± 83.67	389.72 ± 5.33
Pr6-4	359.12 ± 40.123	392.78 ± 5.98	409.79 ± 85.66	396.87 ± 5.15
Pr6-5	439.86 ± 28.373	497.49 ± 6.42	470.79 ± 114.95	500.16 ± 5.93
Pr6-6	588.52 ± 26.321	563.62 ± 8.84	540.34 ± 128.02	559.82 ± 8.47
Pr6-7	561.37 ± 29.301	602.36 ± 11.69	560.47 ± 140.71	602.57 ± 11.48
Pr6-8	463.90 ± 31.789	491.65 ± 7.39	512.42 ± 110.52	495.91 ± 6.95
Pr6-9	212.77 ± 45.046	280.49 ± 4.71	304.16 ± 59.59	286.84 ± 3.67
Pr6-10	264.47 ± 31.493	308.17 ± 4.15	314.55 ± 66.94	311.83 ± 3.61
Pr6-11	304.53 ± 35.719	317.48 ± 4.98	340.06 ± 66.42	320.29 ± 4.41
Pr6-12	264.93 ± 39.202	284.73 ± 4.19	319.14 ± 57.77	288.77 ± 3.40
Pr6-13	256.75 ± 31.162	298.11 ± 3.77	312.62 ± 64.18	302.15 ± 3.20
Pr6-14	287.78 ± 58.541	332.50 ± 5.99	363.14 ± 62.71	338.44 ± 5.12
Pr6-15	374.84 ± 34.157	377.80 ± 9.20	388.22 ± 80.41	379.17 ± 8.99
Pr6-16	351.25 ± 38.519	360.41 ± 5.55	396.87 ± 73.65	364.23 ± 5.04
Pr6-17	330.92 ± 20.062	384.37 ± 4.44	337.46 ± 88.79	384.99 ± 4.21
Pr6-18	291.62 ± 33.902	339.96 ± 4.00	358.28 ± 72.13	345.00 ± 3.42
Pr6-19	228.54 ± 35.706	334.31 ± 4.99	306.65 ± 73.20	339.81 ± 4.61
Pr6-20	470.83 ± 26.896	320.37 ± 4.17	436.81 ± 59.67	318.11 ± 3.75
Pr6-21	416.77 ± 100.336	310.00 ± 8.08	420.84 ± 40.61	312.23 ± 6.69
Pr6-22	419.13 ± 51.217	349.45 ± 5.49	319.53 ± 64.55	342.89 ± 4.56

Table 6.2 continued

N	$\frac{^{207}Pb}{^{235}U}$ Age	$\frac{^{206}Pb}{^{238}U}$ Age	$\frac{^{207}Pb}{^{235}U}$ Age	$\frac{^{206}Pb}{^{238}U}$ Age
	^{204}Pb -corrected	^{204}Pb -corrected	^{208}Pb -corrected	^{208}Pb -corrected
Pr6-23	239.42 ± 53.82859	351.69 ± 6.04	376.12 ± 71.06	361.66 ± 5.41
Pr6-24	321.48 ± 37.84176	313.20 ± 4.15	-384.95 ± 69.45	277.29 ± 4.38
Pr6-25	227.20 ± 30.97917	311.25 ± 4.31	263.29 ± 68.86	313.84 ± 3.94
Pr6-26	283.30 ± 49.51305	368.06 ± 8.38	67.33 ± 80.17	355.23 ± 7.79
Pr6-28	131.30 ± 112.499	277.44 ± 12.59	29.68 ± 45.76	272.10 ± 11.59
Pr6-29	187.00 ± 50.18641	286.64 ± 15.77	273.10 ± 61.01	292.53 ± 15.83
Pr6-30	247.58 ± 62.03163	284.68 ± 8.58	325.78 ± 54.42	290.49 ± 7.78
Pr6-31	238.67 ± 50.5391	334.75 ± 12.69	308.82 ± 74.36	339.73 ± 12.38
Pr6-32	325.20 ± 52.69022	340.85 ± 8.30	277.22 ± 72.28	337.86 ± 7.23
Pr6-33	294.67 ± 55.41028	325.87 ± 10.20	295.56 ± 68.97	326.25 ± 9.37
Pr6-34	339.69 ± 87.7291	363.96 ± 12.69	-673.43 ± 74.78	318.61 ± 11.07
Pr6-35	506.61 ± 88.78428	344.14 ± 11.69	784.91 ± 54.13	372.96 ± 10.35
Pr6-36	191.67 ± 50.19229	292.49 ± 8.30	290.01 ± 62.10	299.22 ± 7.86
Pr6-37	360.92 ± 32.00429	314.47 ± 9.08	346.29 ± 65.87	313.66 ± 8.75
Pr6-38	208.08 ± 58.67619	279.17 ± 9.91	221.27 ± 55.35	280.34 ± 9.37
Pr6-39	298.34 ± 48.60186	292.41 ± 8.44	242.97 ± 58.57	289.02 ± 7.72

6.5.2 Badlands

This sample shows narrow banding of alternating white and translucent material around a cloudy white centre. The outer parallel bands are several millimetres wide and are highlighted by the UV image (Figure 6.6).

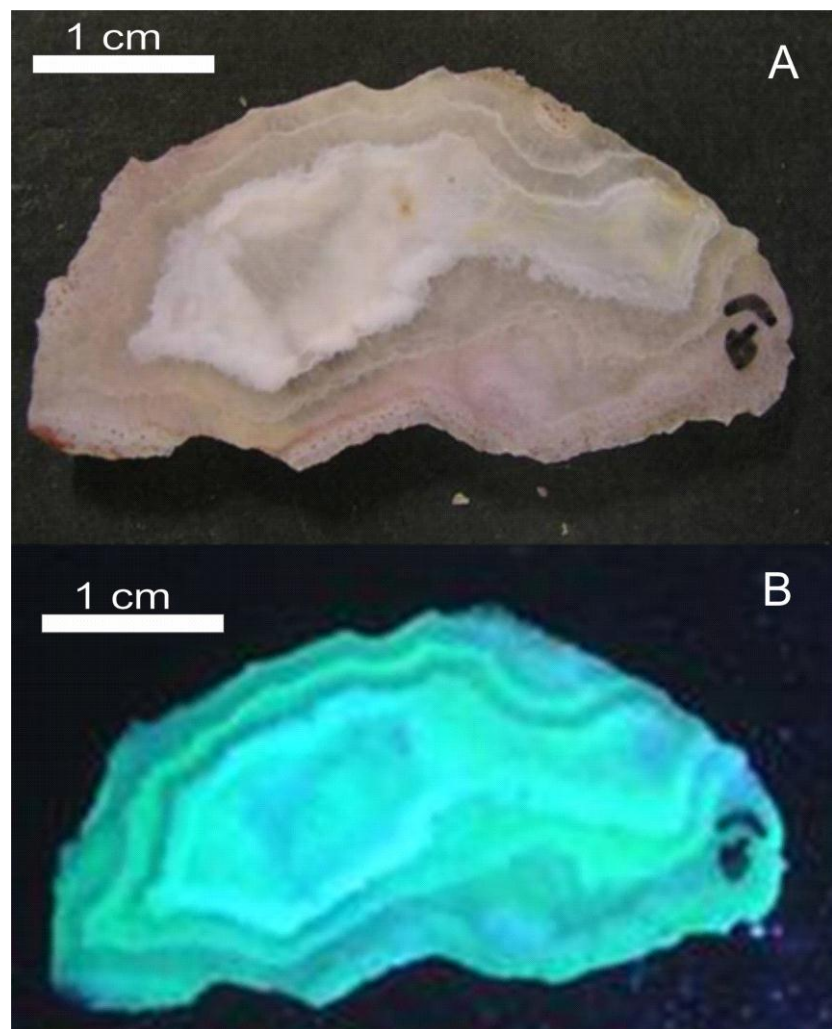


Figure 6.6 A) Badlands in plain light and B) under UV light.

Sixteen SHRIMP spots were analysed showing concentrations of uranium that ranged between 9 and 28 ppm and an average of 16 ppm. Relatively precise U-Pb dating of this sample is possible because of its low non-radiogenic Pb abundance as shown by the high $^{206}\text{Pb}/^{204}\text{Pb}$ ratio (range between 390 and 4649 and an average of 1275, Table

6.1). The $^{232}\text{Th}/^{238}\text{U}$ ratio varies between 6×10^{-6} and 0.00164 with an average of 7.7×10^{-5} . This value is small enough indicating negligible radiogenic ^{208}Pb contribution and consequently increasing the reliability of the $^{208}\text{Pb}/^{206}\text{Pb}$ lead correction compared to the $^{204}\text{Pb}/^{206}\text{Pb}$ lead correction.

The data show some scatter along the $^{207}\text{Pb}/^{235}\text{U} - ^{206}\text{Pb}/^{238}\text{U}$ ^{208}Pb -correct concordia diagram indicating variability in ages which could be the result of partial or complete resetting of the U/Pb system through process such as a loss of radiogenic products, through volume diffusion or leaching by fluids, or by multiple growth episodes. This single resetting episode would be defined by the lower intercept at 99 ± 280 Ma. There is also a possibility that the variability is caused by Pb mobility as a result of multiple resetting episodes. The age of formation is given by the upper intercept at 554 ± 74 Ma.

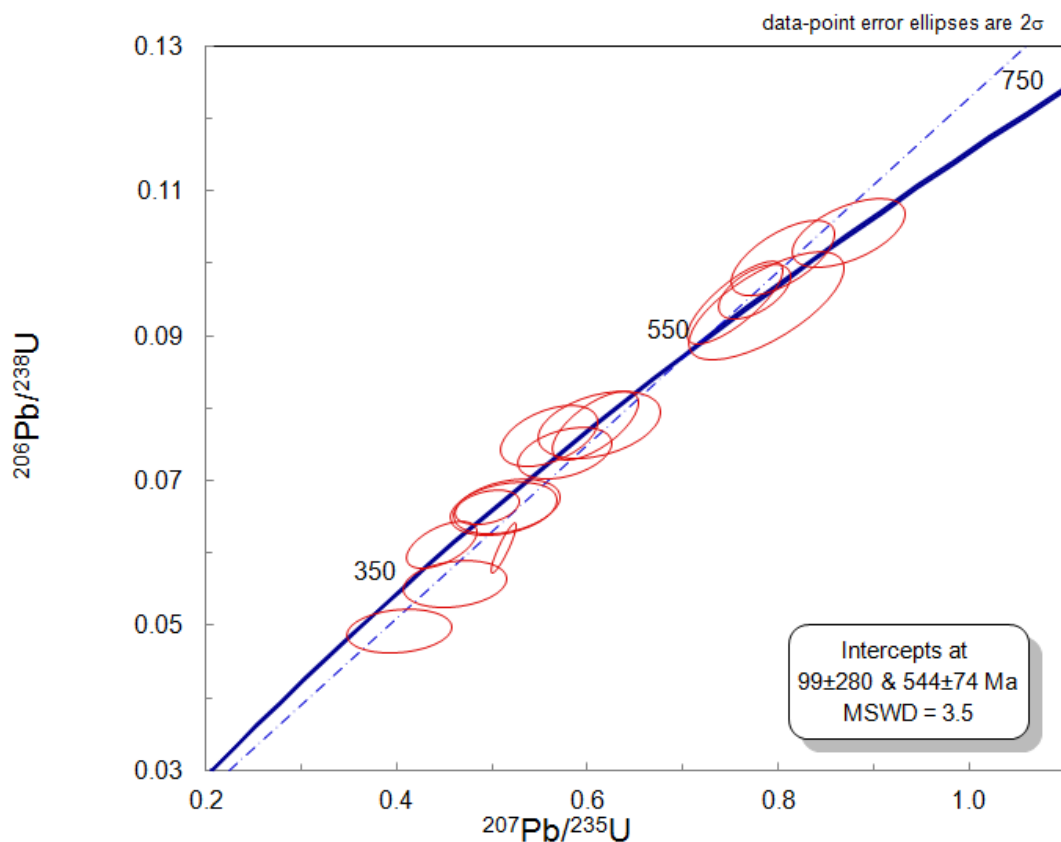


Figure 6.7 $^{207}\text{Pb}/^{235}\text{U}$ vs. $^{206}\text{Pb}/^{238}\text{U}$ concordia diagram corrected for ^{208}Pb .

6.5.3 Prairie

This sample shows typical 1 to 5 mm thick agate style banding highlighted by the change of colour from white to yellowish-brown and greyish-brown and clearly highlighted by fluorescence under the short wave UV-light (Figure 6.8). This banding appears to be overprinted by patches of less regular colloform to fragmented silica, which in places shows its own bands and variation in colour and UV light response.

The area chosen for SHRIMP analysis was selected to encompass both regularly banded agate and the fragmented to colloform silica (Figure 6.9). A total of 39 spots were analysed with approximately half of the analysed spots located within the regularly banded agate.

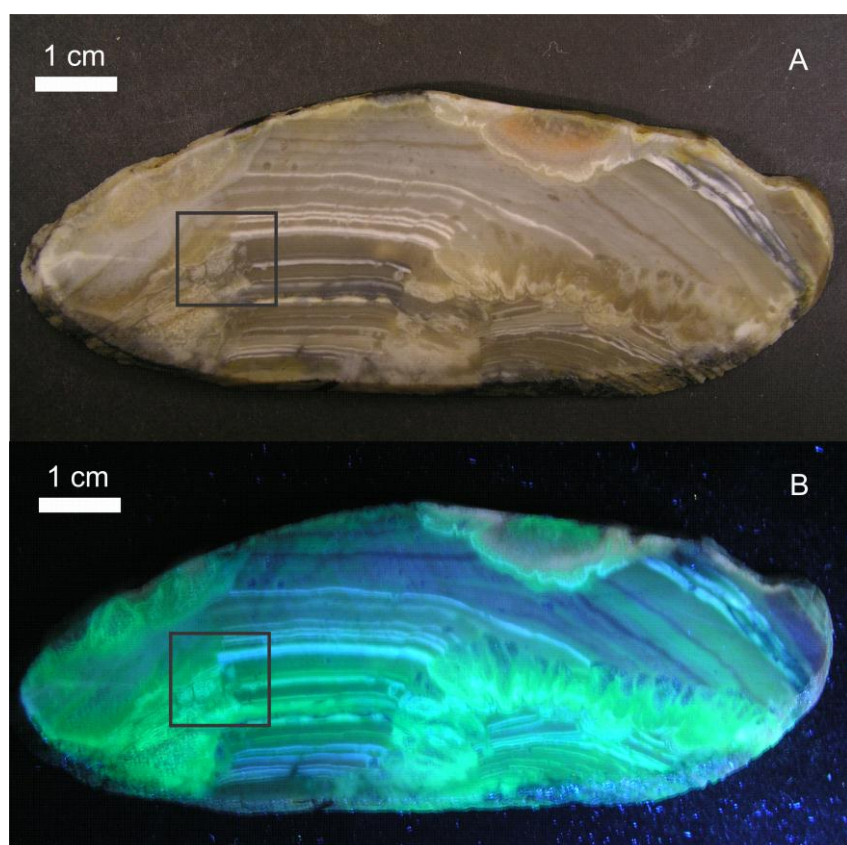


Figure 6.8 Prairie sample under plain and UV light, highlighting the difference between the opal and host rock. Square shows area selected for SHRIMP analyses.

The sample has uranium concentrations from 9 to 36 ppm with an average of 20 ppm (Table 6.1). One analysis with U concentration less than 5 ppm and one analysis with very low $^{204}\text{Pb}/^{206}\text{Pb}$ were rejected from the dataset (spots Pr6-3 and Pr6-27 respectively). The spots in the banded agate tend to show a slightly lower

concentration of uranium (9–22 ppm) as compared to the colloform agate (20–37 ppm).

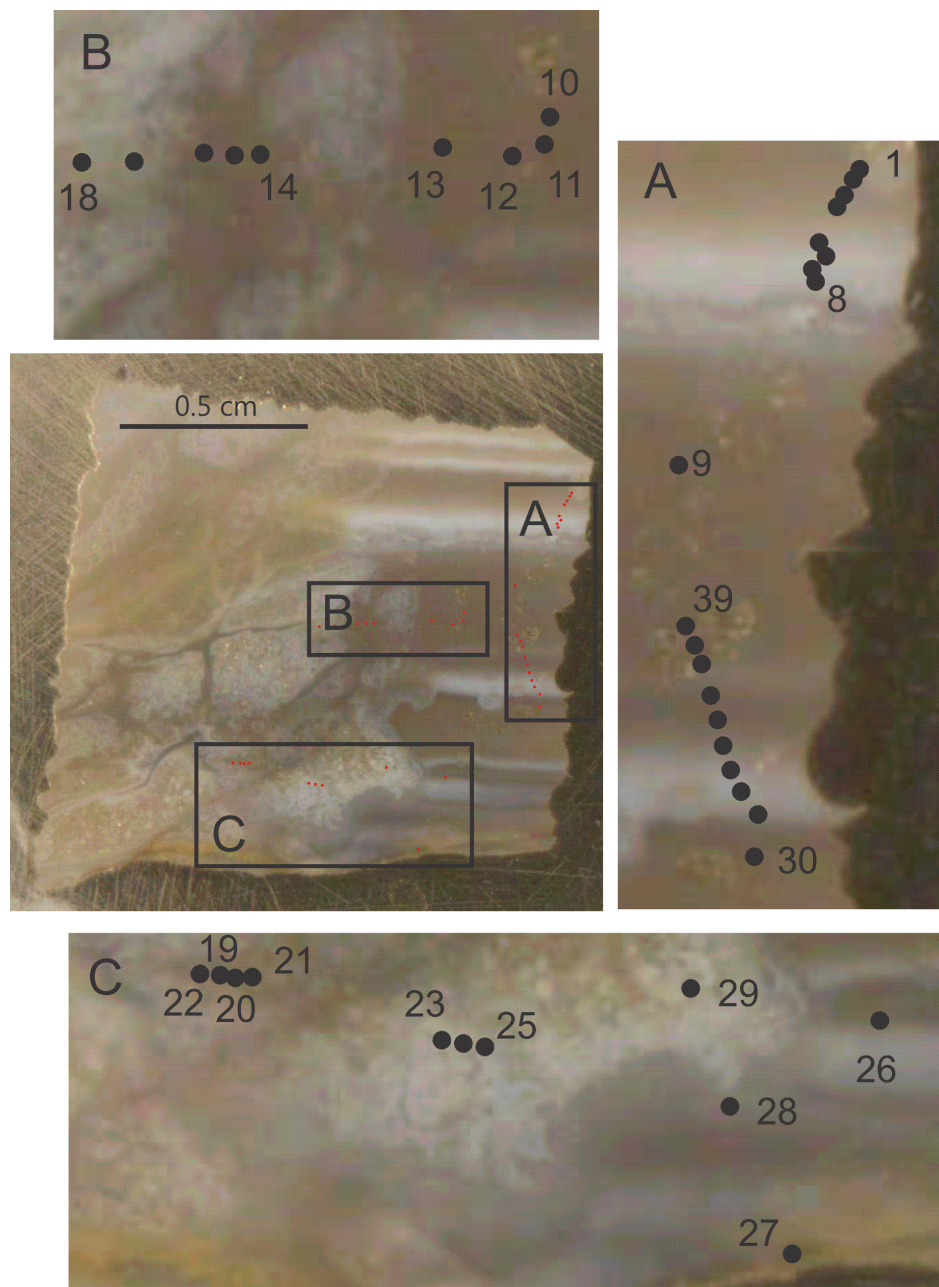


Figure 6.9 Location of SHRIMP spots on Prairie sample (spots Pr6-3 and Pr6-27 are excluded from the dataset).

The $^{206}\text{Pb}/^{204}\text{Pb}$ ratios are low, varying from 74 to 925 but with most around 250. The $^{232}\text{Th}/^{238}\text{U}$ ratio varies between 0.0001 and 0.002 with an average of 0.0003. This is low enough to make the resulting radiogenic ^{208}Pb contribution negligible.

The $^{207}\text{Pb}/^{235}\text{U} - ^{206}\text{Pb}/^{238}\text{U}$ ^{208}Pb -corrected concordia displays an estimated age of ~330 Ma excluding the four significantly older analyses. Wide variation of the ages suggests that the U-Pb system of agate sample did not remain closed or reflect multiple growth.

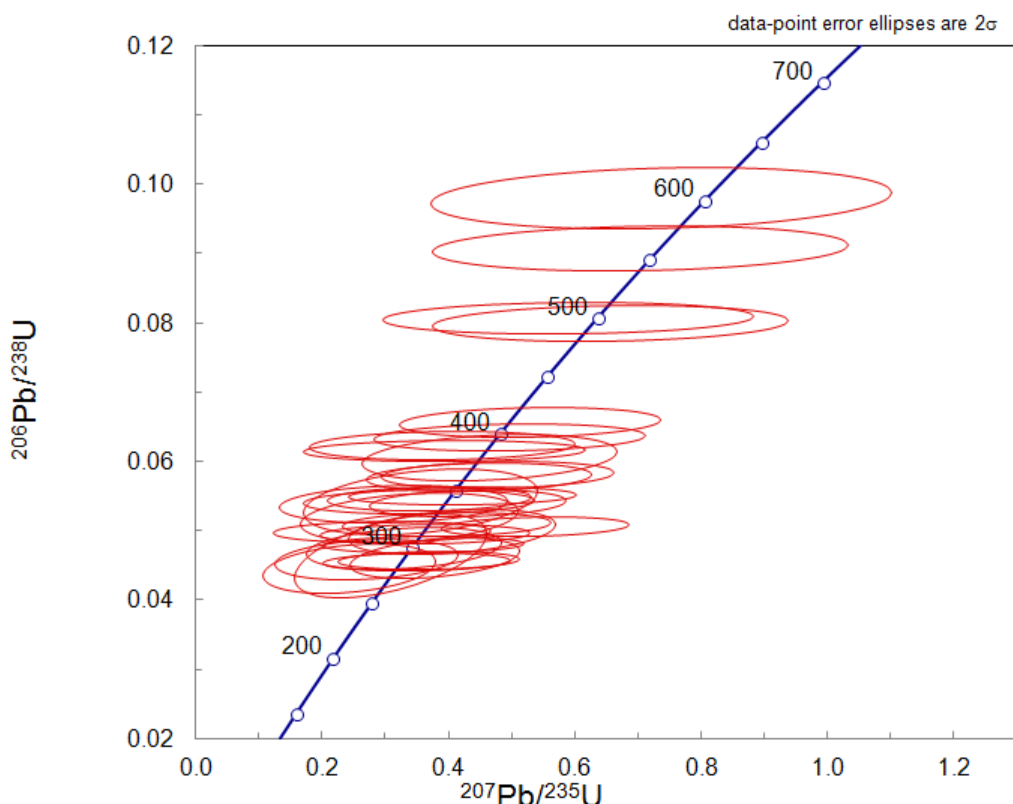


Figure 6.10 $^{207}\text{Pb}/^{235}\text{U}$ vs. $^{206}\text{Pb}/^{238}\text{U}$ concordia diagram corrected for ^{208}Pb .

This conclusion is also suggested by the correlation between the distribution of U and agate form (i.e. banded or colloform). With a few exceptions U concentration in the banded areas of the sample is about two times smaller compared to that observed in the colloform agate. This difference suggests that the modification of U-Pb system accompanied U mobility, rather than Pb loss or gain, however, the calculated ages do not show any correlation to the uranium concentration.

The banded agate analyses form a profile parallel to the banding and four significantly older samples (Pr6-5, Pr6-6, Pr6-7 and Pr6-8) within the banding are located close together and show a range between 495 ± 7 Ma and 602 ± 11 Ma. The rest of the

samples are younger and show a range between 272 ± 11 Ma and 409 ± 6 Ma. The colloform samples produce a similar range between 277 ± 4 Ma and 384 ± 4 Ma.

Two possible scenarios can explain observed variation of $^{206}\text{Pb}/^{238}\text{U}$ ages:

- (i) Primary agate is represented by the banded parts of the sample with the old ages. These parts represent the least disturbed areas with the ages closer to the original age of the samples. Later remobilisation of silica accompanied by the addition of U resulted in formation of colloform agate and alteration of some bands in the banded parts of the sample. Youngest ages obtained from the colloform opal could be close to the age of this secondary remobilisation process.
- (ii) Colloform agate represents primary sample and its age is close to formation of the sample. Secondary silica remobilisation resulted in the formation of regular banding in some parts of the sample. This formation was accompanied by partial U loss from these areas which resulted in the older apparent ages obtained for the thin regular banding. This scenario is contradicted by the apparent textural relationships between different types of the agate, suggesting that the colloform agate crosscuts regular banding and, therefore, is younger than this banding (Figure 6.10).

It is impossible to resolve if the difference between ages of colloform agate and thick homogenous bands reflects two different mobilisation events or just a different response to a single event. In any case, 272 ± 11 Ma can be considered as the oldest limit for the last remobilisation U-Pb system observed in this sample.

6.6 Discussion

All of the agate samples have low uranium concentrations, however, they are sufficient to obtain meaningful ages because of the antiquity of the materials. Nevertheless, low uranium content resulted in increased errors in the calculated ages. The U-Pb ages range from ~38 to ~600 Ma.

The calculated ages represent the average age of mineral deposition assuming closed system behaviour from that time until the present or the average age of a continuous depositional process, however, a spread in ages is evident in all samples suggesting

that the U-Pb system did not remain closed, there is more than one age population and possibly differing degrees of open system behaviour.

The spread in ages can be explained by either; a continuous deposition event, a series of individual deposition events, or reworking due to silica remobilisation which resets the U-Pb system. Silica remobilisation in the agate may have occurred due to digenesis of the limestone host, by circulating waters or deeper thermal events. This resetting produces younger ages and is not the age of deposition.

One interpretation of these ages is that the oldest ages suggest that the agates were not penecontemporaneous with the host rock (Minnelusa Formation). The older Prairie ages (~500 Ma) are similar to the age of formation of the Badlands sample at 554 ± 74 Ma and may correlate to the age of exposure of the entire Precambrian complex at ~520 Ma. This indicates that the agate is present as allochthonous clasts rather than as authigenic sedimentary agate. The younger ages of the Prairie sample are within the depositional timeframe of the Minnelusa limestone at ~300 Ma and may represent real ages or the age of resetting (open system). The age of SG7 and the lower age of the Badlands sample may correlate to the 50–80 Ma Laramide Orogeny.

An alternative view is that agate with ages older than the Minnelusa Formation (Prairie and Badlands) show a major U mobility issue resulting in unreliable ages. The mobility of U in this system may be the result of either episodic, continuous or combination of both, however, further research would need to be undertaken to provide further clarification but it does prove that the system did not remain closed. Subsequently, the SG7 sample, which doesn't show a large range in ages may be considered the most reliable age of formation. This sample is also similar in age to the White River Group which records a global climatic shift towards drier conditions near the end of the Eocene-Oligocene (Terry, 2001). The high silica content of these tuffs in the White River Group, increased mobility of U near the surface and an increasingly drier climate are ideal conditions for the deposition of agate.

It is not known if remobilisation/resetting through silica mobilisation will primarily occur along planes of weaknesses parallel to the banding, consequently identifying areas that have undergone remobilisation is impossible and the sequence of layers may not have ages in chronological order. Consequently, age interpretations for agate

is complicated and further investigation into the ages of each individual band within the agate would be needed to resolve the depositional model.

7 CONCLUSIONS

The overall consistency of U-Th-Pb systematics in a number of samples with ages varying from ~40 thousand years to ~640 million years and of various origins suggest that SHRIMP can be used to accurately date a variety of U-rich opals. The enrichment in U, relative to Th and Pb, reduces uncertainties associated with correction for initial Th and Pb, required for the age calculations and makes opal suitable for both U-Pb and U-series dating.

7.1 Advantages and disadvantages of the technique

The SHRIMP analytical procedure developed in this study has several advantages over other dating techniques that have been used on opal. Primarily it provides a significant increase in the spatial resolution of the area analysed without the need for mechanical separation of samples, albeit with larger errors. The inhomogeneity of uranium concentrations and ages in all of the samples presented in this study show the necessity for increased spatial resolution and insitu analyses. Another advantage is the ability to analyse all required isotopes in a single run without having to make a chemical separation of individual elements resulting in simultaneous U-Pb and U-series analysis. This is particularly important since the ages of different parts of the same sample can vary significantly and fall within the ranges where either U-Pb or U-series systems are applicable for the purpose of dating.

There are two main limitations of the dating technique – low uranium concentration and a high proportion of common lead. Opal with uranium concentration less than 4 ppm cannot be analysed. Opal with uranium concentrations between 4 and 50 ppm can be analysed, but remain problematic because of the very low counting rates of Pb isotopes as well as the less abundant isotopes of ^{234}U and ^{230}Th .

The ^{206}Pb - ^{238}U and ^{207}Pb - ^{235}U systems had proved to be effective in dating opal older than 300 kyr, but the proportion of initial (common) Pb, the amount of excess ^{234}U and the loss-gain of other intermediate daughters in the ^{238}U decay chain needs to be taken into account. The proportion of common lead present in the sample may

contribute to a possible inaccurate estimate of age, especially for the ^{207}Pb - ^{235}U system, where only very small amounts of radiogenic ^{207}Pb are generated in samples younger than ~ 1.5 Ma. Consequently the uncertainty and accuracy of ^{235}U - ^{207}Pb ages reduces significantly with increasing proportion of common Pb and decreasing age of samples. However, when ^{206}Pb / ^{204}Pb ratios in the samples are high (close to or in excess of 1000), this uncertainty becomes insignificant for accurate age estimation. If common lead is high then a correction can be applied using both ^{204}Pb and ^{208}Pb . The ^{204}Pb in many opal samples is barely distinguishable above the background, which combined with the very low counting rate of ^{206}Pb in the younger samples, makes ^{204}Pb correction rather imprecise or even impossible. Alternatively, corrections based on ^{208}Pb can be applied and are advantageous due to the fact that ^{232}Th is typically absent in opal and the resulting ^{208}Pb is almost entirely common (non-radiogenic) and can be used for the correction.

7.2 U-series and U-Pb ages

The simultaneous analyses of U-Pb and U-Th systematics allow for ages to be calculated using both systems where there is a very large age range within the opal. Ages for opal younger than ~ 300 kyr were calculated using ^{238}U - ^{234}U - ^{230}Th relationships which are free of potential problems associated with the disequilibrium of decay products at the lower end of ^{238}U decay chain. Low Th concentrations in opals eliminate the necessity to correct for initial ^{230}Th . Samples older than ~ 300 kyr can be dated using U-Pb and ages up to several hundred million years have been calculated. The ^{235}U - ^{207}Pb ages can place accurate timing constraints on relatively old opal samples and the effect of intermediate decay products on the ^{235}U - ^{207}Pb system is smaller, compared to the ^{206}Pb - ^{238}U system.

The calculated ages for individual layers represent the time of formation for that particular layer, whereas average ages represent the average age of the time of deposition for a particular section of opal analysed. It is clear in some opals that resetting/remobilisation has occurred and consequently the calculated age may not represent age of formation but rather the age of final U remobilisation. Relationships between the layers, microstructures and ages of the opal are keys to determining the complex depositional history of some of these opals.

7.3 Rates of deposition

Layering in opal is evident on macro as well as micro scale and is correlated with the sequence of silica deposition layers. Depositional growth rates were calculated for opal that show layering (from the vadose zone at Yucca Mountain and from the saturated zone in Yalgoo) and was only possible due to the increased spatial resolution. The combined U-Pb and U-series ages were used to support a model of slow mineral deposition (rates of millimetres per million years). Consequentially, the precipitation of opal was determined to be slow and continuous at a varying rate despite the environment being either saturated or unsaturated. Correlation with global temperatures, suggests that the opal deposition rate increases under the cooler climate conditions. Ages and growth rates calculated in this research are in excellent agreement with the published SHRIMP and TIMS analyses for the same samples further indicating the validity of this technique.

7.4 Opal from various environments

One of the clear outcomes of this research is that opal, providing it has the required amount of uranium, can be dated despite the environment of formation. Opal that has been formed from groundwater in either a saturated or unsaturated environment from either a volcanic or sedimentary host rock has been successfully dated using both U- series and U-Pb systematics. These different environments cause opals to have different forms such as veins, hemispheres or as banded agate and a different depositional history which can be resolved through age calculations. However, interpretation of the age patterns and the strategy of work required to get reliable ages depend very much on the processes that formed and transformed the opal in each particular case.

REFERENCES

- AMELIN Y. AND BACK M. 2006. Opal as a U-Pb geochronometer: Search for a standard. *Chemical Geology* **232**, 67-86.
- AMELIN Y. V. AND NEYMARK L. A. 1999. Opal as a uranium-lead geochronometer. *Proceedings of the 9th Annual V.M. Goldschmidt Conference*, Lunar Planetary Institute, Houston, Texas **971**, 8.
- ANAND R. R. AND PAINE M. 2002. Regolith geology of the Yilgarn Craton, Western Australia: implications for exploration. *Australian Journal of Earth Sciences* **49**, 162.
- ARAKEL A. V. 1982. Genesis of calcrete in Quaternary soil profiles, Hutt and Leeman Lagoons, Western Australia. *Journal of Sedimentary Petrology* **52**, 109-125.
- BACON C. R., PERSING H. M., WOODEN J. L. AND IRELAND T. R. 2000. Late Pleistocene granodiorite beneath Crater Lake caldera, Oregon, dated by ion microprobe. *Geology* **28**, 467-470.
- BRADDOCK W.A. 1963. Geology of the Jewel Cave SW Quadrangle, Custer County, South Dakota. *U.S. Geological Survey Bulletin* **1063-G**, 217-268.
- BAJO C., RYBACH L. AND WEIBEL M. 1983. Extraction of uranium and thorium from Swiss granites and their microdistribution: 2 Microdistribution of uranium and thorium. *Chemical Geology* **39**, 299-318.
- BATEMAN H. 1910. Solution of a system of differential equations occurring in the theory of radioactive transformations. *Proceedings of the Cambridge Philosophical Society* **15**, 423-427.
- BEA F. 1999. Uranium. In: C.P. Marshall and R.W. Fairbridge, Editors, *Encyclopedia of geochemistry*, Kluwer Academic Publisher, Dordrecht, 645-648.
- BERGER A. AND LOUTRE M.F. 1991. Insolation values for the climate of the last 10 million years. *Quaternary Sciences Review* **10**, 297-317.
- BUESCH D.C., SPENGLER R.W., MOYER T.C. AND GESLIN J.K. 1996. Proposed stratigraphic nomenclature and macroscopic identification of lithostratigraphic units of the Paintbrush Group exposed at Yucca Mountain, Nevada. *U.S. Geological Survey Open-File Report 94-469*, 45.
- BOURDON B., TURNER S., HENDERSON G. M. AND LUNDSTROM C. C. 2003. Introduction to U-series geochemistry. In: BOURDON B., HENDERSON G. M., LUNDSTROM C. C. & TURNER S. P. (eds.), *Uranium-series geochemistry. Reviews in Mineralogy and Geochemistry*, **52** Mineralogical Society of America and Geochemical Society, Washington, 1-21.
- BOWLER J. M. 1976. Aridity in Australia: age, origins and expression in Aeolian landform and sediments. *Earth Science Review* **12**, 279-310.
- BREDEHOFT J. D. 1992. Response of the ground-water system at Yucca Mountain to an earthquake. In: *Ground water at Yucca Mountain, how high can it rise? Final report of the*

Panel on Coupled Hydrologic/Tectonic/Hydrothermal Systems at Yucca Mountain. National Academy Press, Washington, 212-222.

BROOKINS D. 1988. Eh–pH Diagrams for Geochemistry, Springer-Verlag, Berlin, 176.

BUTT C. R. M., HORWITZ R. C. AND MANN A. W. 1977. Uranium occurrences in calcrete and associated sediments in Western Australia. *CSIRO Division of Mineralogy, Report FP16*. CSIRO, Perth.

BUTT C. R. M. 1985. Granite weathering and silcrete formation of the Yilgarn Block, Western Australia. *Australian Journal of Earth Sciences* **32**, 415-432.

BYERS JR. F. M., CARR W. J., ORKILD P. P., QUINLIVAN W. D. AND SARGENT K. A. 1976. Volcanic suites and related cauldrons of the Timber Mountain-Oasis Valley Caldera Complex, southern Nevada. *U.S. Geological Survey Professional Paper* 919.

CASSIDY K. F., CHAMPION D. C., KRAPEŽ B., BARLEY M. E., BROWN S. J. A., BLEWETT R. S., GROENEWALD P. B. AND TYLER I. M. 2006. A revised geological framework for the Yilgarn Craton Western Australia. Geological Survey of Western Australia. Record 2006/8.

CHAMPION D. C. AND CASSIDY K. C. 2002. Granites of the northern Murchison Province: their distribution, age, geochemistry, petrogenesis, relationship with mineralisation, and implications for tectonic environment. In: CASSIDY K. C., CHAMPION D. C., MCNAUGHTON N. J., FLETCHER I. R., WHITAKER A. J., BASTRAKOVA I. V. AND BUDD A. R. (eds), *Characterisation and metallogenetic significance of Archaean granitoids of the Yilgarn Craton, Western Australia. AMIRA P482/ MERIWA M281* Minerals and Energy Research Institute of Western Australia Report 222, 5.1–5.54.

CHENG H., EDWARDS R. L., HOFF J., GALLUP C. D., RICHARDS D. A. AND ASMEROM Y. 2000. The half-lives of uranium-234 and thorium-230. *Chemical Geology* **169**, 17-33.

CHERNIAK D.J. AND WATSON E.B. 2000. Pb diffusion in zircon. *Chemical Geology* **172**, 5-24.

CHRISTIANSEN R. L., LIPMAN P. W., CARR M. J., BYERS JR F. M., ORKILD P. P., and SARGENT K. A. 1977. The Timber Mountain – Oasis Valley caldera complex of southern Nevada. *Geological Society of America Bulletin* **88**, 943-959.

CHURCHILL D. M. 1973. The ecological significance of tropical mangroves in the Early Tertiary floras of southern Australia. *Geological Society of Australia, Special Publication* **4**, 79-68.

CLARKE J. 2003. The occurrence and significance of biogenic opal in the regolith. *Earth Science Reviews* **60**, 175-194.

CLARKE J. D. A. 1993. Stratigraphy of the Lefroy and Cowan palaeodrainages, Western Australia. *Journal of the Royal Society of Western Australia* **76**, 13-23.

COCKBAIN A. E. AND HOCKING R. M. 1989. Revised stratigraphic nomenclature in Western Australia Phanerozoic Basins. *Geological Survey of Western Australia* **15**.

COLLINS G. AND STEUART P., 2000. Annual report for the period of 1 January to 31 December 2000. E59/642,P59/1397, Anglogold Australasia Limited, Bridgewell.

COWART J. B. AND BURNETT W. C. 1994. The distribution of uranium and thorium decay-series radionuclides in the environment—a review. *Journal of Environmental Quality* **23**, 651–662.

CRERAR D.A., AXTMANN E.V. AND AXTMANN R.C. 1981. Growth and ripening of silica polymers in aqueous solutions. *Geochimica et Cosmochimica Acta* **45**, 1259-1266.

DAHL P. S., HAMILTON M. A., WOODEN J. L. AND FREI R. 2003. Evidence for 2480 Ma rifting in the Black Hills, S. Dakota: U-Pb ages of sphene and zircon from the Blue Draw metagabbro sil, and their tectonic significance. *Geological Society of America Abstracts with Programs* **35**, 506.

DAHL P. S., FOLAND K. A., GARDNER E. T., HOLM D. K. AND HUBACHER F. A. 1999. New constraints on the timing of Early Proterozoic tectonism in the Black Hills (SouthDakota), with implications for docking of the Wyoming province to Laurentia. *Geologic Society of America Bulletin* **111**, 1335-1349.

DAHL P. S. AND FREI R. 1998. Single-phase dating of coexisting garnet and saulolite in the Black Hills collisioinal orogen (South Dakota), with implications for Early Proterozoic Tectonism. *U.S. Geology* **26**, 111-114.

DEWITT E., REDDEN J. A., WILSON A. B., BUSHER D. AND DERSCH J. S. 1986. Mineral resourcespotential and geology of the Black Hills National Forest, South Dakota and Wyoming. *United States Geologic Survey Bulletin* **1580**, 135.

DEWITT E., REDDEN J. A., BUSCHER D. AND. WILSON A.B. 1989. Geologic map of the Black Hills area, South Dakota and Wyoming: U.S. *Geological Survey Miscellaneous Investigations Series Map I-1910*, scale 1:250,000. U.S. Geological Survey, Rapid City.

DOVE P. M. AND CRERAR D. A. 1990. Kinetics of quartz dissolution in electrolyte solutions using a hydrothermal mixed flow reactor. *Geochimica et Cosmochimica Acta* **54**, 955-969.

DOVE P. M. AND RIMSTIDT J. D. 1994. Silica-Water Interactions. In: HEANEY P.J., PREWITT C.T. & GIBBS G.V. (eds), *Silica physical behaviour, geochemistry and materials application, Reviews in Mineralogy and Geochemistry* **29**, Mineralogical Society of America and Geochemical Society, Washington, 259-308.

DUBLYANSKY Y. V., FORD D. AND REUTSKI V. 2001. Traces of epigenetic hydrothermal activity at Yucca Mountain, Nevada: preliminary data on the fluid inclusion and stable isotope evidence. *Chemical Geology* **173**, 125-149.

DUBLYANSKY Y., SMIRNOV S. Z. AND PALYANOVA G. P. 2004. Comment on “Physical and stable-isotope evidence for formation of secondary calcite and silica in the unsaturated zone, Yucca Mountain, Nevada” by J. F. Whelan, J. B. Paces and Z. E. Peterman. *Applied Geochemistry* **19**, 1865 –1877.

DUBLYANSKY Y., SMIRNOV S. Z. AND PASHENKO S. E. 2003. Identification of the deep-seated component in paleo fluidscirculation through a potential nuclear waste disposal site: Yucca Mountain, Nevada, USA. *Journal of Geochemical Exploration* **78-79**, 39-43.

ELZEA J. M., ODOM I. E. AND MILES W. J. 1994. Distinguishing well ordered opal-CT and opal-C from high temperature cristobalite by x-ray diffraction. *Analytica Chimica Acta* **286**, 107-116.

- ELZEA J. M. AND RICE S. B. 1996. TEM and x-ray diffraction evidence for cristobalite and tridymite stacking sequence in opal. *Clays and Clay Minerals* **44**, 492-500.
- EWING R. C., MEDLDRUM A., WANG L., WEBER W. J. AND CORRALES L. R. 2003. Radiation effects in zircon. In: HANCHAR J. M. AND HOSKIN P.W.O. (eds), *Zircon. Reviews in Mineralogy and Geochemistry* **53**. Mineralogical Society of America and Geochemical Society, Washington, 387-420.
- FABRYKA-MARTIN J. T., WIGHTMAN S. J., ROBINSON B. A. AND VESTAL E. W. 1994. Infiltration processes at Yucca Mountain inferred from chlorine and chlorine-36 distributions. *Los Alamos National Laboratory Report LA-CST-TIP-94-022*.
- FLEISCHER R. L. AND RABBE O. G. 1978. Recoiling alpha-emitting nuclei. Mechanisms for uranium-series disequilibrium. *Geochimica et Cosmochimica Acta* **42**, 973-978.
- FLINT A. L. AND FLINT L. E. 1994. Spatial distribution of potential near surface moisture flux at Yucca Mountain. In : High Level Radioactive Waste Management *Proceedings of the Fifth Annual International Conference*. American Nuclear Society, Illinois, 2352-2358.
- FLÖRKE O.W., JONES J.B. AND SEGNIT E.R. 1975. Opal-CT crystals. *Neues Jahrbuch für Mineralogie, Monatshefte* **1975**, 369-377.
- FLÖRKE O. W., JONES J. B. AND SEGNIT E. R. 1973. The genesis of hyalite. *Neues Jahrbuch für Mineralogie, Monatshefte* 1973, 82-89.
- FLÖRKE O. W., KÖHLER-HERBERTZ B., LANGER K. AND TÖNGES I. 1982. Water Microcrystalline Quartz of Volcanic Origin: Agates. *Contributions to Mineralogy and Petrology* **80**, 324-333.
- FORESTER R. M. AND SMITH A. J. 1994. Late glacial climate estimates for southern Nevada: the ostracode fossil record. In : High Level Radioactive Waste Management *Proceedings of the Fifth Annual International Conference*. American Nuclear Society, Illinois, 2553-2561.
- FORESTER R. M., BRADBURY J. P., CARTER C., ELVIDGE-TUMA A. B., HEMPHILL M. L., LUNDSTROM S. C., MAHAN S.A., MARSHALL B. D., NEYMARK L. A., PACES J. B., SHARPE S. E., WHELAN J. F. AND WIGAND P. E. 1999. The climatic and hydrologic history of southern Nevada during the late Quaternary. *U.S. Geological Survey Open-File Report*, 98-635.
- FRIDRICH, C. J., DUDLEY W. W. AND STUCKLESS J. S. 1994. Hydrogeologic analysis of the saturated-zone ground-water system, under Yucca Mountain, Nevada. *Journal of Hydrology* **154**, 133-168.
- GASCOYNE M. 1992. Geochemistry of the actinides and their daughters. In: IVANOVICH M. & HARMON R. S. (eds.), *Uranium-series disequilibrium: Application to earth, marine, and environmental sciences*, 2nd edn, Clarendon Press, Oxford, 34-61.
- GASCOYNE M., MILLER N. H. AND NEYMARK L. A. 2002. Uranium-series disequilibrium in tuffs from Yucca Mountain, Nevada, as evidence of pore-fluid flow over the last million years. *Applied Geochemistry* **17**, 781-792.
- GASCOYNE M. AND SCHWARCZ H. P. 1986. Radionuclide migration over recent geological time in a granitic pluton. *Isotope Geoscience* **59**, 75-85.

- GEISLER T., PIDGEON R. T., VAN BRONSWIJK W. AND KURTZ R. 2002. Transport of uranium, thorium and lead in metamict zircon under low-temperature hydrothermal conditions. *Chemical Geology* **191**, 141-154.
- GOSSELIN D. C., PAPIKE J. J., ZARTMAN R. E., PETERMAN Z. E. AND LAUL J. C. 1988. Archean rocks of the Black Hills, South Dakota: Reworked basement from the southern extension of the Trans-Hudson orogen. *Geological Society of America Bulletin* **100**, 1244-1259.
- GÖTZE J., TICHOMIROWA M., FUCHS H., PILOT J. AND SHARP Z. D. 2001. Geochemistry of agates: a trace element and stable isotope study. *Chemical Geology* **175**, 523-541.
- GÖTZE J., MÖCKEL R., KEMPE U., KAPITONOV I. AND VENNEMANN T. 2009. Characteristics and origin of agates in sedimentary rocks from the Dryhead area, Montana, USA. *Mineralogical Magazine* **73**, 673-690.
- GRAETSCH H. 1994. Structural characteristics of opaline and microcrystalline silica minerals. In: HEANEY P.J., PREWITT C.T. & GIBBS G.V. (eds), *Silica physical behaviour, geochemistry and materials application, Reviews in Mineralogy and Geochemistry*, **29** Mineralogical Society of America and Geochemical Society, Washington, 209-229.
- GRAETSCH H., FLÖRKE O. W. AND MIEHE G. 1985. The nature of water in chalcedony and Opal-C from Brazilian agate geodes. *Physics and Chemistry of Minerals* **12**, 300 - 306.
- GRIES J. P. 1996. Roadside Geology of South Dakota. Mountain Press Publishing Company. USA.
- GUTHRIE V. A. AND KLEEMAN J. D. 1986. Changing uranium distributions during weathering of granite. *Chemical Geology* **54**, 113-126.
- HARRIS C. 1989. Oxygen-isotope zonation of agates from Karoo volcanics of the Skeleton coast, Namibia. *American Mineralogist* **74**, 476-481.
- HEANEY P. J. 1993. A proposed mechanism for the growth of chalcedony. *Contributions to Mineralogy and Petrology* **115**, 66-74.
- HEANEY P. J. 1994. Structure and chemistry of the low-pressure silica polymorphs. In: HEANEY P. J., PREWITT C. T., & GIBBS G. V. (eds.), *Silica: physical behaviour, geochemistry and materials application. Reviews in Mineralogy and Geochemistry*, **29** Mineralogical Society of America and Geochemical Society, Washington, 1-40.
- HEANEY P. J. AND DAVIS A. M. 1995. Observation and origin of self-organized textures in agate. *Science* **269**, 1562-5.
- HEVESI J. A., FLINT A. L. AND ISTOK J. D. 1992. Precipitation estimation in mountainous terrain using multivariate geostatistics: II. Isohyetal maps. *Journal of Applied Meteorology* **31**, 677-678.
- HOCKING R. M., LANGFORD R. L., THORNE A. M., SANDERS A. J., MORRIS P. A., STRONG C. A. AND GOZZARD J. R. 2001. A classification system for regolith in Western Australia. *Geological Survey of Western Australia* **2001/4**, Western Australia Geological Survey, Perth, 22.
- HOLT E.W. 2002. $^{18}\text{O}/^{16}\text{O}$ evidence for an early, short-lived (-10 yr), fumarolic event in the Topopah Spring Tuff near the proposed high-level nuclear waste repository within Yucca Mountain, Nevada, USA. *Earth & Planetary Science Letters* **201**, 559-573.

HOSKIN P.W.O AND SCHALTEGGER U. 2003. The composition of zircon and igneous and metamorphic petrogenesis. In: HANCHAR J. M. AND HOSKIN P.W.O. (eds), *Zircon. Reviews in Mineralogy and Geochemistry* **53**. Mineralogical Society of America and Geochemical Society, Washington, 27-55.

ICENHOWER J. P. AND DOVE P. M. 2000. The dissolution kinetics of amorphous silica into sodium chloride solutions: Effects of temperature and ionic strength. *Geochimica et Cosmochimica Acta* **64**, 4193-4203.

IVANOVICH M. & HARMON R. S. 1992. Uranium-series disequilibrium: Application to earth, marine, and environmental sciences. 2nd edn, Clarendon Press, Oxford, 910.

JACKSON M. J. AND VAN DE GRAAFF W. J. E. 1981. Geology of the Officer Basin, Western Australia. *Bulletin / Department of National Development and Energy, Bureau of Mineral Resources, Geology and Geophysics, 0084-7089* **206**, Australian Government Publishing Service, Canberra, 102.

JAFFEY A. H., FLYNN K. F., GLENDEIN L. F., BENTLEY W. C. AND ESSLING A. M. 1971. Precision measurements of half-lives and specific activities of ^{235}U and ^{238}U . *Physical Review C* **4**, 1889-1906.

JONES J. B., SANDERS J. V. AND SEGNIK E. R. 1964. Structure of opal. *Nature* **204**, 990-991.

JONES J. B. AND SEGNIK E. R. 1971. The nature of opal. I. Nomenclature and constituent phases. *Journal of Geological Society of Australia* **18**, 57-68.

JOUZEL J., LORIUS C., PETIT J. R., GENTHON C., BARKOV N. I., KOTLYAKOV V. M. AND PETROV V. M. 1987. VOSTOK ice core: a continuous isotope temperature record over the last climatic cycle (160,000 years). *Nature* **329**, 403-408.

KERN A. M. AND COMMANDER P. 1993. Cainozoic stratigraphy in the Roe Palaeodrainge of the Kalgoorlie region, Western Australia. *Geological Survey of Western Australia Report* **34**, 85-95.

KESLER S. E. 2005. Ore-forming fluids. *Elements* **1**, 13-18.

KNAUTH L. P. 1994. Petrogenesis of chert. In: HEANEY P. J., PREWITT C. T., & GIBBS G. V. (eds.), *Silica: physical behaviour, geochemistry and materials application. Reviews in Mineralogy and Geochemistry*, **29** Mineralogical Society of America and Geochemical Society, Washington, 233-258.

KU T. L., LOU S., LESLIE B. W. AND HAMMOND D. E. 1992. Decay series disequilibria applied to the study of rock-water interaction and geothermal systems. In: IVANOVICH M. & HARMON R. S. (eds.), *Uranium-series disequilibrium: Application to earth, marine, and environmental sciences*, 2nd Edn, Clarendon Press, Oxford, 631-668.

LANGER K. AND FLÖRKE O. W. 1974. Near infrared absorption spectra ($4,000\text{-}9,000\text{ cm}^{-1}$) of opals and the role of water in these $\text{SiO}_2\text{.nH}_2\text{O}$ minerals. *Fortschritte der Mineralogie* **52**, 17-51.

LANGMUIR D. 1978. Uranium solution-mineral equilibria at low temperatures with application to sedimentary ore deposits. *Geochimica et Cosmochimica Acta* **42**, 547-569.

- LANGMUIR D. AND HERMAN J. S. 1980. The mobility of thorium in natural waters at low temperatures. *Geochimica et Cosmochimica Acta* **44**, 1753–1766.
- LEE S. Y. AND GILKES R. J. 2005. Groundwater geochemistry and composition of hardpans in southwestern Australian regolith. *Geoderma* **126**, 59-84.
- LISENBEY, A.L. 1978. Laramide structure of the Black Hills Uplift, South Dakota-Wyoming-Montana, in Laramide folding associated with basement block faulting in the western United States. In: MATTHEWS V. III (Ed), *Geological Society of America Memoir* **151**, 165-196.
- LUDWIG K. R. 1987. PBDAT for MSDOS, A computer program for IBM PC compatibles for processing raw Pb-U-Th isotope data. *U.S. Geological Survey Open-File Report*, 88–542.
- LUDWIG K. R. 1999. Using Isoplot/Ex, Version 2, A geochronological toolkit for Microsoft Excel, *Berkley Geochronological Center Special Publication No 1a*. Berkeley Geochronological Center, Berkeley, USA.
- LUDWIG K. R., LINDSEY D. A., ZELINSKI R. A. AND SIMMONS K. R. 1980. U-Pb ages of uraniferous opal and implication for the history of beryllium, fluorine, and uranium mineralization at Spor Mountain, Utah. *Earth Planetary Science Letters* **46**, 221-232.
- LUDWIG K. R. AND PACES J. B. 2002. Uranium-series dating of pedogenic silica and carbonate, Crater Flat, Nevada. *Geochimica et Cosmochimica Acta* **66**, 3, 487-506.
- MANN A. W. AND HORWITZ R. C. 1979. Groundwater calcrete deposits in Australia some observations from Western Australia. *Journal of the Geological Society of Australia: An International Geoscience Journal of the Geological Society of Australia* **26**, 293-303.
- MARTIN J. E., FOSTER SAWYER J., FAHRENBACH M. D., TOMHAVE D. W. AND SCHULZ L. D. 2004. Geological Map of South Dakota, 1:500 000. South Dakota Geological Survey General Map 10. *South Dakota Geological Survey*. South Dakota.
- MARSHALL B. D., NEYMARK L. A. AND PETERMAN Z. E. 2003. Estimation of past seepage volumes from calcite distribution in the Topopah Spring Tuff, Yucca Mountain, Nevada. *Journal of Contaminant Hydrology* **62–63**, 237-247.
- MCCOMBS J. A., DAHL P. S. AND HAMILTON M. A. 2004. U-Pb ages of Neoarchean granitoids from the Black Hills, South Dakota, USA: implications for crustal evolution in the Archean Wyoming province. *Precambrian Research* **130**, 161-184.
- MEIJER A. 2002. Conceptual model of the controls on natural water chemistry at Yucca Mountain, Nevada. *Applied Geochemistry* **17**, 793-805.
- MERINO E., DUTTA P., RIPLEY E. M. AND WANG Y. 2001. High-temperature, closed-system origin of agates in basalts: new evidence. *Geological Society of America Annual Meeting*, 158-0.
- MERINO E., WANG Y AND DELOULE É. 1995. Genesis of agates in flood basalts: Twisting of chalcedony fibers and trace element geochemistry. *American Journal of Science* **295**, 1156–1176.
- MILNES A. R AND TWIDALE C. R. 1983. An overview of silicification in Cainozoic landscapes of arid central and southern Australia. *Australian Journal of Soil Research* **21**, 387-410.

- MONTAZER P. AND WILSON W. E. 1984. Conceptual hydrological model of flow in the unsaturated zone, Yucca Mountain, Nevada. *U.S. Geological Survey Water -Resources Investigations Report 84-4345*. U.S. Geological Survey, Colorado.
- MORETE S. 1977. Exploration 1976 Nangcarrong Springs Claim Block, Murchison Region, Western Australia. *Ural Report 56 A6837 I435*, Uranerz Australia. Australia.
- MOXON T. 2002. Agate; a study of ageing. *European Journal of Mineralogy* **14**, 1109-1118.
- MOXON T. AND RIOS S. 2004. Moganite and water content as a function of age in agate. *European Journal of Mineralogy* **16**, 269-278.
- MOXON T. AND REED J. B. 2006. Age and chalcedony from igneous and sedimentary hosts aged from 13 to 3480 Ma: a cathodoluminescence study. *Mineralogical Magazine* **70**, 485-498.
- MOXON T., NELSON D. R. AND ZHANG M. 2006. Agate recrystallisation:evidence from samples found in Archaean and Proterozoic host rocks, Western Australia. *Australian Journal of Earth Sciences* **53**, 235-248.
- MOYER T. C., GESLIN J. K. AND FLINT L. E. 1996. Stratigraphic relations and hydrologic properties of the Paintbrush Tuff nonwelded (PTn) hydrologic unit, Yucca Mountain, Nevada. *U.S. Geological Survey Open-File Report 95-397*, 151.
- MUELLER A. G., CAMPBELL I. H., SCHIÖTTE L., SEVIGNY J. H. AND LAYER P. W. 1996. Constraints on the age of granitoid emplacement, metamorphism, gold mineralization, and subsequent cooling of the Archean greenstone terrane at Big Bell, Western Australia. *Economic Geology* **91**, 896–915.
- MUHLING P. C. AND LOW G. H. 1977. Yalgoo, Western Australia. *Geological Survey of Western Australia 1:250 00 Geological Series Explanatory Notes*. **50-2**, 36.
- MYERS J. S. AND HOCKING R. M. 1998. Geological Map of Western Australia 1:2500000 (13th Edition). Western Australian Geological Survey. Perth.
- NATIONAL RESEARCH COUNCIL. 1992. Ground water at Yucca Mountain, how high can it rise?: *Final report of the Panel on Coupled Hydrologic/Tectonic/Hydrothermal Systems at Yucca Mountain*. Washington, D.C. National Academy Press. 231.
- NEMCHIN A. A., NEYMARK L. A. AND SIMONS S. L. 2006. U-Pb SHRIMP dating of uraniferous opals. *Chemical Geology* **227**, 113-132.
- NEYMARK L. A. 2011. Potential effects of alpha-recoil on uranium-series dating of calcrete. *Chemical Geology* **282**, 98-112.
- NEYMARK L. A. AND AMELIN Y. V. 2008. Natural radionuclide mobility and its influence on U-Th-Pb dating of secondary minerals from the unsaturated zone at Yucca Mountain, Nevada. *Geochimica et Cosmochimica Acta* **72**, 2067-2089.
- NEYMARK L. A., AMELIN Y. V. AND PACES J. B. 2000a. ^{206}Pb - ^{230}Th - ^{234}U - ^{238}U and ^{207}Pb - ^{235}U geochronology of Quaternary opal, Yucca Mountain, Nevada. *Geochimica et Cosmochimica Acta* **64**, 2913-2928.

NEYMARK L. A., AMELIN Y. V., PACES J. B. AND PETERMAN Z. E. 2002. U-Pb ages of secondary silica at Yucca Mountain, Nevada: Implications for the paleohydrology of the unsaturated zone. *Applied Geochemistry* **17**, 709-734.

NEYMARK L. A., AMELIN Y. V., PACES J. B., WHELAN J. F. AND PETERMAN Z. E. 2000b. U-Pb dating of chalcedony and opal above and below the modern water table at Yucca Mountain, southern Nevada. *Geological Society of America Abstracts with Programs* **32**, A-259.

NEYMARK L. A. AND PACES J. B. 1996. Mixed isotopic ages as a consequence of very slow rates of deposition in Quaternary subsurface fracture-coatings. In: *Program and Abstracts of the Geological Society of America Annual Meeting* **28**, N7, A139.

NEYMARK L. A. AND PACES J. B. 2000. Consequences of slow growth for $^{230}\text{Th}/\text{U}$ dating of Quaternary opals, Yucca Mountain, NV, USA. *Chemical Geology* **164**, 143-160.

NEYMARK L. A. AND PACES J. B. 2013. Ion-probe U-Pb dating of authigenic and detrital opal from Neogene-Quaternary alluvium. *Earth and Planetary Science Letters* **361**, 98-109.

NEYMARK L. A., PACES J. B. AND AMELIN Y. V. 1998. Neogene to Quaternary U-Th-Pb geochronology using opal, Yucca Mountain, Nevada, USA. *Mineralogical Magazine* **62A**, 1077-1078.

NEYMARK L. A., PACES, J. B., WOODEN J. L. AND BUESCH D. C. 2007. U-Pb dating of opal in deeply buried soils, Yucca Mountain, Nevada, using secondary ion mass spectrometry. *Geological Society of America Denver Annual Meeting. Abstracts with Programs* **39**, 604.

O'LEARY D. W. 2007. Tectonic models for Yucca Mountain, Nevada. In; STUCKLESS J. S. AND LEVICH R. A. (eds.), *The geology and climatology of Yucca Mountain and vicinity, south Nevada and California*, Geological Society of America Memoirs **199**, 105-153.

OSMOND J. K. AND COWART J. B. 1992. Groundwater. In: IVANOVICH M. & HARMON R.S. (eds.), *Uranium-series disequilibrium: Application to earth, marine, and environmental sciences*, 2nd edn, Clarendon Press, Oxford, 290-334.

OSMOND J. K. AND IVANOVICH M. 1992. Uranium-series mobilization and surface hydrology. In: IVANOVICH M. & HARMON R.S. (eds.), *Uranium-series disequilibrium: Application to earth, marine, and environmental sciences*, 2nd edn, Clarendon Press, Oxford, 259-290.

PACES J.B., LUDWIG K.R., PETERMAN Z.E. AND NEYMARK L.A. 2002. $^{234}\text{U}/^{238}\text{U}$ evidence for local recharge and patterns of ground-water flow in the vicinity of Yucca Mountain, Nevada, USA. *Applied Geochemistry* **17**, 751-779.

PACES J. B., NEYMARK L. A., KWAK L. M. AND PETERMAN Z. E. 1996. U-series dating of secondary minerals in unsaturated-zone tuffs indicating low paleo water flux through Yucca Mountain, Nevada. In: *Program and Abstracts of the Geological Society of America Annual Meeting* **28**, N7, A139.

PACES J. B., NEYMARK L. A., MARSHALL B. D., WHELAN J. F. AND PETERMANZ. E. 1998. Inferences for Yucca Mountain unsaturated zone hydrology from secondary minerals. In: *High Level Radioactive Waste Management, Proceedings of the Eighth Annual International Conference*. American Nuclear Society, Illinois, 36-39.

PACES J. B., NEYMARK L .A., MARSHALL B. D., WHELAN J. F. AND PETERMAN Z. E. 2001. Ages and origins of calcite and opal in the Exploratory Studies Facility tunnel, Yucca Mountain, Nevada. *U.S. Geological Survey Water-Resources Investigations Report 01-4049*, U.S. Geological Survey, Denver.

PACES J. B., NEYMARK L. A., PERSING H. M., WOODEN J. L. 2000. Demonstrating slow growth rates in opal from Yucca Mountain, Nevada, using microdigestion and ion-probe uranium-series dating. In: *Program and Abstracts of the Geological Society of America Annual Meeting* Reno, NV, A-259.

PACES J. B., NEYMARK L. A., WHELAN J. F., WOODEN J. L. LUND S. P. AND MARSHALL B. D. 2010. Limited hydrologic response to Pleistocene climate change in deep vadose zones – Yucca Mountain, Nevada. *Earth and Planetary Science Letters* **300**, 287-298.

PACES J. B., NEYMARK L. A., WOODEN J. L. AND PERSING H. M. 2004a. Improved spatial resolution for U-series dating of opal at Yucca Mountain, Nevada, USA, using ion-microprobe and microdigestion methods. *Geochimica et Cosmochimica Acta* **68**, 1591-1606.

PACES J. B., NEYMARK L. A. AND WOODEN J. L. 2004b. Variations in Pleistocene fracture flow at Yucca Mountain, Nevada, investigated by ion microprobe U-series dating and cathodoluminescence of unsaturated-zone opal. *Geological Society of America Annual Meeting*, Denver, Colorado, November 7-10, 2004, Paper No. **38-2**.

PAN L., WU Y. S., ZHANG K. 2004. A modeling study of flow diversion and focusing in unsaturated fractured rocks. *Vadose Zone Journal* **3**, 233–246.

PARRISH R. R. 1990. U-Pb dating of monazite and its application of geological problems. *Canadian Journal of Earth Sciences* **10**, 1431-1450.

PASHENKO S. E. AND DUBLYANSKY Y. V. 2002a. The role of radon and colloids in distorting the U–Pb age dates of geologically young materials deposited in open cavities. *Geochimica et Cosmochimica Acta* **67**, A581.

PASHENKO S. E. AND DUBLYANSKY Y. V. 2002b. Limitations of the U–Pb method when dating uraniferous opals deposited in open cavities: implications for the thermochronology of Yucca Mountain. In: *Program and Abstracts of the Geological Society of America Annual Meeting* **34**, 309.

PASHENKO S. E. AND DUBLYANSKY Y. V. 2006. Migration of radiogenic lead isotopes during formation of minerals in open cavities in the presence of colloids: theoretical aspects as applied to U–Pb dating of young minerals. *Russian Geology and Geophysics* **47**, 201–215.

PIDGEON R. T. AND HALLBERG J. A. 2000. Age relationships in supracrustal sequences of the northern part of the Murchison Terrane, Archaean Yilgarn Craton, Western Australia: a combined field and zircon U-Pb study. *Australian Journal of Earth Sciences* **47**, 153-165.

PIDGEON R. T. AND WILDE S.A. 1990. The distribution of 3.0 Ga and 2.7 Ga volcanic episodes in the Yilgarn Craton of Western Australia. *Precambrian Research* **48**, 309-325.

PORCELLI D. AND SWARZENSKI P. W. 2003. The behavior of U- and Th-series nuclides in groundwater. In: BOURDON B., HENDERSON G.M., LUNDSTROM C.C. & TURNER S.P. (Eds.), *Uranium-series geochemistry. Reviews in Mineralogy and Geochemistry*, **52** Mineralogical Society of America and Geochemical Society, Washington, 317-361.

- RAMA AND MOORE W. S. 1984. Mechanisms of transport of U-Th series radioisotopes from solids into water. *Geochimica et Cosmochimica Acta* **48**, 395-399.
- RATTE J. C. AND ZARTMAN R. E. 1970. Bear Mountain gneiss dome, Black Hills, South Dakota age and structure. *Geological Society of America Abstracts with Programs* **2**, 345.
- REDDEN J. A., PETERMAN Z. E., ZARTMAN R. E. AND DEWITT E. 1990. U-Th-Pb geochronology and preliminary interpretation of Precambrian tectonic events in the Black Hills, South Dakota. In: LEWRY J.F. AND STAUFFER M.R. (Ed), *The Trans-Hudson orogen: Geological Association of Canada Special Paper* **37**, 229-251.
- REID M. R., COATH C. D., HARRISON T. M. AND MCKEEGAN K. D. 1997. Prolonged residence times for the youngest rhiolites associated with Long Valley Caldera: ^{230}Th - ^{238}U ion microprobe dating of young zircons. *Earth and Planetary Science Letters* **150**, 27-39.
- RICE S. B., FREUND H., HUANG W. L., CLOUSE J. A. AND ISAACS C. M. 1995. Application of Fourier transform infrared spectroscopy to silica diagenesis: the opal-A to opal-CT transformation. *Journal of Sedimentary Research* **A65**, 639-674.
- RIMSTIDT J. D. AND BARNES H. L. 1980. The kinetics of silica-water reactions. *Geochimica et Cosmochimica Acta* **44**, 1683-1699.
- ROGERS J. J. W. AND ADAM J. A. S. 1969. Thorium. In: WEDEPHOL K.H. (Ed), *Handbook of geochemistry*, II-5, Springer-Verlag, Berlin.
- ROGNON R. AND WILLIAMS M. A. J. 1977. Late Quaternary climatic changes in Australia and North Africa: a preliminary interpretation. *Palaeogeography, Palaeoclimatology, Palaeoecology* **21**, 285-327.
- ROSHOLT J. N. AND BARTLE A. J. 1969. Uranium, thorium, and lead systematics in Granite Mountains, Wyoming. *Earth and Planetary Science Letters* **7**, 141-7.
- RUTHERFORD I. E. AND SODDY F. 1902. The cause and nature of radioactivity I, II. *Philosophical Magazine* **IV**, 370-396, 569-585.
- SANDERS C. C. 1974. Calcrete in Western Australia. *Geological Survey of Western Australia Annual Report for 1993*, Geological Survey of Western Australia, Perth, 12-14.
- SASS J. H., LACHENBRUCH A. H., DUDLEY JR. W. W., PRIEST S. S. AND MUNROE R. J. 1988. Temperature, thermal conductivity, and heat flow near Yucca Mountain, Nevada: Some tectonic and hydrologic implications. *U.S. Geological Survey Open-file Report* 87-649.
- SAWYER D. A., FLECK R. J., LANPHERE M. A., WARREN R. G., BROXTON D. E. AND HUDSON M. R. 1994. Episodic Caldera Volcanism in the Miocene southwestern Nevada volcanic field: revised stratigraphic framework, $40\text{Ar}/39\text{Ar}$ geochronology, and implications for magmatism and extension. *Geological Society American Bulletin* **106**, 1304-1318.
- SCHEEPERS R. AND ROZENDAAL A. 1993. Redistribution and fractionation of U, Th and rare earth elements during weathering of subalkaline granites in SW Cape Province, South Africa. *Journal of African Earth Sciences* **17**, 41-50.
- SCHIØTTE L. AND CAMPBELL I. H. 1996. Chronology of the Mount Magnet granite-greenstone terrain, Yilgarn Craton, Western Australia: implications for field based predictions of the relative timing of granitoid emplacement. *Precambrian Research* **78**, 237-260.

SCOTT R. B. AND BONK J. 1984. Preliminary geologic map of Yucca Mountain, Nye County, Nevada with geologic sections. *U.S. Geological Survey Open-File Report 84-494*.

SILVER L. T., WILLIAMS I. S. AND WOODHEAD J. A. 1980. Uranium in granites from the southwestern United States: actinide parent-daughter systems, sites and mobilization, first year report. *U.S. Department of Energy Open File Report GJBX-45*, U.S. Department of Energy, Nevada.

SPAGGIARI C. V. 2006. Interpreted bedrock geology of the northern Murchison Domain, Youanmi Terrane, Yilgarn Craton. *Geological Survey of Western Australia 2006/10*, 1-19.

STACEY J. S. AND KRAMERS J. D. 1975. Approximation of Terrestrial Lead Isotope Evolution by a 2-Stage Model. *Earth and Planetary Science Letters 26*, 207-221.

STROBEL M. L., JARRELL G. J., SAWYER J. F., SCHLEICHER J. R. AND FAHRENBACH M. D. 1999. Distribution of hydrogeologic units in the Black Hills area, South Dakota: U.S. Geological Survey Hydrologic Investigations Atlas **HA-743**, 3 sheets, scale 1:100,000.

STUCKLESS J. S. AND DUDLEY W. W. 2002. The geohydrologic setting of Yucca Mountain, Nevada. *Applied Geochemistry 17*, 659-682.

SZYMANSKI J. S., 1989. Conceptual Consideration of the Yucca Mountain Groundwater System with Special Emphasis on the Adequacy of this System to Accommodate a High-Level Nuclear Waste Repository. *Yucca Mountain Project Office, Nevada Operations Office*. U.S. Department of Energy, Nevada.

SZABO B. J. AND KYSER T. K. 1985. Uranium, thorium isotopic analyses and uranium-series ages of calcite and opal, and stable isotopic compositions of calcite from drill cores UE25a#1, USW G-2 and USW G-3/GU-3, Yucca Mountain, Nevada. *Open file report 85-224*. Department of the Interior Geological Survey.

SZABO B. J. AND KYSER T. K. 1990. Ages and stable isotope compositions of secondary calcite and opal in drill cores from Tertiary volcanic rocks of the Yucca Mountain area, Nevada. *Geological Society of America Bulletin 102*, 1714-1719.

TAYLOR G. AND BUTT C. R. M. 1998. The Australia regolith and mineral exploration. *AGSO Journal of Australian Geology and Geophysics 17*, 55-67.

TERRY D. O. JR. 2001. Paleopedology of the Chadron Formation of northwestern Nebraska: implications for paleoclimatic change in the North American midcontinent across the Eocene-Oligocene boundary. *Paleogeography, Paleoceanography, Paleoecology 168*, 1-38.

THOMPSON R. S., ANDERSON K. H. AND BARTLEIN P. J. 1999. Quantitative paleoclimatic reconstructions from late Pleistocene plant macrofossils of the Yucca Mountain region. *U.S. Geological Survey Open-File Report 99-338*.

TUCCI P. AND BURKHARDT D. J. 1995. Potentiometric-surface map, 1993, Yucca Mountain and vicinity, Nevada. *U.S. Geological Survey Water-Resources Investigations Report 95-4149*.

U.S. DEPARTMENT OF ENERGY. 1998. Yucca Mountain site description; North Las Vegas, Nevada. *Yucca Mountain site characterization project*. U.S. Department of Energy. United States of America.

- VAN DE GRAAFF W. J. E., CROWE R. W. A., BUNTING J. A. AND JACKSON M. J. 1977. Relict early Cainozoic drainages in arid Western Australia. *Zeitschrift Fur Gelomorphologie* **21**, 379-400.
- VAN KRANENDONK M. J. AND IVANIC T. J. 2009. A new lithostratigraphic scheme for the northeastern Murchison Domain, Yilgarn Craton. *Geological Survey of Western Australia, Annual Review* **2007-08**, 34–53.
- VAN KRANENDONK M. J., IVANIC T. J., WINGATE T. D., KIRKLAND C. L. AND WYCZE S. 2013. Long-lived autochthonous development of the Archean Murchison Domain, and implications for Yilgarn Craton tectonics. *Precambrian Research* **229**, 49-92.
- WANG Y. AND MERINO E. 1990. Self –organizational origin of agates: Banding, fiber twisting, composition, and dynamic crystallization model. *Geochimica et Cosmochimica Acta* **54**, 1627-1638.
- WANG Y. AND MERINO E. 1995. Origin of fibrosity and banding in agates from flood basalts. *American Journal of Science* **295**, 49-77.
- WANG J. S. Y. AND NARASIMHAN T. N. 1985. Hydrologic mechanisms governing fluid flow in a partially saturated, fractured, porous medium. *Water Resources Research* **21**, 1861-1874.
- WANG J. S. Y. AND NARASIMHAN T. N. 1993. Unsaturated flow in fractured porous media. In: BEAR J., TSANG C. AND DE MARSILY G. (Eds.), *Flow and Contaminant Transport in Fractured Rock*. Academic Press, California, 325–394.
- WATKINS K. P. AND HICKMAN A. H. 1990. Geological evolution and mineralization of the Murchison Province Western Australia. *Geological Survey of Western Australia Bulletin* **137**. Department of Mines, Western Australia.
- WHELAN J. F., NEYMARK L. A., MOSCATI R. J., MARSHALL B. D. AND ROEDDER E. 2008. Thermal history of the unsaturated zone at Yucca Mountain, Nevada, USA. *Applied Geochemistry* **23**, 1041–1075.
- WHELAN J. F., PACES J. B. AND PETERMAN Z. E. 2002. Physical and stable isotope evidence for formation of secondary calcite and silica in the unsaturated zone, Yucca Mountain, Nevada. *Applied Geochemistry* **17**, 735-750.
- WHELAN J. F., VANIMAN D. T., STUCKLESS J. S. AND MOSCATI R. J. 1994. Paleoclimatic and paleohydrologic records from secondary calcite: Yucca Mountain, Nevada. In: High Level Radioactive Waste Management, *Proceedings of the Fifth International Conference*. American Nuclear Society, Illinois, 2738-2745.
- WHELAN J. F., MOSCATI R. J. 1998. 9 m.y. record of southern Nevada climate from Yucca Mountain secondary minerals. In: High Level Radioactive Waste Management, *Proceedings of the Eighth Annual International Conference*. American Nuclear Society, Illinois, 12–15.
- WHELAN J. F., MOSCATI R. J., ALLERTON S. B. M. AND MARSHALL B. D. 1998. Applications of isotope geochemistry to the reconstruction of Yucca Mountain paleohydrology – status of investigations: June 1996. *U.S. Geological Survey Open-File Report 98-83*. U.S. Geological Survey.
- WIENDENBECK M. AND WATKINS K. P. 1993. A time scale for granitoid emplacement in the Archean Murchison Province, Western Australia, by single zircon geochronology. *Precambrian Research* **61**, 1-26.

WILLIAMS L. A., PARKS G. A. AND CRERAR D. A. 1985. Silica diagenesis, I. Solubility controls. *Journal of Sedimentary Petrology* **55**, 301-311.

WILSON N. S. F., CLINE J. S. AND AMELIN Y. V. 2003. Origin, timing and temperature of secondary calcite-silica mineral formation at Yucca Mountain, Nevada. *Geochimica et Cosmochimica Acta* **67**, 1145-1176.

WU Y., PAN L., ZHANG W. AND BODVARSSON G. S. 2002 Characterization of flow and transport processes within the unsaturated zone of Yucca Mountain, Nevada, under current and future climates. *Journal of Contaminant Hydrology* **54**, 215-247.

ZIELINSKI R. 1982. Uraniferous opal, Virgin Valley, Nevada: conditions of formation and implications for uranium exploration. *Journal of Geochemical Exploration* **16**, 197-216.

ZHANG K., WU Y. AND PAN L. 2006. Temporal damping effect of the Yucca Mountain fracture unsaturated rock on transient infiltration pulses. *Journal of Hydrology* **327**, 235-248.

"Every reasonable effort has been made to acknowledge the owners of copyright material. I would be pleased to hear from any copyright owner who has been omitted or incorrectly acknowledged."